A MULTISCALE STUDY OF NITI SHAPE MEMORY ALLOYS

A Thesis
Presented to
The Academic Faculty

by

Reza Mirzaeifar

In Partial Fulfillment
of the Requirements for the Degree
Doctor of Philosophy in the
George W. Woodruff School of Mechanical Engineering

Georgia Institute of Technology
August 2013

A MULTISCALE STUDY OF NITI SHAPE MEMORY ALLOYS

Approved by:

Prof. Reginald DesRoches, Advisor
School of Civil and Environmental Engineering
Georgia Institute of Technology

Prof. Ken Gall, Advisor
George W. Woodruff School of Mechanical Engineering and School of Materials Science and Engineering
Georgia Institute of Technology

Prof. Arash Yavari, Advisor
George W. Woodruff School of Mechanical Engineering and School of Civil and Environmental Engineering
Georgia Institute of Technology

Prof. Ting Zhu
George W. Woodruff School of Mechanical Engineering
Georgia Institute of Technology

Prof. Hamid Garmestani
School of Materials Science and Engineering
Georgia Institute of Technology

Date Approved: 17 July 2013

To My Wife, Shima,

&

My parents, Maryam and Ahmad.

ACKNOWLEDGEMENTS

I would like to express my deepest gratitude to my advisors, Dr. Reginald DesRoches, Dr. Arash Yavari, and Dr. Ken Gall. I cannot find words to express my gratitude to Dr. DesRoches for his continuous invaluable help and immense support in all stages of this thesis. My sincere appreciation goes to Dr. Yavari for his precious guidance, motivation and support during various stages of my research. I express my appreciation to Dr. Gall for all I have learned from him and for his valuable comments. I would like to thank my advisors for being open to ideas and creating an environment where I could develop my independent thinking and research skills.

I would also like to thank my committee members Dr. Ting Zhu and Dr. Hamid Garmestani for all their valuable insight and comments. In addition I would like to thank Dr. Darel Hodgson from Nitinol Technology Inc. for kindly providing the NiTi samples, and also Dr. Shane Johnson for his help and support in the lab. I also want to extend my gratitude to my fellow labmates and friends who made my life more enjoyable during my PhD studies.

Above all I would like to give my special appreciation to my parents for their endless love, support and encouragement throughout my life and for all sacrifices they have made to give me the opportunity of chasing my dreams. I would also like to thank my brothers and sister for supporting me spiritually throughout my life.

Last but not the least, I would like to thank my beloved wife Shima, whose role in my life was and remains immense, for her sacrifices, emotional support, encouragement, and patience throughout the long journey of my PhD studies.

TABLE OF CONTENTS

LIST OF TABLES

LIST OF FIGURES

SUMMARY

Shape memory alloys (SMAs) are widely used in a broad variety of applications in multiscale devices ranging from nano-actuators used in nano-electrical-mechanical systems (NEMS) to large energy absorbing elements in civil engineering applications. This research introduces a multiscale analysis for SMAs, particularly Nickel-Titanium alloys (NiTi). SMAs are studied in a variety of length scales ranging from macroscale to nanoscale. In macroscale, a phenomenological constitutive framework is adopted and developed by adding the effect of phase transformation latent heat. Analytical closed-form solutions are obtained for modeling the coupled thermomechanical behavior of various large polycrystalline SMA devices subjected to different loadings, including uniaxial loads, torsion, and bending. Thermomechanical responses of several SMA devices are analyzed using the introduced solutions and the results are validated by performing various experiments on some large SMA elements. In order to study some important properties of polycrystalline SMAs that the macroscopic phenomenological frameworks cannot capture, including the texture and intergranular effects in polycrystalline SMAs, a micromechanical framework with a realistic modeling of the grains based on Voronoi tessellations is used. The local form of the first law of thermodynamics is used and the energy balance relations for the polycrystalline SMAs are obtained. Generalized coupled thermomechanical governing equations considering the phase transformation latent heat are derived for polycrystalline SMAs. A three-dimensional finite element framework is used and different polycrystalline samples are modeled. By considering appropriate distributions of crystallographic orientations in the grains obtained from experimental texture measurements of NiTi samples the effects of texture and the tension-compression asymmetry on the thermomechanical response of polycrystalline SMAs are studied. The interaction between the stress state (tensile or compressive), number of grains, and the texture on the thermomechanical response of polycrystalline SMAs is also

studied. For studying some aspects of the thermomechanical properties of SMAs that cannot be studied neither by the phenomenological constitutive models nor by the micromechanical models, molecular dynamics simulations are used to explore the martensitic phase transformation in NiTi alloys at the atomistic level. The martensite reorientation, austenite to martensite phase transformation, and twinning mechanisms in NiTi nanostructures are analyzed and the effect of various parameters including the temperature and size on the phase transformation at the atomistic level is studied. Results of this research provide insight into studying pseudoelasticity and shape memory response of NiTi alloys at different length scales and are useful for better understanding the solid-to-solid phase transformation at the atomistic level, and the effects of this transformation on the microstructure of polycrystal SMAs and the macroscopic response of these alloys.

CHAPTER I

INTRODUCTION

Since the first observation of the shape memory effect (SME) in some alloys [35, 36], studying shape memory alloys (SMAs) has been an active field of research. The unique ability of shape memory alloys in recovering large inelastic strains and also generating high stresses caused a considerable increase in manufacturing devices made of these materials in recent years. The SMAs are now used in applications in a wide variety of devices ranging from simple parts like cell phone antennas or eyeglass frames to complicated devices in mechanical [30, 80, 191], biomechanical [154], aerospace [70], and civil engineering [44].

The unique macroscopic properties of SMAs are based on the solid-solid phase transition of the underlying lattice between a high symmetry cubic lattice (austenite) and a low symmetry lattice (martensite). It is shown that when the SMA atoms are arranged in the cubic austenite lattice form, the entropy and internal energy are higher compare to the martensite lattice. The competition between the entropy and internal energy is reflected in the free energy $F = U - TS$, where U is the internal energy, S is the entropy and T is temperature. It is known that at higher temperatures the entropy overcomes the competition and the austenite phase is preferred while at lower temperatures the internal energy determines the stability and the martensite phase is preferred [83, 84]. For a comprehensive discussion on general properties of SMAs and the phase transformation phenomenon, readers are referred to Müller and Seelecke [133], Müller and Xu [134].

As a result of the solid-solid phase transformation (usually called martensitic phase transformation), and according to the specific way the transformation occurs, SMAs exhibit two significant macroscopic phenomena: the shape memory effect and pseudoelasticity. Each of these two macroscopic responses to mechanical and/or thermal loading is the origin of a vast range of applications for SMAs. In this thesis we mostly focus on the pseudoelasticity of SMAs. This phenomenon occurs when the austenite phase is loaded isothermally to

full transformation to detwinned martensite and then unloaded to the stress free state. During loading, after an initial elastic response, a large amount of inelastic deformation strain is produced. By unloading strain is completely recovered during transformation of martensite back to the austenite. Note that the load-deflection response during a pseudoelastic loading-unloading is temperature dependent.

Shape memory alloys have been used in a broad range of applications in multiscale devices ranging from nano-actuators used in nano-electrical-mechanical systems (NEMS) to large devices used in civil engineering applications. The objective of this thesis is introducing a multiscale analysis for SMAs, particularly Nickel-Titanium alloys (NiTi). Appropriate experiments are also performed for studying the mechanical and thermomechanical response of NiTi shape memory alloys at different length scales. The research covers three different scales, and an appropriate strategy is used for studying the thermomechanical response of the material in each scale.

1.1 Phenomenological macroscale modeling

Considerable increase in the use of active (multifunctional) materials in recent years has led to an excessive interest in analysis of different types of active materials in various shapes. Among several types of active materials, SMAs have been extensively studied and have also been used in a wide variety of applications ranging from biomechanics [154] to aerospace [70], and civil engineering [44].

While searching for new shape memory alloys for improving their pseudoelastic response is still an active field of research [181, 188], a large effort has been made by many researchers to introduce more precise analytical and numerical methods for analyzing pseudoelastic and SME response of SMA structures. The transformation between the two stable phases, called martensitic phase transformation, results in significant challenges in introducing realistic constitutive relations for shape memory alloys. The response of an SMA single crystal is distinctly different from polycrystalline SMAs. There are micromechanical approaches for developing SMA constitutive relations for modeling the behavior of single

crystals [60, 64, 68]. Using micromechanics for capturing the polycrystalline SMAs response can be seen in Patoor et al. [152] and Lagoudas et al. [95]. A polycrystalline SMA consists of many grains with different crystallographic orientations. The phase transformation strongly depends on the crystallographic orientation and modeling the macroscopic response of SMAs by considering different phase transformation conditions in grains is extremely difficult. Considering the complexity of microstructure in polycrystalline SMAs one is forced to use macroscopic phenomenological constitutive equations for modeling the martensitic transformation in large SMA devices. These models are based on continuum thermomechanics and construct a macroscopic free energy potential (Helmholtz or Gibbs free energy) depending on the state and internal variables used to describe the measure of phase transformation. Consequently, evolution equations are postulated for the internal variables and the second law of thermodynamics is used in order to find thermodynamic constraints on the material constitutive equations. In recent years, different constitutive models have been introduced by different choices of thermodynamic potentials, internal state variables, and their evolution equations. For a comprehensive list of one-dimensional and three-dimensional phenomenological SMA constitutive equations with different choices of thermodynamic potentials and internal state variables the reader is referred to Birman [23], Lagoudas et al. [95], and Lagoudas [92]. Besides different choices of potential energy and internal state variables, by considering the experimental results for the response of SMAs, various choices have been made for the hardening function. Among the most widely accepted models, we can mention the cosine model [103], the exponential model [180], and the polynomial model [28]. Lagoudas et al. [96] unified these models using a thermodynamic framework. In this thesis, we use a phenomenological constitutive equation using the Gibbs free energy as the thermodynamic potential, the martensitic volume fraction and transformation strains as the internal state variables, and the hardening function in polynomial form.

Large polycrystalline SMAs are studied in this thesis using a phenomenological macroscopic framework. Micromechanical properties are used for obtaining the macroscopic free energy potential, and the phenomenological constitutive equations are derived using this

energy potential. The macroscopic phenomenological constitutive models are usually implemented in a numerical framework, particularly the finite element method, for simulating the mechanical response of SMA polycrystallines. Along with the recent increase in the use of SMA devices in a wide variety of applications, various numerical methods have been developed for analyzing these devices [107, 116, 161]. Due to the complexity of the nonlinear numerical algorithms that are currently used for modeling shape memory alloys, there are numerous parameters that can affect the accuracy of these methods in analyzing even a simple SMA structure. Also, numerical simulations have many drawbacks in modeling SMAs, including the convergence issues and the time consuming iterative simulations. The necessity of validating the outputs of numerical simulations along with the difficulty of performing experimental tests on SMAs, is the main motivation for seeking analytical or semi-analytical solutions for some SMA devices. In this research, closed-form solutions are presented for studying various SMA devices subjected to different types of loading including uniaxial tension-compression, torsion, bending, and also thick walled SMA cylinders subjected to internal pressure.

1.1.1 Pure torsion of SMA circular bars

Recent studies have shown that SMAs can be efficiently used in improving the response of structures, e.g. buildings and bridges subjected to earthquake loads [9, 10, 44]. The unique ability of SMAs in recovering large scale strains (pseudoelasticity) makes them a desirable option for energy dissipating devices in multiple-frame structures like bridges. Recently, Speicher et al. [173] introduced a new device with shape memory alloy helical springs that can be used as bracing elements in buildings. SMA helical springs were subjected to cyclic loads and it was shown that Nitinol helical springs are efficient devices for recentering and damping in a vast range of structures besides their ability in minimizing the residual deformations in structures after an earthquake. In addition of being potential energy dissipating devices, SMA helical springs have a vast range of industrial applications as active actuators [48, 100].

The simplest method for analyzing helical springs is to assume that each portion of a

spring acts as a straight bar under torsion. It can be shown that when the spring index (the ratio of mean coil radius to the cross section radius) is large and the helix angle is small, this assumption leads to fairly accurate results [190]. In a series of studies Ancker and Goodier [6–8] investigated the accuracy of this assumption in some detail and modified it to obtain a more accurate solution for helical springs considering the curvature effects. In one of the first studies on SMA helical springs, Tobushi and Tanaka [184] considered the pure torsion assumption for analyzing a helical spring under axial load. They used Tanaka's constitutive model [177] but in the stress-strain relation the hardening during phase transformation is ignored and the material is treated as perfectly plastic. Although this assumption simplifies the solution remarkably, experimental results show that the hardening response in stress-strain relations for polycrystalline SMAs can not be ignored. In another effort for analyzing SMA helical springs, Toi et al. [185] modified the Brinson's one-dimensional constitutive model [29] for SMAs and implemented it in an incremental finite element formulation using Timoshenko beam elements. In their study, helical SMA springs are modeled numerically and simulation outputs are compared with experimental results.

In the present study, pure torsion of SMA bars with circular cross sections is considered. This is the first step in analysis of SMA helical springs with large spring index and small helix angle. We should mention that torsion of SMA bars have been studied by several researchers in recent years. Lim and McDowell [108] reported the behavior of SMA thin-walled tubes subjected to axial-torsional proportional and nonproportional loading by conducting several experiments. Chung et al. [39] presented a numerical simulation for pseudoelastic behavior of shape memory alloy circular rods under tension/torsion combined loadings. Brinson's phase transformation formulation and an analogy with traditional plasticity were used.

Clearly pure torsion is an important benchmark problem that can be used in validating various numerical simualtions of SMAs. Pure torsion is also important as a first step in analysis of SMA springs. A general three-dimensional constitutive relation for shape memory alloys is first reduced to an appropriate one-dimensional form suitable for implementation in pure torsion. An explicit expression is derived for shear stress as a function of geometric specifications, material constants and shear strain. Response of circular bars in torsion is

carefully analyzed by considering different possibilities that may happen for various loading levels and some case studies are presented for investigating the effect of material properties and temperature on the behavior of circular bars in loading and unloading conditions.

1.1.2 Helical SMA springs and pure torsion of SMA curved bars

The pseudoelastic response of SMAs is hysteretic. This phenomenon provides ideal energy dissipating and damping capabilities for SMAs and enables them to be used in passive control of structures under earthquake loads. DesRoches and Delemont [43] investigated the effectiveness of shape memory alloy restrainer bars to reduce the seismic vulnerability of bridges. DesRoches and Smith [44] provided a critical review of the state-of-the-art in the use of shape memory alloys for applications in seismic resistant design. McCormick et al. [123] studied seismic vibration control using superelastic shape memory alloys by considering NiTi wires and bars. Auricchio et al. [15] studied the damping properties of SMAs numerically and experimentally by considering uniaxial loading of SMA bars and wires of different size and chemical composition. Recently, Speicher et al. [173] proposed a new device with an SMA helical spring as a potential bracing element in buildings. It is shown that this device can be used as an efficient recentering system to improve the performance of structures during seismic events.

During an earthquake event, the helical spring device will likely see 20-25 cycles into the transformation stress range, depending on the properties of the structure in which it is being used, and the magnitude of the ground shaking. It is well known that SMAs experience changes in behavior (typically referred to as the fatigue effect) with increased cycling resulting in an accumulation of irreversible strain and a slight decrease in forward transformation stress. Previous studies by the second author have shown that these changes have minimal effect on the resulting behavior of the system in which the SMA is used [10]. Moreover, this effect can be minimized by mechanical training of the SMA material prior to implementation in the device [122]. In this thesis, we will not consider the fatigue effect in analyzing the SMA springs. The necessity of having an accurate analytical and numerical modeling of the proposed SMA device besides its vast applications [48, 100, 104] motivated

the authors to seek analytical and numerical solutions for these springs.

In one of the first studies of SMA helical springs, Tobushi and Tanaka [184] analyzed a helical spring under axial load assuming that each small segment is in pure torsion. They used Tanaka's constitutive model [177] but in the stress-strain relation the hardening during phase transformation is ignored and the material is treated as perfectly plastic. Although this assumption simplifies the solution remarkably, experimental results show that the hardening response in stress-strain relations for polycrystalline SMAs can not be ignored. In another effort Toi et al. [185] modified the Brinson's one-dimensional constitutive model [29] and implemented it in an incremental finite element formulation using Timoshenko beam elements. In their study, SMA helical springs are modeled numerically and simulation outputs are compared with experimental results. Using beam elements for analysis of helical springs decreases the computational time remarkably but an accurate stress analysis cannot be done and as we will see in the sequel, the stress and martensitic volume fraction distributions in the cross section of SMA helical springs cannot be captured using beam elements.

In this thesis, we propose three different analysis strategies besides the experimental results for studying SMA helical springs subjected to axial load. The simplest method for analyzing helical springs is to assume that each portion of the spring acts as a straight bar under torsion. It can be shown that when the spring index (the ratio of mean coil radius to the cross section radius) is large and the helix angle is small, this assumption leads to fairly accurate results [190]. Readers are referred to Ancker and Goodier [6, 7, 8] for a detailed discussion on the accuracy of this assumption and modifications to obtain a more accurate solution for elastic helical springs considering the curvature and pitch effects. In the present study, as the first approximation we introduce an exact solution for analysis of SMA helical springs by ignoring the curvature and pith effects. Although the analysis of helical springs based on the straight bar torsion model (SBTM) is of enough accuracy for most practical helical elastic springs, it will be shown that in the case of an SMA spring, curvature plays a significant rule and an accurate stress analysis in the cress section cannot be obtained based on SBTM. On the other hand, nearly all the practical helical springs have small to

large spring indices but small pitch angles [190]. In order to capture a more accurate stress analysis and covering a wider range of practical springs, the curvature correction is added to SBTM and a curved bar torsion model (CBTM) is presented. In addition to these two analytical models, a three-dimensional finite element simulation method is developed for analysis of SMA helical springs. Experimental test data on a Nitinol spring subjected to axial compression are compared with the analytical, and numerical results, the accuracy of each method in predicting the global force-displacement and stress analysis is investigated. It is shown that the SBTM calculates the global force-displacement response with good accuracy but for a precise stress and martensitic volume fraction distribution, the curvature correction should be used. Both analytical methods are remarkably fast compared to the finite element simulations and can be used for studying the effect of changing any of the material or geometrical parameters on the spring response even for an optimization process that needs a large number of simulations. In the numerical results, in addition to the comparisons that are presented for studying the accuracy of different proposed methods, many case studies are presented for studying the effect of changing material parameters and the ambient temperature on the spring hysteretic response. Some recommendations are also made for improving SMA springs as dampers and energy absorbing devices.

1.1.3 SMA thick-walled cylinders subjected to internal pressure

Highly non-linear coupled material response of SMAs – a consequence of the solid-to-solid phase transformation – restricts the applicability of the available solution methods for analysis of many SMA structures among which finite element method is the most common. There are rare attempts for analyzing even simple SMA structures using analytical or semi-analytical methods. The availability of closed-form solutions for SMA structures is primarily affected by the constitutive relations in use. In addition to the constitutive relations, the complexity of the structure can play a key role in finding closed-form solutions. Lagoudas et al. [94] presented a one-dimensional reduction of the unified SMA constitutive relations of Lagoudas et al. [96] and using this model proposed closed form expressions for the martensitic volume fraction and transformation strains in uniaxial loading of an SMA prismatic

bar. However, an explicit constitutive relation for the axial stress component as a function of axial displacement was not introduced; a numerical method was necessary for solving the loading/unloading response of bars (see Lagoudas [92]). They used this solution technique in conjunction with finite element method for dynamic analysis of polycrystalline SMA rods. Feng and Sun [51] presented an algorithm for analyzing shakedown of SMA structures subjected to cyclic or varying loads. They used a plasticity framework and calculated a lower bound of loads for transformational shakedown of SMAs without the necessity of a step-by-step analysis along the loading history.

In another attempt for finding semi closed-form solutions for two-dimensional SMA structures, Birman [24] considered an infinite shape memory alloy plate with a circular hole subjected to biaxial tensile stresses applied at infinity. The solution was obtained by the plane stress assumption based on the two-dimensional form of Tanaka's constitutive relations [178]. He presented two different solutions for stress analysis that are called by him "closed-form-solution" and "exact solution". In the latter, it is assumed that for the SMA with phase transformation, the ratio of the radial to circumferential stress is identical to that in the elastic case. As it will be shown in this thesis, this assumption cannot be justified. In the "closed-form" solution, there are some unrealistic simplifying assumptions; the elastic stress distribution in the region in which phase transformation has started is considered for calculating the inner boundary of pure austenite region. As we will show shortly, this assumption can be used only for some specific loading conditions and by spread of the transformed region, this assumption becomes less and less accurate. Additionally, in Birman's closed-form solution, for obtaining the stress-strain relations, the transformation strains are related to the martensitic volume fraction by constant multipliers. Although this assumption remarkably simplifies the solution, it can be replaced by a more realistic formulation that will be presented in this thesis. One of the main challenges in obtaining closed-form solutions for structures made of phase transforming materials is introducing an accurate solution for the regions that are completely transformed to martensite. Although the response of the structure is elastic for the fully martensite regions, it is necessary to consider the history of loading and the final values of transformation strain components to

obtain the solution in these regions. In the present semi-analytic analysis we will explain how to obtain the solution for these regions.

In a recent attempt, Mirzaeifar et al. [127] developed an exact solution for pure torsion of shape memory alloy circular bars. A general three-dimensional constitutive relation for shape memory alloys was first reduced to an appropriate one-dimensional form suitable for pure torsion. An explicit expression was derived for shear stress as a function of geometric specifications, material constants, and shear strain that enabled the solution to be obtained analytically. Response of circular bars in torsion was then analyzed by considering different possibilities that may happen in various loading levels.

Among various shapes in which SMAs are used, cylindrical shells are of particular interest in applications including spinal vertebrae spacers [115], special cardiovascular stents [91], and active catheters [98], which are in the form of thin shells. Li and Sun [102] studied the superelastic response of nano-grained SMA micro tubes under uniaxial tension. Their experimental results show that the nucleated macroscopic martensite band in a micro tube under uniaxial loading takes the shape of a spiral that surrounds the tube axis for several circles. Feng and Sun [52] studied the response of SMA micro tubes subjected to a combined tensile and torsional loading experimentally. He and Sun [72] studied the effect of tube geometry on the helix-shaped deformation domains that are observed in SMA tubes during the stress-induced martensitic phase transformation of the material under uniaxial stretching.

In this thesis, SMA thick-walled cylinders are considered. Two extreme cases of long and short cylinders can be reduced to plane strain and plane stress, respectively. SMA short cylinders or rings have many engineering applications, e.g. the SMA pipe couplings [30, 80], tube wall joints [191], and active stiffener strips [86]. Shape memory alloys have suitable mechanical characteristics that make them desirable in pressure vessels and pipes as active layers, which are in the form of long thick cylinders [143, 144].

In the present study, SMA short and long thick-walled cylinders are considered. For short cylinders in the form of a ring or stiffener strip, in the absence of axial forces, plane stress condition is a good approximation. Long cylinders can be reduced to a plane

strain problem. Using these assumptions the three-dimensional problem is reduced to a two-dimensional one. Constitutive equations are reduced to appropriate two-dimensional relations and an explicit expression is obtained for the martensitic volume fraction and transformation strains in both cases. The cylinder is partitioned into a finite number of annular regions and simplifying assumptions are made in each annular region in order to obtain an explicit expression for the stress components as functions of displacements. These stress-displacement expressions are then used to write the equilibrium equations in terms of radial displacements in each annular region. The global solution for the cylinder is finally obtained by putting the solutions of annular regions together and by enforcing the continuity conditions at the interfaces and at the inner and outer boundary regions. Our semi-analytic approach can be used to validate numerical methods like the finite element method.

1.1.4 superelastic bending of shape memory alloy beams

In many SMA devices, the SMA instrument is subjected to local or global bending. This is the main motivation for several reported works on bending analysis of SMAs in the literature. The bending of beams made of single crystal SMAs and the propagation of phase boundaries was studied by Purohit and Bhattacharya [160]. They used additional kinetic relations in conjunction with the constitutive assumptions and balance laws to determine the propagation of phase boundaries. The solutions for single crystalline beams consider a jump in the material properties before and after the phase transformation, and there is no intermediate condition between these two cases. In polycrystalline materials, which are used in the majority of SMA engineering applications, the phase transformation does not occur simultaneously in all the grains. This causes a considerable difference between the material properties in single crystals and polycrystalline samples. While the material in a beam made of a single crystal SMA is austenite or martensite with some phase boundaries, the continuous change of material properties in polycrystalline SMAs makes modeling the bending of beams made of these materials a challenging problem (see [5, 182, 183] for studying polycrystalline SMAs using a constitutive model based on the response of single

crystal SMAs).

Among the solutions presented for modeling bending in polycrystallline SMAs a large number are purely numerical [13, 118]. In an early work, Atanackovic and Achenbach [12] used a simplified multi-linear constitutive equation for obtaining the moment-curvature relation of a pseudoelastic beam. Plietsch et al. [157] presented a closed-form solution for bending of SMA beams by considering a multi-linear stress-strain response. Auricchio and Sacco [18] studied the SMA wires subjected to cyclic stretching-bending loads using a one-dimensional constitutive model. In their work the thermomechanical coupling was also considered and the finite element method was used for solving the governing equations. Auricchio et al. [19] implemented one-dimensional constitutive equations into a finite element model for studying the shape memory effect for SMA beams in bending. The material response in tension and compression was assumed asymmetric and the numerical results were compared with experiments. Recently, Flor et al. [54] presented some numerical simulation and experimental analysis of SMA wires in bending. They considered tension-compression asymmetry in their model and a numerical scheme was used for calculating the bending response. Their model is developed only for the loading phase; unloading was not studied in either their experiments or numerical simulations.

The existing numerical methods of modeling SMAs suffer from the high computational cost, and convergence difficulties particularly for modeling the unloading process or considering the geometric nonlinearities. The results obtained by these numerical methods are highly sensitive to a large number of secondary parameters, e.g. the mesh size, tolerance criteria, number of loading steps. The numerical simulations may give erroneous results due to an improper choice for any of these parameters. On the other hand, the semi-analytic solutions in the literature are based on oversimplified constitutive relations or use unrealistic simplifying assumptions. In this thesis, we introduce a closed-form solution for analyzing the superelastic bending of shape memory alloys. A three-dimensional constitutive model is reduced to an appropriate one-dimensional constitutive equation. Closed-form expressions are obtained for the martensitic volume fraction and stress distributions in the cross section

of SMA beams in bending. The EulerBernoulli beam theory (assuming the plane cross sections remain plane and perpendicular to the centerline after deformation) is used and the the bending moment-curvature relation is obtained analytically. A method is presented for solving the bending of superelastic SMAs analytically. In addition to the J_2-based model that predicts a symmetric response in tension and compression, a more accurate solution based on $J_2 - I_1$ transformation function is also presented and the effect of considering the tension-compression asymmetry (which is a well-known response for most SMAs [5, 59]) in the bending response is studied.

It is worth noting that for modeling the tension-compression asymmetry, the $J_2 - J_3$ model gives more accurate results because of its capability in modeling the negative volume change during martensitic transformation [162]. However, The $J_2 - J_3$-based model cannot be used for developing a closed-form solution in this thesis. Experiments have shown that the $J_2 - I_1$-based model can predict the superelastic response of SMAs with a good accuracy for all the parameters except the volumetric transformation strain (see Section 4 in Qidwai and Lagoudas [162]). Also, the material parameters in the $J_2 - I_1$-based model can be calibrated for modeling a realistic volumetric transformation strain, but in this case the tension-compression asymmetry is not modeled correctly, and we will not use this calibration method in our solution.

An important capability of our model is its applicability in extracting the tensile properties of materials when the compression and bending test results are available but the tension properties are practically difficult to be measured experimentally, e.g. in the micro scale applications of SMAs.

SMAs have recently attracted considerable interest for applications as actuators in micro-electro-mechanical systems (MEMS) [22, 82, 168] due to their relatively high work output per unit volume [90]. One of the traditional methods for studying the mechanical properties of a material in the micro and nano scales is testing pillars. These pillars are produced by focused ion beam (FIB) micromachining [189]. Recently, the pseudoelasticity, crystal orientation effect, and size dependency have been extensively studied experimentally

for nickel-titanium and Cu-Al-Ni micropillars [40, 57, 81, 117, 165]. In order to have a precise description of the micropillars response in MEMS applications, it is ideal to extract the material response in tension, compression, and bending experimentally. However, among the reported works on studying the shape memory micropillars response the majority of experiments are performed for compressive loading [57, 81, 117, 165], and there are a few experimental works on bending [40]. While performing bending tests on micropillars one faces some technical difficulties [40]. Tensile tests in nano and micro scales are considerably more difficult because a special geometric shape should be created at the pillar head for attaching the tensile tool to the pillar [87, 88]. As we explain in §4.6, our analytical solution for bending can be used for extracting the tensile properties when the bending and compressive responses are known.

The material properties in compression are calibrated from the available experimental data. The material-independent properties in tension are assumed, and bending is simulated using these properties in tension and compression. The predicted bending response is compared with the experimental data, and a trial and error approach is used for improving the assumed tensile material properties for finding the best match between the experimental and analytical results in bending. It is worth noting that the iterations for improving the initial guess are performed without a considerable computational cost; the closed-form solutions are obtained in a few seconds. Such a method is extremely time consuming if the available numerical solutions are used for modeling the bending response. We will implement this method for analyzing bending of a nickel-titanium micropillar using the available experimental data.

1.2 Analysis of the coupled thermomechanical response of SMAs

In the next step, the effect of phase transformation induced latent heat is added to the solutions obtained based on the phenomenological constitutive framework and the coupled thermomechanical response of SMAs is also studied.

The martensitic phase transformation in SMAs is associated with generation or absorption of latent heat in forward (austenite to martensite) and reverse (martensite to austenite)

transformations. This has been shown in many experiments and the heat of transformation and the associate temperatures for the start and end of forward/reverse martensitic transformation can be determined by differential scanning calorimeter or DSC [3, 71, 112]. In the majority of the previous works in which loading is assumed quasi-static, it is assumed that material is exchanging the phase transformation-induced latent heat with the ambient such that the SMA device is always isothermal and in a temperature identical with the ambient during loading and unloading. We will show in this thesis that the definition of quasi-static loading that guarantees an isothermal process is not absolute; it is affected by a number of parameters, e.g. the ambient condition and size of the structure. In other words, it will be shown that a very slow loading rate that can be considered a quasi-static loading for an SMA wire with a small diameter may be far from being quasi-static and isothermal for a bar with larger diameters. This size effect phenomenon has been reported previously in some experiments [44, 124], but we are not aware of any analytical or numerical analysis of this phenomenon in the literature. In some of the previously reported works in the literature, the effect of this latent heat and its coupling with mechanical response of SMAs was considered along with some simplifying assumptions.

In the literature, two extreme cases of isothermal and adiabatic processes are considered for quasi-static and dynamic loading conditions, respectively. Chen and Lagoudas [38] considered impact-induced phase transformation and assumed adiabatic conditions for solving the problem of SMA rods subjected to an impact load. Lagoudas et al. [94] considered the dynamic loading of polycrystalline shape memory alloy rods. They compared the effect of considering adiabatic and isothermal assumptions on the response of SMA bars subjected to axial loading. In some other works, more realistic heat transfer boundary conditions capable of modeling a heat exchange greater than zero (corresponding to the adiabatic process) and less than the maximum possible value (corresponding to an isothermal process) are considered. In these works, to simplify the coupled thermomechanical relations, it is assumed that the nonuniformity of temperature distribution is negligible. Auricchio et al. [16] studied the rate-dependent response of SMA rods by taking the latent heat effect and the heat exchange with ambient into consideration. The authors used the fact that for a wire

with a small diameter temperature in the cross section is distributed uniformly during loading and unloading. A simplified one-dimensional constitutive relation and an approximate heat convection coefficient were considered for obtaining the thermomechanical governing equations. In a similar work, Vitiello et al. [187] used the one-dimensional Tanaka's model [177, 179] in conjunction with the energy balance equation to take into account the latent heat effect. The solution was restricted to very slender cylinders with small Biot numbers. In this special case, temperature nonuniformity in the cross section is neglected and the governing equations are simplified by assuming a uniform temperature distribution at each time increment. Messner and Werner [125] studied the local increase of temperature near a moving phase transformation front due to the latent heat of phase transformation in one-dimensional SMAs subjected to tensile loading. They modeled the effect of phase transformation latent heat by a moving heat source. A constant value is considered for the latent heat generated by phase transformation. This assumption is unrealistic for polycrystalline SMAs because the amount of generated heat is specified by a set of coupled equations and depends on many variables, e.g. stress and martensitic volume fraction. Iadicola and Shaw [77] used a special plasticity-based constitutive model with an up-down-up flow rule within a finite element framework and investigated the trends of localized nucleation and propagation phenomena for a wide range of loading rates and ambient thermal conditions. The local self-heating due to latent heat of phase transformation and its effect on the number of nucleations and the number of transformation fronts were studied. The effect of ambient condition was also considered by assuming various convection coefficients.

Bernardini and Vestroni [20] studied the non-linear dynamic response of a pseudoelastic oscillator embedded in a convective environment. In this work, a simplified one-dimensional equation is considered by assuming the whole pseudoelastic device in a uniform temperature at each time step and the dynamic response of pseudoelastic oscillator is studied. Chang et al. [34] presented a thermomechanical model for a shape memory alloy (SMA) wire under uniaxial loading implemented in a finite element framework. They assumed the temperature distribution in the cross section of wire to be uniform but a nonuniform distribution is assumed along the SMA wire. It is assumed that the phase transformation initiates in

a favorable point of the wire (this point is defined by a geometric imperfection or stress concentration). The phase transformation front moves along the wire with a specific finite velocity. They studied the movement of phase transformation front and the temperature change along the wire analytically and experimentally. In this thesis, we will consider a three-dimensional phenomenological macroscopic constitutive relation in conjunction with the energy balance equation for deriving the coupled thermomechanical equations governing the SMAs considering the effect of latent heat and the heat flux in the material due to temperature nonuniformity caused by the generated heat during forward phase transformation and the absorbed heat during the reverse phase transformation. The constitutive relations can be used for calculating the continuum tangent moduli tensors for developing numerical formulations [126, 161], but coupling these equations with the energy relation in the rate form is extremely difficult in numerical methods. An alternative method for analysis of SMAs is using analytic and semi-analytic solutions with an explicit form of the constitutive relations for a specific geometry and loading [127, 129, 131]. In this thesis, for the special one-dimensional cases of pure torsion and uniaxial tension-compression, an explicit expression is given for the stress-strain relation and the coupled energy equation is given in a rate form. For deriving the one-dimensional governing equations, a nonuniform distribution is considered in the cross section for all the variables including the stress, temperature, transformation strain and martensitic volume fraction. In the uniaxial loading case it is assumed that the material does not contain a favorable point for the initiation of phase transformation along the length (all the parameters are independent of axial location). These equations are discretized for wires and bars with circular cross sections using an explicit finite difference method. The discretized form of convection boundary conditions is also derived. For modeling SMA wires and bars operating in still air and exposed to air or fluid flow with a known speed, free and forced convection coefficients are calculated for slender wires and thick cylindrical bars in air and fluid using the experimental and analytical formulas in the literature. The results of the present formulation are compared with some experiments to verify the capability of our approach in modeling the rate dependency and calculating accurate temperature changes during loading-unloading. Several case studies

are presented for studying the loading rate and ambient effects on the coupled thermomechanical response of SMA wires and bars in uniaxial loading and also SMA bars subjected to pure torsion.

The thermomechanical response is studied experimentally as well. An infrared camera is used in the experiments to measure the temperature changes due to the phase transformation latent heat at the surface of SMA specimens subjected to various loadings. The theoretical coupled thermomechanical models can be calibrated using the experimentally measured temperatures at the surface. The calibrated model is then used for calculating the temperature distribution inside the device (which is practically difficult to be measured in tests). The obtained full temperature distribution is the basis for studying the complex effects of size, loading rate, and ambient condition on the response of SMA devices.

1.3 Micromechanical modeling

Shape memory alloys, particularly the near-equiatomic TiNi alloys, are currently used in applications in a wide variety of devices. SMA materials used in most applications are polycrystalline in nature. The cast SMA materials contain a random distribution of crystal orientations in the grains. However, in most applications, SMAs are processed by casting, followed by hot-working (i.e. drawing or rolling) and suitable heat treatments [182]. It is known that the deformation processing has a significant effect on the response of polycrystalline SMAs. For example, while the material response for a cast NiTi sample is almost symmetric in tension and compression, a cast, hot rolled, then cold drawn material exhibits a very large asymmetry in tension-compression response [56]. In some special samples, the maximum transformation strain in tension is reported more than two times the maximum transformation strain in compression for the hot rolled, then cold drawn material with a significant difference between the stress levels in the stress-strain plateau [56]. This significant tension-compression stress-strain asymmetry in processed SMAs is due to the strong crystallographic texture. Gall and Sehitoglu [59] studied the role of texture on tension-compression asymmetry in polycrystalline NiTi. The crystallographic texture of some NiTi samples was determined by X-ray diffraction. The samples they studied were cold drawn,

annealed, straightened, centerless ground, aged 0.25 h at 550°C, and machined into dog-bone specimens with the loading axis parallel to the drawing direction. It was shown that for these samples the majority of the grains are oriented along the [111] crystallographic direction, which is soft under tensile loading and hard under compression. As a result of this textured orientation, a significant tension-compression asymmetry is observed in the stress-strain response of NiTi samples.

Macroscopic phenomenological constitutive frameworks are efficient tools for modeling the mechanical or thermomechanical response of polycrystalline SMAs in engineering applications [99, 129, 146, 162, 180]. However, these models are not appropriate for modeling the response of SMAs at the microscale, and consequently are not able to model some important aspects of the response of SMAs such as the phase transformation initiation and propagation among the grains. As mentioned earlier, the crystallographic texture is a key property in studying polycrystalline SMAs. A simplified method for studying the role of texture on the mechanical response of polycrystalline SMAs is using phenomenological constitutive equations and selecting appropriate transformation functions for modeling the asymmetry in SMAs [14, 162]. However, a more precise analysis of the crystallographic texture and its effects on the thermomechanical response can only be achieved by using constitutive models based on the micro-mechanics of single crystals for studying polycrystal structures [62, 183]. In these models, a polycrystalline material can be modeled by assigning a separate crystal orientation to each grain. Using this method, a preferred orientation of the crystallographic texture can be modeled, which leads to the actual thermomechanical response of polycrystalline SMAs without using an approximate phenomenological framework.

In the micromechanical models, the overall transformation strain is related to the stress-free transformation strains of all the correspondence martensite variant pairs (CVPs) obtained from the crystallographic data by using a volume fraction coefficient for each variant. Some studies based on these micromechanical models ignore the microstructure of grains and the intergranular interactions by using different averaging schemes [49, 59, 114, 151, 175]. Although these models are appropriate for studying the global response of the material, and

are capable of analyzing important properties such as the role of texture on the tension-compression asymmetry [59], the grain boundary interactions, and the intergranular effects are not considered in these models. To further understand the behavior of polycrystalline shape memory alloys, it is necessary to use the micromechanical constitutive frameworks in conjunction with an accurate model of microstructure by simulating the polycrystal as a cluster of grains. The finite element method is an efficient tool for studying polycrystalline SMAs using the micromechanical framework. Gall et al. [62] and Lim and McDowell [110] employed a three-dimensional finite element modeling to examine the thermomechanical behavior of a polycrystalline NiTi shape memory alloy in the pseudoelastic regime. In these works, a simplified geometric model was used in which all the grains are assumed as identical hexagonal prisms. Thamburaja and Anand [182] used a crystal-mechanics-based constitutive framework and the finite element modeling for studying the effect of crystallographic texture on the response of polycrystalline SMAs. They modeled the microstructure in the polycrystal by assuming all the grains as cubes stacked adjacent to each other forming a larger cube representing the polycrystal structure. A similar microstructure was used for studying the superelastic behavior of textured NiTi polycrystalline materials in tension-torsion [183] and the thermal effects in the superelasticity of crystalline SMAs [5]. To further understand the intergranular interactions in polycrystalline SMAs, we use a more realistic polycrystal structure by implementing Voronoi tessellations to generate the polycrystalline grain structure of micro-scaled NiTi shape memory alloys.

Another significant contribution of the present work is in presenting an accurate thermomechanical framework for studying the effect of phase transformation latent heat in polycrystalline SMAs. There are several attempts in the literature for coupling the latent heat effect to the mechanical response of polycrystalline SMAs. A group of these works use the averaging schemes in studying the polycrystal, and because the physical shape of grains is not modeled, the temperature should also be studied as an averaged parameter in the whole material [49]. In another attempt to better understand the thermomechanical response of polycrystalline SMAs, Anand and Gurtin [5] coupled the energy balance equation with the mechanical constitutive relations for the simplified microstructure model with

cubic grains. In this work the strain rate effect on the response of NiTi shape memory alloys was studied. Lim and McDowell [110] introduced a simplified expression for the volumetric heat generation due to phase transformation and studied the coupled thermomechanical response of textured polycrystal samples in which the microstructure was constructed by identical grains as hexagonal prisms. In this work, it was assumed that the volumetric heat generation is proportional to the rate of change of overall martensitic volume fraction by using a constant relating the heat generation to the sum of the rate of martensitic volume fraction changes in all the active variants. In this thesis, we use a comprehensive description of the energy balance equation in SMAs for calculating the latent heat during phase transformation. It will be shown that the volumetric heat generation/absorption is related to the rate of change of martensitic volume fractions and stress. Derivatives of the latent heat with respect to temperature and strain are also calculated for implementation in an incremental finite element framework.

Several case studies are considered in this thesis for further understanding some important phenomena in the thermomechanical response of polycrystalline SMAs. The role of texture on tension-compression asymmetry is studied and it is shown that adding more grains with a favorable crystal orientation changes the semi-symmetric response of an untextured sample toward an asymmetric response observed in single crystals. The effect of crystallographic texture on the phase transformation initiation and propagation is studied and it is shown that while the phase transformation propagates almost equally in tension and compression for an untextured material, the spatial distribution of the martensite phase is remarkably more rapid in compression when the grains have a favorable [111] crystallographic orientation.[1] The effects of size and the number of grains on the mechanical response of polycrystalline SMAs subjected to both tensile and compressive loads are studied and it is shown that the number of grains has a strong effect on the initiation of phase transformation at the grain boundaries and the propagation of martensite region inside the polycrystal. Some case studies are presented for micro-scaled polycrystalline beams subjected to bending

[1]It is worth noting that the spatial spread of phase transformation *initiation* is more rapid in tension as reported by Gall et al. [62]. However, we study the propagation of martensitic volume fraction as a function of average strain as discussed in §4.5.2.

and it is shown how the stress and martensitic volume fraction distributions are affected by the texture in the beam. The load-deflection response of textured and untextured beams in bending are also compared. The thermomechanical response of polycrystalline SMAs is studied by implementing the coupled energy balance and constitutive equations. It is shown that the latent heat is the origin of rate dependency in the response of SMAs at the microscale. Also it is shown that the effect of loading rate on changing the slope of stress-strain plateau and changing the hysteresis area is consistent with the results previously observed at the macroscale. The effect of latent heat on the propagation of phase transformation between the grains is also studied and it is shown that the phase transformation is slightly suppressed in fast loadings due to the temperature changes. The temperature changes at the microscale are compared with those obtained previously at the macroscale based on experimental observations and phenomenological modelings. It is shown that the temperature changes at different scales have similarities.

1.4 Nanoscale study

The shape memory effect (SME) and the pseudoelastic (PE) response of SMAs are both due to the ability of changing the crystallographic structure by a displacive phase transformation between the cubic austenite parent phase (the high symmetry B2 phase preferred at high temperatures) and the low symmetry martensite phase (monoclinic B19' crystal structure preferred at low temperatures) in response to mechanical and/or thermal loadings. There are two major motivations for studying the microscopic behavior of SMAs: better understanding of the macroscopic behavior of SMAs, and analyzing the nanoscale actuators made of these materials. SMAs have recently attracted considerable interest for applications as actuators in micro-electro-mechanical systems (MEMS) [22, 82, 168] due to their relatively high work output per unit volume [90].

In recent years, several works have been reported on studying PE and SME in various metals and alloys. Sato et al. [166] used the embedded atom method (EAM) in molecular dynamics (MD) simulation to study the microscopic mechanism for phase transformation of NiTi alloy. Stress-induced martensitic transformation was studied for tensile simulation

using four different strain rates and it was shown that the relationship between stress and martensite ratio does not depend on the strain rate. The phase transformation between the B2 and B19' structures was studied in Ni-Ti and it was shown that there are multiple pathways between the parent phase and the martensite phase regardless of the strain rate. In this work a simulation box with free surfaces was considered and the initial temperature was kept constant at 0K by thermal control using the velocity scaling method for structural relaxation from the initial state. Park [149] studied the martensitic phase transformation in Ni-Al nanowires. In this work, atomistic simulation was used to demonstrate the stress-induced martensitic phase transformation in intermetallic nickel aluminum (NiAl) nanowires. It was shown that the martensitic phase transformation occurs by the propagation and annihilation of {101} twinning planes and transforms the initially B2 NiAl nanowires to a body-centered tetragonal (BCT) phase. PE was studied for these nanowires and it was shown that the instability of the resulting BCT phase allows pseudoelastic recovery of inelastic strains on the order of 40% at all deformation temperatures. The MD simulations in this work were performed using the the Sandia developed code, Warp [158]. The thermomechanical behavor of NiAl nanowires was studied by Sutrakar and Mahapatra [176]. In this work, The asymmetric stress-strain behavior under tension/compression in an initial $< 100 >$ B2-NiAl nanowire was investigated considering two different surface configurations. It wa shown that under tensile loading, the nanowire undergoes a stress-induced martensitic phase transformation from an initial B2 phase to body centered tetragonal (BCT) phase via twinning along {110} plane with failure strain of $\sim$0.30. On the other hand, a compressive loading causes failure of these nanowires via brittle fracture after compressive yielding, with a maximum failure strain of $\sim$-0.12. It was observed that the brittle fracture in compression occurs via slip along {110} plane without any phase transformations. In addition to the alloys, similar PE and SME responses are discovered recently in single crystalline Cu [106], Ni [105], Au [46], and some other fcc metallic nanowires [150] through atomistic simulations.

In this work, we focus on the MD simulation of NiTi alloys. Zhong et al. [195] studied the structure and geometrical limit of nanoscale twins in NiTi shape memory alloys using

atomistic simulations. In this work, the crystallographic theory of twinned martensite was combined with atomistic simulations, and the nanoscale twins and martensitic phase transformations in NiTi with the multilattice structure was studied. Molecular dynamics simulations was used to predict the phase transformation temperatures, which obtained consistent with experimental measurements. The shape memory behavior of a NiTi nanoparticle was analyzed using molecular dynamics simulations by Mutter and Nielaba [136]. By considering a nano particle with different Ni contents, it was shown that heating the particle leads to a shape memory effect without a phase transition to the austenite, but by variant reorientation and twin boundary formation at a certain temperature. Recently [196] performed MD simulations to study the atomistic mechanisms governing the pseudoelasticity and shape memory in NiTi nanostructures. For a $< 110 >$ oriented nanopillar subjected to compressive loadingunloading, they observed either a pseudoelastic or shape memory response, depending on the applied strain and temperature that control the reversibility of phase transformation and deformation twinning.

In this thesis, we study the stress induced phase transformation in NiTi alloys with a focus on tensile loading-unloading. In addition to the temperature and stress induced austenite to martensite phase transformation, the reorientation in martensite at lower temperatures is also studied. The alloyed NiTi system is created by generating atomic positions as in the bulk corresponding to the B2 crystal structure which is equivalent to a body centered cubic (BCC) lattice with the Ni atoms at the corners of the unit cell and a single Ti atom at the body center. Different crystal orientations are considered and the effect of orientation on the stress-strain response and hysteretic behavior is studied. Also, by considering different simulation boxes and various temperatures, the size and temperature effects on the pseudoelastic response of NiTi alloys are studied. Several new aspects of the austenite-martensite phase transformation and reorientation of martensite variants are introduced in Chapter 5.

In summary, this thesis has the following major objectives:

- Introducing fast and accurate analyzing strategies for large SMA tools with engineering applications by developing analytical solutions for modeling various shapes of

SMA devices subjected to different loading conditions.

- Studying the thermomechanical coupling in SMAs by adding the phase transformation latent heat to the closed-form solutions and making these models more accurate in studying various SMA devices

- Better understanding the phase transformation and thermomechanical coupling in SMAs by studying the microstructure and analyzing size, texture and loading rate effects at microscale

- Fundamental study of martensitic phase transformation in NiTi at the atomistic level by analyzing temperature driven phase transformation, martensite reorientation, stress induced phase transformation and twinning in NiTi systems at nanoscale.

This thesis is organized as follows. The macroscopic phenomenological models, developing closed-form solutions based on these models, the thermomechanical theoretical studies in macroscale, and the experiments for studying the thermomechanical response of large polycrystalline SMAs are given in Chapter 2. The thermomechanical coupling in SMAs due to the phase transformation latent heat is studied in Chapter 3. The micromechanical model is explained in Chapter 4. Chapter 5 contains various studies on NiTi shape memory alloys at nanoscale.

CHAPTER II

PHENOMENOLOGICAL MACROSCALE MODELING

2.1 Introduction

In this chapter various large polycrystalline SMA devices are studied using a phenomenological macroscopic framework. The macroscopic phenomenological constitutive models for studying the martensitic phase transformation are derived based on continuum thermomechanics framework in which a macroscopic free energy potential (Helmholtz or Gibbs free energy) is postulated depending on the state and internal variables used to describe the measure of phase transformation. Evolution equations are constructed for calculating the change of internal variables and the second law of thermodynamics is used in order to find thermodynamic constraints on the material constitutive equations. In recent years, different constitutive models have been introduced by different choices of thermodynamic potentials, internal state variables, and their evolution equations (a brief review of these models is presented in Chapter 1). In this chapter, we develop a phenomenological constitutive framework using the Gibbs free energy as the thermodynamic potential, the martensitic volume fraction and transformation strains as the internal state variables, and the hardening function in polynomial form. Two different transformation functions are considered: a J_2-based model with symmetric tension-compression response, and a $J_2 - I_1$-based model for considering the tension-compression asymmetry that is observed in experiments. Closed-form solutions are presented for studying various SMA devices subjected to different types of loading including uniaxial tension-compression, torsion, bending, and also thick walled SMA cylinders subjected to internal pressure. In each case, the constitutive equations are reduced to an appropriate one or two dimensional form for studying the pseudoelastic response of SMAs. Closed-form expressions are given for the stress and martensitic volume fraction distributions and the governing equations are obtained analytically.

2.2 Pure Torsion of SMA Circular Bars

In this section, an analytical solution is presented for the pure torsion of SMA bars with circular cross sections. We reduced a general phenomenological macroscopic constitutive model for polycrystalline SMAs and obtained an explicit expression for the shear stress in circular SMAs bars in pure torsion. It is shown that in the most general case, the cross section in loading and unloading may be divided into three regions with different responses. The stress-strain relation in these regions is derived and the shear stress distribution is calculated for different twist angles both in loading and unloading. Several case studies are presented for analyzing the response of SMA bars with different material properties at various temperatures. The twist angle is obtained as a function of the applied torque in loading-unloading cycles. The presented solution can be used as a benchmark problem for validating numerical simulations of SMAs. This method will also be exploited to analyze SMA helical springs in the next section.

2.2.1 General constitutive model

In the present study, we consider the transformation strain $\boldsymbol{\epsilon}^t$ and the martensitic volume fraction ξ as the internal state variables.[1] The Gibbs free energy G for polycrystalline SMAs is given by [28, 162]:

$$G(\boldsymbol{\sigma}, T, \boldsymbol{\epsilon}^t, \xi) = -\frac{1}{2\rho}\boldsymbol{\sigma} : \mathbb{S} : \boldsymbol{\sigma} - \frac{1}{\rho}\boldsymbol{\sigma} : \left[\boldsymbol{\alpha}\left(T - T_0\right) + \boldsymbol{\epsilon}^t\right] + c\left[(T - T_0) - T\,\ln\left(\frac{T}{T_0}\right)\right] - s_0 T + u_0 + \frac{1}{\rho}f(\xi), \tag{2.1}$$

where, $\mathbb{S}, \boldsymbol{\alpha}, c, \rho, s_0$ and u_0 are the effective compliance tensor, effective thermal expansion coefficient tensor, effective specific heat, mass density, effective specific entropy, and effective specific internal energy at the reference state, respectively. The symbols $\boldsymbol{\sigma}$, T, T_0, $\boldsymbol{\epsilon}^t$ and ξ represent the Cauchy stress tensor, temperature, reference temperature, transformation strain and martensitic volume fraction, respectively. All the effective material properties

[1] The portion of strain that is recovered due to reverse phase transformation from detwinned martensite to austenite is considered as the transformation strain. See Patoor et al. [152] for a detailed description of the transformation strain and martensitic volume fraction.

are assumed to vary with the martensitic volume fraction (ξ) as follows

$$\mathbb{S} = \mathbb{S}^A + \xi\Delta\mathbb{S}, \boldsymbol{\alpha} = \boldsymbol{\alpha}^A + \xi\Delta\boldsymbol{\alpha}, c = c^A + \xi\Delta c, s_0 = s_0^A + \xi\Delta s, u_0 = u_0^A + \xi\Delta u_0, \quad (2.2)$$

where the superscripts A and M represent the austenite and martensite phases, respectively. The symbol $\Delta(.)$ denotes the difference of a quality $(.)$ between the martensitic and austenitic phases, i.e. $\Delta(.) = (.)^M - (.)^A$. In (2.1), $f(\xi)$ is a hardening function that models the transformation strain hardening in the SMA material. In the Boyd-Lagoudas' polynomial hardening model, this function is given by

$$f(\xi) = \begin{cases} \frac{1}{2}\rho b^M \xi^2 + (\mu_1 + \mu_2)\,\xi, & \dot{\xi} > 0, \\ \\ \frac{1}{2}\rho b^A \xi^2 + (\mu_1 - \mu_2)\,\xi, & \dot{\xi} < 0, \end{cases} \quad (2.3)$$

where, ρb^A, ρb^M, μ_1 and μ_2 are material constants for transformation strain hardening. The first condition in (2.3) represents the forward phase transformation ($A \to M$) and the second condition represents the reverse phase transformation ($M \to A$). The constitutive relation of a shape memory material can be obtained by using the total Gibbs free energy as

$$\boldsymbol{\epsilon} = -\rho\frac{\partial G}{\partial \boldsymbol{\sigma}} = \mathbb{S} : \boldsymbol{\sigma} + \boldsymbol{\alpha}\,(T - T_0) + \boldsymbol{\epsilon}^t. \quad (2.4)$$

Considering the fact that any change in the state of the system is only possible by a change in the internal state variable ξ [25], the evolution of the transformation strain tensor is related to the evolution of the martensitic volume fraction as

$$\dot{\boldsymbol{\epsilon}}^t = \boldsymbol{\Gamma}\dot{\xi}, \quad (2.5)$$

where $\boldsymbol{\Gamma}$ represents a transformation tensor related to the deviatoric stress tensor and determines the flow direction as

$$\boldsymbol{\Gamma} = \begin{cases} \frac{3}{2}\frac{H}{\overline{\sigma}}\boldsymbol{\sigma}', & \dot{\xi} > 0, \\ \\ \frac{H}{\overline{\epsilon}^{tr}}\boldsymbol{\epsilon}^{tr}, & \dot{\xi} < 0. \end{cases} \quad (2.6)$$

In (2.6), H is the maximum uniaxial transformation strain and $\boldsymbol{\epsilon}^{tr}$ represents the transformation strain at the reverse phase transformation. The terms $\boldsymbol{\sigma}'$, $\overline{\sigma}$ and $\overline{\epsilon}^{tr}$ are the

deviatoric stress tensor, the second deviatoric stress invariant and the second deviatoric transformation strain invariant, respectively, and are expressed as

$$\boldsymbol{\sigma}' = \boldsymbol{\sigma} - \frac{1}{3}(\mathrm{tr}\,\boldsymbol{\sigma})\mathbf{I}, \quad \overline{\sigma} = \sqrt{\frac{3}{2}\boldsymbol{\sigma}' : \boldsymbol{\sigma}'}, \quad \overline{\epsilon}^{tr} = \sqrt{\frac{3}{2}\boldsymbol{\epsilon}^{tr} : \boldsymbol{\epsilon}^{tr}}, \tag{2.7}$$

where, $\mathbf{I}$ is the identity tensor.

An additional constraint on the material behavior is obtained by using the Second Law of Thermodynamics in the form of positivity of the rate of entropy production density [162]:

$$\boldsymbol{\sigma} : \dot{\boldsymbol{\epsilon}}^t - \rho\frac{\partial G}{\partial \xi}\dot{\xi} = \pi\dot{\xi} \geq 0, \tag{2.8}$$

where, π is a thermodynamic force and can be obtained by substituting (2.1) and (2.5) into (2.8) as

$$\begin{aligned}\pi = \boldsymbol{\sigma} : \boldsymbol{\Gamma} + \frac{1}{2}\boldsymbol{\sigma} : \Delta\mathbb{S} : \boldsymbol{\sigma} + \Delta\boldsymbol{\alpha} : \boldsymbol{\sigma}\,(T - T_0\,) \\ +\rho\Delta c\left[(T - T_0) - T\,\ln\left(\frac{T}{T_0}\right)\right] + \rho\Delta s_0 T - \frac{\partial f}{\partial \xi} - \rho\Delta u_0.\end{aligned} \tag{2.9}$$

Now, the transformation function that controls the onset of direct and reverse phase transformation is defined as

$$\Phi = \begin{cases} \pi - Y, & \dot{\xi} > 0, \\ -\pi - Y, & \dot{\xi} < 0, \end{cases} \tag{2.10}$$

where, Y is a measure of internal dissipation due to microstructural changes during phase transformation. The transformation function represents the elastic domain in the stress-temperature state. In other words, when $\Phi < 0$ the material response is elastic and the martensitic volume fraction does not change ($\dot{\xi} = 0$). During the forward phase transformation from austenite to martensite ($\dot{\xi} > 0$) and the reverse phase transformation from martensite to austenite ($\dot{\xi} < 0$), the state of stress, temperature and martensitic volume fraction should remain on the transformation surface, which is characterized by $\Phi = 0$. It can be seen that transformation surface in the stress-temperature space is represented by two separate faces that are defined by $\xi = 0$ and $\xi = 1$. Any state of stress-temperature inside the inner surface ($\xi = 0$) represents the austenite state with an elastic response. Outside the surface $\xi = 1$, the material is fully martensite and behaves elastically. For any

state of stress-temperature on or in between these two surfaces the material behavior is inelastic and a forward transformation occurs. A similar transformation surface exists for the reverse phase transformation.

2.2.2 Reduction of the constitutive equations for pure torsion

Analysis of solid members with a uniform cross section of general shape in torsion is a classical problem in elasticity and is commonly referred to as the Saint-Venant's problem after the French mathematician Barré de Saint-Venant. In 1784, Coulomb [41] presented a solution for prismatic bars with circular cross sections in torsion. For many years, this formulation was used for torsional analysis of bars with arbitrary cross sections. Later it was shown that the Coulomb's formulation, which ignores the cross section warpage[2] is not valid, in general. There were many unsuccessful attempts for formulating the torsion of a bar with a general cross section consistent with elasticity equations (for a historical review see [73]). Finally, In 1874, Saint-Venant published the correct formulation of torsion problem in a series of three papers [73]. Based on the general solution of Saint-Venant, it can be shown that the no warpage assumption is valid for bars with circular cross section [172] and some other special cross sections [37]. According to Saint-Venant's solution the state of stress and strain is one dimensional and shear strain varies linearly from the central axis toward the outer radius.[3]

In the case of circular bars, the general three-dimensional constitutive relations introduced in the previous section can be reduced to a one-dimensional constitutive equation. The stress, strain, and transformation strain tensors have the following forms:

$$\boldsymbol{\sigma} = \begin{bmatrix} 0 & 0 & 0 \\ 0 & 0 & \tau_{\theta z} \\ 0 & \tau_{\theta z} & 0 \end{bmatrix}, \ \boldsymbol{\epsilon} = \begin{bmatrix} 0 & 0 & 0 \\ 0 & 0 & \epsilon_{\theta z} \\ 0 & \epsilon_{\theta z} & 0 \end{bmatrix}, \ \boldsymbol{\epsilon}^t = \begin{bmatrix} 0 & 0 & 0 \\ 0 & 0 & \epsilon^t_{\theta z} \\ 0 & \epsilon^t_{\theta z} & 0 \end{bmatrix}, \tag{2.11}$$

[2] In a cross section with warpage, the planar cross sections perpendicular to the axis of the bar before deformation will not remain planar after deformation.

[3] Considering a cross section in the xy plane (z is along the bar axis), the state of shear strain at a point in the cross section is, $\gamma_{zx} = 2\epsilon_{zx} = \theta\left(\frac{\partial \psi}{\partial x} - y\right)$ and $\gamma_{zy} = 2\epsilon_{zy} = \theta\left(\frac{\partial \psi}{\partial y} + x\right)$, where θ is the twist angle per unit length and ψ represents the warping function that represents the cross section deformation along the z axis. Clearly, zero warpage is identical with the linear distribution of shear strains through the thickness [172].

where $\tau_{\theta z}$, $\epsilon_{\theta z}$ and $\epsilon^t_{\theta z}$ are the shear stress, shear strain and transformation shear strains, respectively. Using tr$\boldsymbol{\sigma} = 0$ in (2.7) the deviatoric stress tensor will be the same as the stress tensor, $\boldsymbol{\sigma}^{'} = \boldsymbol{\sigma}$. The second deviatoric stress and transformation strain invariants are reduced to read:

$$\overline{\sigma} = \sqrt{3}|\tau_{\theta z}|, \quad \overline{\epsilon}^{tr} = \frac{2}{\sqrt{3}}|\epsilon^{tr}_{\theta z}|. \tag{2.12}$$

The transformation tensor for the pure torsion is expressed as:

$$\mathbf{\Gamma}^{+} = \frac{\sqrt{3}}{2} H \operatorname{sgn}(\tau_{\theta z}) \begin{bmatrix} 0 & 0 & 0 \\ 0 & 0 & 1 \\ 0 & 1 & 0 \end{bmatrix}, \; \mathbf{\Gamma}^{-} = \frac{\sqrt{3}}{2} H \operatorname{sgn}(\epsilon^{tr}_{\theta z}) \begin{bmatrix} 0 & 0 & 0 \\ 0 & 0 & 1 \\ 0 & 1 & 0 \end{bmatrix}, \tag{2.13}$$

where sgn(.) is the sign function and the superscripts + and - for $\mathbf{\Gamma}$ represent the forward and inverse phase transformations, respectively. Substituting (2.13) into (2.9) and (2.10) and using the following relation between the constitutive model parameters:

$$\begin{aligned} &\rho\Delta u_0 + \mu_1 = \frac{1}{2}\rho\Delta s_0(M_s + A_f), \rho b^A = -\rho\Delta s_0(A_f - A_s), \\ &\rho b^M = -\rho\Delta s_0(M_s - M_f), Y = -\frac{1}{2}\rho\Delta s_0(A_f - M_s) - \mu_2, \\ &\mu_2 = \frac{1}{4}(\rho b^A - \rho b^M), \end{aligned} \tag{2.14}$$

explicit expressions for the martensitic volume fraction in direct and inverse phase transformation are obtained as

$$\xi^{+} = \frac{1}{\rho b^M} \left\{ \sqrt{3} H |\tau_{\theta z}| + 2\tau^2_{\theta z}\Delta S_{44} + f^{+}(T) \right\}, \tag{2.15}$$

$$\xi^{-} = \frac{1}{\rho b^A} \left\{ \sqrt{3} H \tau_{\theta z} \operatorname{sgn}(\epsilon^{tr}_{\theta z}) + 2\tau^2_{\theta z}\Delta S_{44} + f^{-}(T) \right\}, \tag{2.16}$$

where

$$f^{+}(T) = \rho\Delta c \left[(T - T_0) - T \ln\left(\frac{T}{T_0}\right) \right] + \rho\Delta s_0(T - M_s), \tag{2.17}$$

$$f^{-}(T) = \rho\Delta c \left[(T - T_0) - T \ln\left(\frac{T}{T_0}\right) \right] + \rho\Delta s_0(T - A_f). \tag{2.18}$$

The parameters M_s and A_f are the martensitic start and austenite finish temperatures, respectively. By substituting the explicit expression of the martensitic volume fraction in

(2.5) and after integrating from zero to an arbitrary time, the transformation shear strain can be calculated. The constitutive relation (2.4) is now reduced to read:

$$\epsilon_{\theta z} = \frac{1+\nu}{E_A + \xi^{\pm}\ (E_M - E_A)}\tau_{\theta z} + \frac{1}{\rho b^{\pm}}\ \left\{\frac{3}{2}H^2\tau_{\theta z} + \sqrt{3}H\tau_{\theta z}^2\ \aleph^{\pm}\ \Delta S_{44} + \frac{\sqrt{3}}{2}H\ \aleph^{\pm}\ f^{\pm}(T)\right\}, \tag{2.19}$$

where ν is Poisson's ratio that is assumed to be the same for both phases. The + and - symbols are used for the direct and reverse phase transformations, respectively, and the other parameters are: $\aleph^{+} = \mathrm{sgn}(\tau_{\theta z})$, $\aleph^{-} = \mathrm{sgn}(\epsilon^{tr}_{\theta z})$, $\rho b^{+} = \rho b^{M}$ and $\rho b^{-} = \rho b^{A}$. For a bar with a circular cross section, the shear strain in (2.19) can be related to twist angle per unit length as $\epsilon_{\theta z} = \frac{1}{2}r\theta$, where r is the distance from the axis of the bar. Substituting (2.15) into (2.19) and considering the special case in which both the shear stress and the shear transformation strains are positive, (2.19) can be rewritten as:

$$\tau_{\theta z}^4 + F_1\tau_{\theta z}^3 + (F_2 + F_2^* r\theta)\tau_{\theta z}^2 + (F_3 + F_3^* r\theta)\tau_{\theta z} + (F_4 + F_4^* r\theta) = 0, \tag{2.20}$$

where,

$$\begin{aligned}
F_1 &= -\frac{\sqrt{3}H}{\Delta S_{44}},\\
F_2 &= \frac{1}{4}\,\frac{3\,\Delta E\,H^2 + 4\,\Delta E\,\Delta S_{44} f^{\pm}(T) + 2\,\rho\,b^{\pm}E_A\Delta S_{44}}{\Delta E\,{\Delta S_{44}}^2},\\
F_3 &= \frac{\sqrt{3}}{12}\,\frac{6\,\Delta E\,H^2 f^{\pm}(T) + 3\,\rho\,b^{\pm}E_A H^2 + 2(1+\nu)\,(\rho\,b^{\pm})^2}{H\Delta E\,{\Delta S_{44}}^2},\\
F_4 &= \frac{1}{4}\,\frac{f^{\pm}(T)\,(\Delta E\,f^{\pm}(T) + \rho\,b^{\pm}E_A)}{\Delta E\,\Delta S_{44}^2},\\
F_2^* &= -\frac{1}{6}\,\frac{\rho\,b^{\pm}\sqrt{3}}{\Delta S_{44}H},\\
F_3^* &= -\frac{1}{4}\,\frac{\rho\,b^{\pm}}{\Delta S_{44}^2},\\
F_4^* &= -\frac{\sqrt{3}}{12}\,\frac{\rho\,b^{\pm}\,(\Delta E\,f^{\pm}(T) + \rho\,b^{\pm}E_A)}{H\Delta E\,\Delta S_{44}^2},
\end{aligned} \tag{2.21}$$

in which $\Delta E = (E_M - E_A)$. The relation (2.20) is a quartic equation that can be solved analytically using Ferrari's method[4] for finding the shear stress $\tau_{\theta z}$ as a function of twist

[4]In 1540, Lodovico Ferrari found the solution of quartic equation by reducing it to a cubic equation. However, because the solution for cubic equations was not available at the time, his solution was not published. Four years later Ferrari's teacher, Gerolamo Cardano, published the solution of both quartic and cubic equations in his book *Ars Magna* [32].

angle in an arbitrary radius as:

$$\tau_{\theta z} = \wp^{\pm}(r,\theta). \tag{2.22}$$

The explicit expression for the shear stress (2.22) is given by using the constants in (2.21) and introducing the following parameters:

$$\begin{aligned}
&G_1 = -\frac{3}{8}(F_1)^2 + F_2,\ G_1^* = F_2^*,\ G_2 = \frac{1}{8}(F_1)^3 - \frac{1}{2}F_1F_2 + F_3,\ G_2^* = -\frac{1}{2}F_1F_2^* + F_3^*,\\
&G_3 = -\frac{3}{256}(F_1)^4 + \frac{1}{16}(F_1)^2F_2 - \frac{1}{4}F_1F_3 + F_4,\ G_3^1 = \frac{1}{16}(F_1)^2F_2^* - \frac{1}{4}F_1F_3^* + F_4^*,\\
&K_1 = -\frac{1}{12}(G_1)^2 - G_3,\ K_1^* = -\frac{1}{6}G_1G_1^* - G_3^1,\ K_1^\diamond = -\frac{1}{12}(G_1^*)^2,\\
&K_2 = -\frac{1}{108}(G_1)^3 + \frac{1}{3}G_1G_3 - \frac{1}{8}(G_2)^2,\ K_2^* = -\frac{1}{36}(G_1)^2G_1^* + \frac{1}{3}G_1G_3^* + \frac{1}{3}G_3G_1^* - \frac{1}{4}G_2G_2^*,\\
&K_2^\diamond = -\frac{1}{36}G_1G_1^* + \frac{1}{3}G_1^*G_3^* - \frac{1}{8}(G_2^*)^2,\ K_2^\circ = -\frac{1}{108}(G_1^*)^3,
\end{aligned} \tag{2.23}$$

and,

$$\begin{aligned}
\mathcal{R} = &-\frac{1}{2}K_2 - \frac{1}{2}K_2^*r\theta - \frac{1}{2}K_2^\diamond r^2\theta^2 - \frac{1}{2}K_2^\circ r^3\theta^3\\
&+\Bigg[\frac{1}{4}(K_2)^2 + \frac{1}{2}K_2K_2^*r\theta + \frac{1}{2}K_2K_2^\diamond r^2\theta^2 + \frac{1}{2}K_2K_2^\circ r^3\theta^3 + \frac{1}{4}(K_2^*)^2r^2\theta^2 +\\
&\quad\frac{1}{2}K_2^*r^3\theta^3K_2^\diamond + \frac{1}{2}K_2^*K_2^\circ r^4\theta^4 + \frac{1}{4}(K_2^\diamond)^2r^4\theta^4 + \frac{1}{2}K_2^\diamond K_2^\circ r^5\theta^5 + \frac{1}{4}(K_2^\circ)^2r^6\theta^6 +\\
&\quad\frac{1}{27}(K_1)^3 + \frac{1}{9}(K_1)^2K_1^*r\theta + \frac{1}{9}(K_1)^2K_1^\diamond r^2\theta^2 + \frac{1}{9}K_1(K_1^*)^2r^2\theta^2 + \frac{2}{9}K_1K_1^*K_1^\diamond r^3\theta^3 +\\
&\quad\frac{1}{9}K_1(K_1^\diamond)^2r^4\theta^4 + \frac{1}{27}(K_1^*)^3r^3\theta^3 + \frac{1}{9}(K_1^*)^2K_1^\diamond r^4\theta^4 + \frac{1}{9}K_1^*(K_1^\diamond)^2r^5\theta^5 + \frac{1}{27}(K_1^\diamond)^3r^6\theta^6\Bigg]^{\frac{1}{2}},\\
&\mathcal{U} = (\mathcal{R})^{\frac{1}{3}},\ \mathcal{Q} = K_2 + K_2^*r\theta + K_2^\diamond r^2\theta^2 + K_2^\circ r^3\theta^3,\ \alpha = G_1 + G_1^*r\theta,\ \beta = G_2 + G_2^*r\theta,\\
&\mathcal{P} = K_1 + K_1^*r\theta + K_1^\diamond r^2\theta^2,\ \mathcal{Y} = -\frac{5}{6}\alpha + \mathcal{U} - \frac{1}{3}\frac{\mathcal{P}}{\mathcal{U}},\ \mathcal{W} = \sqrt{\alpha + 2\mathcal{Y}}.
\end{aligned} \tag{2.24}$$

The quartic equation (2.20) has four roots. Among these, only one satisfies the continuity condition for the shear stress distribution at r_1 (see (2.26)). This admissible solution is expressed as:

$$\tau_{\theta z} = \wp^{\pm}(r,\theta) = -\frac{1}{4}F_1 + \frac{1}{2}\mathcal{W} - \frac{1}{2}\sqrt{-3\alpha - 2\mathcal{Y} - 2\frac{\beta}{\mathcal{W}}}, \tag{2.25}$$

where $\wp^+$ and $\wp^-$ are solutions for loading and unloading, respectively. In loading, $\wp^+(r,\theta)$ is calculated by considering the parameters with (+) sign in (2.21) and in unloading $\wp^-(r,\theta)$ is calculated by considering the parameters with (-) sign in (2.21).

Table 2.1: SMA material parameters

Material constants	A generic SMA (Material I) [161]	$Ni_{50.8}Ti_{49.2}$ (Material II) [173]	Material III [185]
E^A	70.0×10^9Pa	48.5×10^9Pa	34×10^9Pa
E^M	30.0×10^9Pa	38.2×10^9Pa	28.5×10^9Pa
$\nu^A = \nu^M$	0.3	0.42	0.33
α^A	22.0×10^{-6}/K	-	-
α^{M}	10.0×10^{-6}/K	-	-
$\rho\Delta c = c^M - c^A$	0.0 J/(m^{3}K)	0.0 J/(m^{3}K)	0.0 J/(m^{3}K)
H	0.05	0.047	0.047
$\frac{d\sigma}{dT}$	7.0×10^6Pa/K	6.0×10^6Pa/K	9.8×10^6Pa/K
A_f	315.0 K	288.15 K	292.6 K
A_s	295.0 K	258.15 K	273.7 K
M_s	291.0 K	258.15 K	252.9 K
M_f	271.0 K	218.15 K	220.8 K

2.2.3 Torsion of a SMA bar with circular cross section

In this section several case studies are presented for torsion of circular SMA bars. In these numerical examples, two different sets of material parameters are used as shown in Table 2.1. The first set of properties are some generic values given in [161] and later used by many researchers in reporting numerical simulations of SMAs. The second set of parameters are based on an experimental work by Jacobus *et al.* [79] on $Ni_{50}Ti_{50}$ alloy. The required material constants for the reduced constitutive model are extracted from the experimental data by Qidwai and Lagoudas [162].

2.2.4 Thin-walled SMA tube

As the first case study, a thin-walled SMA tube with radius $R = 3mm$ and length $L = 4cm$ is considered. The tube is fixed at one end and the other end is twisted. The material properties (Material I) in Table 2.1 are used. The temperature is assumed to be $T = 315$K. We compare the results of the present analytic solution with a finite element simulation. The details of implementing the reduced constitutive equation in a displacement based finite element formulation is given in [126]. The three-dimensional constitutive relations of §2.5.1 are used and an appropriate user subroutine (UMAT) is written by FORTRAN in the commercially available finite element program ABAQUS that enables this code to model SMA structures using solid elements and some two-dimensional elements. The developed

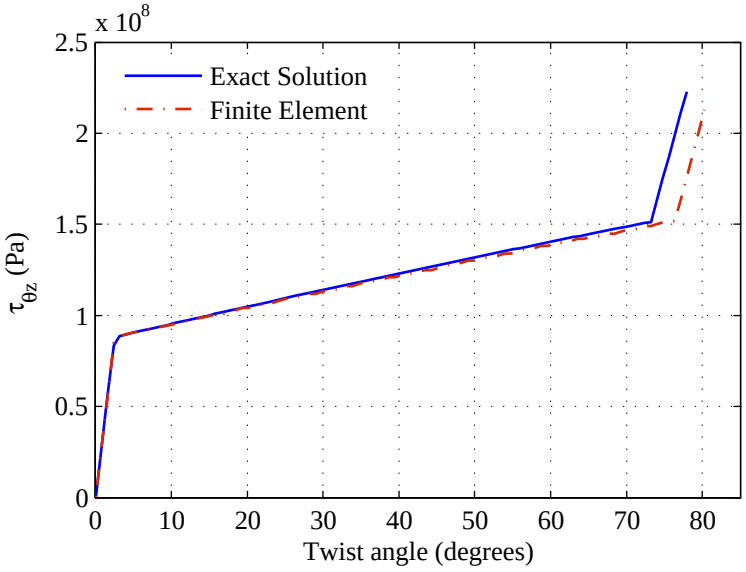

Figure 2.1: Torsion of a SMA thin walled tube in loading.

finite element code was validated by previously reported works for SMA structures using some case studies like uniaxial tension, bending of beams and deflection analysis of cylindrical panels [126]. In modeling torsion problems, quadratic axisymmetric elements with additional twist degree of freedom are used.[5]

As the thickness of the tube is very small[6] the radial change of martensitic volume fraction and stress is negligible. As a result, only one element is used in the radial direction. Although the stress distribution is constant along the axial direction, for avoiding high aspect ratio in the elements, 40 elements are used in the axial direction. The torsional loading is divided into 200 steps and the tolerance of 1×10^{-6} is considered for the convergence of transformation function (see Qidwai and Lagoudas [161]).

Figure 2.30 compares the results of the present formulation with those of the finite element simulations. Note that in the finite element results, the average stress value in the middle of thickness is shown. As it is seen, the numerical simulation predicts the completion of phase transformation in a larger twist angle compared to the exact solution. This difference can be reduced by increasing the number of finite elements, load steps

[5]Element CGAX8 in ABAQUS.

[6]In the finite element model, a tube with inner and outer radii, $r_i = 2.9mm$ and $r_o = 3.1mm$ is modeled.

and iterations for achieving the equilibrium in the finite element simulation. It is worth mentioning that the results of the present closed-form solution are obtained without a massive computation in contrast with the finite element (or other numerical simulations) that require a massive iterative computational process. In the present case study, due to the small thickness of the tube, only one element through the thickness and a small number of elements (even one element) along the length is adequate. However, in more complicated problems such as solid bars, with the increase of the element numbers in the model, the problem becomes challenging from the computational point of view and the present analytical solution would be much more efficient.

2.2.5 SMA solid bars

In this section the loading and unloading of SMA solid prismatic bars with circular cross sections is considered. All the cases are presented for a bar with radius $R = 25$mm with different material properties and different temperatures. In the first case we consider the loading of a bar, which is in the fully austenite phase at rest. In torsion of such a bar, in general, a cross section may be divided into three regions as shown in Figure 2.2. In the inner region (Region I), the material is in the austenite phase and the relation $\tau_{\theta z} = G_A r\theta$ with $G_A = \frac{E_A}{2(1+\nu)}$ is valid. In Region II, the phase transformation has started ($0 < \xi < 1$) and the relation $\tau_{\theta z} = \wp^+(r, \theta)$ expressed in (2.22) is valid. In the outer region (Region III) the phase transformation is completed and the material is in the martensite phase. In this region stress is calculated as $\tau_{\theta z} = \tau^f_{\theta z} + G_M r(\theta - \theta^f)$, where $\tau^f_{\theta z}$ and θ^f are the shear stress and the twist angle at which the phase transformation is completed ($\xi = 1$). For a bar in the austenite phase with $\theta = 0$, increasing the twist angle the phase transformation starts from the outer radius and spreads toward the center. With more increase of the twist angle, the third region with fully transformed martensite spreads from the outer radius toward the center. For any value of the twist angle, as the material response in the austenite core is elastic, r_1 can be calculated by setting $\xi = 0$ in $(2.15)_1$ and replacing $\tau_{\theta z}$ with $G_A r\theta$. The radius of the inner elastic region r is calculated as:

$$r_1 = -\frac{1}{4}\frac{\sqrt{3}H - \sqrt{3\,H^2 - 8\,\Delta S_{44} f^+(T)}}{\Delta S_{44} G_A \theta}. \tag{2.26}$$

This equation can also be used for calculating the value of twist angle required for the start of phase transformation, which will obviously happen in the outermost layer $r = R$.

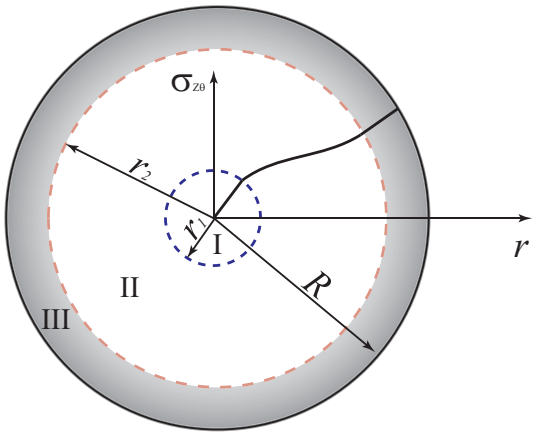

Figure 2.2: Schematic of stress distribution in a circular bar. Regions I, II, and III are the austenite core, transition region, and the martensite outer layer, respectively.

Consider an SMA solid bar with radius $R = 25$mm and the material properties (Material I) in Table 2.1. All the results are presented for different twist angles per unit length. Temperature is assumed to be $T = 315$K. The shear stress distribution for various twist angels is shown in Figure 2.3. Distribution of the martensitic volume fraction for these twist angles is depicted in Figure 2.4. As it is shown in Figures 2.3 and 2.4 for the twist angle $\theta = 4$rad/m, the cross section is divided into three regions. For the inner region with $0 < r < 0.84$mm, the material is in the austenite phase. The annulus $0.84\text{mm} < r < 23.7\text{mm}$ is the phase transformation region and for $r > 23.7$mm the phase transformation is completed and the material is in the martensite phase.

In the unloading of the SMA bar, all the points inside the elastic region will unload elastically in the stress-strain space with the rate of G_A ($\Delta\tau_{\theta z} = G_A r \Delta\theta$). For any point outside the elastic core with a martensitic volume fraction of $0 < \xi^* \leq 1$ an elastic unloading with the rate of $G_{eff} = G_A + \xi(G_M - G_A)$ occurs until the stress level at the point reaches

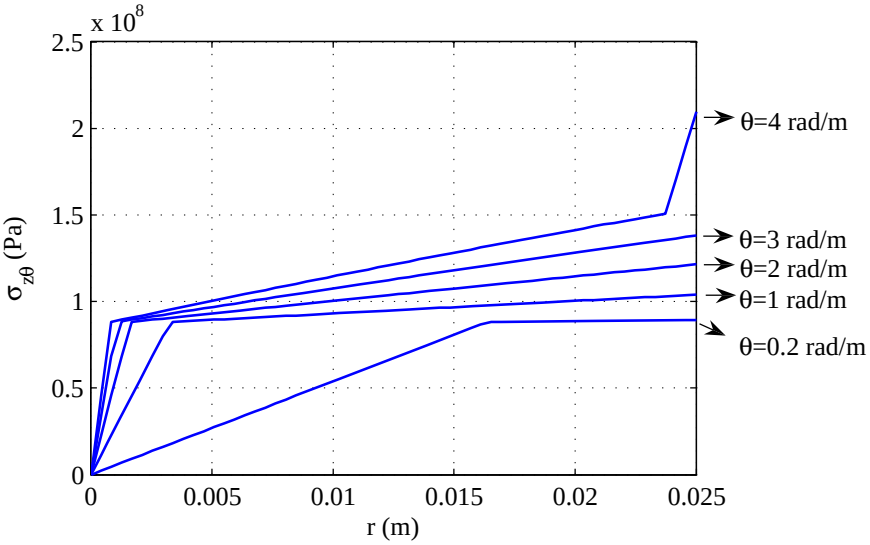

Figure 2.3: Shear stress for various twist angels in loading.

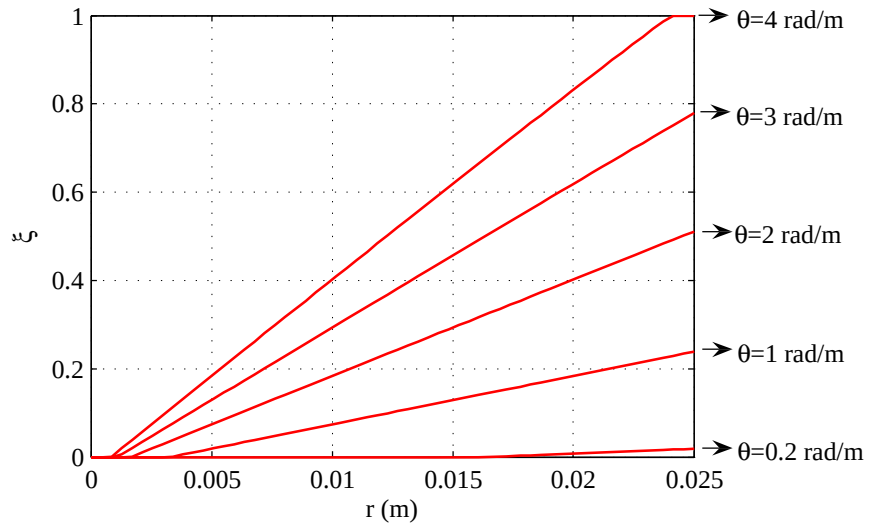

Figure 2.4: Martensitic volume fraction for various twist angels in loading.

the value of [7]:

$$\tau_{\theta z} = -\frac{1}{4}\,\frac{\sqrt{3}H - \sqrt{3\,H^2 - 8\;\Delta S_{44} f^-(T) + 8\,\Delta S_{44}\xi^*\,\rho b^A}}{\Delta S_{44}}. \tag{2.27}$$

After reaching this stress, the stress-strain relation $\tau_{\theta z} = \wp^-(r,\theta)$ for unloading expressed in (2.22) will determine the shear stress for any twist angle. The cross section will be divided into three regions in unloading: the austenite core with elastic unloading, the transition region with $0 < \xi \leq 1$, which has inelastic loading but elastic loading, and the outer region with inelastic loading and unloading. It is clear that in some special unloaded twist angles the third region does not exist. As another case study, the bar of the previous example loaded to $\theta = 4$rad/m is unloaded to different twist angles. The stress distribution for the unloading is shown in Figure 2.5. The martensitic volume fraction distribution corresponding to these twist angles are shown in Figure 2.6.

As it is shown in Figures 2.5 and 2.6, in the unloading up to $\theta = 3.8$rad/m all the points in the cross section have an elastic unloading and phase transformation does not start during unloading (the martensitic volume fraction does not change). However, for larger values of unloading twist, all the three regions can be distinguished. It is obvious that stress and martensitic volume fraction distributions in this case are history dependent and are not identical in loading and unloading for the same values of twist angle (compare Figures 2.5 and 2.6 with Figures 2.3 and 2.4). Note that, at the present temperature ($T = A_f = 315$K) all the loading induced stresses recover during a complete unloading.

In the next case study, the effect of temperature on the response of the bar is studied. Shear stress distribution for the twist angle of $\theta = 3.8$rad/m is depicted in Figure 2.7 for three different temperatures. It is seen that increasing temperature, the stress corresponding to the onset of phase transformation increases and consequently the radius of the elastic core increases as well. Also, for lower temperatures Region III starts to spread toward the center for lower values of twist angle per unit length.

Next we study the effect of material properties on the response of circular bars in torsion. Two identical bars with material constants I and II are considered. Both bars are initially

[7] This stress level is calculated by replacing ξ^- with ξ^* in $(2.15)_2$ and solving for $\tau_{\theta z}$.

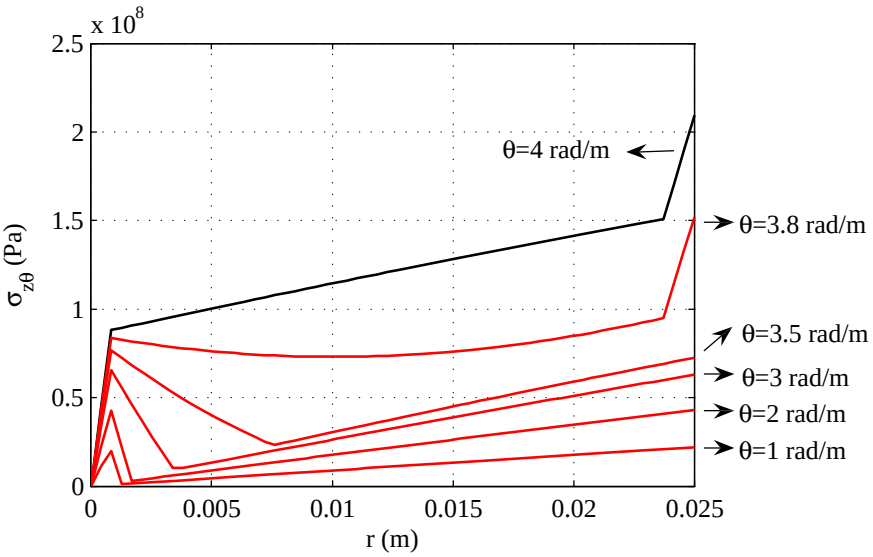

Figure 2.5: Shear stress for various twist angels in unloading.

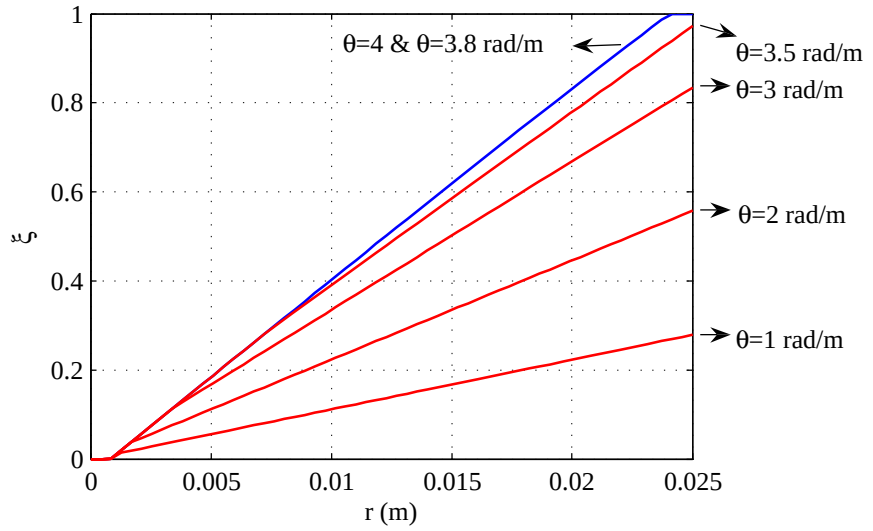

Figure 2.6: Martensitic volume fraction for various twist angels in unloading.

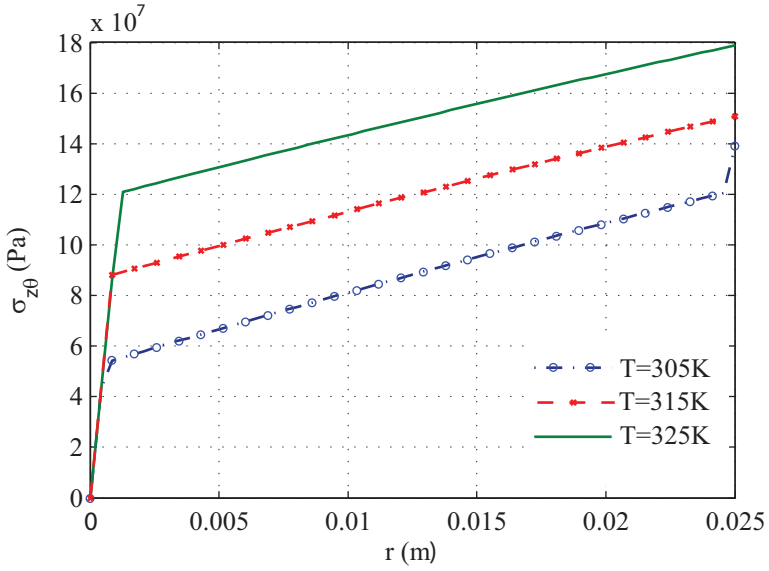

Figure 2.7: Shear stress distribution for three different temperatures.

in the austenite finish temperature ($T = 315$K for Material I and $T = 281.6$K for Material II). As it is shown in Figure 2.8, in loading for Material II the phase transformation starts at a higher stress level and the radius of the elastic core is larger. In unloading, the bar made of Material II has a lower stress level in the region with reverse phase transformation. As it will be shown shortly, the difference between shear stress distribution for these two materials will significantly affect the torque applied to the bar in loading and unloading. It is worth noting that, as the elastic properties of these two materials are almost the same, the difference in material response is mainly caused by the difference in the parameters $f^{\pm}(T)$.

All the previous case studies were presented for different twist angles. In some cases, it is necessary to calculate the response of the bar with respect to the applied torque. For this purpose the present formulation can be used for calculating the necessary torque for producing a specific twist angle as:

$$\mathbb{T}^{+} = 2\pi \int_0^{r_1} G_A \theta r^3 dr + 2\pi \int_{r_1}^{r_2} \wp^{+}(r,\theta) r^2 dr + 2\pi \int_{r_2}^{R} \left(\tau_{\theta z}^{f} + G_M r(\theta - \theta^{f})\right) r^2 dr, \quad (2.28)$$

$$\mathbb{T}^{-} = 2\pi \int_0^{r_1^*} G_A \theta r^3 dr + 2\pi \int_{r_1^*}^{r_2^*} \left(\tau_{\theta z}^{\ell} - G_{eff} r \Delta\theta\right) r^2 dr + 2\pi \int_{r_2^*}^{R} \wp^{-}(r,\theta) r^2 dr, \quad (2.29)$$

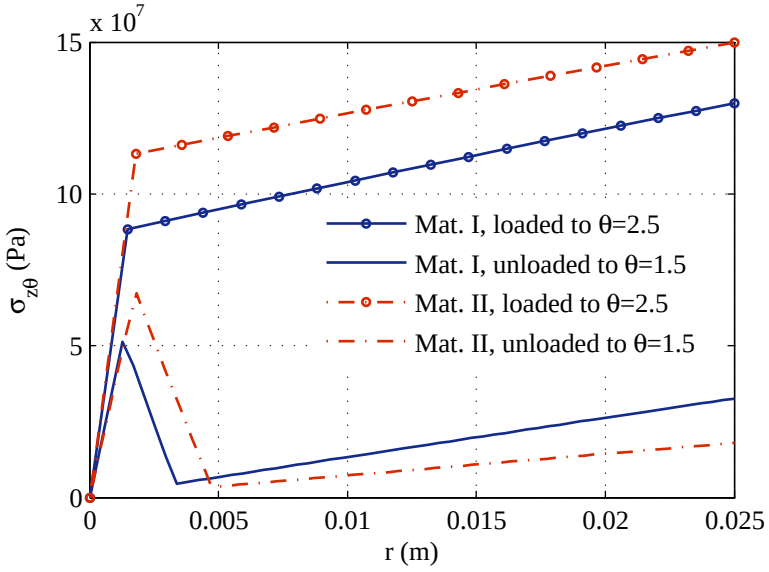

Figure 2.8: Shear stress for two different material properties in loading and unloading.

where r_1 and r_2 are the inner and outer radii of Regions II as shown in Figure 2.2 in loading. The parameters r_1^* and r_2^* are the inner and outer radii of Region II with phase transformation during the loading phase but in an elastic unloading. The parameter $\tau_{\theta z}^{\ell}$ represents the value of shear stress for any point at the end of the loading phase and $\Delta\theta$ is the amount of reverse twist angle during unloading. The loading-unloading cycle for a bar with the same geometry as those of the previous examples is depicted in Figure 2.9 for three different temperatures. Material I is used for this case study. As it is shown in this figure, the twist angle is fully recovered during unloading for temperatures above the austente finish temperature and after removing the applied torque no residual twist is remained in the bar. For $T = 305$K, which is below the austenite finish temperature, when the applied torque is removed, a residual twist is observed. In all the three temperatures, the area of the hysteresis loop remains constant; the loops are rigidly translated in the torque-twist plane.

As shown in Figure 2.9, for temperatures below the austenite finish temperature a residual twist angle and consequently a residual stress distribution exists after removing the applied torque. As another case study, a bar at $T = 305$K is loaded to different

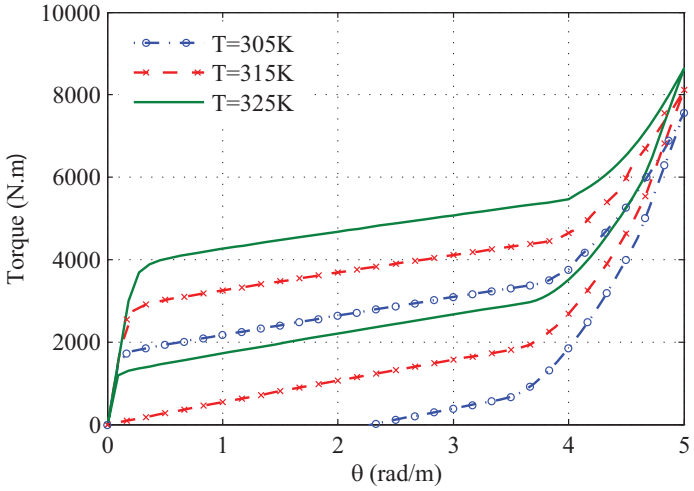

Figure 2.9: Torque versus twist angle in a loading-unloading cycle for Material I at different temperatures.

maximum twist angles and the applied torque is removed to study the residual twist and stress distributions. Figure 2.10 shows the applied torque versus twist angle for this bar. As it is shown, for a bar loaded to $\theta = 4$ and 6 rad/m after removing the torque, the bar has a residual twist angle of $\theta = 2.31$rad/m. In the case of loading the bar to $\theta = 2$rad/m, after removing the external torque, the residual twist angle is $\theta = 1.78$rad/m. Distribution of residual shear stress for these bars is shown in Figure 2.11. As it is shown, removing the external torque the bar is in a state of self-equilibrated residual stress distribution.

The loading-unloading hysteresis loop in torsion for different material properties is studied in the next case study. Figure 2.12 shows the applied torque versus the twist angle for a bar of the previous examples made of Materials I and II (both bars are in the austenite finish temperature). As it is shown in this figure, the hysteresis loop area is larger for Material I. This can be explained by looking at the stress distribution shown in Figure 2.8. For Material II, the phase transformation starts at a higher stress level in loading and the reverse phase transformation occurs at lower stress levels in unloading.

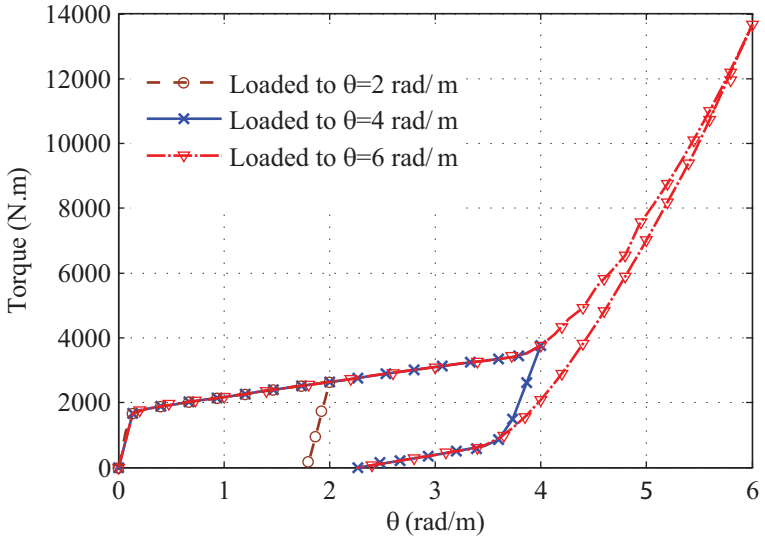

Figure 2.10: Torque versus twist angle for T=305K at different maximum loading twist angles.

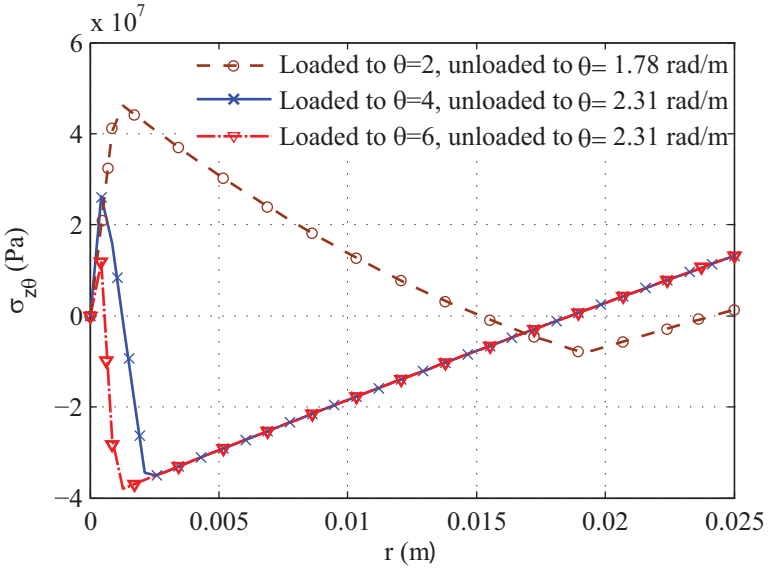

Figure 2.11: Residual stress distribution for T=305K for identical bars loaded to different maximum twist angles.

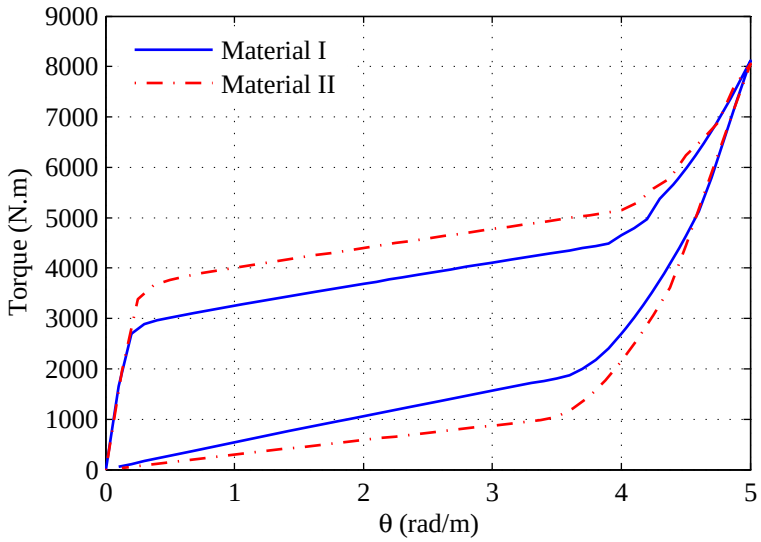

Figure 2.12: Torque versus twist angle in loading-unloading cycle for two different material properties.

2.3 Shape Memory Alloy Helical Springs

In this section, the pseudoelastic response of shape memory alloy helical springs under axial force is studied both analytically and numerically. In the analytical solution two different approximations are considered. In the first approximation, both the curvature and pitch effects are assumed to be negligible. This is the case for helical springs with large ratios of mean coil radius to the cross sectional radius (spring index) and small pitch angles. Using this assumption, analysis of the helical spring is reduced to that of the pure torsion of a straight bar with circular cross section. A three-dimensional phenomenological macroscopic constitutive model for polycrystalline SMAs is reduced to the one-dimensional pure shear case and a closed-form solution for torsional response of SMA bars in loading and unloading is obtained. In the next step, the curvature effect is included and the SMA helical spring is analyzed using the exact solution presented for torsion of curved SMA bars. In this refined solution, the effect of the direct shear force is also considered. In the numerical analyzes, the three-dimensional constitutive equations are implemented in a finite element method and using solid elements the loading-unloading of an SMA helical

spring is simulated. Analytical and numerical results are compared and it is shown that the solution based on the SMA curved bar torsion gives an accurate stress analysis in the cross section of the helical SMA spring in addition to the global load-deflection response. All the results are compared with experimental data for a Nitinol helical spring. Several case studies are presented using the proposed analytical and numerical solutions and the effect of changing different parameters such as the material properties and temperature on the loading-unloading hysteretic response of SMA helical springs is studied. Finally, some practical recommendations are given for improving the performance of SMA helical springs used as energy dissipating devices, for example for seismic applications.

In this section, we present two different analytical methods for calculating the loading-unloading response of SMA helical springs under axial loads. For helical springs with a large spring index (defined as $m = R_m/R$, where R_m is the mean coil radius and R is the cross section radius) and a small helix angle, both the curvature and pitch effects can be ignored without losing much accuracy[8]. In this special case, the pure torsion analysis of a straight bar can be used for analyzing the helical springs. For most practical springs, the pitch angle is smaller than 15°, but the spring index varies in a wide range. The curvature correction is added to the theory used for studying the pure torsion of a straight bar and a more precise solution is introduced for analyzing SMA helical springs with smaller spring indices.

2.3.1 Analysis based on exact solution for pure torsion of SMA bars

We presented an exact solution for pure torsion of SMA straight bars with circular cross section in section 2.2. This solution is used here for analyzing the SMA helical springs and it is denoted by SBTM (straight bar torsion model) throughout the text. Considering a straight bar with a general cross section in the xy plane (z is along the bar axis), the state of shear strain at a point in the cross section is, $\gamma_{zx} = 2\epsilon_{zx} = \theta\left(\frac{\partial\psi}{\partial x} - y\right)$ and $\gamma_{zy} = 2\epsilon_{zy} = \theta\left(\frac{\partial\psi}{\partial y} + x\right)$, where θ is the twist angle per unit length and ψ represents the

[8]It is known that for helical springs with $m > 4$ and a pitch angle smaller than 15°, the error of using SBTM for analyzing helical spring leads to less than 2% error with common engineering materials used in practical springs (see Ancker and Goodier [6] and Wahl [190] for more details).

warping function representing the cross sectional deformation along the z axis. For circular [172] and some other special cross sections [37], the warpage is zero and the shear strains distribute linearly through the thickness. For a bar with a circular cross section, the shear strain in (2.19) can be related to twist angle per unit length as $\epsilon_{\theta z} = \frac{1}{2} r\theta$, where r is the distance from the axis of the bar. The shear stress $\tau_{\theta z}$ as a function of twist angle in an arbitrary radius is given explicitly in (2.22). For an SMA bar under torsion (with the axis of bar along z direction), in the most general case the cross section may be divided into three regions (see Section 2.2 and Mirzaeifar et al. [127] for more details). In the inner region, the material is in the austenite phase and the relation $\tau_{\theta z} = G_A r\theta$ with $G_A = \frac{E_A}{2(1+\nu)}$ holds. In the middle region, the phase transformation has started ($0 < \xi < 1$) and the relation $\tau_{\theta z} = \wp^+(r, \theta)$ expressed in (2.22) is valid. In the outer region the phase transformation is completed and the material is in the martensite phase. In this region stress is calculated as $\tau_{\theta z} = \tau^f_{\theta z} + G_M r(\theta - \theta^f)$, where $\tau^f_{\theta z}$ and θ^f are the shear stress and the twist angle at which the phase transformation has been completed ($\xi = 1$) everywhere. For a bar in the austenite phase with $\theta = 0$, by increasing the twist angle, the phase transformation starts from the outer radius and spreads toward the center. With more increase of the twist angle, the third region with fully transformed martensite spreads from the outer radius toward the center. The outer radius of the inner and middle regions are denoted by r_1 and r_2 in the sequel. During the loading phase, in any cross section the resultant torque is given by (2.28). In unloading, the cross section is divided into three sections as well. The material in the inner region is in the austenite phase and has experienced both elastic loading and unloading (the outer radius of this region is denoted by r^*_1). In the middle region the bar has experienced phase transformation during loading but the unloading was elastic (the outer radius of this region is denoted by r^*_2). The martensitic volume fraction for any material point in this region is unchanged during unloading. The outer region of the cross section of a bar during unloading in torsion contains the material that has experienced phase transformation during both loading and unloading phases. During unloading, the torque in the cross section is given by (2.29), where the parameter $\tau^\ell_{\theta z}$ represents the value of shear stress for any point at the end of the loading phase and $\Delta\theta$ is the amount of reverse twist angle during unloading.

Since in this assumption the spring is considered as a straight bar of length $l = 2\pi N R_m$, where N is the number of active coils, the total angular deflection of one end of the bar with respect to the other end is given by $\Theta = 2\pi N R_m \theta$. Because the effective moment arm of the axial load F is equal to R_m, the deflection of the spring at the end point is given by

$$\delta = \Theta R_m = 2\pi N R_m^2 \theta. \tag{2.30}$$

For any deflection of the spring ends (2.30) is used for finding the twist angle per unit length θ. Substituting this value in (2.22), the shear stress distribution in the cross section is calculated. Having the shear stress distribution, the resultant torque in the cross section is obtained by (2.28) or (2.29) and the axial force corresponding to the assumed end displacement is calculated by dividing the torque by the coil mean radius: $F = \mathbb{T}^{\pm}/R_m$. In this approximation, the effect of direct shear force on the cross section is ignored along with the curvature and pitch effects. In the following section, a curvature correction is added to the analysis and in each cross section both the torque and direct shear forces are taken into consideration.

2.3.2 Curvature correction

Although the analysis of helical springs based on SBTM is of enough accuracy for most practical helical springs, there have been many efforts in the literature for improving this theory [6–8, 190]. It is known that due to the curvature effect, the shear stress distribution in the cross section is not axisymmetric. In this section, a curvature correction is implemented in the solution presented in the previous section. The solution of this section is applicable for SMA helical springs with large spring indices but small pitch angles. This includes nearly all the practical helical springs [190]. This solution method is denoted by CBTM (curved bar torsion model) throughout the text.

First, we consider the pure torsion of an SMA curved bar. A slice of such a bar is shown in Figure 2.13. Applying a torque the two faces of this cross section will rotate with respect to each other by an angle $d\beta$. Since the initial length of the filament passing through the points a and b are not the same, the strain distribution in the cross section is not axisymmetric. This will result in a non axisymmetric stress distribution with a larger value for the material

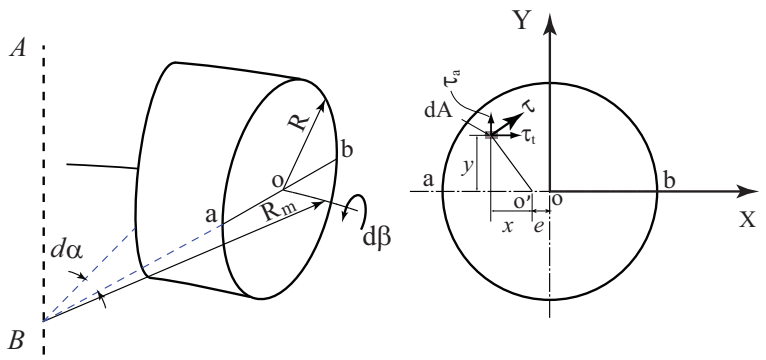

Figure 2.13: Torsion of a curved bar.

points near the axis AB. The non axisymmetric shear stress distribution in the cross section can be decomposed into an axial component τ_a and a transverse component τ_t as shown in Figure 2.13. If we assume that the cross section is rotating about an axis passing through the center o (at the center of rotation, the shear stress is zero), and considering the fact that the shear stress at b is larger than the stress at a, such a distribution cannot be in equilibrium; there will be a torque in the cross section [190]. So, it can be concluded that for a curved bar under torsion, the zero shear stress point or the center of rotation does not coincide with the cross section center. Considering the symmetry conditions in the cross section, the forces caused by the transverse shear stress component τ_t are in equilibrium when the rotation center is anywhere on the axis ab. The rotation center o' is shown in Figure 2.13. The distance e for finding the location of the rotation center is found by the method presented in the sequel.

In the coordinate system xy with the origin o', when the slice sides rotate by the amount $d\beta$ with respect to each other the relative movement of the ends of any filament corresponding to dA in Figure 2.13 is $\sqrt{x^2+y^2}\, d\beta$. Considering the fact that the length of this filament in the undeformed configuration is $(R_m - e - x)d\alpha$, the shear strain corresponding to this point in the cross section is

$$\gamma = \frac{\sqrt{x^2+y^2}}{R_m - e - x}\frac{d\beta}{d\alpha}, \tag{2.31}$$

where the shear strain γ is along the direction of τ in Figure 2.13. The geometrical parameters in (2.31) are shown in Figure 2.13. Now, the expression given for the shear strain in (2.31) should be replaced with the expression $r\theta$ (that is the strain in the straight bar case) in (2.20) and all the coefficients in Appendix A. The new quartic equation obtained by this substitution is solved to find the explicit expression for the shear stress in the regions with phase transformation. We denote the shear stress in this case by $\tau = \hat{\wp}^{\pm}(x, y, e, d\beta/d\alpha)$, where the explicit expression for shear stress is similar to that given in Appendix A by replacing the parameter $r\theta$ with the shear strain of a curved bar in (2.31). For a curved bar under pure torsion, the resultant force in the cross section should be zero. Due to symmetry of the transverse shear stress about the axis ab, the forces caused by this stress component are in static equilibrium. The static equilibrium for the forces caused by the axial component of the shear stress is expressed by

$$\int_A \tau_a dA = \int_{A_1} \frac{G_A x}{R_m - e - x} \frac{d\beta}{d\alpha} dA_1 + \int_{A_2} \hat{\wp}^{\pm}(x, y, e, d\beta/d\alpha) \frac{x}{\sqrt{x^2 + y^2}} dA_2 + \int_{A_3} \left(\tau_a^f + \frac{G_M x}{R_m - e - x} \frac{d\beta - d\beta^f}{d\alpha} \right) dA_3 = 0, \tag{2.32}$$

where A_1 is that portion of the section that has not experienced the phase transformation. The portion of the cross section with phase transformation is denoted by A_2 and the parts in which the phase transformation has been completed by A_3. For each material point with completed phase transformation ($\xi = 1$), the parameter τ_a^f is the the axial component of shear stress corresponding to $d\beta^f$ that is the twist angle of phase transformation completion for that material point. Now, the only unknown parameter in (2.32) is the position of the rotation center e. In contrast with the elastic torsion of a bar, in the case of an SMA curved bar the second and third integrals in (2.32) cannot be calculated analytically. We use trapezoidal numerical integration method. In our numerical examples, we well compare the results of the present model with those of a three-dimensional finite element simulation.

For analyzing SMA helical springs based on the pure torsion of an SMA curved bar, a minor correction is needed to take into account the direct shear force in the cross section. In an SMA helical spring a direct shear force F and a torque $R_m F$ are acting in each cross

section. The equilibrium equations in the cross section in this case read

$$\int_A \tau_a dA = F, \qquad \text{and} \qquad \int_A \tau_a x dA + \int_A \tau_t y dA = R_m F, \tag{2.33}$$

where in the most general case, the cross section is divided into three regions similar the previous cases. For analyzing the SMA spring using the curved bar theory, a predefined displacement is considered for the spring ends. The total rotation of the spring ends with respect to each other is calculated by $\hat{\Theta} = \delta / R_m$. The twist angle per curvature angle is given by

$$\frac{d\beta}{d\alpha} = \frac{\delta}{2\pi R_m N}. \tag{2.34}$$

The expression in Appendix A (by replacing $r\theta$ with the shear strain of a curved bar in (2.31)) is used to calculate the shear stress. Since the axial force F is unknown, in contrast with the pure torsion case the parameter e cannot be obtained directly by solving (2.33). Hence, first an initial value[9] is considered for e. Using this value the axial force F is calculated using both expressions in (2.33). A trial and error method is then used to find the value of e for which the difference of the axial forces calculated from the two conditions in (2.33) is smaller than a tolerance (1N in the numerical examples of this paper).

2.3.3 Helical SMA spring test

An SMA helical spring shown in Figure 2.14 is used for obtaining the experimental results. The spring has a mean coil radius of $R_m = 2.1$cm, an initial length of 12.98cm and the cross section radius of 6.25mm [173]. The helical spring is placed in a cylindrical shape tension/compression device and a 250kN MTS Universal Testing Machine is used for compressing the spring. The tension/compression device is a cylindrical-shaped damper that provides the ability to test a variety of SMA elements [173]. The body and the shaft of the device are made out of standard 304 stainless steel cylinders. The nitinol helical spring is loaded on the the center shaft using a nut. the outer cylinder covers both the spring and

[9]The loading/unloading response of the SMA spring is analyzed by applying the total axial deflection incrementally. In the first few increments the entire cross section is in the austenite phase and hence the location of the rotation center is calculated easily as the shear stress expression in (2.33) is integrable. For the subsequent load increments, the initial guess for the parameter e for each increment is the value obtained in the previous increment.

center shaft. the spring ends are free to rotate during loading and unloading (see [173] for pictures of the test devise). The quasi-static loading rate is set to 0.127cm/s. Using this loading rate, the temperature change due to the latent heat is negligible and the test can be considered isothermal. Compression tests are done in the ambient temperature of 27°C. The experimental setup and the test procedure are explained in detail in Speicher et al. [173]. This reference contains a comprehensive study of three different SMA devices for applications as bracing elements in buildings.

Figure 2.14: The SMA helical spring used in the experimental study.

The spring is made from Nitinol Alloy 508 (50.8% at.% Nickel). A simple tension test is carried out on a bar of the same alloy and a stabilized loading-unloading cycle for this specimen is shown in Figure 2.15(a). Due to the thermal and mechanical treatments done on the initial SMA stock for producing a helical spring, the material properties for the spring may have a slight difference with the properties of SMA stock. The properties of Material II given in Table 2.1 are calibrated by comparing the results of analytical and numerical analyses with the experimental results of Speicher et al. [173] done on the SMA helical spring and the simple tension test in Figure 2.15(a). The response of material with calibrated properties in simple tension is compared against the experimental results in Figure 2.15(a). In order to take the uncertainty effect in calculating the material properties into consideration, we will present a discussion on the effect of changing material properties on the spring response in the sequel.

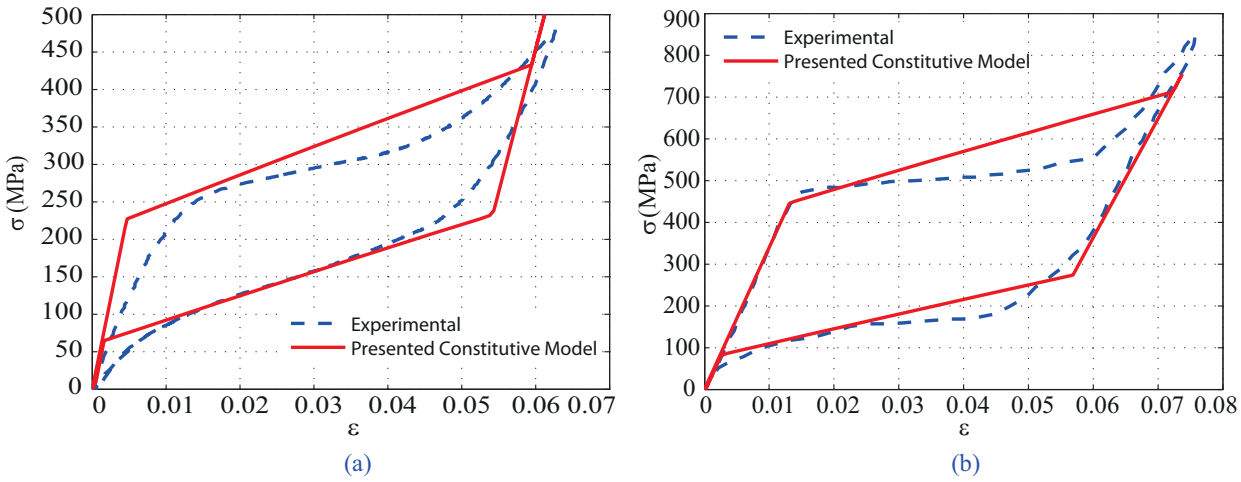

Figure 2.15: The calibrated material properties versus experiments in simple tension test for the material used in (a) Speicher et al. [173] and (b) Toi et al. [185] tests on SMA helical springs.

2.3.4 Finite element simulation of SMA helical springs

For analyzing SMA helical springs using the finite element method, the three-dimensional constitutive relations of §2.5.1 are used and an appropriate user subroutine (UMAT) is written by FORTRAN in the commercially available finite element program ABAQUS that enables this code to model SMA structures using solid elements and some two-dimensional elements. The details of implementing the constitutive equation in a displacement based finite element formulation is given in Qidwai and Lagoudas [161] and many case studies for validating the model are presented in [126, 127, 131]. In the present study, for comparison purposes the spring is modeled three dimensionally (in contrast with some finite element models in the literature that use beam elements for modeling the SMA helical springs [185]). Three dimensional quadratic brick elements with reduced integration (element C3D20R in ABAQUS) are used in the finite element model of the helical spring. A convergence analysis is performed for choosing the appropriate number of elements by considering the shear stress distribution in the cross section and the load-displacement response as the convergence criteria. The stress distribution is considered to be converged when the maximum difference is smaller than 0.1MPa and the convergence criterion of the maximum difference for the

load-displacement response is 10N. We observe that the convergence is achieved by using 7500 elements. All the finite element simulations are done using this mesh. A schematic of the finite element mesh is shown in Figure 2.16.

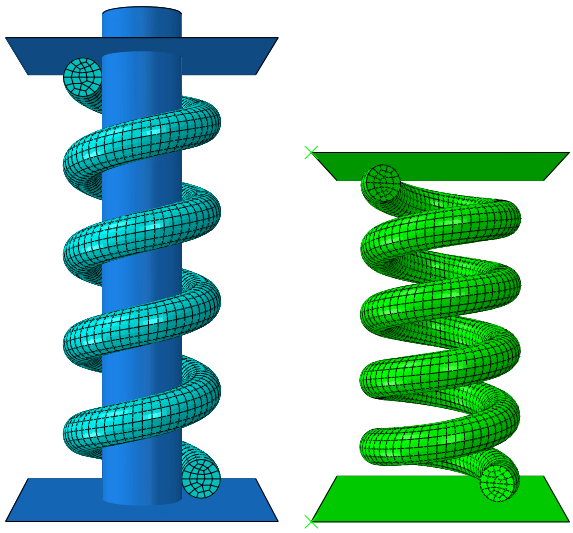

Figure 2.16: Finite element model of the SMA spring in the initial (left) and compressed (right) configurations

.

For simulating the spring in compression, two rigid surfaces in contact with the spring ends are considered (see Figure 2.16). The lower rigid surface is constrained in all directions and a time varying boundary condition is defined for the upper surface for modeling compression. A node to surface contact with a friction coefficient of 0.1 is defined between the solid elements in the end rings and the shell elements in the upper and lower rigid surfaces. The supporting shaft in the experiments is modeled with a cylindrical rigid surface inside the helical spring with a diameter slightly (0.2mm) smaller than the inner radius of the coil (this shaft is shown in Figure 2.16 (left) but not in Figure 2.16 (right) to show the spring more clearly). For avoiding high local stresses and the convergence problems in the finite element solution, the contact between the solid elements of the spring and the rigid cylindrical surface is considered frictionless. Both spring ends are free to rotate in the numerical simulation. The automatic time increment option in ABAQUS is used with an initial guess of dividing the loading and unloading steps into 100 increments and the

non-linear geometry option is activated. The geometry of the spring modeled in the finite element simulation is exactly the same as the helical spring in the experimental tests (see §2.3.3).

2.3.5 Numerical results for studying SMA helical springs

In this section, several case studies are presented for demonstrating the efficiency of the proposed analytical solution for analyzing SMA helical springs. The accuracy of the proposed exact solution for pure torsion of SMA bars with circular cross section was studied Section 2.2. As mentioned in §2.3.4, the developed finite element code for analyzing SMA structures was verified in several case studies in the previous works of the authors [126, 127, 129]. In the sequel, the accuracy of the proposed model for analyzing SMA carved bars is studied by comparing the results of this model with those of finite element simulations. Then, an SMA helical spring is considered and the results obtained based on the straight bar torsion, curved bar torsion and finite element simulations are compared. A case study is presented for comparing the analytical and numerical results against the experimental results as well. The effect of changing material properties and temperature on the response of SMA helical spring subjected to axial loading-unloading cycle is studied and some practical recommendations are given for improving the behavior of SMA helical springs used for damping and dissipating energy in recentering devices in buildings subjected to external loads especially during seismic events.

2.3.5.1 Verification of the curved SMA bar torsion

In order to verify the proposed solution for the SMA curved bar torsion problem, a case study is considered and the analytical results are compared with the finite element simulation outputs. Consider an SMA curved bar with $R_m = 2$cm, the cross section radius $R = 6$mm, and angle $\alpha = 20^\circ$ (see Figure 2.13). For verification purposes, the material properties of a generic SMA as reported previously in the literature [161] are used. These properties are given in Table 2.1 as Material I. The left end of the bar is constrained and a twist angle of 0.04rad is applied to the right end. The bar is considered to be in the austenite finish temperature, $T = 315$K.

The finite element model of the SMA curved bar is shown in Figure 2.17(a). The details of modeling this bar in the finite element code ABAQUS are explained in §2.3.4. The martensitic volume fraction distribution in the cross section of this bar is shown in Figure 2.17(b). It is seen that in contrast with the straight bar torsion [127], in the case of a curved bar, the martensitic volume fraction distribution is not axisymmetric as the zero stress point o' is not in the cross section center.

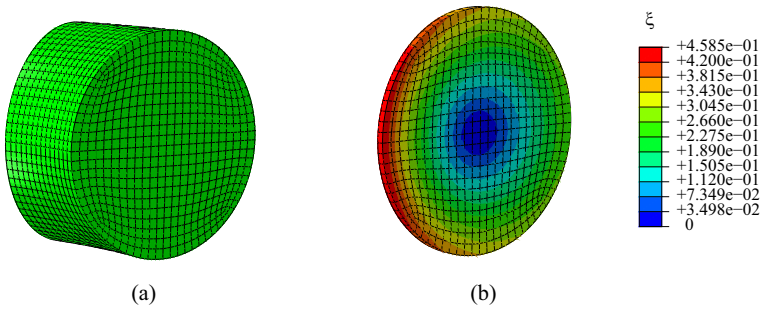

Figure 2.17: (a) Finite element model for simulating torsion of an SMA curved bar, and (b) the non-axisymmetric distribution of martensitic volume fraction for the torsion of a curved bar.

Distribution of the axial component of shear stress τ_a along the diameter ab (see Figure 2.13) calculated by our method and the finite element simulation is shown in Figure 2.18. The shear stress is plotted along this diameter in the coordinate system XY with the origin at o (see Figure 2.13). The zero shear stress occurs at a point with a distance $e = 0.1mm$ from the center of the cross section. Although e is very small, it has a significant effect on the stress and martensitic volume fraction distributions in the cross section. The non symmetry of the shear stress distribution is clearly seen in Figurer 2.18 ($\tau_a = 120.1$ MPa at point a and $\tau_a = 104.3$ MPa at point b).

The martensitic volume fraction distribution along the diameter ab is shown in Figure 2.19. The curvature clearly affects the phase transformation and as it is shown the material points closer to the axis have higher volume fractions compared to the outer points. This non symmetry is seen in the finite element results as well (see Figure 2.17(b)). As it is shown in Figures 2.18 and 2.19, there is good agreement between the results of our method

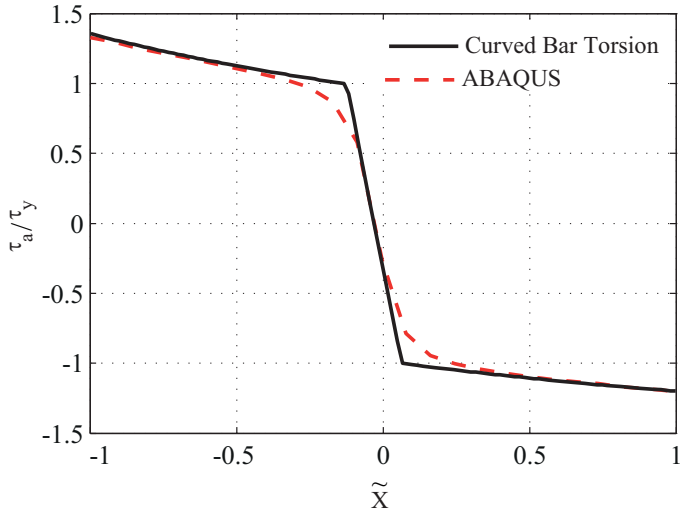

Figure 2.18: Distribution of τ_a in an SMA curved bar subjected to torsion along diameter ab in Figure 2.13 ($\tilde{X} = X/R$ and $\tau_y = 88.1$MPa is the shear stress at the start of phase transformation obtained by solving (2.15) for $\xi^+ = 0$).

and the finite element simulation results.

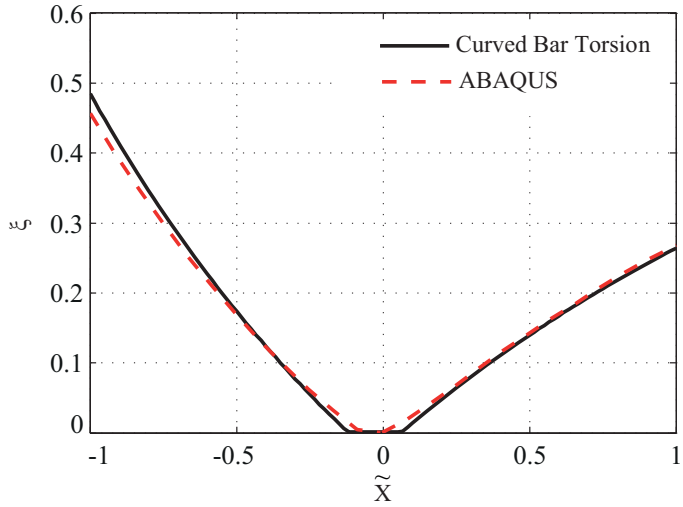

Figure 2.19: Distribution of the martensitic volume fraction in an SMA curved bar subjected to torsion along diameter ab in Figure 2.13 ($\tilde{X} = X/R$).

2.3.5.2 Analytical and numerical results for SMA helical springs

In this section, by considering a practical case study we will compare the results of our analytical formulation with the results of a finite element simulation. We consider an SMA helical spring with dimensions given in §2.3.3. Details of the finite element modeling are given in the previous section. The Nitinol Alloy 508 (50.8% at.% Nickel) material properties are considered for all the case studies. As expressed in §4, these properties are calibrated from a simple tensiom test and the experimental tests on the SMA helical spring and are given in Table 2.1 as Material II. A loading-unloading cycle with maximum stroke of $\delta = 2.75$cm is considered. The spring is at the ambient temperature $T = 27°$C. A schematic of the undeformed spring in the finite element model is shown in Figure 2.16(left). The finite element mesh at the end of loading cycle is shown in Figure 2.16(right).

The load deflection plots in the loading-unloading cycle obtained based on SBTM, CBTM, and the finite element simulation are compared in Figure 2.20. As it is shown in this figure, adding the curvature correction to the straight bar theory increases the agreement between the analytical and numerical results. The difference between the results of the curved bar theory and the numerical simulations perhaps is caused by ignoring bending due to the pitch effect in the analytical solution. However, considering the remarkable computational time reduction in using the analytical results reveals the value of analyzing the SMA helical springs using our proposed analytic solution. The finite element simulation takes almost two hours on a 2GHz CPU with 2GB RAM while the analytic solution results based on the curved bar torsion are obtained in less than 2 minutes and the solution based on the straight bar torsion is obtained in a few seconds on the same system (the solution based on CBTM takes more time because the parameter e should be obtained iteratively as was explained in §2.3.2). The decrease in the computational time will be even more significant when repetitive simulations are needed, e.g. in most optimization procedures [67, 147].

The axial component of shear stress τ_a in the cross section on a horizontal diameter

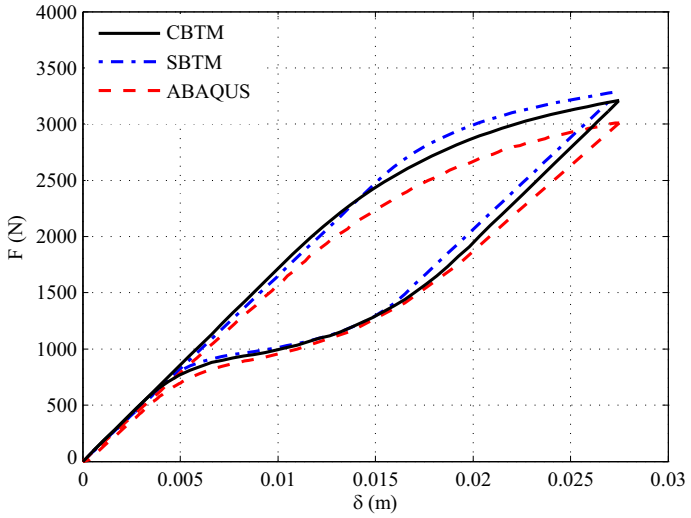

Figure 2.20: Axial force versus axial displacement for an SMA helical spring calculated by the analytic solutions (CBTM: curved bar torsion model, STBM: straight bar torsion model) and the finite element simulation.

(like the diameter ab in Figure 2.13) is calculated using SBTM, CBTM and finite element simulations[10] and the results are compared in Figure 2.21. The martensitic volume fraction distributions obtained by these solution methods are depicted in Figure 2.22. As it is shown in Figures 2.21 and 2.22, unlike the load-displacement response, the stress and martensitic volume fraction distributions are highly affected by adding the curvature correction to SBTM. It is evident that CBTM predicts the stress and martensitic volume fraction distributions with a good agreement with the three-dimensional finite element simulations. As it is shown in Figure 2.21, in contrast with the pure torsion of a curved bar, the zero shear stress point (the rotation center o') located at a point toward the outer surface of the curved bar (compare the zero stress points in Figures 2.18 and 2.21 and see the diameter ab in Figure 2.13). This phenomenon is due to direct shear force in the cross section in formulating the SMA helical spring. Also, it is worth noting that, unlike the elastic curved

[10]In practice, when a helical spring is loaded between two planar plates (like the experimental test and the finite element simulation in the present paper), the applied end loads are eccentric with respect to the spring axis and hence the spring is subjected to a global bending . This global bending causes a lateral deflection with respect to the spring axis that is maximum at the middle of the spring. To avoid this global bending effect, the finite element results are reported for a cross section in the first upper ring of the spring [190].

bar torsion, in the SMA helical spring the zero shear stress point is not fixed in the cross section; it moves during loading and unloading. Figure 2.23 shows the movement of the rotation center in the SMA helical spring cross section. It is seen that when the cross section is in the austenite phase and the spring response is elastic, the rotation center is fixed. When phase transformation occurs during loading and unloading, the zero shear stress point moves toward the outer surface of the curved bar and comes back to the elastic position.

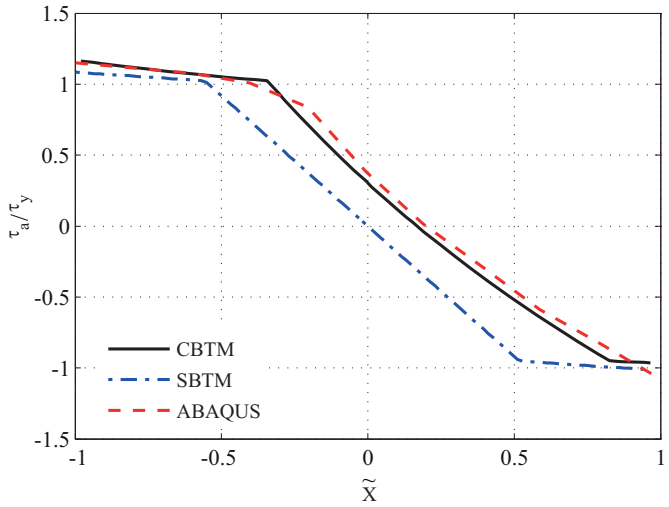

Figure 2.21: Distribution of τ_a in the cross section of an SMA spring subjected to axial compression (along a diameter like ab in Figure 2.13). CBTM: curved bar torsion model, STBM: straight bar torsion model, $\tilde{X} = X/R$ and $\tau_y = 138.2$MPa is the shear stress at the start of phase transformation obtained by solving (2.15) for $\xi^+ = 0$.

2.3.5.3 Experimental results

In this section, we use the experimental data of an SMA helical spring from a previous work of the second author [173] for studying the accuracy of our analytical and numerical models. In performing the experiments, a setup as explained in §2.3.3 is used. The SMA helical spring is placed in a tension/compression cylindrical device. In order to increase the initial stiffness of the device (that is preferred when the spring is used for energy dissipation in seismic events), a precompression of 1.15cm is given to the spring by tightening a nut on

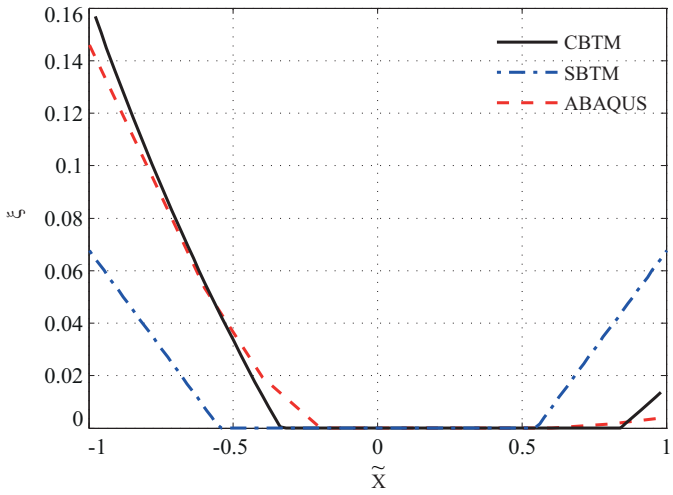

Figure 2.22: Distribution of martensitic volume fraction in the cross section of an SMA spring subjected to axial compression (along a diameter like ab in Figure 2.13). CBTM: curved bar torsion model, STBM: straight bar torsion model, $\tilde{X} = X/R$.

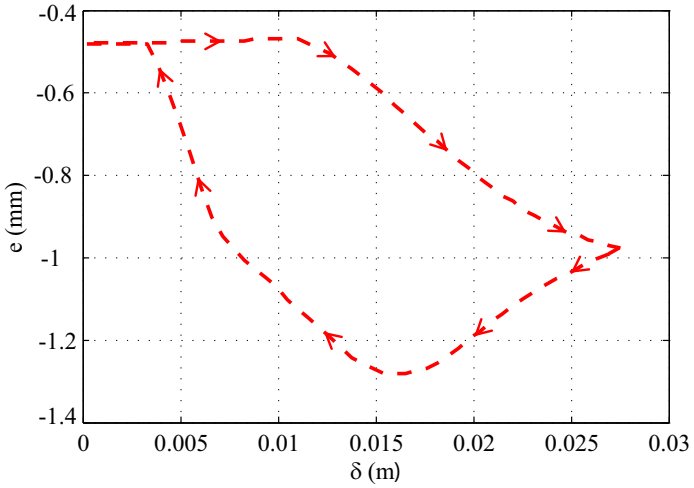

Figure 2.23: The location of torsion centroid (o') in the cross section of the SMA helical spring during loading and unloading phases.

the shaft that carries the spring (see Speicher et al. [173] for more details on the experimental setup). The spring is studied under various loading-unloading cycles. We will compare our analytical and numerical simulation results with those of an experiment in which the spring is compressed to $\delta_{pc} = 1.6$cm and then unloaded (δ_{pc} is the displacement of the ends of a precompressed spring). The results of loading-unloading cycle for this spring obtained by SBTM, CBTM, finite element simulation, and experimental results are compared in Figure 2.24.

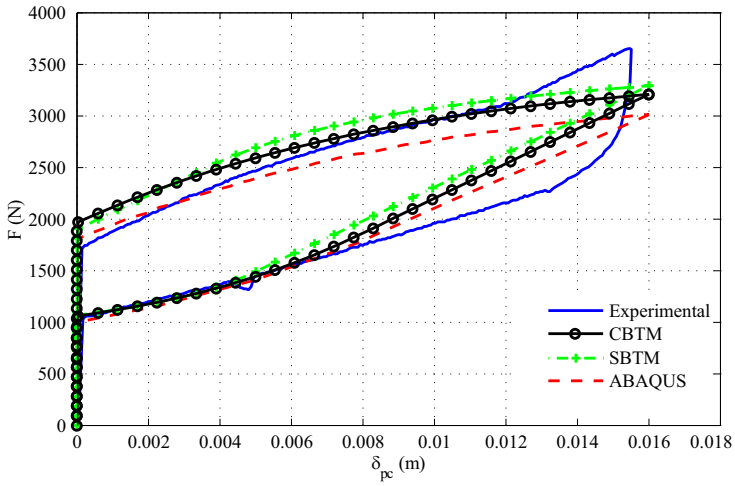

Figure 2.24: Axial force versus axial displacement (considering the pre-compression) for an SMA helical spring calculated by the analytic solutions (CBTM: curved bar torsion model, STBM: straight bar torsion model), finite element simulations, and experimental tests.

As it is shown in Figure 2.24, due to the precompression effect the spring does not respond to the axial forces smaller than the precompression force. The presented analytical and numerical analysis predict the precompression force with less than 10% error compared to the experimental results. A good agreement is seen between the analytical, numerical and experimental results during the loading-unloading phase. At the end of loading, a sudden jump occurs in the experimental load-deflection curve. This jump may be caused by a contact between the spring rings[11]. The contact at the end of the loading phase causes severe

[11] As shown in Figure 2.14 due to manufacturing difficulties, the helical spring does not have a perfectly uniform shape and the first and last rings have smaller pitch angles compare to the other rings. An initial contact occurs in these rings at the end of the loading phase.

local stress concentration and local phase transformation at the contact points. The locally contact induced phase transformation may be an explanation for a slight disagreement that is seen between the analytical and experimental results at the beginning of the unloading phase[12]. However, all the results are in good agreement for the rest of the unloading phase.

Two other case studies are considered for validating the presented analytical formulation with the experimental results. Toi et al. [185] presented experimental results for SMA helical springs in tension and compared them with their finite element simulation results. In the numerical simulations presented by Toi et al. [185], an incremental finite element using linear Timoshenko beam elements is formulated using a total Lagrangian approach for the superelastic, large deformation analysis of SMA helical springs. A simple tension test is carried out on the material of springs as shown in Figure 2.15(b). The presented constitutive model is calibrated using these results and the calibrated properties for this material are given in Table 2.1 as Material III. Figure 2.15(b) compares the simulated response of material using the presented constitutive model with the experimental results for simple tension. Two different springs are considered in experiments. Both springs have a mean coil radius of R_m=3.65mm, and the cross section radius of 0.5mm. One of the springs has a total length of 5mm and 5 turns and the other one has a total length of 10mm with 10 turns. Both springs are subjected to tension and tests are carried out at $T = 305K$. The analytical results obtained by the present CBTM are compared with the experimental and numerical results of Toi et al. [185] in Figure 2.25. A good agreement is seen between the CBTM and the finite element simulation results using Timoshenko beam elements. Both the numerical and analytical results have a slight difference with the experiments. This difference is most likely caused by the non-linearity effects due to the extreme amount of elongation in the experiments.

[12]It is worth noting that in modeling the loading-unloading phase even in a simple uniaxial case, the constitutive equation used in this chapter (the Boyd-Lagoudas' polynomial hardening model) shows a slight difference at the beginning of the unloading phase. Some improvements are provided for the hardening function to reduce this difference (see Chapter 3 in Lagoudas [92]). As we are seeking closed-form solutions in this chapter, the the polynomial hardening function is preferred.

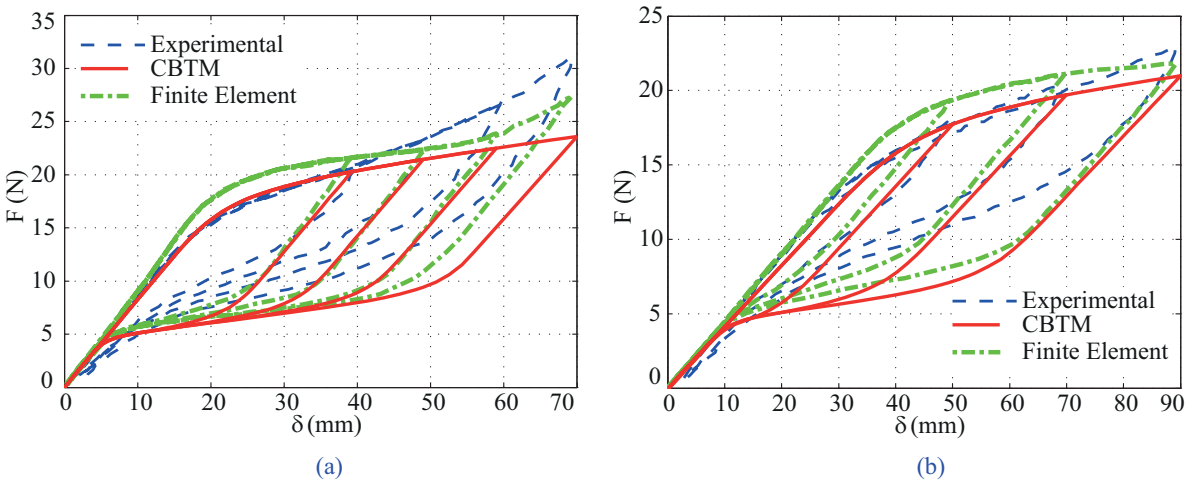

Figure 2.25: Axial force versus axial displacement.

2.3.5.4 Uncertainty in material properties

As mentioned earlier, making an SMA helical spring from a straight bar is done by performing a set of thermal and mechanical treatments on the initial SMA stock. Due to this complicated thermomechanical treatment, the material properties are not the same as the initial stock and in practice if a number of helical springs are made from an SMA stock, a slight difference may be seen in the material properties of these springs. DesRoches [42] presented a detailed study of the effect of a change in the material properties of SMAs in uniaxial tension on the hysteretic response and energy dissipation capability of these materials. The properties given in Table 2.1 for Material II are calibrated by comparing the results of analytical and numerical analyses with the experimental results done on the present SMA helical spring. However, in order to take the uncertainty of the material properties into consideration, we present a discussion on the effect of changing material properties on the spring response in this section. The numerical results presented in this section can also be used in designing SMA helical springs for various applications. All the numerical results in this section are presented based on CBTM and the spring is considered to be at $T = 27°\text{C}$.

Two of the material properties that have a significant influence on the SMA helical spring response in loading-unloading are the austenite and martensite elastic moduli. In

practice, the elastic modulus of different SMAs covers a wide range (see Toi et al. [185] for an SMA with $E_A = 34$GPA, $E_M = 28.5$GPA and Jacobus et al. [79] for an SMA with $E_A = 72$GPA, $E_M = 30$GPA). The effect of a decrease and increase in the elastic moduli of a material with properties given in Table 2.1 is shown in Figure 2.26. As it is shown in this figure, increasing E_A and E_M causes a remarkable increase in the hysteresis area that is strongly preferred for springs as energy absorbing devices. Note that this area is proportional to the amount of absorbed energy in an loading-unloading cycle.

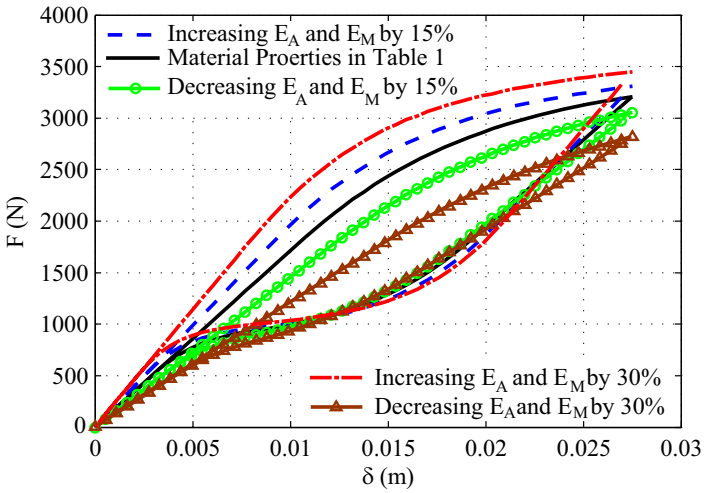

Figure 2.26: The effect of change of austenite and martensite elastic moduli on the loading-unloading response of a shape memory alloy helical spring.

The effects of an increase or decrease in the parameter $d\sigma/dT$ by the amounts of 15% and 30% are shown in Figure 2.27. The parameter $d\sigma/dT$ is the transformation curve slope in stress-temperature space and as expressed in (**??**), it is related to the specific entropy difference $\rho\Delta s_0$ (see Qidwai and Lagoudas [162] for more details on the physics of the material properties and for a detailed experimental technique for measuring these properties). As it is shown in Figure 2.27, an increase in the parameter $d\sigma/dT$ decreases the hysteresis area but remarkably increases the spring stiffness. This figure leads to an important conclusion for designing SMA helical springs as energy absorbing devices. It shows that in the cases that a stiffer spring is needed, SMA materials with larger $d\sigma/dT$ are preferred while the springs made of SMA materials with lower $d\sigma/dT$ have lower stiffness

and larger hysteresis area.

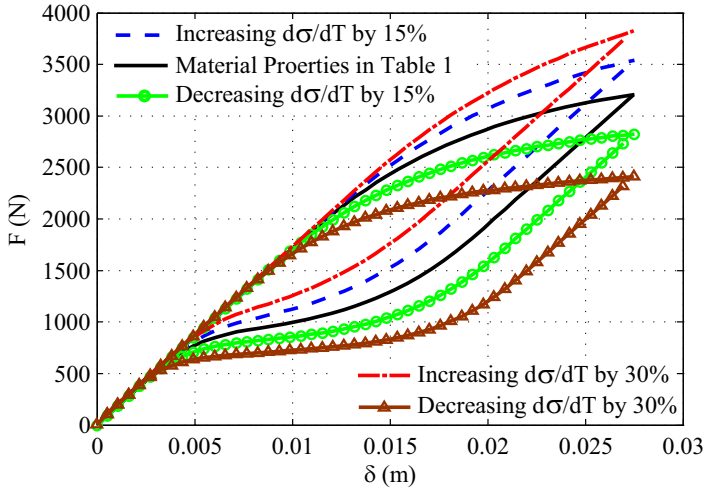

Figure 2.27: The effect of change of the parameter $d\sigma/dT$ on the loading-unloading response of a shape memory alloy helical spring.

2.3.5.5 The effect of ambient temperature on the SMA spring response

As mentioned in §2.3.3, a slow loading rate is considered in the experimental and analytical analyses of the SMA helical spring in this chapter. In slow loadings, the isothermal assumption is valid and the spring can be considered to be in the same temperature with the ambient environment during loading and unloading. Since one of the applications of SMA helical springs is seismic retrofit of buildings [173], the spring may be used in various areas or at different times of a year. Therefore, it is important to study the effect of ambient temperature on the spring response. Three common temperatures are considered in Figure 2.28 and the spring loading-unloading response in these temperatures is calculated (the results are obtained using CBTM). As it is shown in this figure, the ambient temperature has a considerable effect on the SMA helical spring response and at higher temperatures the hysteresis area decreases remarkably while the stiffness is increased. The spring loading-unloading cycle has a larger hysteresis area at lower temperatures but the stiffness is lower compare to higher temperatures.

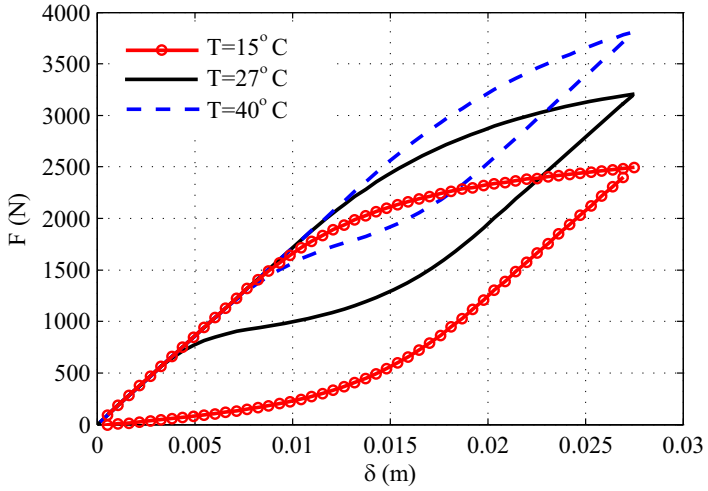

Figure 2.28: The effect of temperature change on the loading-unloading response of shape memory alloy helical spring.

2.3.5.6 CBTM and STBM for analyzing different spring geometries

As mentioned in the previous sections, introducing the curvature effect in the solution based on the torsion of straight bars for analyzing helical SMA springs (SBTM), a more accurate method (CBTM) is obtained for SMA springs with smaller indices. Because the CBTM needs an iterative procedure for finding the location of torsion centroid, it is remarkably more time consuming compared to the STBM. From a design point of view it would be interesting to find the range of spring indices for which the STBM gives acceptable accuracy and a criterion for the necessity of using CBTM. In this section an SMA helical spring with properties given in Table 2.1 as Material II is considered. The mean coil radius is R_m =2cm and the total length of the spring is 11cm. The spring has 5 turns and it is subjected to tension causing a maximum elongation of 6cm. The cross section radius is considered variable for obtaining different helix indices. Temperature is assumed to be $T = 300$K. Figure 2.29(a) shows the maximum shear stress in the cross section and Figure 2.29(b) shows the maximum volume fraction in the cross section for different helix indices obtained by SBTM and SBTN. As it is shown in these figures decreasing the spring index, the difference between CBTM and SBTM increases. The results calculated by SBTM for

both the maximum shear stress and the martensitic volume fraction deviate more than 5% from the CBTM results for the helix indices smaller than 5. This difference increases considerably for the calculated maximum shear stress for spring indices smaller than 2.12 for which CBTM predicts completion of phase transformation and a sharp increase in the shear maximum stress in the cross section.

The analysis of maximum shear stress as a function of geometric properties, e.g. the spring index for different spring geometries can also be used in a design procedure for calculating the critical geometries for which the maximum shear stress reaches a critical value. This critical value can be considered as the stress corresponding to the end of reversible stress-strain response for the SMA material. As an example, if the maximum stress in the pseudoelastic stress-strain response is $\tau_{max} = 300$MPa, for spring indices smaller than 2.11, the maximum shear stress is more than the critical value and elongating the spring more than the considered value (6cm) will cause a nonrecoverable overstretching of the spring (see Figure 2.29(a)). Similar design graphs can be obtained by the present formulation for different geometric properties, material properties, and loading conditions.

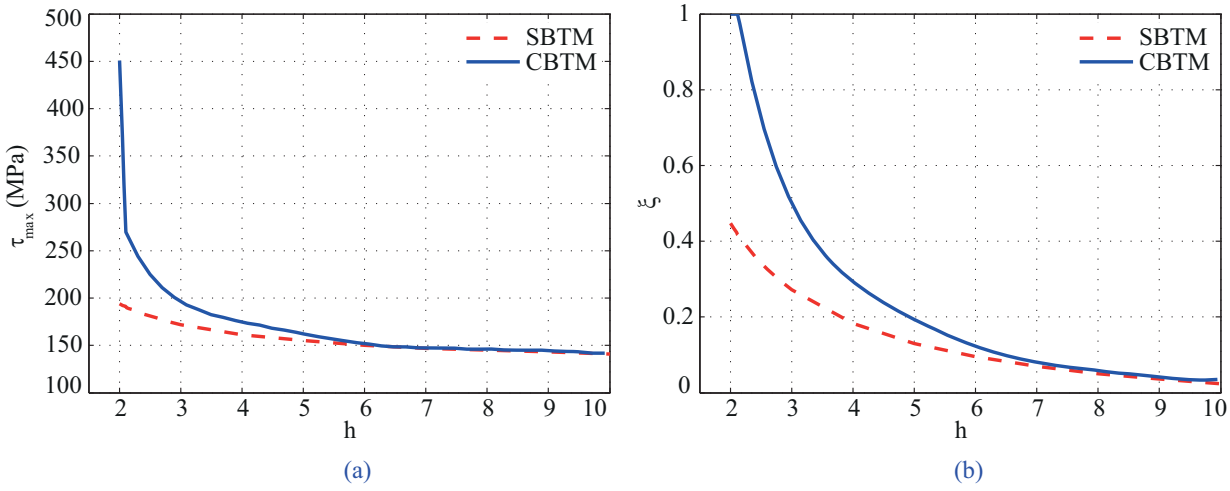

Figure 2.29: Comparison between the STBM and CBTM results for various helix indices for (a) .

2.4 Shape Memory Alloy Thick-Walled Cylinders Subjected to Internal Pressure

In this section, a semi-analytic solution is presented for the analysis of shape memory alloy thick-walled cylinders subjected to internal pressure in both plane stress and plane strain conditions. First, a two-dimensional reduction of Boyd-Lagoudas's polynomial SMA constitutive model is obtained for both plane stress and plane strain. Then, the thick-walled cylinder is divided into a finite number of narrow annular regions and the loading is partitioned into a finite number of increments. Appropriate assumptions are made in each region in order to find a closed-form solution for the equilibrium equations in terms of radial displacements within the regions in which the phase transformation has started but has not completed. Considering the history of loading and the final values of transformation strain components, another solution is given for those regions and load increments for which the material is completely transformed to martensite. By satisfying the continuity condition at the interfaces between the annular regions and the boundary conditions at the inner and outer radii, a semi-analytic solution is obtained for any value of internal pressure. Several numerical examples are presented for different loading phases and the results of the proposed solution are compared with those of three-dimensional finite element simulations in both plane stress and plane strain cases. In contrast with finite element simulations, the results of the present semi-analytic solution are not severely affected by the number of load steps, and they are independent of the criteria for satisfaction of the constitutive relation convergence, and the number of iterations for convergence in considering geometric nonlinearities. Considering the numerical stability of the present semi-analytic method, we believe that it can be used in validating the results of common numerical methods in analyzing shape memory alloy structures.

2.4.1 Martensitic volume fraction for plane strain and plane stress conditions

A thick-walled SMA cylinder subjected to uniform internal pressure p is considered (see Figure 2.30). For a relatively short cylinder with open ends and in the absence of axial loads, plane stress is a good approximation. For long cylinders, cross sections far from

the ends are in a plane strain condition. In both cases, the three-dimensional constitutive relations presented in the previous section can be reduced to two-dimensional constitutive equations.

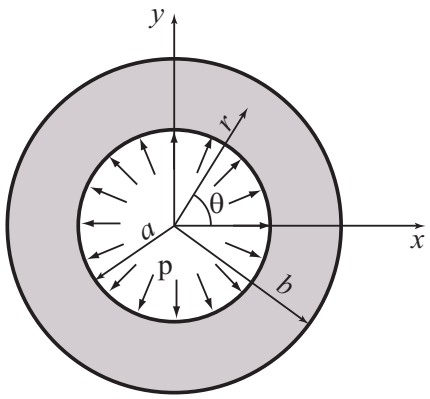

Figure 2.30: Cross section of a thick-walled SMA cylinder subjected to uniform internal pressure.

The only nonzero stress components for the axisymmetric plane stress case are σ_r and σ_θ. In this case the trace of stress tensor is $\mathrm{tr}\boldsymbol{\sigma} = \sigma_r + \sigma_\theta$. In the plane strain case, the stress component along the axis of the cylinder is denoted by σ_z, and trace of the stress tensor is $\mathrm{tr}\boldsymbol{\sigma} = \sigma_r + \sigma_\theta + \sigma_z$. It is worth mentioning that in contrast with the classical elasticity problems, the out of plane component of stress cannot be expressed by $\sigma_z = \nu(\sigma_r + \sigma_\theta)$ due to the transformation strain terms. However, for any value of σ_r and σ_θ, by enforcing the plane strain condition $\epsilon_z = 0$, σ_z can be calculated. We will present a brief discussion on calculating σ_z for SMAs in plane strain in the sequel. In these special cases (plane stress and plane strain), the deviatoric stress tensor in $(2.7)_1$ can be rewritten as

$$
\begin{aligned}
{}^{e}\boldsymbol{\sigma}' &= \frac{1}{3}\begin{bmatrix} 2\sigma_r - \sigma_\theta - \sigma_z & 0 & 0 \\ 0 & 2\sigma_\theta - \sigma_r - \sigma_z & 0 \\ 0 & 0 & 2\sigma_z - \sigma_r - \sigma_\theta \end{bmatrix}, \\
{}^{s}\boldsymbol{\sigma}' &= \frac{1}{3}\begin{bmatrix} 2\sigma_r - \sigma_\theta & 0 & 0 \\ 0 & 2\sigma_\theta - \sigma_r & 0 \\ 0 & 0 & -\sigma_r - \sigma_\theta \end{bmatrix},
\end{aligned}
\tag{2.35}
$$

where the left superscripts ${}^{e}(.)$ and ${}^{s}(.)$ represent a parameter in plane strain and plane stress, respectively. This notation will be used throughout the paper. Substituting (2.35) into $(2.6)_1$, the transformation tensor for the forward phase transformation can be obtained. By substituting the transformation tensor into (2.9) the thermodynamic forces for the plane strain and plane stress conditions are obtained as follows:

$$ {}^{e}\pi = H\ {}^{e}\sigma_{\text{eff}} + \frac{1}{2}\Delta S_{11}\ {}^{e}\sigma^{*}_{\text{eff}} + \aleph \qquad \text{and} \qquad {}^{s}\pi = H\ {}^{s}\sigma_{\text{eff}} + \frac{1}{2}\Delta S_{11}\ {}^{s}\sigma^{*}_{\text{eff}} + \aleph, \tag{2.36} $$

where

$$ \begin{aligned} {}^{e}\sigma_{\text{eff}} &= (\sigma_r^2 + \sigma_\theta^2 + \sigma_z^2 - \sigma_r\sigma_\theta - \sigma_r\sigma_z - \sigma_\theta\sigma_z)^{1/2}, \\ {}^{s}\sigma_{\text{eff}} &= (\sigma_r^2 + \sigma_\theta^2 - \sigma_r\sigma_\theta)^{1/2}, \\ {}^{e}\sigma^{*}_{\text{eff}} &= \left[\sigma_r^2 + \sigma_\theta^2 + \sigma_z^2 - 2\nu(\sigma_r\sigma_\theta + \sigma_r\sigma_z + \sigma_\theta\sigma_z)\right], \\ {}^{s}\sigma^{*}_{\text{eff}} &= (\sigma_r^2 + \sigma_\theta^2 - 2\nu\sigma_r\sigma_\theta), \\ \aleph &= (\Delta\alpha_{11}\sigma_r + \Delta\alpha_{22}\sigma_\theta)(T - T_0) - \rho\,\Delta c\left[(T - T_0) - T\ \ln\left(T/T_0\right)\right] \\ &\quad + \rho\,\Delta s_0 T - \rho b^M \xi - (\mu_1 + \mu_2) - \rho\,\Delta u_0, \\ \Delta S_{11} &= \frac{1}{E^M} - \frac{1}{E^A}. \end{aligned} \tag{2.37} $$

The parameters E^M and E^A represent the elastic moduli for the martensite and austenite phases, respectively, and ν is the Poisson's ratio, which is assumed to be the same for both phases. Now, (2.10) and (2.36) are used in obtaining an explicit expression for the martensitic volume fraction ξ. During the forward phase transformation from austenite to martensite ($\dot{\xi} > 0$), the state of stress, temperature and martensitic volume fraction should remain on the transformation surface characterized by $\Phi = \pi - Y = 0$. By substituting (2.36) into this condition and using the relations between the constitutive model parameters (2.14) an explicit expression is obtained for the martensitic volume fraction in plane strain and plain stress states as:

$$ {}^{e}\xi = \frac{1}{\rho b^M}\ \left[H\ {}^{e}\sigma_{\text{eff}} + \frac{1}{2}\Delta S_{11}\ {}^{e}\sigma^{*}_{\text{eff}} + f(T) + \widehat{T}\ \right], \tag{2.38} $$

$$ {}^{s}\xi = \frac{1}{\rho b^M}\ \left[H\ {}^{s}\sigma_{\text{eff}} + \frac{1}{2}\Delta S_{11}\ {}^{s}\sigma^{*}_{\text{eff}} + f(T) + \widehat{T}\ \right], \tag{2.39} $$

where

$$f(T) = (\Delta\alpha_{11}\sigma_r + \Delta\alpha_{22}\sigma_\theta)(T - T_0) - \rho\,\Delta c\,[(T - T_0) - T\ \ln(T/T_0)]\,, \quad (2.40)$$

$$\widehat{T} = \rho\,\Delta s_0(T - M_s). \quad (2.41)$$

Transformation surface in the stress-temperature space is represented by two separate faces related to $\xi = 0$ and $\xi = 1$. To obtain the transformation surface in the plane strain case, for each value of the radial and circumferential stresses the plane strain condition in the reference temperature $T = T_0$ is given by the following algebraic equation (see the constitutive relation in (2.4))

$$\epsilon_z = D_{eq}(\sigma_r - \nu\sigma_\theta - \nu\sigma_z) + \frac{1}{2}\frac{H}{{}^e\sigma_{\text{eff}}}\,(2\sigma_z - \sigma_r - \sigma_\theta)\ {}^e\xi = 0, \quad (2.42)$$

where, $(H/2{}^e\sigma_{\text{eff}})(2\sigma_z - \sigma_r - \sigma_\theta)\ {}^e\xi$ is the out of plane transformation strain ϵ_z^t (calculating the transformation strain components will be expressed in more detail in §4). The martensitic volume fraction is expressed in (2.38) and the effective compliance component D_{eq} is

$$D_{eq} = \frac{1}{E^A + \ {}^e\xi(E^M - E^A)}. \quad (2.43)$$

In the plane strain case, for any known $(\sigma_r, \sigma_\theta)$ stress state, (2.42) is an algebraic equation with σ_z as the only unknown. For finding the transformation function, for each value of the circumferential and radial stresses, (2.42) is solved numerically [55] and σ_z is calculated. Having the stress components, (2.38) and (2.39) are used to obtain the transformation functions in both plane stress and plane strain cases. At a given temperature, the transformation functions $\xi = 0$ and $\xi = 1$ are represented by curves in $(\sigma_r, \sigma_\theta)$ stress space. Figure 2.31 shows the transformation function in the start and finish of phase transformation for both the plane stress and plane strain conditions (material properties of Table **??** are used in plotting these curves). For any state of stress inside the $\xi = 0$ region, the material is in the fully austenine phase. The stress points outside $\xi = 1$ represent a fully martensite case, and any stress state between these two surfaces represents the material with phase transformation $0 < \xi < 1$.

As it is shown in Figure 2.31, in the plane strain case the $\xi = 1$ curve is stretched along the $\sigma_r = \sigma_\theta$ line. For studying this phenomenon, the out of plane stress obtained

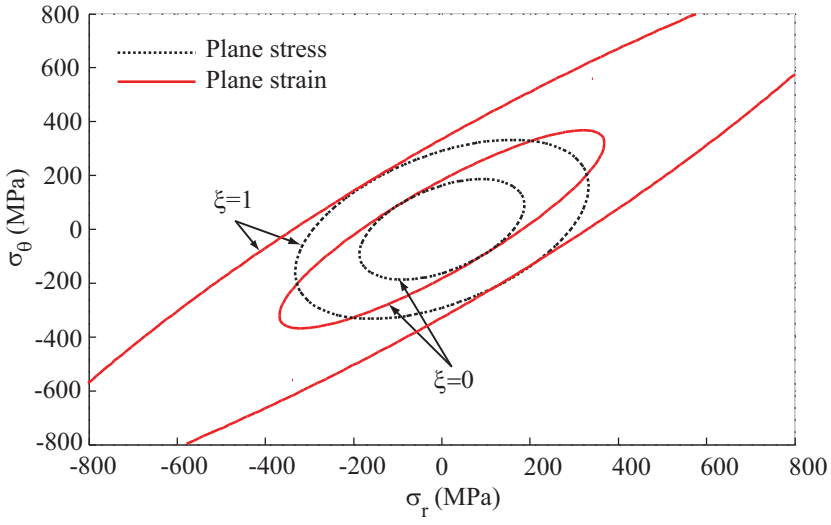

Figure 2.31: Transformation function in $\sigma_r - \sigma_\theta$ space at $T = 315K$ for both plane stress and plane strain cases.

from solving the plane strain condition in (2.42) for any $(\sigma_r, \sigma_\theta)$ stress sate is plotted in Figure 2.32. As it is shown in this figure, for any $(\sigma_r, \sigma_\theta)$ stress state inside the $\xi = 0$ curve (see Figure 2.31) the value of σ_z is identical with the elastic case ($\sigma_z = \nu(\sigma_r - \sigma_\theta)$). Between the $\xi = 0$ and $\xi = 1$ curves, σ_z varies nonlinearly and is obtained from solving (2.42) and for any state of stress outside the $\xi = 1$ curve, the value of σ_z is not unique and depends on the loading path[13]. By increase of stresses on the $\sigma_r = \sigma_\theta$ path, the solution of (2.42) approaches $\sigma_z = \sigma_r = \sigma_\theta$, i.e. the hydrostatic stress state. Note that the presented constitutive relations are based on J_2 plasticity and the transformation function is an open surface along the hydrostatic pressure in this case (see Qidwai and Lagoudas [162]). See the open curve in Figure 2.31 for the plane strain case.

The elastic radial and hoop stress distribution for a thick-walled cylinder in plane stress or plane strain (see Figure 2.30) can be expressed as [27]:

$$\sigma_r = \frac{pa^2(r^2 - b^2)}{r^2(b^2 - a^2)} \qquad \text{and} \qquad \sigma_\theta = \frac{pa^2(r^2 + b^2)}{r^2(b^2 - a^2)}. \tag{2.44}$$

[13]For calculating σ_z outside the $\xi = 1$ curve, the plane strain condition $\epsilon_z = \frac{1}{E_M}(\sigma_r - \nu\sigma_\theta - \nu\sigma_z) + \tilde{\epsilon}_z^t = 0$ is solved in which $\tilde{\epsilon}_z^t$ is the final value of axial transformation strain during loading at the point that phase transformation has been completed. We will discuss this case in more detail in §6.

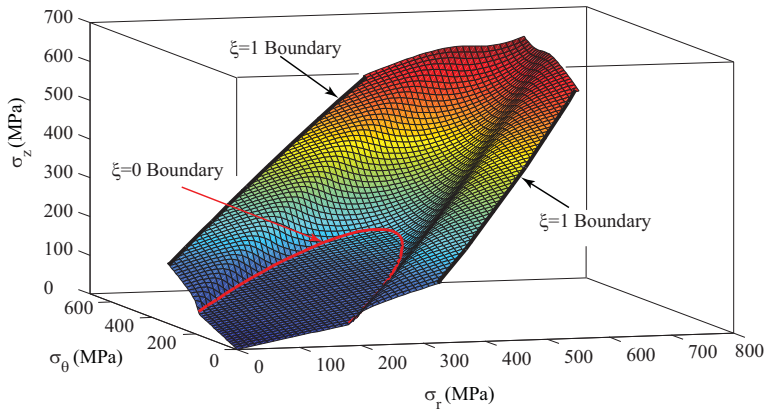

Figure 2.32: σ_z in plane strain as a function of σ_r and σ_θ.

The axial stress component in plane strain for an elastic cylinder is expressed as $\sigma_z = \nu(\sigma_r - \sigma_\theta)$. Considering (2.38), (2.39), (2.44), and using the dimensionless quantities $R = r/a$ and $\beta = b/a$, the following expressions are obtained for the martensitic volume fraction in plane strain and plane stress as functions of internal pressure (using $\Delta c = \Delta\alpha_{11} = \Delta\alpha_{22} = 0$):

$$
\begin{aligned}
{}^{e}\xi = {} & \frac{H}{\rho b^M}\frac{p}{R^2(\beta^2-1)}\sqrt{4\,\nu^2R^4 - 4\,\nu\,R^4 + 3\,\beta^4 + R^4} \\
& + \frac{\Delta S_{11}}{\rho b^M}\frac{p^2}{R^4(1-\beta^2)^2}(\beta^4 + R^4 - 2\,\nu^2R^4 + \nu\beta^4 - \nu R^4) + \frac{\widehat{T}}{\rho b^M}, \qquad (2.45) \\
{}^{s}\xi = {} & \frac{H}{\rho b^M}\frac{p}{R^2(\beta^2-1)}\sqrt{3\beta^4 + R^4} \\
& + \frac{\Delta S_{11}}{\rho b^M}\frac{p^2}{R^4(1-\beta^2)^2}(\beta^4 + R^4 + \nu\beta^4 - \nu R^4) + \frac{\widehat{T}}{\rho b^M}. \qquad (2.46)
\end{aligned}
$$

In deriving (2.45) and (2.46), the elastic stress distribution is considered for the cylinder, so this relation represents an exact expression only for the phase transformation innermost radius

at the initiation of phase transformation, which is characterized by $\xi = 0$. Solving (2.45)

and (2.46) for the parameter p by setting $\xi = 0$ gives:

$$
\begin{aligned}
{}^{e}p = \frac{R_0^2(\beta^2-1)}{2\,\Delta S_{11}(\beta^4+R_0^4-2\,\nu^2 R_0^4+\nu\beta^4-\nu R_0^4)}\Big(&-H\sqrt{4\,\nu^2 R_0^4-4\,\nu\,R_0^4+3\,\beta^4+R_0^4} \\
&+\Big[H^2(4\,\nu^2 R_0^4-4\,\nu\,R_0^4+3\,\beta^4+R_0^4)-4\,\widehat{T}\,\Delta S_{11}(\beta^4+R_0^4-2\,\nu^2 R_0^4+\nu\beta^4-\nu R_0^4)\Big]^{\frac{1}{2}}\Big), \quad (2.47)
\end{aligned}
$$

$$
\begin{aligned}
{}^{s}p = \frac{R_0^2(\beta^2-1)}{2\,\Delta S_{11}(\beta^4+R_0^4+\nu\beta^4-\nu R_0^4)}\Big(&-H\sqrt{3\beta^4+R_0^4} \\
&+\sqrt{3H^2\beta^4+H^2R_0^4-4\,\widehat{T}\,\Delta S_{11}(\beta^4+R_0^4+\nu\beta^4-\nu R_0^4)}\;\Big). \quad (2.48)
\end{aligned}
$$

Since (2.45) and (2.46) are solved for ($\xi = 0$), we denote the parameter R in this special case by R_0 where $R_0 = r_0/a$ and r_0 is the inner radius of the region in which the phase transformation has not started ($\xi = 0$). Equations (2.47) and (2.48) can be used for exact prediction of phase transformation initiation that starts from the inner radius ($R_0 = 1$). Note that in the phase transformation initiation the whole cylinder is in the austenite phase and the elastic stress distribution in (2.44) is valid, so (2.47) and (2.48) present the exact solution in this case. Figure 2.33 shows this pressure for different values of β and for three different temperatures in both plane stress and plane strain.

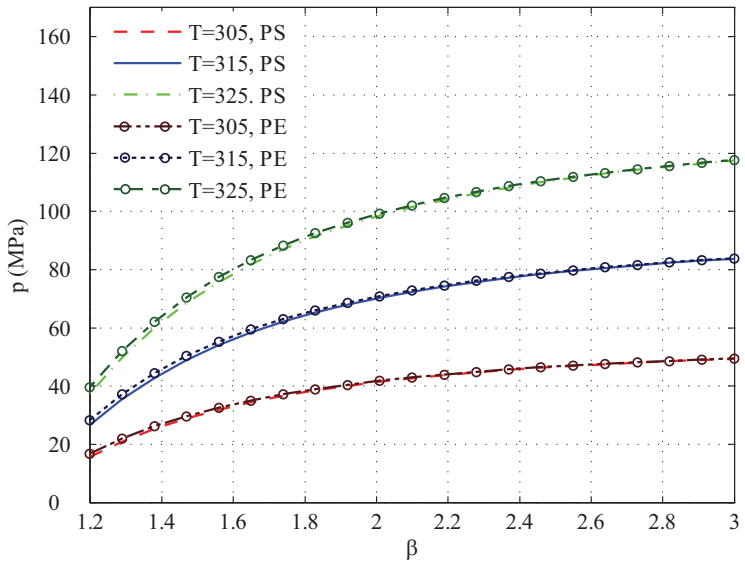

Figure 2.33: Exact value for the minimum pressure required for phase transformation initiation in SMA thick-walled cylinders in both plane stress (PS) and plane strain (PE).

As the elastic stress distribution is assumed in deriving (2.45)-(2.48), by spread of the

regions with phase transformation toward the outer radius, the precision of these relations is reduced as stress distribution in areas with phase transformation is different from the elastic stress distribution. Using (2.45) and (2.46), Figure 2.34 shows an approximate solution for the spread of phase transformation boundary (R_0) as the pressure increases for three different values of temperature. These results are obtained for a thick-walled cylinder with $\beta = 3$ in both plane stress and plane strain. The results of Figure 2.34 are exact for $R_0 = 1$ since the phase transformation boundary is at the inner radius in this case and the whole cylinder is in the fully austenite phase with elastic stress distribution. However, when the phase transformation boundary is spread through the outer radius ($R_0 > 1$) the elastic stress distribution is not valid in a portion of the thickness and the results of Figure 2.34 are approximate. The exact value for R_0 for different internal pressures will be given in the sequel.

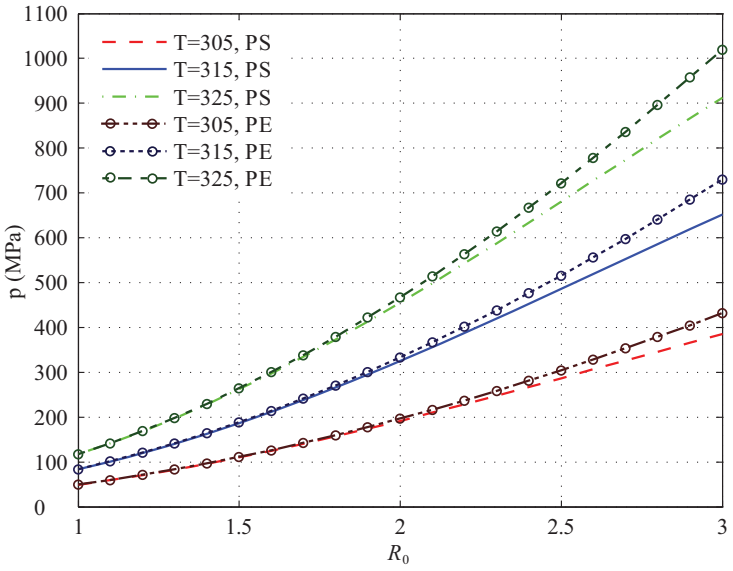

Figure 2.34: An approximate value for the spread of phase transformation boundary in SMA thick-walled cylinders in both plane stress (PS) and plane strain (PE).

2.4.2 Transformation strains and their derivatives with respect to stress components

In this section, the two-dimensional form of the constitutive relations are expressed for material points with $0 < \xi < 1$. Substituting the transformation tensor into (2.5) and after integration, the following expressions are obtained for the transformation strain components in plane stress and plane strain:

$$
\begin{aligned}
&{}^{e}\epsilon_r^t = \frac{1}{2}\frac{H}{{}^{e}\sigma_{\text{eff}}}\left(2\sigma_r - \sigma_\theta - \sigma_z\right)\xi, \quad {}^{e}\epsilon_\theta^t = \frac{1}{2}\frac{H}{{}^{e}\sigma_{\text{eff}}}\left(2\sigma_\theta - \sigma_r - \sigma_z\right)\xi, \\
&{}^{e}\epsilon_z^t = \frac{1}{2}\frac{H}{{}^{e}\sigma_{\text{eff}}}\left(2\sigma_z - \sigma_r - \sigma_\theta\right)\xi, \qquad (2.49) \\
&{}^{s}\epsilon_r^t = \frac{1}{2}\frac{H}{{}^{s}\sigma_{\text{eff}}}(2\sigma_r - \sigma_\theta)\xi, \quad {}^{s}\epsilon_\theta^t = \frac{1}{2}\frac{H}{{}^{s}\sigma_{\text{eff}}}(2\sigma_\theta - \sigma_r)\xi, \qquad (2.50)
\end{aligned}
$$

with the effective stresses expressed in (2.37). Using $\Delta c = \Delta\alpha_{11} = \Delta\alpha_{22} = 0$, substituting (2.38) into (2.49) leads to the following expression for the transformation strain components for the plane stress case:

$$
{}^{s}\epsilon_r^t = {}^{s}\mathscr{F}\,(2\sigma_r - \sigma_\theta), \quad {}^{s}\epsilon_\theta^t = {}^{s}\mathscr{F}\,(2\sigma_\theta - \sigma_r), \qquad (2.51)
$$

and the transformation strain components in the plane strain case are obtained by substituting (2.39) into (2.50) as:

$$
{}^{e}\epsilon_r^t = {}^{e}\mathscr{F}\,(2\sigma_r - \sigma_\theta - \sigma_z), \quad {}^{e}\epsilon_\theta^t = {}^{e}\mathscr{F}\,(2\sigma_\theta - \sigma_r - \sigma_z), \quad {}^{e}\epsilon_z^t = {}^{e}\mathscr{F}\,(2\sigma_z - \sigma_r - \sigma_\theta), \qquad (2.52)
$$

where

$$
{}^{s}\mathscr{F} = \left(\frac{H^2}{2\rho b^M} + \frac{H\Delta S_{11}}{4\rho b^M}\frac{{}^{s}\sigma_{\text{eff}}^*}{{}^{s}\sigma_{\text{eff}}} + \frac{H\ \widehat{T}}{2\rho b^M}\frac{1}{{}^{s}\sigma_{\text{eff}}}\right), \qquad (2.53)
$$

$$
{}^{e}\mathscr{F} = \left(\frac{H^2}{2\rho b^M} + \frac{H\Delta S_{11}}{4\rho b^M}\frac{{}^{e}\sigma_{\text{eff}}^*}{{}^{e}\sigma_{\text{eff}}} + \frac{H\ \widehat{T}}{2\rho b^M}\frac{1}{{}^{e}\sigma_{\text{eff}}}\right). \qquad (2.54)
$$

Differentials of transformation strains in (2.51) and (2.52), after some lengthy algebraic manipulations, can be written as

$$d({}^{e}\epsilon_r^t) = \frac{1}{2\rho b^M}\Bigg\{\left[2H^2 + H\ {}^{e}\mathcal{G} + 2\frac{H\ \widehat{T}}{{}^{e}\sigma_{\text{eff}}} + \left(\frac{1}{2}H\ {}^{e}\mathcal{A} - \frac{H\ \widehat{T}\ {}^{e}\mathcal{M}}{({}^{e}\sigma_{\text{eff}})^2}\right)\ (2\sigma_r - \sigma_\theta - \sigma_z)\right]d\sigma_r$$
$$+\left[-H^2 - \frac{1}{2}H\ {}^{e}\mathcal{G} - \frac{H\ \widehat{T}}{{}^{e}\sigma_{\text{eff}}} + \left(\frac{1}{2}H\ {}^{e}\mathcal{B} - \frac{H\ \widehat{T}\ {}^{e}\mathcal{N}}{({}^{e}\sigma_{\text{eff}})^2}\right)\ (2\sigma_r - \sigma_\theta - \sigma_z)\right]d\sigma_\theta$$
$$+\left[-H^2 - \frac{1}{2}H\ {}^{e}\mathcal{G} - \frac{H\ \widehat{T}}{{}^{e}\sigma_{\text{eff}}} + \left(\frac{1}{2}H\ {}^{e}\mathcal{C} - \frac{H\ \widehat{T}\ {}^{e}\mathcal{O}}{({}^{e}\sigma_{\text{eff}})^2}\right)\ (2\sigma_r - \sigma_\theta - \sigma_z)\right]d\sigma_z\Bigg\}, \tag{2.55}$$

$$d({}^{e}\epsilon_\theta^t) = \frac{1}{2\rho b^M}\Bigg\{\left[-H^2 - \frac{1}{2}H\ {}^{e}\mathcal{G} - \frac{H\ \widehat{T}}{{}^{e}\sigma_{\text{eff}}} + \left(\frac{1}{2}H\ {}^{e}\mathcal{A} - \frac{H\ \widehat{T}\ {}^{e}\mathcal{M}}{({}^{e}\sigma_{\text{eff}})^2}\right)\ (2\sigma_\theta - \sigma_r - \sigma_z)\right]d\sigma_r$$
$$+\left[2H^2 + H\ {}^{e}\mathcal{G} + 2\frac{H\ \widehat{T}}{{}^{e}\sigma_{\text{eff}}} + \left(\frac{1}{2}H\ {}^{e}\mathcal{B} - \frac{H\ \widehat{T}\ {}^{e}\mathcal{N}}{({}^{e}\sigma_{\text{eff}})^2}\right)\ (2\sigma_\theta - \sigma_r - \sigma_z)\right]d\sigma_\theta$$
$$+\left[-H^2 - \frac{1}{2}H\ {}^{e}\mathcal{G} - \frac{H\ \widehat{T}}{{}^{e}\sigma_{\text{eff}}} + \left(\frac{1}{2}H\ {}^{e}\mathcal{C} - \frac{H\ \widehat{T}\ {}^{e}\mathcal{O}}{({}^{e}\sigma_{\text{eff}})^2}\right)\ (2\sigma_\theta - \sigma_r - \sigma_z)\right]d\sigma_z\Bigg\}, \tag{2.56}$$

$$d({}^{e}\epsilon_z^t) = \frac{1}{2\rho b^M}\Bigg\{\left[-H^2 - \frac{1}{2}H\ {}^{e}\mathcal{G} - \frac{H\ \widehat{T}}{{}^{e}\sigma_{\text{eff}}} + \left(\frac{1}{2}H\ {}^{e}\mathcal{A} - \frac{H\ \widehat{T}\ {}^{e}\mathcal{M}}{({}^{e}\sigma_{\text{eff}})^2}\right)\ (2\sigma_z - \sigma_r - \sigma_\theta)\right]d\sigma_r$$
$$+\left[-H^2 - \frac{1}{2}H\ {}^{e}\mathcal{G} - \frac{H\ \widehat{T}}{{}^{e}\sigma_{\text{eff}}} + \left(\frac{1}{2}H\ {}^{e}\mathcal{B} - \frac{H\ \widehat{T}\ {}^{e}\mathcal{N}}{({}^{e}\sigma_{\text{eff}})^2}\right)\ (2\sigma_z - \sigma_r - \sigma_\theta)\right]d\sigma_\theta$$
$$+\left[2H^2 + H\ {}^{e}\mathcal{G} + 2\frac{H\ \widehat{T}}{{}^{e}\sigma_{\text{eff}}} + \left(\frac{1}{2}H\ {}^{e}\mathcal{C} - \frac{H\ \widehat{T}\ {}^{e}\mathcal{O}}{({}^{e}\sigma_{\text{eff}})^2}\right)\ (2\sigma_z - \sigma_r - \sigma_\theta)\right]d\sigma_z\Bigg\}, \tag{2.57}$$

for plane strain and

$$d({}^{s}\epsilon_r^t) = \frac{1}{2\rho b^M}\Bigg\{\left[2H^2 + H\ {}^{s}\mathcal{G} + 2\frac{H\ \widehat{T}}{{}^{s}\sigma_{\text{eff}}} + \left(\frac{1}{2}H\ {}^{s}\mathcal{A} - \frac{H\ \widehat{T}\ {}^{s}\mathcal{M}}{({}^{s}\sigma_{\text{eff}})^2}\right)\ (2\sigma_r - \sigma_\theta)\right]d\sigma_r$$
$$+\left[-H^2 - \frac{1}{2}H\ {}^{s}\mathcal{G} - \frac{H\ \widehat{T}}{{}^{s}\sigma_{\text{eff}}} + \left(\frac{1}{2}H\ {}^{s}\mathcal{B} - \frac{H\ \widehat{T}\ {}^{s}\mathcal{N}}{({}^{s}\sigma_{\text{eff}})^2}\right)\ (2\sigma_r - \sigma_\theta)\right]d\sigma_\theta\Bigg\}, \tag{2.58}$$

$$d({}^{s}\epsilon_\theta^t) = \frac{1}{2\rho b^M}\Bigg\{\left[-H^2 - \frac{1}{2}H\ {}^{s}\mathcal{G} - \frac{H\ \widehat{T}}{{}^{s}\sigma_{\text{eff}}} + \left(\frac{1}{2}H\ {}^{s}\mathcal{A} - \frac{H\ \widehat{T}\ {}^{s}\mathcal{M}}{({}^{s}\sigma_{\text{eff}})^2}\right)\ (2\sigma_\theta - \sigma_r)\right]d\sigma_r$$
$$+\left[2H^2 + H\ {}^{s}\mathcal{G} + 2\frac{H\ \widehat{T}}{{}^{s}\sigma_{\text{eff}}} + \left(\frac{1}{2}H\ {}^{s}\mathcal{B} - \frac{H\ \widehat{T}\ {}^{s}\mathcal{N}}{({}^{s}\sigma_{\text{eff}})^2}\right)\ (2\sigma_\theta - \sigma_r)\right]d\sigma_\theta\Bigg\}, \tag{2.59}$$

for plane stress, where

$$
\begin{aligned}
&{}^{e}\mathcal{M} = \frac{2\sigma_r - \sigma_\theta - \sigma_z}{2\ {}^{e}\sigma_{\text{eff}}},\ {}^{e}\mathcal{N} = \frac{2\sigma_\theta - \sigma_r - \sigma_z}{2\ {}^{e}\sigma_{\text{eff}}},\ {}^{e}\mathcal{O} = \frac{2\sigma_z - \sigma_r - \sigma_\theta}{2\ {}^{e}\sigma_{\text{eff}}},\\
&{}^{e}\mathcal{A} = \frac{\Delta S_{11}}{({}^{e}\sigma_{\text{eff}})^2}\left[{}^{e}\sigma_{\text{eff}}\left(2\sigma_r - 2\nu\sigma_\theta - 2\nu\sigma_z\right) - {}^{e}\mathcal{M}\ {}^{e}\sigma^*_{\text{eff}}\right],\\
&{}^{e}\mathcal{B} = \frac{\Delta S_{11}}{({}^{e}\sigma_{\text{eff}})^2}\left[{}^{e}\sigma_{\text{eff}}\left(2\sigma_\theta - 2\nu\sigma_r - 2\nu\sigma_z\right) - {}^{e}\mathcal{N}\ {}^{e}\sigma^*_{\text{eff}}\right],\\
&{}^{e}\mathcal{C} = \frac{\Delta S_{11}}{({}^{e}\sigma_{\text{eff}})^2}\left[{}^{e}\sigma_{\text{eff}}\left(2\sigma_z - 2\nu\sigma_r - 2\nu\sigma_\theta\right) - {}^{e}\mathcal{O}\ {}^{e}\sigma^*_{\text{eff}}\right],\\
&{}^{s}\mathcal{M} = \frac{2\sigma_r - \sigma_\theta}{2\ {}^{s}\sigma_{\text{eff}}},\ {}^{s}\mathcal{N} = \frac{2\sigma_\theta - \sigma_r}{2\ {}^{s}\sigma_{\text{eff}}},\\
&{}^{s}\mathcal{A} = \frac{\Delta S_{11}}{({}^{s}\sigma_{\text{eff}})^2}\left[{}^{s}\sigma_{\text{eff}}\left(2\sigma_r - 2\nu\sigma_\theta\right) - {}^{s}\mathcal{M}\ {}^{s}\sigma^*_{\text{eff}}\right],\ {}^{s}\mathcal{B} = \frac{\Delta S_{11}}{({}^{s}\sigma_{\text{eff}})^2}\left[{}^{s}\sigma_{\text{eff}}\left(2\sigma_\theta - 2\nu\sigma_r\right) - {}^{s}\mathcal{N}\ {}^{s}\sigma^*_{\text{eff}}\right],\\
&{}^{e}\mathcal{G} = \Delta S_{11}\ \frac{{}^{e}\sigma^*_{\text{eff}}}{{}^{e}\sigma_{\text{eff}}},\ {}^{s}\mathcal{G} = \Delta S_{11}\ \frac{{}^{s}\sigma^*_{\text{eff}}}{{}^{s}\sigma_{\text{eff}}}.
\end{aligned}
\tag{2.60}
$$

On the other hand by considering the fact that the transformation strains (in both plane stress and plane strain) are functions of material constants and the stress components, their differentials can be expressed as

$$
\begin{aligned}
d({}^{e}\epsilon^t_r) &= \frac{\partial({}^{e}\epsilon^t_r)}{\partial\sigma_r}d\sigma_r + \frac{\partial({}^{e}\epsilon^t_r)}{\partial\sigma_\theta}d\sigma_\theta + \frac{\partial({}^{e}\epsilon^t_r)}{\partial\sigma_z}d\sigma_z,\\
d({}^{e}\epsilon^t_\theta) &= \frac{\partial({}^{e}\epsilon^t_\theta)}{\partial\sigma_r}d\sigma_r + \frac{\partial({}^{e}\epsilon^t_\theta)}{\partial\sigma_\theta}d\sigma_\theta + \frac{\partial({}^{e}\epsilon^t_\theta)}{\partial\sigma_z}d\sigma_z,\\
d({}^{e}\epsilon^t_z) &= \frac{\partial({}^{e}\epsilon^t_z)}{\partial\sigma_r}d\sigma_r + \frac{\partial({}^{e}\epsilon^t_z)}{\partial\sigma_\theta}d\sigma_\theta + \frac{\partial({}^{e}\epsilon^t_z)}{\partial\sigma_z}d\sigma_z,
\end{aligned}
\tag{2.61}
$$

and

$$
d({}^{s}\epsilon^t_r) = \frac{\partial({}^{s}\epsilon^t_r)}{\partial\sigma_r}d\sigma_r + \frac{\partial({}^{s}\epsilon^t_r)}{\partial\sigma_\theta}d\sigma_\theta, \qquad d({}^{s}\epsilon^t_\theta) = \frac{\partial({}^{s}\epsilon^t_\theta)}{\partial\sigma_r}d\sigma_r + \frac{\partial({}^{s}\epsilon^t_\theta)}{\partial\sigma_\theta}d\sigma_\theta. \tag{2.62}
$$

Now, comparing (2.55)-(2.57) with (2.61) and (2.58)-(2.59) with (2.62) term by term, the derivatives of transformation strain components with respect to stress components can be obtained. Note that the expressions in (2.51) and (2.52) are valid only in regions that contain both austenite and martensite ($0 < \xi < 1$). In the following sections, the constitutive equations are linearized using the calculated derivatives of transformation strain components. The closed-form solutions are considered for two different cases. We will present the linearized constitutive equations for the the regions with partial phase transformation ($0 < \xi < 1$) in §2.4.3. the constitutive equation of §5 is applicable for the whole cylinder

when the material in the inner radius is not completely transformed to martensite. The linearized constitutive relations for regions fully transformed to martensite ($\xi = 1$) is given in §2.4.4. When the martensitic volume fraction reaches the value $\xi = 1$ at the inner radius, increase of pressure will cause the extension of martensite region toward the outer radius and the constitutive relations of §2.4.4 should be considered in analyzing regions that are fully transferred to martensite.

2.4.3 Semi-analytic solutions when the inner radius is not completely transformed to martensite

As was shown in Section 2.4.1, for a thick-walled cylinder subjected to internal pressure, the phase transformation initiates from the inner radius and spreads toward the outer radius for both plane stress and plane strain. So, it can be concluded that when the inner radius is not completely converted to martensite, throughout the thickness, the transformation strains can be expressed by (2.51) and (2.52) for the regions in which $0 < \xi < 1$ and they would be zero in the regions in which phase transformation has not started yet.

The solution in this case is obtained by splitting the applied pressure into a finite number of increments. By assuming that the solution is known in the nth increment[14], and by considering the derivatives of the transformation strain with respect to the stress components, a linearized constitutive relations is used for finding the solution in the $(n+1)$th increment. The transformation strains in the ith annular region for the $(n+1)$th increment

[14] Zero internal pressure can be considered for the first increment. However, it is more efficient to consider a pressure for which the whole cylinder is in the austenite phase as the first increment. The value of the pressure that causes phase transformation to start was calculated in (2.47) and (2.48).

of loading can be expressed as:

$$
\begin{aligned}
{}^{n+1}({}^{e}\epsilon_r^t)^i &= {}^{n}\left(\frac{\partial\ {}^{e}\epsilon_r^t}{\partial\sigma_r}\right)^i \left({}^{n+1}\sigma_r^i - {}^{n}\sigma_r^i\right) + {}^{n}\left(\frac{\partial\ {}^{e}\epsilon_r^t}{\partial\sigma_\theta}\right)^i \left({}^{n+1}\sigma_\theta^i - {}^{n}\sigma_\theta^i\right) \\
&+ {}^{n}\left(\frac{\partial\ {}^{e}\epsilon_r^t}{\partial\sigma_z}\right)^i \left({}^{n+1}\sigma_z^i - {}^{n}\sigma_z^i\right) + {}^{n}({}^{e}\epsilon_r^t)^i, \qquad (2.63) \\
{}^{n+1}({}^{e}\epsilon_\theta^t)^i &= {}^{n}\left(\frac{\partial\ {}^{e}\epsilon_\theta^t}{\partial\sigma_r}\right)^i \left({}^{n+1}\sigma_r^i - {}^{n}\sigma_r^i\right) + {}^{n}\left(\frac{\partial\ {}^{e}\epsilon_\theta^t}{\partial\sigma_\theta}\right)^i \left({}^{n+1}\sigma_\theta^i - {}^{n}\sigma_\theta^i\right) \\
&+ {}^{n}\left(\frac{\partial\ {}^{e}\epsilon_\theta^t}{\partial\sigma_z}\right)^i \left({}^{n+1}\sigma_z^i - {}^{n}\sigma_z^i\right) + {}^{n}({}^{e}\epsilon_\theta^t)^i, \qquad (2.64) \\
{}^{n+1}({}^{e}\epsilon_z^t)^i &= {}^{n}\left(\frac{\partial\ {}^{e}\epsilon_z^t}{\partial\sigma_r}\right)^i \left({}^{n+1}\sigma_r^i - {}^{n}\sigma_r^i\right) + {}^{n}\left(\frac{\partial\ {}^{e}\epsilon_z^t}{\partial\sigma_\theta}\right)^i \left({}^{n+1}\sigma_\theta^i - {}^{n}\sigma_\theta^i\right) \\
&+ {}^{n}\left(\frac{\partial\ {}^{e}\epsilon_z^t}{\partial\sigma_z}\right)^i \left({}^{n+1}\sigma_z^i - {}^{n}\sigma_z^i\right) + {}^{n}({}^{e}\epsilon_z^t)^i, \qquad (2.65)
\end{aligned}
$$

for plane strain and

$$
{}^{n+1}({}^{s}\epsilon_r^t)^i = {}^{n}\left(\frac{\partial\ {}^{s}\epsilon_r^t}{\partial\sigma_r}\right)^i \left({}^{n+1}\sigma_r^i - {}^{n}\sigma_r^i\right) + {}^{n}\left(\frac{\partial\ {}^{s}\epsilon_r^t}{\partial\sigma_\theta}\right)^i \left({}^{n+1}\sigma_\theta^i - {}^{n}\sigma_\theta^i\right) + {}^{n}({}^{s}\epsilon_r^t)^i, \qquad (2.66)
$$

$$
{}^{n+1}({}^{s}\epsilon_\theta^t)^i = {}^{n}\left(\frac{\partial\ {}^{s}\epsilon_\theta^t}{\partial\sigma_r}\right)^i \left({}^{n+1}\sigma_r^i - {}^{n}\sigma_r^i\right) + {}^{n}\left(\frac{\partial\ {}^{s}\epsilon_\theta^t}{\partial\sigma_\theta}\right)^i \left({}^{n+1}\sigma_\theta^i - {}^{n}\sigma_\theta^i\right) + {}^{n}({}^{s}\epsilon_\theta^t)^i, \qquad (2.67)
$$

for plane stress. In deriving (2.63)-(2.67), continuous functions of transformation strain derivatives are replaced by piece-wise constant functions. The cylinder is divided into a finite number of narrow annular regions as shown in Figure 2.35. The transformation strain derivatives are assumed constant in each region. Increasing the number of annular regions, the accuracy of this method increases.

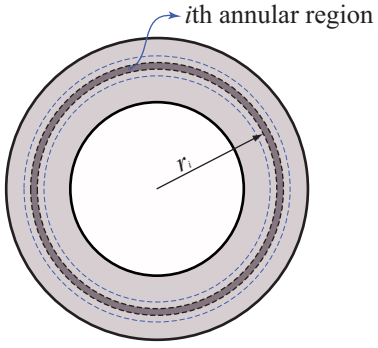

Figure 2.35: Partitioning the cylinder's cross section into a finite number of narrow annular regions.

By applying the load incrementally, the stress components, transformation strain components, and the transformation strain derivatives are known in the nth increment. We start from a load value for which the whole cylinder is in the austenite phase. In this case, the stress components for the first increment are calculated from the elastic solution. Increasing the internal pressure incrementally, the start of phase transformation is checked in each annular region by calculating the martensitic volume fraction using (2.38) and (2.39). For each annular region, the phase transformation starts at a specific load increment. For this special increment, equations (2.63)-(2.67) should be considered with a minor modification. Figure 2.36 shows the circumferential transformation strain surface in the stress space for plane stress. At the start of phase transformation in an annular region, the *(n+1)*th stress state corresponds to a generic point B that lies between $\xi = 0$ and $\xi = 1$ curves (see Figure 2.31 and note that a part of these curves is shown in Figure 2.36) while the stress state in the nth increment lies inside the $\xi = 0$ curve (point A in Figure 2.36). For this increment, neither the elastic solution nor the solution presented in (2.66) and (2.67) can be used as in deriving these equations it is assumed that the stress state in the nth increment corresponds to a point on the transformation strain surface located between $\xi = 0$ and $\xi = 1$ curves. However, these relations can be used for this special increment with the following minor modification. The loading path between the stress states A and B is assumed linear as shown in Figure 2.36. The intersection of this line with $\xi = 0$ curve is found numerically (point k in Figure 2.36) and the stress components corresponding to this point are used instead of ${}^n\sigma_r^i$ and ${}^n\sigma_\theta^i$ in (2.66) and (2.67). It is obvious that the parameters ${}^n({}^s\epsilon_r^t)^i$ and ${}^n({}^s\epsilon_\theta^t)^i$ are zero for this increment since $\xi = 0$ at k (see (2.49) and (2.50)). In the plane strain case, the same procedure is used for finding the circumferential and radial stress components at the onset of phase transformation in each region. The axial stress component is calculated by ${}^n\sigma_z^i = \nu({}^n\sigma_r^i + {}^n\sigma_\theta^i)$ (see the plane strain condition in (2.42) with ${}^e\xi = 0$).

The total strain components for the ith annular region at the *(n+1)*th load increment

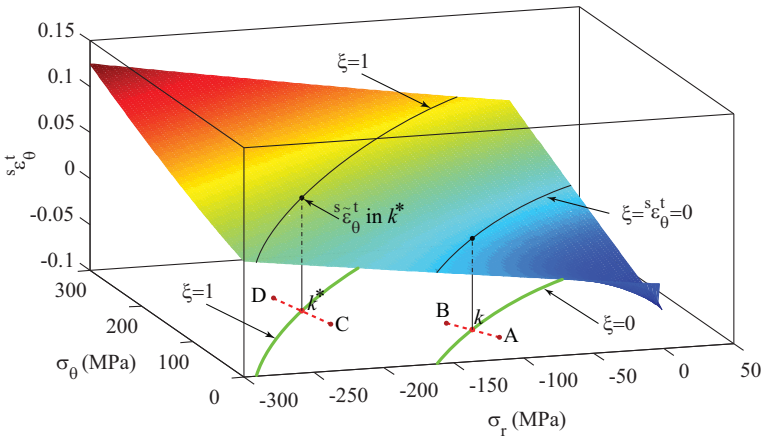

Figure 2.36: Method of calculating the circumferential transformation strain for the special increments in which phase transformation starts and completes in the plane stress case.

can be expressed as:

$$\begin{aligned}
{}^{n+1}({}^{e}\epsilon_r)^i &= {}^{n}S_{11}^{i}\ {}^{n+1}\sigma_r^i + {}^{n}S_{12}^{i}\ {}^{n+1}\sigma_\theta^i + {}^{n}S_{13}^{i}\ {}^{n+1}\sigma_z^i + {}^{n}d_1^i, \\
{}^{n+1}({}^{e}\epsilon_\theta)^i &= {}^{n}S_{21}^{i}\ {}^{n+1}\sigma_r^i + {}^{n}S_{22}^{i}\ {}^{n+1}\sigma_\theta^i + {}^{n}S_{23}^{i}\ {}^{n+1}\sigma_z^i + {}^{n}d_2^i, \\
0 &= {}^{n}S_{31}^{i}\ {}^{n+1}\sigma_r^i + {}^{n}S_{32}^{i}\ {}^{n+1}\sigma_\theta^i + {}^{n}S_{33}^{i}\ {}^{n+1}\sigma_z^i + {}^{n}d_3^i,
\end{aligned} \tag{2.68}$$

in plane strain and

$${}^{n+1}({}^{s}\epsilon_r)^i = {}^{n}S_{11}^{i}\ {}^{n+1}\sigma_r^i + {}^{n}S_{12}^{i}\ {}^{n+1}\sigma_\theta^i + {}^{n}d_1^i, \quad {}^{n+1}({}^{s}\epsilon_\theta)^i = {}^{n}S_{21}^{i}\ {}^{n+1}\sigma_r^i + {}^{n}S_{22}^{i}\ {}^{n+1}\sigma_\theta^i + {}^{n}d_2^i, \tag{2.69}$$

in plane stress. The parameters S and d in (2.68) for the plane strain are expressed as

$$
\begin{aligned}
&{}^nS^i_{11} = {}^nD^i_{eq} + {}^n\left(\frac{\partial\ {}^e\epsilon^t_r}{\partial\sigma_r}\right)^i,\ {}^nS^i_{12} = -\nu\ {}^nD^i_{eq} + {}^n\left(\frac{\partial\ {}^e\epsilon^t_r}{\partial\sigma_\theta}\right)^i,\ {}^nS^i_{13} = -\nu\ {}^nD^i_{eq} + {}^n\left(\frac{\partial\ {}^e\epsilon^t_r}{\partial\sigma_z}\right)^i,\\
&{}^nS^i_{21} = -\nu\ {}^nD^i_{eq} + {}^n\left(\frac{\partial\ {}^e\epsilon^t_\theta}{\partial\sigma_r}\right)^i,\ {}^nS^i_{22} = {}^nD^i_{eq} + {}^n\left(\frac{\partial\ {}^e\epsilon^t_\theta}{\partial\sigma_\theta}\right)^i,\ {}^nS^i_{23} = -\nu\ {}^nD^i_{eq} + {}^n\left(\frac{\partial\ {}^e\epsilon^t_\theta}{\partial\sigma_z}\right)^i,\\
&{}^nS^i_{31} = -\nu\ {}^nD^i_{eq} + {}^n\left(\frac{\partial\ {}^e\epsilon^t_z}{\partial\sigma_r}\right)^i,\ {}^nS^i_{32} = -\nu\ {}^nD^i_{eq} + {}^n\left(\frac{\partial\ {}^e\epsilon^t_z}{\partial\sigma_\theta}\right)^i,\ {}^nS^i_{33} = {}^nD^i_{eq} + {}^n\left(\frac{\partial\ {}^e\epsilon^t_z}{\partial\sigma_z}\right)^i,\\
&{}^nd^i_1 = -{}^n\left(\frac{\partial\ {}^e\epsilon^t_r}{\partial\sigma_r}\right)^i\ {}^n\sigma^i_r - {}^n\left(\frac{\partial\ {}^e\epsilon^t_r}{\partial\sigma_\theta}\right)^i\ {}^n\sigma^i_\theta - {}^n\left(\frac{\partial\ {}^e\epsilon^t_r}{\partial\sigma_z}\right)^i\ {}^n\sigma^i_z + {}^n({}^e\epsilon^t_r)^i,\\
&{}^nd^i_2 = -{}^n\left(\frac{\partial\ {}^e\epsilon^t_\theta}{\partial\sigma_r}\right)^i\ {}^n\sigma^i_r - {}^n\left(\frac{\partial\ {}^e\epsilon^t_\theta}{\partial\sigma_\theta}\right)^i\ {}^n\sigma^i_\theta - {}^n\left(\frac{\partial\ {}^e\epsilon^t_\theta}{\partial\sigma_z}\right)^i\ {}^n\sigma^i_z + {}^n({}^e\epsilon^t_\theta)^i,\\
&{}^nd^i_3 = -{}^n\left(\frac{\partial\ {}^e\epsilon^t_z}{\partial\sigma_r}\right)^i\ {}^n\sigma^i_r - {}^n\left(\frac{\partial\ {}^e\epsilon^t_z}{\partial\sigma_\theta}\right)^i\ {}^n\sigma^i_\theta - {}^n\left(\frac{\partial\ {}^e\epsilon^t_z}{\partial\sigma_z}\right)^i\ {}^n\sigma^i_z + {}^n({}^e\epsilon^t_z)^i,\\
&{}^nD^i_{eq} = \frac{1}{E^A + {}^n\xi^i(E^M - E^A)}.
\end{aligned}
\tag{2.70}
$$

For the plane stress case in (2.69), these parameters should be replaced by

$$
\begin{aligned}
&{}^nS^i_{11} = {}^nD^i_{eq} + {}^n\left(\frac{\partial\ {}^s\epsilon^t_r}{\partial\sigma_r}\right)^i,\ {}^nS^i_{12} = -\nu\ {}^nD^i_{eq} + {}^n\left(\frac{\partial\ {}^s\epsilon^t_r}{\partial\sigma_\theta}\right)^i,\\
&{}^nS^i_{21} = -\nu\ {}^nD^i_{eq} + {}^n\left(\frac{\partial\ {}^s\epsilon^t_\theta}{\partial\sigma_r}\right)^i,\ {}^nS^i_{22} = {}^nD^i_{eq} + {}^n\left(\frac{\partial\ {}^s\epsilon^t_\theta}{\partial\sigma_\theta}\right)^i,\\
&{}^nd^i_1 = -{}^n\left(\frac{\partial\ {}^s\epsilon^t_r}{\partial\sigma_r}\right)^i\ {}^n\sigma^i_r - {}^n\left(\frac{\partial\ {}^s\epsilon^t_r}{\partial\sigma_\theta}\right)^i\ {}^n\sigma^i_\theta + {}^n({}^s\epsilon^t_r)^i,\\
&{}^nd^i_2 = -{}^n\left(\frac{\partial\ {}^s\epsilon^t_\theta}{\partial\sigma_r}\right)^i\ {}^n\sigma^i_r - {}^n\left(\frac{\partial\ {}^s\epsilon^t_\theta}{\partial\sigma_\theta}\right)^i\ {}^n\sigma^i_\theta + {}^n({}^s\epsilon^t_\theta)^i.
\end{aligned}
\tag{2.71}
$$

All the coefficients in (2.70) and (2.71) are assumed to be known in the nth loading increment. Also, all the coefficients are considered constant within each narrow region. By inverting (2.68) and (2.69), the stress-strain relations are obtained for the ith region at the $(n+1)$th load increment as follows

$$
{}^{n+1}\sigma^i_r = {}^nC^i_{11}\ {}^{n+1}(\epsilon_r)^i + {}^nC^i_{12}\ {}^{n+1}(\epsilon_\theta)^i + {}^ne^i_1 \quad \text{and} \quad {}^{n+1}\sigma^i_\theta = {}^nC^i_{21}\ {}^{n+1}(\epsilon_r)^i + {}^nC^i_{22}\ {}^{n+1}(\epsilon_\theta)^i + {}^ne^i_2.
\tag{2.72}
$$

Equation (2.72) is applicable in both plane strain and plane stress cases. For plane strain, the parameters ϵ_r and ϵ_θ are replaced by ${}^e\epsilon_r$ and ${}^e\epsilon_\theta$ and the coefficients $C_{mn},\ m,n = 1,2,3$ are the components of the inverse of matrix S, a 3×3 matrix with components given in

(2.70). The parameters $e_m,\ m = 1, 2$ in the plane strain case are expressed by

$$
\begin{aligned}
{}^{n}e_1^i &= -{}^{n}C_{11}^i\ {}^{n}d_1^i - {}^{n}C_{12}^i\ {}^{n}d_2^i - {}^{n}C_{13}^i\ {}^{n}d_3^i, \\
{}^{n}e_2^i &= -{}^{n}C_{21}^i\ {}^{n}d_1^i - {}^{n}C_{22}^i\ {}^{n}d_2^i - {}^{n}C_{23}^i\ {}^{n}d_3^i,
\end{aligned} \tag{2.73}
$$

with the parameters $d_m,\ m = 1, 2, 3$ given in (2.70). For plane stress, the parameters ϵ_r and ϵ_θ in (2.72) are replaced by ${}^{s}\epsilon_r$ and ${}^{s}\epsilon_\theta$, respectively. The coefficients $C_{mn},\ m, n = 1, 2$ are the components of the inverse of matrix S, a 2×2 matrix with components introduced in (2.71). The parameters $e_m,\ m = 1, 2$ in plane stress are given by

$$
{}^{n}e_1^i = -{}^{n}C_{11}^i\ {}^{n}d_1^i - {}^{n}C_{12}^i\ {}^{n}d_2^i \qquad \text{and} \qquad {}^{n}e_2^i = -{}^{n}C_{21}^i\ {}^{n}d_1^i - {}^{n}C_{22}^i\ {}^{n}d_2^i, \tag{2.74}
$$

where $d_m,\ m = 1, 2$ are given in (2.71).

In the absence of body forces, the equations of equilibrium for an axisymmetric problem in cylindrical coordinates are reduced to:

$$
\frac{d\sigma_r}{dr} + \frac{\sigma_r - \sigma_\theta}{r} = 0. \tag{2.75}
$$

Note that $\epsilon_r = \frac{\partial u}{\partial r}$ and $\epsilon_\theta = \frac{u}{r}$, where u represents the radial displacement. Substituting (2.72) into (2.75) and considering the strain-displacement relations, the equilibrium equation in terms of radial displacement is obtained as:

$$
\frac{d^2({}^{n+1}u^i)}{dr^2} + \frac{1}{r}\frac{d({}^{n+1}u^i)}{dr} - {}^{n}f^i\frac{{}^{n+1}u^i}{r^2} + {}^{n}g^i\frac{1}{r} = 0, \tag{2.76}
$$

where ${}^{n+1}u^i$ is the radial displacement in the $(n+1)$th loading increment in the ith annular region and

$$
{}^{n}f^i = \frac{{}^{n}C_{22}^i}{{}^{n}C_{11}^i}, \quad {}^{n}g^i = \frac{{}^{n}e_1^i - {}^{n}e_2^i}{{}^{n}C_{11}^i}. \tag{2.77}
$$

Considering constant values for the above parameters in each annular region, a closed-form solution can be obtained for (2.76) as:

$$
{}^{n+1}u^i(r) = \begin{cases}
{}^{n+1}A_1^i r^{\sqrt{{}^{n}f^i}} + {}^{n+1}A_2^i r^{-\sqrt{{}^{n}f^i}} + \frac{{}^{n}g^i}{{}^{n}f^i - 1} r & {}^{n}f^i > 0, \\
{}^{n+1}A_1^i \sin\left(\sqrt{-{}^{n}f^i}\ln r\right) + {}^{n+1}A_2^i \cos\left(\sqrt{-{}^{n}f^i}\ln r\right) + \frac{{}^{n}g^i}{{}^{n}f^i - 1} r & {}^{n}f^i < 0,
\end{cases} \tag{2.78}
$$

where ${}^{n+1}A_1^i$ and ${}^{n+1}A_2^i$ are integration constants that should be found in the *(n+1)*th increment of loading. Substituting (2.78) into the strain-displacement relations and considering (2.72), the stress components within the ith region are obtained. For $(2.78)_1$ these components are expressed as

$$
\begin{aligned}
{}^{n+1}\sigma_r = {}& {}^{n+1}A_1^i \left[r^{\sqrt{{}^n f^i}-1}\left({}^nC_{11}^i\sqrt{{}^n f^i} + {}^nC_{12}^i\right)\right] + {}^{n+1}A_2^i \left[r^{-\sqrt{{}^n f^i}-1}\left({}^nC_{12}^i - {}^nC_{11}^i\sqrt{{}^n f^i}\right)\right] \\
& + \left({}^nC_{11}^i + {}^nC_{12}^i\right)\frac{{}^n g^i}{{}^n f^i - 1} + {}^n e_1^i, \qquad (2.79) \\
{}^{n+1}\sigma_\theta = {}& {}^{n+1}A_1^i \left[r^{\sqrt{{}^n f^i}-1}\left({}^nC_{21}^i\sqrt{{}^n f^i} + {}^nC_{22}^i\right)\right] + {}^{n+1}A_2^i \left[r^{-\sqrt{{}^n f^i}-1}\left({}^nC_{22}^i - {}^nC_{21}^i\sqrt{{}^n f^i}\right)\right] \\
& + \left({}^nC_{21}^i + {}^nC_{22}^i\right)\frac{{}^n g^i}{{}^n f^i - 1} + {}^n e_2^i. \qquad (2.80)
\end{aligned}
$$

For $(2.78)_2$ the same procedure is followed. The solutions expressed in (2.78)-(2.80) are used for the regions in which the martensitic volume fraction is $0 < \xi < 1$. For those regions in which phase transformation has not started and the material is purely austenite, the above solution should be converted to the elastic solution by eliminating the last term in (2.78) and the last two terms in (2.79) and (2.80).

2.4.4 Closed-form solutions when the inner radius is completely transformed to martensite

For a special value of internal pressure, the inner radius completely transforms to martensite[15]. For pressures lower than this value, the solution proposed in §2.4.3 would be applicable. By increasing the pressure, the fully martensite region will spread toward the outer radius and the previous solution is not valid in this region. For the ith narrow annular region in which the material is fully transformed to martensite in the *(n+1)*th increment, the strain components can be expressed as

$$
\begin{aligned}
{}^{n+1}({}^e\epsilon_r)^i &= S_{11}^M\ {}^{n+1}\sigma_r^i + S_{12}^M\ {}^{n+1}\sigma_\theta^i + S_{13}^M\ {}^{n+1}\sigma_z^i + ({}^e\tilde{\epsilon}_r^t)^i, \\
{}^{n+1}({}^e\epsilon_\theta)^i &= S_{21}^M\ {}^{n+1}\sigma_r^i + S_{22}^M\ {}^{n+1}\sigma_\theta^i + S_{23}^M\ {}^{n+1}\sigma_z^i + ({}^e\tilde{\epsilon}_\theta^t)^i, \qquad (2.81) \\
0 &= S_{31}^M\ {}^{n+1}\sigma_r^i + S_{32}^M\ {}^{n+1}\sigma_\theta^i + S_{33}^M\ {}^{n+1}\sigma_z^i + ({}^e\tilde{\epsilon}_z^t)^i,
\end{aligned}
$$

[15] An explicit expression can not be obtained for this pressure. In each load increment, the martensitic volume fraction in all the annular regions is monitored to find the pressure that causes full transformation to martensite in different regions.

for plane strain and

$$^{n+1}(^{s}\epsilon_r)^i = S_{11}^M\,{}^{n+1}\sigma_r^i + S_{12}^M\,{}^{n+1}\sigma_\theta^i + (^{s}\tilde{\epsilon}_r^t)^i \quad \text{and} \quad {}^{n+1}(^{s}\epsilon_\theta)^i = S_{21}^M\,{}^{n+1}\sigma_r^i + S_{22}^M\,{}^{n+1}\sigma_\theta^i + (^{s}\tilde{\epsilon}_\theta^t)^i, \tag{2.82}$$

for plane stress, where

$$S_{mn}^M = \begin{cases} \frac{1}{E^M} & \text{for } m = n, \\ -\frac{\nu^M}{E^M} & \text{for } m \neq n. \end{cases} \tag{2.83}$$

In (2.83), $m, n = 1, 2, 3$ for plane strain and $m, n = 1, 2$ for plane stress. The terms $(^{e}\tilde{\epsilon}_r^t)^i$, $(^{e}\tilde{\epsilon}_\theta^t)^i$, and $(^{e}\tilde{\epsilon}_z^t)^i$ in (2.81) and $(^{s}\tilde{\epsilon}_r^t)^i$ and $(^{s}\tilde{\epsilon}_\theta^t)^i$ in (2.82) represent the final transformation strain components in the ith region for the plane stress and plane strain cases, respectively. For calculating these terms, the martensitic volume fraction in each annular region is monitored in all the increments and the first loading increment in which the ith region is fully transformed to martensite is recorded. In this special increment, the stress state for the nth loading increment corresponds to a point located between $\xi = 0$ and $\xi = 1$ curves (see Figure 2.31). Point C in Figure 2.36 shows the stress state of such a point (the material properties of Table **??** and the plane stress condition are used for depicting the circumferential strain surface). The stress state of this annular region in the *(n+1)*th increment corresponds to a point outside the $\xi = 1$ closed curve (point D in Figure 2.36). Approximating the load path between these two points by a line, the stress state corresponding to the intersection of line C-D and $\xi = 1$ curve (point k^* in Figure 2.36) is calculated numerically. For the plane strain case, the stress component σ_z at the corresponding point k^* is calculated by enforcing the plane strain condition as expressed in (2.42). The final transformation strain components are calculated by substituting the stress sate of this point in (2.49) and (2.50) for the plane strain and plane stress cases, respectively (the circumferential transformation strain component corresponding to k^* in the plane stress is shown in Figure 2.36). The accuracy of the final transformation strains calculated by this method increases by increasing the number of load increments. We will compare the final transformation strains calculated by our method with those of a finite element simulation in a few numerical examples.

Using the inverses of (2.81) and (2.82), the stress-strain relations are expressed as:

$$ {}^{n+1}\sigma_r = C_{11}^M\ {}^{n+1}(\epsilon_r)^i + C_{12}^M\ {}^{n+1}(\epsilon_\theta)^i + \tilde{e}_1^i \quad \text{and} \quad {}^{n+1}\sigma_\theta = C_{12}^M\ {}^{n+1}(\epsilon_r)^i + C_{22}^M\ {}^{n+1}(\epsilon_\theta)^i + \tilde{e}_2^i, \tag{2.84} $$

where this relation is applicable for both plane stress and plane strain. For considering the relation in plane strain, ϵ_r and ϵ_θ are replaced by ${}^e\epsilon_r$ and ${}^e\epsilon_\theta$, respectively. The coefficients $C_{mn}^M,\ m,n = 1,2,3$ are the components of the inverse of matrix S^M, a 3×3 matrix with components given in (2.83). The parameters $\tilde{e}_m,\ m = 1,2$ in the plane strain case are

$$ \tilde{e}_1^i = -C_{11}^M({}^e\tilde{\epsilon}_r^t)^i - C_{12}^M({}^e\tilde{\epsilon}_\theta^t)^i - C_{13}^M({}^e\tilde{\epsilon}_z^t)^i \quad \text{and} \quad \tilde{e}_2^i = -C_{21}^M({}^e\tilde{\epsilon}_r^t)^i - C_{22}^M({}^e\tilde{\epsilon}_\theta^t)^i - C_{23}^M({}^e\tilde{\epsilon}_z^t)^i. \tag{2.85} $$

For the plane stress case, ϵ_r and ϵ_θ in (2.84) are replaced by ${}^s\epsilon_r$ and ${}^s\epsilon_\theta$, respectively. The coefficients $C_{mn}^M,\ m,n = 1,2$ are the components of the inverse of matrix S^M, a 2×2 matrix with components introduced in (2.83). The parameters $\tilde{e}_m,\ m = 1,2$ in this case are expressed by

$$ \tilde{e}_1^i = -C_{11}^M({}^s\tilde{\epsilon}_r^t)^i - C_{12}^M({}^s\tilde{\epsilon}_\theta^t)^i \quad \text{and} \quad \tilde{e}_2^i = -C_{21}^M({}^s\tilde{\epsilon}_r^t)^i - C_{22}^M({}^s\tilde{\epsilon}_\theta^t)^i. \tag{2.86} $$

Substituting (2.84) into (2.75) and considering the strain-displacement relations, the equilibrium equation in terms of radial displacement in the ith region is obtained. Using assumptions similar to those in the previous section, the radial displacement for the ith region in the *(n+1)*th loading increment ${}^{n+1}u^i$, which is fully transformed to martensite can be expressed as:

$$ {}^{n+1}u^i = {}^{n+1}A_1^i r + \frac{{}^{n+1}A_2^i}{r} - \frac{1}{2}\tilde{g}^i r \ln r + \frac{1}{4}\tilde{g}^i r, \tag{2.87} $$

where

$$ \tilde{g}^i = \frac{\tilde{e}_1^i - \tilde{e}_2^i}{C_{11}^M}. \tag{2.88} $$

Substitution of (2.87) into (2.84) and using the strain-displacement relations gives the stress

components in the ith fully martensite region as:

$$
\begin{aligned}
{}^{n+1}\sigma_r = {}& {}^{n+1}A_1^i \left(C_{11}^M + C_{12}^M\right) + \frac{{}^{n+1}A_2^i}{r^2}\left(C_{12}^M - C_{11}^M\right) + C_{11}^M(-\frac{1}{2}\tilde{g}^i \ln r - \frac{1}{4}\tilde{g}^i) \\
& + C_{12}^M(-\frac{1}{2}\tilde{g}^i \ln r + \frac{1}{4}\tilde{g}^i) + \tilde{e}_1^i, \qquad (2.89) \\
{}^{n+1}\sigma_\theta = {}& {}^{n+1}A_1^i \left(C_{12}^M + C_{22}^M\right) + \frac{{}^{n+1}A_2^i}{r^2}\left(C_{22}^M - C_{12}^M\right) + C_{12}^M(-\frac{1}{2}\tilde{g}^i \ln r - \frac{1}{4}\tilde{g}^i) \\
& + C_{22}^M(-\frac{1}{2}\tilde{g}^i \ln r + \frac{1}{4}\tilde{g}^i) + \tilde{e}_2^i. \qquad (2.90)
\end{aligned}
$$

The solution expressed in (2.89) and (2.90) is valid from the inner radius up to the annular region in which the martensitic volume fraction is $\xi < 1$. For the other regions through the outer radius the solution expressed in §2.4.3 should be used.

2.4.5 Solution procedure

Using Equations (2.47) and (2.48) or Figure 2.33, the pressure for initiation of phase transformation in the cylinder is calculated. For any applied pressure below this minimum, the elastic solution is valid and for pressures above this minimum the subsequent procedure should be followed.

The cylinder is divided into N_1 narrow annular regions with the ith region $r^i < r < r^{i+1}$ (see Figure 2.35). The loading is divided into N_2 increments. The first increment corresponds to zero internal pressure or any internal pressure for which the whole cylinder is in the austenite phase (see Figure 2.33). Assuming that for the nth loading increment the solution is known, in the *(n+1)*th increment the following procedure is considered. The radial stress component in the innermost radius is assumed to be ${}^{n+1}\sigma_r^1 = -\,{}^{n+1}p$ that is the internal pressure corresponding to the *(n+1)*th load increment. As the circumferential stress component is unknown, a typical value ${}^{n+1}\sigma_\theta^1 = \hat{\sigma}$ is assumed for initiating the solution procedure (*e.g.* $\hat{\sigma} = {}^{n}\sigma_\theta^1$). In the plane strain case, the axial stress component σ_z in the inner radius is calculated by enforcing the plane strain condition given in (2.42). Equations (2.38) and (2.39) are used for calculating the martensitic fraction ξ at $r = a$. Depending on the calculated martensitic fraction in the inner radius, two cases are possible:

Case I: $0 < \xi^1 < 1$. Equations (2.73), (2.74), and (2.77) are used for calculating the previously introduced constants in the first annular region. By substituting these

coefficients into (2.79) and (2.80), the unknown constants ${}^{n+1}A_1^1$ and ${}^{n+1}A_2^1$ are calculated. Now, the stress components can be calculated in r^2 by means of (2.79), (2.80), and by assuming the other parameters to be constants in the first annular region. The calculated stress components for the outer radius of the first region are considered as the stresses in the inner radius of the second region and the calculations are repeated. In the plane strain case, the axial stress component in the inner radius of each region is calculated by enforcing the condition (2.42). These calculations are continued up to the last region. Now, the calculated radial stress for the external radius $r = b$ should satisfy the boundary condition $\sigma_r = 0$. If this condition is not satisfied, the assumed circumferential stress in the innermost region ($\hat{\sigma}$) is corrected (e.g. by a fraction of residual radial stress at the external boundary[16]) and the procedure is repeated until satisfaction of the stress boundary condition at $r = b$. As it will be shown in the numerical results, the number of iterations for achieving the consistent stress distribution is small. Note that if in any region in $a < r < b$ the martensitic fraction becomes zero, the solution procedure should be switched to an elastic solution by eliminating the last term in (2.78) and the last two terms in (2.79) and (2.80).

Case II: $\xi^1 = 1$. As was explained in §6, to obtain the solution in this case, for each annular region, the special step in which that region is fully converted to martensite should be obtained (using (2.38) and (2.39)). In this special load increment the method of §6 and Figure 2.36 is used for calculating the parameters $(\tilde{\epsilon}_r^t)^i$ and $(\tilde{\epsilon}_\theta^t)^i$. For any annular region in which the material is fully transformed to martensite, the previous procedure of Case I should be used by replacing (2.73), (2.74), (2.77), (2.79), and (2.80) by (2.85), (2.86), (2.88), (2.89), and (2.90), respectively. Note that, at the inner radius of each narrow annular region, the martensitic volume fraction is calculated and when it becomes less than 1 the solution is switched to that of Case I.

[16]For the numerical results presented in this section, in the kth iteration ${}_k\hat{\sigma} = {}_{k-1}\hat{\sigma} - 0.1({}_{k-1}\sigma_r)_{r=b}$, where the left subscripts are used for indicating the iteration number. Using this method and by considering a tolerance of $0.1MPa$ for the residual radial stress at the outer radius, the boundary condition in the outer radius is satisfied for all the case studies in less than 10 iterations

2.4.6 Numerical results

In this section, the SMA thick-walled cylinder shown in Figure 1 is considered with a=0.1m, b=0.3m and T=315K. The outer radius is chosen three times the inner radius for satisfying the thick-walled condition for the cylinder. The cylinder is subjected to different internal pressures and the stress distribution is calculated using the proposed semi-analytic method in both plane stress and plane strain conditions.

First, a sensitivity analysis is performed for calculating the appropriate number of annular regions N_1 and load increments N_2 (see Appendix A). Based on the sensitivity analysis results, the thickness is divided into $N_1 = 100$ annular regions (see Figure 2.35) and the load is applied in $N_2 = 20$ increments. All the material properties used in the following numerical examples are presented in Table 2.1 (Material I), which are taken from Qidwai and Lagoudas [161].

For validation purposes, the three dimensional constitutive relations are used and an appropriate user subroutine (UMAT) has been written by FORTRAN in the commercially available finite element program ABAQUS that enables this code to model SMA structures using solid elements. For modeling SMA thick-walled cylinders by 3D solid elements, a 15° sector of a short thick-walled cylinder is considered. The axisymmetric boundary conditions are imposed by constraining the boundary nodes from moving along the circumferential direction. For modeling the plane stress condition, both ends of the cylinder are free in moving along the axial direction and the plane strain condition is imposed by constraining both ends in the axial direction. The developed finite element code is validated by comparing with the previously reported works for SMA structures, e.g. uniaxial tension, bending of beams, and deflection analysis of cylindrical panels [126]. Quadratic (20 node cubic) elements are used. One element is considered along the circumferential and axial directions and the thickness is divided into 30 elements. The pressure loading is divided into 100 steps and the tolerance of 1×10^{-6} is considered for the convergence of transformation function (see Mirzaeifar et al. [126]).

A sensitivity analysis is performed for choosing the appropriate number of annular regions N_1 and load increments N_2 in the semi-analytic solution, and the number of elements

and load increments in the finite element simulations. The stress components are considered to be converged when the maximum difference is smaller than $0.1MPa$ and the martensitic volume fraction convergence is achieved when the maximum difference is smaller than 0.001. Figure 2.37(a) shows the effect of increasing the number of annular regions on the martensitic volume fraction distribution in the plane strain case for $p = 200MPa$ and with considering 20 load increments. The convergence is achieved with 100 annular regions for the martensitic volume fraction. The convergence of the circumferential stress in this case for 100 annular regions is shown in Figure 2.37(b). The convergence for radial stress distribution is achieved with 50 annular regions. Our numerical tests show that $N_1 = 100$ is the optimum value.

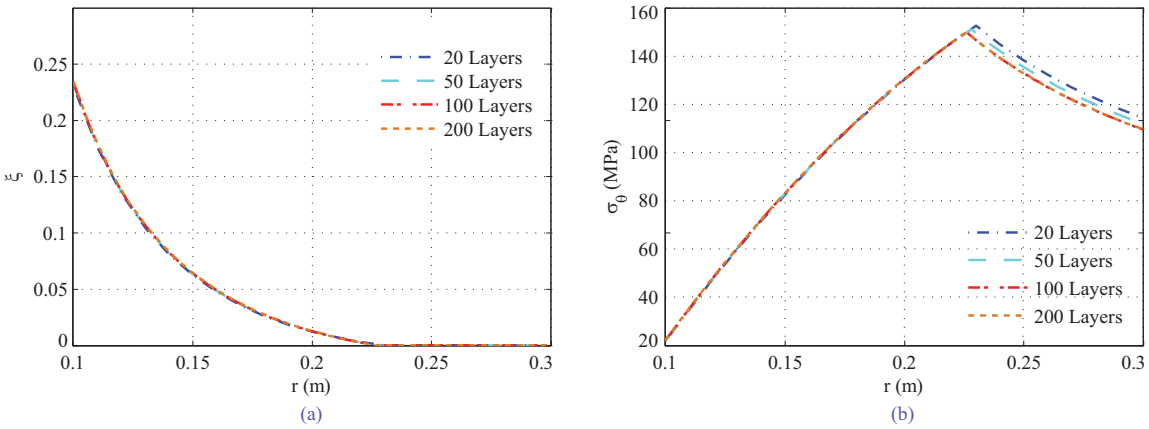

Figure 2.37: The effect of the number of annular regions in the semi-analytic solution on (a) martensitic volume fraction, and (b) circumferential stress in the plane strain case ($p = 200MPa$ and 20 load increments).

Figure 2.38(a) shows the effect of increasing the number of loading increments on the martensitic volume fraction distribution in the plane strain case for $p = 200MPa$ when the number of annular regions is $N_1 = 100$. Convergence is achieved with 10 load increments for the martensitic volume fraction. Convergence of the circumferential stress in this case is achieved with 20 load increments as shown in Figure 2.38(b). Convergence for radial stress distribution is achieved with 10 annular regions. It is seen that $N_2 = 20$ is the optimum value. The convergence study for the plane stress case leads to the same optimum number

of annular regions and load increments.

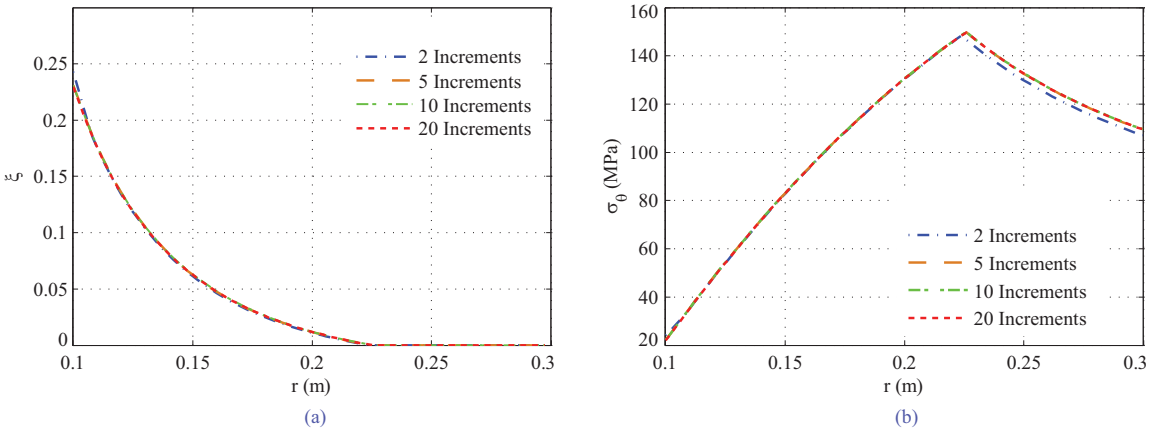

Figure 2.38: The effect of the number of load increments in the semi-analytic solution on (a) martensitic volume fraction, and (b) circumferential stress in the plane strain case ($p = 200MPa$ and 100 annular regions).

Figure 2.39 shows the effect of the number of finite elements on the finite element simulation results for the martensitic volume fraction and circumferential stress component in the plane stress case. As it is shown, results are not sensitive to the number of elements. The same analysis is performed for all the parameters and Mesh 2 (see the caption of Figure 2.39 for mesh definitions) with $30 \times 1 \times 1$ elements in r, θ and z directions is considered for all the studies presented in this paper (20 node cubic elements are used in all cases).

In order to find the appropriate number of load increments in the finite element simulations, a sensitivity analysis for the number of load increments is performed for all the parameters. Figure 2.40 shows the effect of load increment numbers on the volume fraction and circumferential stress component in the plane stress case. As it is seen, the finite element simulation results are not sensitive to the number of load increments as well. It is worth mentioning that the history of these parameters as a function of internal pressure is highly affected by the load increment numbers. For all the case studies presented in this paper 100 load increments are considered. The same sensitivity analysis for the plane strain case and for the other parameters is performed and the results are very similar to those of plane stress.

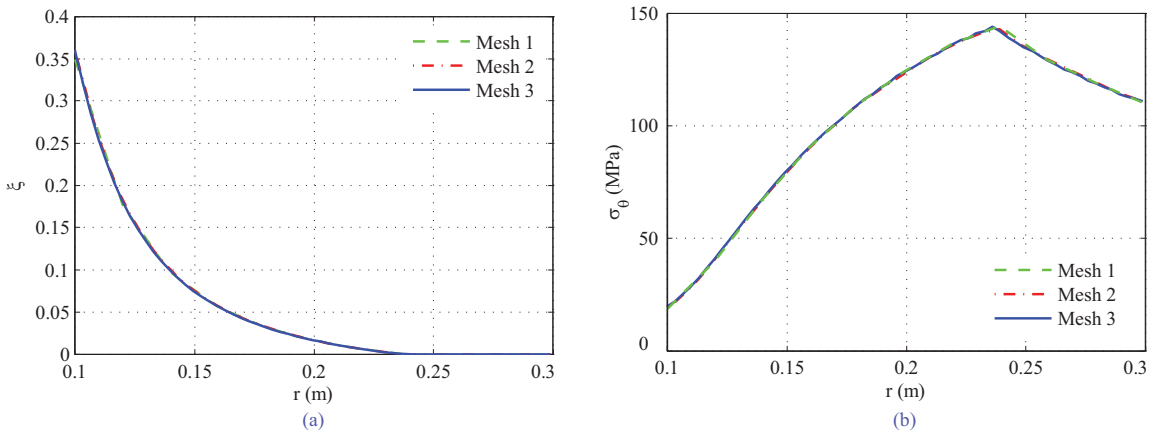

Figure 2.39: The effect of the number of elements in the finite element simulation on (a) martensitic volume fraction, and (b) circumferential stress in the plane stress case for Mesh 1: $10 \times 1 \times 1$ elements (in r, θ and z directions), Mesh 2: $30 \times 1 \times 1$ elements, and Mesh 3: $60 \times 2 \times 1$ elements ($p = 200MPa$ and 100 load increments).

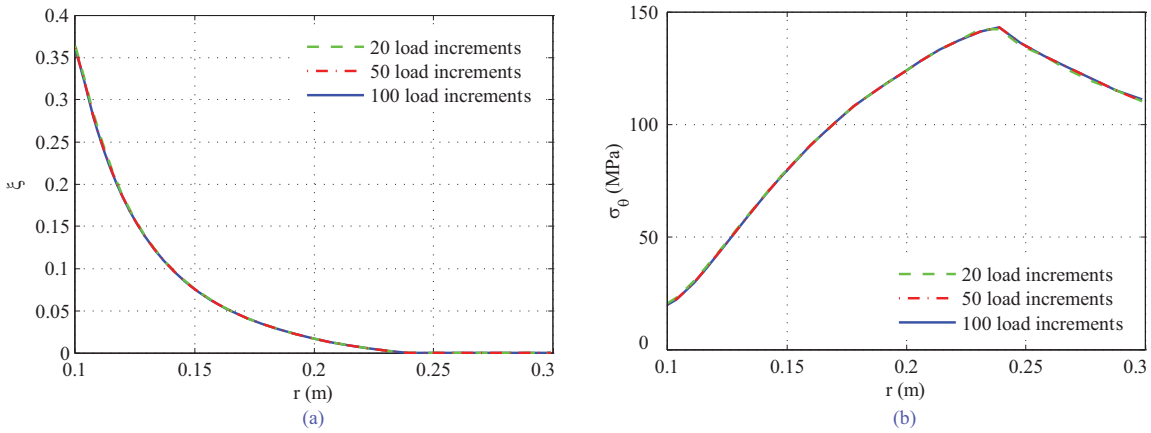

Figure 2.40: The effect of the number of the load increments in the finite element simulations on (a) martensitic volume fraction, and (b) circumferential stress in plane stress ($p = 200MPa$ and $30 \times 1 \times 1$ elements in r, θ and z directions).

Three different values of internal pressure are considered for the first case in §2.4.5. Figure 2.41(a) shows the radial stress distribution for the internal pressures $p = 120, 160$ and $200MPa$ in plane strain. In all the cases, the stress boundary condition in the external radius is satisfied with a tolerance of $0.1MPa$ in less than ten iterations (see §2.4.5 for the solution procedure). This figure also shows the results obtained by the finite element method for each pressure. The circumferential stress distribution for these values of internal pressure is depicted in Figure 2.41(b) in plane strain. As it is shown in this figure, circumferential stress has an ascending distribution in the region in which material transformation has taken place and consequently follows a descending distribution in the fully austenite region. However, as it will be shown in the following case studies, the circumferential stress distribution does not follow this pattern for all the values of internal pressure. The axial stress component in plane strain condition obtained by the semi-analytic solution is compared with the finite element results in Figure 2.41(c). Martensitic volume fraction distribution, calculated by the present method is shown and compared with the finite element results in Figure 2.41(d). By comparing the results presented in Figure 2.41(d) with the approximate results of Figure 2.34, it is seen that the error of Figure 2.34 in predicting the boundary of phase transformation for internal pressures p=120, 160 and 200MPa is 0.8, 11.4 and 27.1 percent, respectively. As expected, the error of calculating the material transformation boundary by considering elastic stress distribution in regions with phase transformation (like that presented in Figure 2.34) increases by increase of the radius at which material transformation has occurred.

The radial stress distribution, circumferential stress distribution, and martensitic volume fraction in plane stress are shown in Figure 2.42. Comparing these distributions in plane stress and plane strain reveals a minor differences in the radial and circumferential stress distributions. It is worth mentioning that for elastic cylinders the radial and circumferential stress distributions are identical in plane stress and plane strain. However, in the present case of an SMA thick-walled cylinder, the phase transformation depends on the three-dimensional state of stress and is affected by the axial stress that exists only in the plane strain case. Therefore, the phase transformation distributions in plane stress and

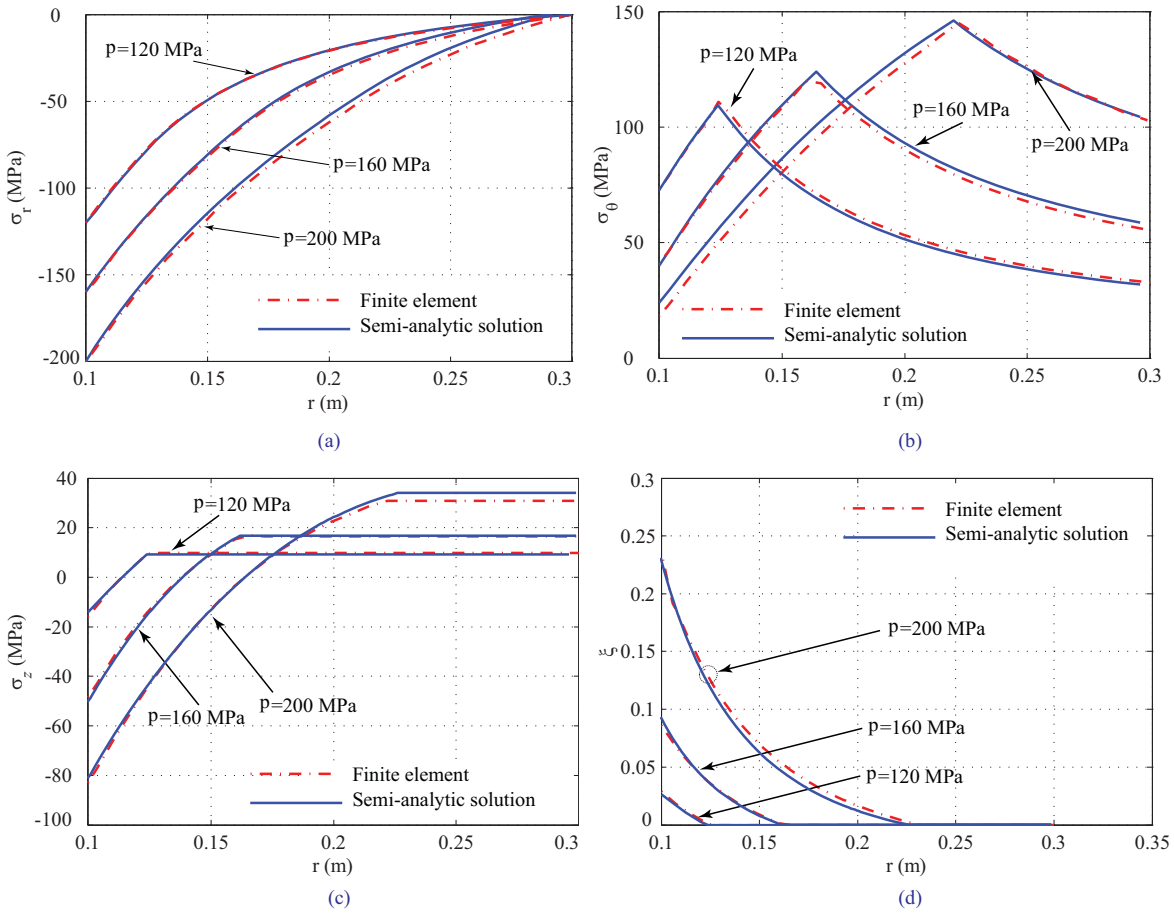

Figure 2.41: Distribution of (a) radial stress, (b) circumferential stress, (c) axial stress, and (d) martensitic volume fraction for a SMA thick-walled cylinder under internal pressure in plane strain with $0 < \xi < 1$ at the inner radius.

plane strain are not the same. This difference is calculated in (2.38)-(2.39) and can clearly be seen by comparing the results in Figures 2.41(d) and 2.42(c). The difference in the phase transformation distribution and the boundary of the region with phase transformation causes a minor difference in the radial and circumferential stress distributions for plane stress and plane strain.

To obtain the internal pressure at which the martensitic volume fraction in the innermost radius reaches $\xi = 1$, a trial and error method is used and the value of this pressure for the present case study is calculated to be $p = 238MPa$ in plane stress and $p = 260MPa$ in plane strain. Distribution of stress components and martensitic volume fraction for these

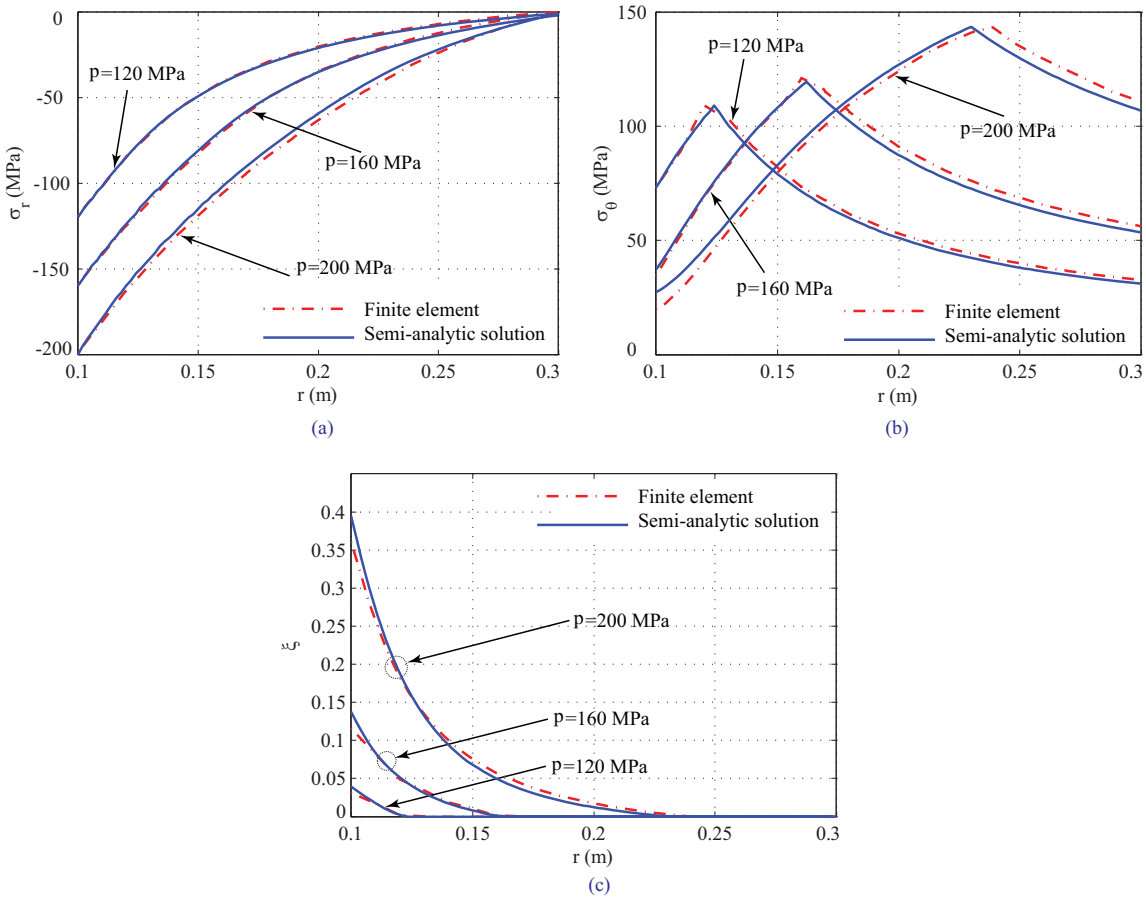

Figure 2.42: Distribution of (a) radial stress, (b) circumferential stress, and (c) martensitic volume fraction for an SMA thick-walled cylinder subjected to internal pressure in plane stress with $0 < \xi < 1$ at the inner radius.

pressures are calculated by the method of §2.4.3 and are depicted in Figures 2.43 and 2.44 for plane strain and plane stress, respectively. For any internal pressure larger than these values, the fully martensite region spreads towards the outer radius and the method of §2.4.4 should be used in any fully transformed annular region. The method of §2.4.4 is used and distribution of stress components is calculated for $p = 300Mpa$ in both plane stress and plane strain cases (see §2.4.5 for the solution procedure in this case).

For the internal pressure $p = 300MPa$, a portion of the cylinder is fully transformed to martensite in both plane stress and plane strain conditions. Figure 2.43 compares the radial, circumferential, and axial stress distributions, and the martensitic volume fraction

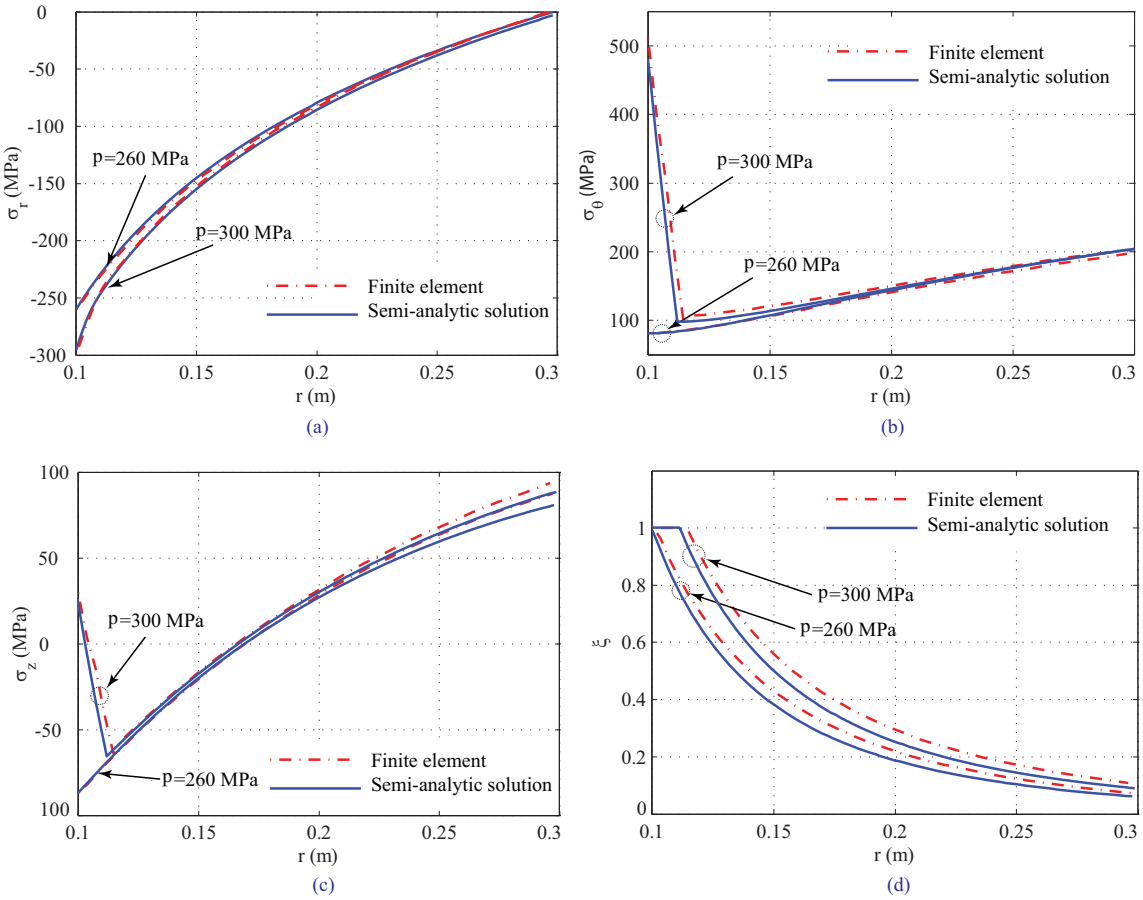

Figure 2.43: Distribution of (a) radial stress, (b) circumferential stress, (c) axial stress, and (d) martensitic volume fraction for an SMA thick-walled cylinder under internal pressure in plane strain with $\xi = 1$ at the inner radius.

calculated by the present semi-analytic method and the three-dimensional finite element simulations in the plane strain case. The radial stress, circumferential stress, and martensitic volume fraction distributions for plane stress are shown and compared with the finite element results in Figure 2.44.

As it is shown in Figures 2.43(b) and 2.44(b), by spread of the fully martensite region, the circumferential stress distribution in the fully transformed region increases considerably. This phenomenon should be considered in the design of SMA thick-walled pipe joints or pressure vessels. A designer should consider that any internal pressure that causes a portion of the cylinder to be fully transformed to martensite will produce an extremely large

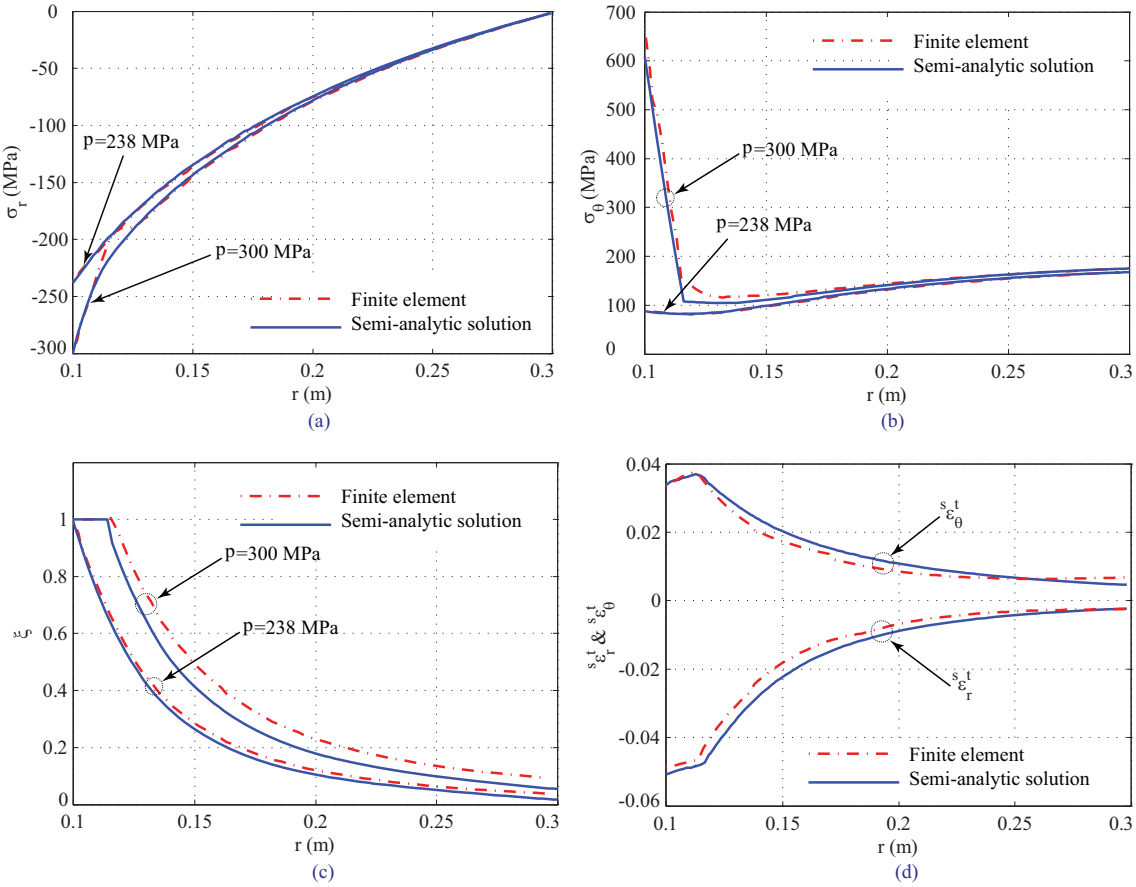

Figure 2.44: Distribution of (a) radial stress, (b) circumferential stress, (c) martensitic volume fraction, and (d) transformation strain components for an SMA thick-walled cylinder under internal pressure in plane stress with $\xi = 1$ at the inner radius.

circumferential stress in the inner radius that should preferably be avoided. Figure 2.43(c) shows the axial stress distribution in the plane strain case. As it is shown the present method of enforcing the plane strain condition for calculating the axial stress component leads to a good agreement between the semi-analytic and numerical simulation results. Distribution of martensitic volume fraction is shown in Figures 2.43(d) and 2.44(c) for plane strain and plane stress, respectively. As it is shown in these figures, for $p = 300MPa$ an annular region attached to the inner radius is completely converted to martensite ($\xi = 1$). As explained in §6 and depicted in Figure 2.36, in the present semi-analytic solution an approximation is used for finding the values of transformation strains in the region that is

completely converted to martensite. In order to study the accuracy of this approximation, the values of transformation strain components in plane stress are calculated for internal pressure $p = 300MPa$. These values are compared with the results of finite element simulations in Figure 2.44(d). As it is seen, the present method predicts the transformation strains in a good agreement with the finite element results. So it can be concluded that choosing appropriate number of load steps in the semi-analytic solution, the proposed approximation will not affect the results. Looking at Figures 2.41 to 2.44 reveals the acceptable agreement between the numerical simulation results and the present semi-analytic solution. It is worth mentioning that the results of the present method are obtained without a massive computation in contrast with the finite element (or other numerical simulations) that require a massive iterative computational process. Since the semi-analytic solution is not affected by those parameters that may make a numerical simulation ill-conditioned (*e.g.* the number of loading steps and the number of convergence iterations in satisfying the constitutive equation (see Qidwai and Lagoudas [161]) or the number of equilibrium iterations in the nonlinear finite element simulation[17]), we believe that our method can be used for validating the accuracy of numerical methods like finite element method in modeling shape memory alloy structures.

2.5 Superelastic Bending of Shape Memory Alloy Beams

In this section a closed-form solution is given for bending analysis of superelastic shape memory alloy beams. Some three-dimensional constitutive relations are reduced to an appropriate one-dimensional form required for formulating the bending problem and explicit expressions are given for the stress and martensitic volume fraction distributions in the beam cross section. These explicit expressions are used for obtaining closed-form relations between bending moment and curvature in pure bending. In addition to the J_2 model based on symmetric tension-compression response, another $J_2 - I_1$-based model is presented that

[17] In the present case studies, the finite element simulation in each load increment (loading was divided into 100 increments) needs up to 20 iterations for satisfying the constitutive equations convergence criteria with a tolerance of 1×10^{-6} for the convergence of transformation function (see Qidwai and Lagoudas [161] and Mirzaeifar et al. [126]). Since the geometry and loading are axisymmetric, the elements in the finite element model are not distorted significantly and less than five iterations were performed for the equilibrium satisfaction due to the nonlinear geometry in the finite element model.

is capable of studying bending in materials that have asymmetric response in tension and compression. Several case studies are presented for studying the accuracy of our method by comparing the results with those of three-dimensional finite element simulations. The effect of taking into account the tension-compression asymmetry in the bending response of shape memory alloys is also studied. In order to study the applicability of the present formulation in the micro scale, some experimental data on the bending of a [111] oriented NiTi micropillar are used. It is shown that the present formulation can be used for calculating the global force-deflection response with a good accuracy compared to the experimental results. Our model is shown to be very useful in finding the stress distributions, which are practically difficult to be measured in experiments. It is also shown that the present formulation can be used to find the tensile response of micropillars (which is very difficult to be measured experimentally) by using the responses in compression and bending. The predicted tensile response is compared with those obtained from analyzing [111] oriented NiTi single crystals, and a good agreement is observed.

2.5.1 Three-dimensional constitutive equations and one-dimensional reduction for bending

In this section we use the three-dimensional phenomenological macroscopic constitutive model for polycrystalline SMAs as explained in Section 2.2. However, in addition to the J_2-based model that is used in the previous sections, we also develop a solution based on the $J_2 - I_1$ transformation functions that is capable of studying bending in materials that have asymmetric response in tension and compression. Assuming the existence of a thermoelastic region (transformation surface) bounded by a smooth hypersurface, which can be described by a transformation function Φ as $\Phi(\boldsymbol{\sigma},\ \pi) = 0$, we choose the following general form for the transformation function [162]

$$\Phi(\boldsymbol{\sigma},\ \pi) = \left[\tilde{\Phi}(\boldsymbol{\sigma}) + \pi\right]^2 - Y^2 = \left[\tilde{\Phi}(\boldsymbol{\sigma}) + \pi + Y\right]\left[\tilde{\Phi}(\boldsymbol{\sigma}) + \pi - Y\right], \tag{2.91}$$

where $\tilde{\Phi}(\boldsymbol{\sigma})$ is the stress related transformation function that will be defined in the following sections and Y is a measure of internal dissipation due to microstructural changes during

phase transformation. The transformation surface that controls the onset of direct (austenite to martensite) and reverse (martensite to austenite) phase transformation is defined as

$$\tilde{\Phi}(\boldsymbol{\sigma}) + \pi = \begin{cases} Y, & \dot{\xi} > 0, \\ -Y, & \dot{\xi} < 0. \end{cases} \tag{2.92}$$

Considering the fact that any change in the state of the system is only possible by a change in the internal state variable ξ [25], the evolution of the transformation strain tensor is related to the evolution of the martensitic volume fraction as $\dot{\boldsymbol{\epsilon}}^t = (\partial\tilde{\Phi}(\boldsymbol{\sigma})/\partial\boldsymbol{\sigma})\dot{\xi} = \boldsymbol{\Gamma}\dot{\xi}$, where $\boldsymbol{\Gamma}$ represents a transformation tensor associated with the chosen transformation function.

By ignoring the shear force in the cross section of an SMA beam subjected to bending, the state of stress and strain is one dimensional. Considering the cross section in the yz-plane and the beam axis along the x-axis, the only non-zero stress component is σ_x. However, the strain and transformation strain tensors have other non-zero components as will be shown in the following two sections where the transformation tensor is obtained.

2.5.1.1 Transformation function based on J_2 with symmetric tension-compression response

By appropriate selection of the function $\tilde{\Phi}(\boldsymbol{\sigma})$, different material responses observed in experiments can be modeled by this constitutive framework. There are numerous selections for the transformation function of SMAs in the literature based on J_2 [161], $J_2 - J_3$ [66], $J_2 - I_1$ [14], and $J_2 - J_3 - I_1$ [162]. The models with a transformation function based on a J_2 invariant are the simplest and the best choice for our purposes of seeking a closed-form solution. However, by developing the constitutive equations based on J_2 invariant, although the majority of the SMA experimentally-observed responses are modeled with good accuracy, the tension-compression asymmetry (that plays an important rule in bending as it will be shown in the numerical results section) cannot be modeled. We will use a J_2-based model and also modify it by using a $J_2 - I_1$ model for taking into account the tension-compression asymmetry. The function $\tilde{\Phi}(\boldsymbol{\sigma})$ for a J_2-invariant based model is given by

$$\tilde{\Phi}(\boldsymbol{\sigma}) = \aleph\sqrt{3J_2} = \aleph\sqrt{\frac{3}{2}\boldsymbol{\sigma}' : \boldsymbol{\sigma}'}, \tag{2.93}$$

where $\aleph$ is a material constant corresponding to the maximum transformation strain during forward phase transformation in tension or compression. In (2.93) the deviatoric stress is $\boldsymbol{\sigma}' = \boldsymbol{\sigma} - \frac{1}{3}(\mathrm{tr}\,\boldsymbol{\sigma})\mathbf{I}$, where $\mathbf{I}$ is the identity matrix. The transformation tensor associated with this function is obtained as $\boldsymbol{\Gamma} = \frac{3\aleph}{2}\frac{\boldsymbol{\sigma}'}{\sqrt{3J_2}}$ [128]. The evolution equation in this case reads $\dot{\boldsymbol{\epsilon}}^t = \boldsymbol{\Gamma}\dot{\xi}$.

For studying pure bending in SMAs using the fact that the only non-zero stress component is σ_x, the second deviatoric stress invariant is simplified and $\sqrt{3J_2} = |\sigma_x|$, where $|.|$ is the absolute value. The transformation tensor for pure bending in the case of J_2-based model is reduced to read

$$\boldsymbol{\Gamma} = \aleph\,\mathrm{sgn}(\sigma_x)\begin{bmatrix} 1 & 0 & 0 \\ 0 & -0.5 & 0 \\ 0 & 0 & -0.5 \end{bmatrix}, \tag{2.94}$$

where sgn(.) is the sign function. Substituting (2.94) into the evolution equation, if we denote the transformation strain along the beam axis by ϵ_x^t, the transformation strain components in the cross section are $\epsilon_y^t = \epsilon_z^t = -0.5\epsilon_x^t$ and the other components are zero during loading. This is equivalent to assuming that phase transformation is an isochoric (volume preserving) process, which is a consequent of considering the transformation function based only on the J_2-invariant. It is worth noting that in developing the three-dimensional constitutive relations a more precise model is obtained by assuming a different transformation tensor related to the second deviatoric transformation strain invariant during reverse phase transformation [127, 128], but in the present case of pure bending in which the normal stress is the only non-zero stress component, the transformation tensors are identical during forward and reverse phase transformations.

2.5.1.2 Modeling tension-compression asymmetry using a $J_2 - I_1$-based transformation function

It is experimentally well known that single crystal and polycrystalline shape memory alloys have a non-symmetric tension-compression response [60, 63, 113, 182]. There have been numerous efforts in the literature for better understanding the origins of this secondary effect in SMAs and introducing appropriate constitutive relations capable of modeling this

effect [17, 145, 153]. Most of the the existing constitutive relations for modeling the tension-compression asymmetry are appropriate only for numerical simulations and not for closed-form solutions because of their complexity. We use the J_2-I_1-based transformation function that enables the constitutive relations to model the tension-compression asymmetry besides relative simplicity compared to the other models [14, 162]. The function $\tilde{\Phi}(\boldsymbol{\sigma})$ for this model is given by

$$\tilde{\Phi}(\boldsymbol{\sigma}) = \eta\ \sqrt{3J_2} + \omega\ I_1 = \eta\ \sqrt{\frac{3}{2}\boldsymbol{\sigma}' : \boldsymbol{\sigma}'} + \omega\ \mathrm{tr}(\boldsymbol{\sigma}), \tag{2.95}$$

where η and ω are material constants related to the maximum transformation strains during forward phase transformation in tension and compression. The transformation tensor associated with the chosen function is given by $\boldsymbol{\Gamma} = \frac{3\eta}{2}\frac{\boldsymbol{\sigma}'}{\sqrt{3J_2}} + \omega\mathbf{I}$ [14]. The evolution function in this case is similar to the J_2 model by replacing the transformation tensor with the previously derived tensor. It is worth noting that by setting $\omega = 0$ in the $J_2 - I_1$ model, the J_2 model is not obtained because the material constants are calibrated separately for these two models. The material constants in (2.95) can be calibrated for modeling the volumetric strain or the tension-compression asymmetry. We will use the later method because we are studying the effect of asymmetry of tension-compression response on the bending of SMAs. However, it is shown that by calibrating the material constants in this manner, the model will predict a positive volumetric transformation strain, which is unrealistic[18] [162]. However, we are interested in the bending problem by considering the axial components of stress and strain. The volumetric transformation strain has no effect on our solution. In the special case that the only non-zero stress component is the normal stress σ_x, the transformation tensor is given by

$$\boldsymbol{\Gamma} = \eta\,\mathrm{sgn}(\sigma_x)\begin{bmatrix} 1 & 0 & 0 \\ 0 & -0.5 & 0 \\ 0 & 0 & -0.5 \end{bmatrix} + \omega\begin{bmatrix} 1 & 0 & 0 \\ 0 & 1 & 0 \\ 0 & 0 & 1 \end{bmatrix}. \tag{2.96}$$

[18] Experiments on polycrystalline NiTi show a negative change of volume during phase transformation. J_2 models predict a zero transformation volumetric strain and the $J_2 - I_1$ model leads to a positive value. $J_2 - J_3 - I_1$ models are able to account for a negative transformation strain.

2.5.2 Stress-strain relationship for SMAs in pure bending

In the one-dimensional case corresponding to pure bending, substituting the transformations functions (2.93) and (2.95) into the expression of thermodynamic force (**??**) and the transformation criteria (2.92) enable us to find an explicit expression for the martensitic volume fraction. Using the relations between the constitutive model parameters (2.14) the explicit expressions for the martensitic volume fraction in direct and inverse phase transformation for J_2 and $J_2 - I_1$ models in pure bending after some mathematical manipulation are simplified to read

$$\xi^{\pm} = \frac{1}{\rho b^{\pm}} \left\{ \aleph |\sigma_x| + \frac{1}{2}\sigma_x^2 \Delta S_{11} + \rho \Delta s_0 (T - T^{\pm}) \right\}, \tag{2.97}$$

for the J_2-based model and

$$\xi^{\pm} = \frac{1}{\rho b^{\pm}} \left\{ \eta |\sigma_x| + \omega \sigma_x + \frac{1}{2}\sigma_x^2 \Delta S_{11} + \rho \Delta s_0 (T - T^{\pm}) \right\}, \tag{2.98}$$

for the $J_2 - I_1$-based model, where the + and - symbols are used for indicating the loading and unloading, respectively, and $T^+ = M_s$, $T^- = A_f$, $\rho b^+ = \rho b^M$, and $\rho b^- = \rho b^A$. Throughout this paper we use the superscripts + and - for any variable for indicating the forward and reverse phase transformations, respectively.

Substituting the transformation tensors (2.94) and (2.96) into the evolution equation, the explicit expressions $\epsilon_x^t = \aleph \ \mathrm{sgn}(\sigma_x)\xi$ and $\epsilon_x^t = [\eta \ \mathrm{sgn}(\sigma_x) + \omega]\xi$ are obtained for the J_2 and $J_2 - I_1$ models, respectively. Considering an SMA beam subjected to bending both the axial stress and transformation strain components are positive in the region that is in tension and negative in the region that is subjected to compression. For the sake of simplicity, we write the transformation strain based on J_2 and $J_2 - I_1$ models with the same equation $\epsilon_x^t = (\ell_c \hat{\eta} + \hat{\omega})\xi$, where the loading coefficient ℓ_c is $+1$ in tension and -1 in compression, and the parameters $(\hat{\eta}, \hat{\omega})$ are replaced with (η, ω) for the $J_2 - I_1$ model and replaced with $(\aleph, 0)$ for the J_2 based model. Substituting the resulting transformation strain into (2.4) gives the following one-dimensional constitutive equation

$$\epsilon_x = (S_{11}^A + \xi \Delta S_{11})\sigma_x + \alpha_A (T - T_0) + (\ell_c \hat{\eta} + \hat{\omega})\xi, \tag{2.99}$$

where $S_{11}^A = 1/E^A,\ \Delta S_{11} = 1/E^M - 1/E^A$ (E^A and E^M are the elastic muduli of austenite and martensite, respectively). Substituting the martensitic volume fractions (2.97), (2.98), and using the Euler beam theory for the strain-curvature relation $\epsilon_x = -\kappa y$, where κ is the axis curvature and y is the distance from the neutral axis into (2.99), the stress-strain relation can be written as the following cubic equation

$$\sigma_x^3 + a\ \sigma_x^2 + b\ \sigma_x + \tilde{c} + \tilde{\kappa} y = 0, \tag{2.100}$$

where $a,\ b,\ \tilde{c}$, and $\tilde{\kappa}$ are constants given by

$$\begin{aligned} a &= \frac{3(\ell_c \hat{\eta} + \hat{\omega})}{\Delta S_{11}}, \quad b = \frac{2\rho \Delta s_0 (T - T^{\pm})}{\Delta S_{11}} + \frac{2(\ell_c \hat{\eta} + \hat{\omega})^2 + 2\rho b^{\pm}\ S_{11}^A}{\Delta S_{11}^2}, \\ \tilde{c} &= \frac{2(\ell_c \hat{\eta} + \hat{\omega})\rho \Delta s_0 (T - T^{\pm}) + 2\rho b^{\pm} \alpha_A (T - T_0)}{\Delta S_{11}^2},\ \tilde{\kappa} = \frac{2\kappa \rho b^{\pm}}{\Delta S_{11}^2}. \end{aligned} \tag{2.101}$$

The cubic equation (2.100) is solved for σ_x as a function of temperature and strain. The acceptable roots[19] for the SMA material in tension and compression are

$$\sigma_t = \frac{1}{6}\left(A - 108\tilde{\kappa} y + \mathscr{P}\right)^{1/3} - \frac{2b - 2a^2/3}{\left(A - 108\tilde{\kappa} y + \mathscr{P}\right)^{1/3}} - \frac{a}{3}, \tag{2.102}$$

$$\begin{aligned} \sigma_c = {} & \frac{-1}{12}\left(A - 108\tilde{\kappa} y + \mathscr{P}\right)^{1/3} + \frac{b - a^2/3}{\left(A - 108\tilde{\kappa} y + \mathscr{P}\right)^{1/3}} - \frac{a}{3} \\ & - \frac{\sqrt{3}}{2} i \left[\frac{1}{6}\left(A - 108\tilde{\kappa} y + \mathscr{P}\right)^{1/3} + \frac{2b - 2a^2/3}{\left(A - 108\tilde{\kappa} y + \mathscr{P}\right)^{1/3}}\right], \end{aligned} \tag{2.103}$$

where $A = 36ab - 108\tilde{c} - 8a^3$, $B = 162\tilde{c} - 54ab + 12a^3$, $C = 12b^3 - 3a^2b^2 - 54ab\tilde{c} + 12a^3\tilde{c} + 81\tilde{c}^2$, and $\mathscr{P} = 12\sqrt{81\tilde{\kappa}^2 y^2 + B\tilde{\kappa} y + C}$. It is worth noting that the expressions for stress in tension and compression are real when the SMA material properties are substituted into the coefficients (2.101). In order to simplify the expressions for stress, we also use the trigonometric form of the roots of the cubic equation (2.100) as [2]

$$\sigma_t = \cos\left(\frac{1}{3}\tan^{-1}\theta\right)\mathscr{G} - a/3, \tag{2.104}$$

$$\sigma_c = \frac{1}{2}\cos\left(\frac{1}{3}\tan^{-1}\theta - \frac{2\pi}{3}\right)\mathscr{G} + \frac{\sqrt{3}}{2}\sin\left(\frac{1}{3}\tan^{-1}\theta - \frac{2\pi}{3}\right)\mathscr{G} - a/3, \tag{2.105}$$

where $\theta = 12\sqrt{-81\tilde{\kappa}^2 y^2 - B\tilde{\kappa} y - C}/(A - 108\,\tilde{\kappa} y)$, and $\mathscr{G} = \frac{1}{3}(A^2 - 144C)^{1/6}$. The explicit expressions in (2.104) give the exact value of stress. However, we need a simplified expression

[19] We choose the real positive root for tension, and the real negative root for compression. If there are more than one positive or negative roots, the acceptable root is distinguished by considering the phase transformation start and finish stresses (2.115).

to calculate an explicit expression for bending moment later. As it will be shown in §2.5.4, the typical values of material properties for SMAs lead to a large value for θ in (2.104). Using the trigonometric identity $\tan^{-1}\theta = \pi/2 - \tan^{-1}(1/\theta)$, the argument of tangent inverse is small and can be approximated as $\tan^{-1}\theta \simeq \pi/2 - 1/\theta$. Substituting this approximation in (2.104) and using the fact that the parameter $\beta = 1/(3\theta)$ is also small, and considering the approximations $\cos\beta \simeq 1 - \beta^2/2$, and $\sin\beta \simeq \beta$, the stresses in tension and compression are given by

$$\sigma_t = \left[\left(1 - \frac{1}{2}\beta^2\right)\cos\varphi + \beta\sin\varphi\right]\mathscr{G} - \frac{a}{3}, \tag{2.106}$$

$$\sigma_c = \left[\left(1 - \frac{1}{2}\beta^2\right)\cos\varphi + \beta\sin\varphi\right]\mathscr{G} + \frac{\sqrt{3}}{2}\left[\beta\cos\varphi - \left(1 - \frac{1}{2}\beta^2\right)\sin\varphi\right]\mathscr{G} - \frac{a}{3}, \tag{2.107}$$

where $\varphi = \pi/6$. After some algebraic simplifications, the stress-strain relationship in tension and compression can be unified using the load condition coefficient ℓ_c as

$$\sigma = \left[\ell_c\left(1 - \frac{1}{2}\beta^2\right)\cos\varphi + \beta\sin\varphi\right]\mathscr{G} - \frac{a}{3}. \tag{2.108}$$

We will present a detailed numerical study of the accuracy of the above approximation for obtaining (2.106) from the exact expressions in (2.104) for different curvature values in §2.5.4. It will be shown that these approximate formulas give accurate results even for large curvatures.

2.5.3 Bending moment-curvature relationship for SMAs in bending

In this section we present a closed-form relationship between the bending moment and curvature in SMAs subjected to bending using the explicit stress-strain relations obtained in the previous section. We will introduce the formulas with some different simplifying assumptions. The accuracy of each approximation is numerically studied in §2.5.4 versus the exact solution that is obtained by using the exact stress-strain relationships (2.104) or (2.102) and using numerical integration in the cross section for obtaining the bending moment-curvature response.

The bending moment-curvature relationship for an SMA beam with an arbitrary cross section is given by $M = \int_\Omega y\sigma(y)dA$, where M is the bending moment, y is the distance

from the neutral axis, and Ω represents the cross section. In the most general case, the cross section is divided into three regions: an elastic core in which the phase transformation has not started, a middle part with phase transformation, and the outer part in which the material is fully transformed to martensite. In order to calculate the total bending moment, the bending moment in each part should be found and summed in the whole cross section. The most complicated section to be solved is the middle part with active phase transformation. However, the bending moment in this section can be calculated explicitly by using the stress distributions given in (2.108). In addition to the bending moment that is obtained using the complete stress expression (2.108), we present two more explicit expressions for the bending moment obtained by imposing simplifications on the stress distribution. We will numerically study the accuracy of these simplifying assumptions in §**??**. The simplified relations can be later used for developing closed-form solutions in more complicated cases, e.g. for studying the large deflection of SMA cantilevers. We start with the complete stress distribution in (2.108). For calculating the bending moment, the stress distribution (2.108) should be used only in the portion of the cross section with phase transformation. We present a method for finding the boundaries of this section in the sequel (see (2.117)). For a rectangular cross section, we can write

$$\begin{aligned}\mathscr{I}^1 = \int y\sigma(y)w dy = {} & \frac{-1}{2916}\,\frac{w\mathscr{G}\sqrt{R}(-54\tilde{\kappa}y + A + B)\sin\varphi}{\tilde{\kappa}^2} - \frac{1}{2916}\,\frac{w\ell_c\mathscr{G}y(3A+2B)\cos\varphi}{\tilde{\kappa}} \\ & + \frac{19}{36}\,wy^2\ell_c\mathscr{G}\cos\varphi - \frac{1}{6}\,wy^2 a - \frac{1}{2^3\ 3^8}\,\frac{w\mathscr{G}\tan^{-1}(S)\,(B^2 - 108C + A\ B)\sin\varphi}{\tilde{\kappa}^2} \\ & + \frac{1}{2^6\ 3^{10}}\,\frac{w\ell_c\mathscr{G}\ln(-R)\,(-1296\,C + 9\,A^2 + 24\,AB + 16\,B^2)\cos\varphi}{\tilde{\kappa}^2} \\ & + \frac{1}{2^5\ 3^{10}}\,\frac{w\ell_c\mathscr{G}\tanh^{-1}(Q)\,[-3888\,C(A+B) + 9\,A^2B + 24\,AB^2 + 16\,B^3]\cos\varphi}{\tilde{\kappa}\sqrt{B^2\tilde{\kappa}^2 - 324\,\tilde{\kappa}^2 C}} + \mathbb{C}_1, \end{aligned} \tag{2.109}$$

where w is the cross section width, $\mathbb{C}_1$ is the constant of integration, and

$$R = -81\,\tilde{k}^2y^2 - Bky - C, \quad Q = \frac{162\,\tilde{k}^2y + B\tilde{k}}{\sqrt{B^2\tilde{k}^2 - 324\,\tilde{k}^2C}}, \quad S = \frac{9\,\tilde{k}}{\sqrt{R}}\left(y + \frac{1}{162}\,\frac{B}{\tilde{k}}\right). \tag{2.110}$$

The other parameters in (2.109) are all defined in the previous sections. We use this expression for calculating the total bending moment in the cross section later on. Before doing that, we first present two more expressions for this integral using the following simplifications. Considering the typical material properties for polycrystalline SMAs, it can be shown

that in the term $\theta = 12\sqrt{-81\tilde{\kappa}^2y^2 - B\tilde{\kappa}y - C}/(A-108\,\tilde{\kappa}y)$, $|-C| \gg |-B\tilde{\kappa}y| > |-81\tilde{\kappa}^2y^2|$. We consider two simplifying approximations in calculating the bending moment by ignoring the first term and the first two terms in the nominator of the expression for θ. The accuracy of these approximations will be numerically studied in §2.5.4.1. By ignoring the first term $(-81\tilde{\kappa}^2y^2)$, the integral required for calculating the bending moment for a rectangular cross section is given by

$$\begin{aligned}\mathscr{I}^2 = \int y\sigma(y)w dy = {} & \frac{6}{5}\,\frac{w\mathscr{G}\left(-B\tilde{\kappa}y - C\right)^{5/2}\sin\varphi}{B^3\tilde{\kappa}^2} + 4\,\frac{w\mathscr{G}C\left(-B\tilde{\kappa}y - C\right)^{3/2}\sin\varphi}{B^3\tilde{\kappa}^2} \\ & + \frac{1}{54}\,\frac{w\mathscr{G}A\left(-B\tilde{\kappa}y - C\right)^{3/2}\sin\varphi}{B^2\tilde{\kappa}^2} + \frac{1}{18}\,\frac{w\mathscr{G}CA\sqrt{-B\tilde{\kappa}y - C}\sin\varphi}{B^2\tilde{\kappa}^2} \\ & + 6\,\frac{w\mathscr{G}C^2\sqrt{-B\tilde{\kappa}y - C}\sin\varphi}{B^3\tilde{\kappa}^2} + \frac{3}{2}\,\frac{w\ell_c\mathscr{G}\tilde{\kappa}y^3\cos\varphi}{B} + \frac{1}{2}\,wy^2\ell_c\mathscr{G}\cos\varphi \\ & - \frac{1}{24}\,\frac{wy^2\ell_c\mathscr{G}A\cos\varphi}{B} - \frac{1}{6}\,wy^2a - \frac{9}{4}\,\frac{wy^2\ell_c\mathscr{G}C\cos\varphi}{B^2} + \frac{1}{2592}\,\frac{w\ell_c\mathscr{G}yA^2\cos\varphi}{B\tilde{\kappa}} \\ & + \frac{1}{12}\,\frac{w\ell_c\mathscr{G}yCA\cos\varphi}{B^2\tilde{\kappa}} + \frac{9}{2}\,\frac{w\ell_c\mathscr{G}yC^2\cos\varphi}{B^3\tilde{\kappa}} - \frac{1}{2592}\,\frac{w\ell_c\mathscr{G}CA^2\ln\left(B\tilde{\kappa}y + C\right)\cos\varphi}{B^2\tilde{\kappa}^2} \\ & - \frac{1}{12}\,\frac{w\ell_c\mathscr{G}C^2A\ln\left(B\tilde{\kappa}y + C\right)\cos\varphi}{B^3\tilde{\kappa}^2} - \frac{9}{2}\,\frac{w\ell_c\mathscr{G}C^3\ln\left(B\tilde{\kappa}y + C\right)\cos\varphi}{B^4\tilde{\kappa}^2} + \mathbb{C}_2, \end{aligned} \tag{2.111}$$

where $\mathbb{C}_2$ is the constant of integration. By ignoring the first two terms, this integral is simplified to read

$$\begin{aligned}\mathscr{I}^3 = \int y\sigma(y)w dy = {} & \frac{9}{8}\,\frac{w\ell_c\mathscr{G}\tilde{k}^2y^4\cos\varphi}{C} + \frac{1}{3}\left(\frac{-1}{12}\,\frac{w\ell_cA\tilde{k}\cos\varphi}{C} - 3\,\frac{w\tilde{k}\sin\varphi}{\sqrt{-C}}\right)\mathscr{G}y^3 \\ & + \frac{w}{2}\left\{\left[\ell_c\cos\varphi\left(1 + \frac{1}{2592}\,\frac{A^2}{C}\right) + \frac{1}{36}\,\frac{A\sin\varphi}{\sqrt{-C}}\right]\mathscr{G} - \frac{1}{3}\,a\right\}y^2 + \mathbb{C}_3, \end{aligned} \tag{2.112}$$

where $\mathbb{C}_3$ is the constant of integration. The integrals (2.109)-(2.112) are calculated for a rectangular cross section. We study the circular cross section later in this section. For obtaining a complete description of the moment-curvature relation, it is necessary to find the boundaries of the region in which the phase transformation occurs. We obtain these boundaries for the loading phase first. Later we show that a different approach should be used for unloading. In the most general case in loading, the cross section is divided into three sections. A schematic of the cross section for a rectangular superelastic beam is shown in Figure 2.45. The fist region includes the neutral axis and the phase transformation has not started in this region ($\xi = 0$). In the second region (region II) the phase transformation has started but has not been completed ($0 < \xi < 1$). The third region (region III) contains the material with completed phase transformation from austenite to martensite ($\xi = 1$).

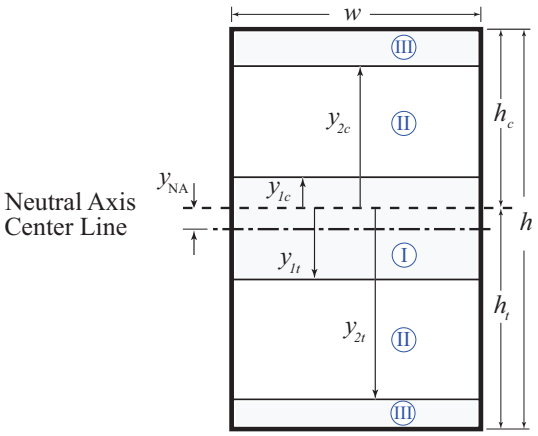

Figure 2.45: A schematic of the rectangular cross section.

When using the J_2-based model, the neutral axis is located at the centroid of the beam ($Y_{NA} = 0$ in Figure 2.45) and the three regions are symmetric with respect to the center line. However, for the $J_2 - I_1$-based model, the neutral axis is not located on the center line. To find the neutral axis location in this case, the force equilibrium in each cross section along the beam axis ($\sum F = 0$) should be enforced, which reads

$$\begin{aligned}
&\frac{1}{2}E^A\kappa y_{1t}^2 + \left(\tilde{\mathcal{I}}\Big|_{y=y_{1t}} - \tilde{\mathcal{I}}\Big|_{y=y_{2t}}\right) + E^M\left[\frac{1}{2}\kappa(y_{2t}^2 - \frac{h_t^2}{4}) - H^t(y_{2t} + \frac{h_t}{2})\right] \\
&-\frac{1}{2}E^A\kappa y_{1c}^2 + \left(\tilde{\mathcal{I}}\Big|_{y=y_{2c}} - \tilde{\mathcal{I}}\Big|_{y=y_{1c}}\right) + E^M\left[\frac{1}{2}\kappa(\frac{h_c^2}{4} - y_{2c}^2) - H^c(\frac{h_c}{2} - y_{2c})\right] = 0, \quad (2.113)
\end{aligned}$$

where H^t and H^c are the maximum transformation strain in tension and compression, respectively. The parameters h_t and h_c are the maximum distance from the neutral axis in the tension and compression regions, respectively (see Figure 2.45). The first three terms in (2.113) correspond to the force in sections below the neutral axis subjected to tension, and the next terms represent the force above the neutral axis in compression (a positive curvature is assumed). The terms containing $\tilde{\mathcal{I}}$ represent the force corresponding to region

II with $0 < \xi < 1$ given by

$$\tilde{\mathcal{I}} = \int \sigma(y)dy = \ell_c \mathscr{G} y \cos\varphi - \frac{1}{12}\frac{\ell_c \mathscr{G} y\left(-27\,B\tilde{k}y + BA + 54\,C\right)\cos\varphi}{B^2} + \frac{1}{2592}\frac{\ell_c \mathscr{G}\ln\left(B\tilde{k}y + C\right)\left(A^2B^2 + 216\,CAB + 11664\,C^2\right)\cos\varphi}{B^3\tilde{k}} - 2\frac{\mathscr{G}\left(-B\tilde{k}y - C\right)^{3/2}\sin\varphi}{B^2\tilde{k}} - \frac{1}{18}\frac{\mathscr{G}\sqrt{-B\tilde{k}y - C}\,(BA + 108\,C)\sin\varphi}{B^2\tilde{k}} - \frac{1}{3}ay + \mathbb{C}_4, \quad (2.114)$$

where $\mathbb{C}_4$ is the constant of integration. In (2.113) we need to calculate the values $y_{1t},\ y_{2t},\ y_{1c}$, and y_{2c} to obtain the neutral axis position. The stress values corresponding to the start and finish of phase transformation during loading phase can be calculated by replacing $\xi^+ = 0$ and $\xi^+ = 1$ into (2.98) and solving for stress. These are given by

$$\sigma_s = \frac{-(\ell_c\hat{\eta} + \hat{\omega}) + \sqrt{(\ell_c\hat{\eta} + \hat{\omega})^2 - 2\Delta S_{11}\rho\Delta s_0(T - M_s)}}{\Delta S_{11}}, \quad (2.115)$$

$$\sigma_f = \frac{-(\ell_c\hat{\eta} + \hat{\omega}) + \sqrt{(\ell_c\hat{\eta} + \hat{\omega})^2 - 2\Delta S_{11}\left(\rho\Delta s_0(T - M_s) - \rho b^M\right)}}{\Delta S_{11}}, \quad (2.116)$$

where the loading factor ℓ_c is equal to $+1$ in tension and -1 in compression. Using these stress values the boundaries of various regions in the cross section are given by

$$y_{1t} = \frac{\sigma_s|_{\ell_c=1}}{\kappa\ E^A}, \quad y_{2t} = \frac{(\hat{\eta} + \hat{\omega})\ E^M + \sigma_f|_{\ell_c=1}}{\kappa\ E^M}, \quad y_{1c} = \frac{\sigma_s|_{\ell_c=-1}}{\kappa\ E^A}, \quad y_{2c} = \frac{(-\hat{\eta} + \hat{\omega})\ E^M + \sigma_f|_{\ell_c=-1}}{\kappa\ E^M}. \quad (2.117)$$

Substituting (2.114)-(2.117) into (2.113) and considering the fact that $h_c = h - h_t$, where h is the cross section height, this equation can be solved for h_t. This gives the neutral axis position corresponding to κ. It is worth noting that this formulation corresponds to the most general case in which the cross section is divided into three regions. It is obvious that if $|y_{2t}| > h_t$ or $y_{2c} > h_c$, region III is not formed in the tension or compression part of the cross section and the above equations can be modified by eliminating the terms associated with this region.

Bending moment at each cross section along the length of the superelastic beam is related to the curvature by

$$M = -\frac{1}{3}E^A\kappa w(y_{1c}^3 - y_{1t}^3) + \left(\mathscr{I}^i\Big|_{y=y_{2c}} - \mathscr{I}^i\Big|_{y=y_{1c}}\right) + E^M w\left[\frac{1}{3}\kappa(\frac{h_c^3}{8} - y_{2c}^3) - H^c(\frac{h_c^2}{4} - y_{2c}^2)\right] + \left(\mathscr{I}^i\Big|_{y=y_{1t}} - \mathscr{I}^i\Big|_{y=y_{2t}}\right) + E^M w\left[\frac{1}{3}\kappa(y_{2t}^3 - \frac{h_t^3}{8}) - H^c(y_{2t}^2 - \frac{h_t^2}{4})\right], \quad (2.118)$$

where the superscript i is replaced by 1, 2, or 3 for different approximations given in (2.109)-(2.112). It is worth noting that when the terms $\mathscr{I}$ are evaluated in tension regions, the loading coefficient $\ell_c = 1$ and in the compression regions $\ell_c = -1$. The solution procedure for the loading phase is as follows. Bending moment along the beam axis is calculated by considering the external force and the boundary conditions. At each cross section bending moment is known and the curvature should be found by solving the nonlinear algebraic equation (2.118). In the case of the J_2-based model, this equation can be solved independently because the neutral axis location is known due to symmetry, i.e. $h_c = h_t = h/2$. However, in the case of using the $J_2 - I_1$-based model, the neutral axis position is unknown and should be obtained by solving (2.113) in which the curvature is assumed known. For solving these equations simultaneously, a numerical scheme is used [55]. In this numerical method, in each iteration, curvature κ in (2.118) is given an initial value. This initial value is substituted into (2.113) and the neutral axis position is obtained. The calculated neutral axis position is returned to evaluate the right-hand side of (2.118). Comparing the calculated bending moment at that cross section with the bending moment obtained from the external force, curvature is modified [55]. The iterations are stopped when a tolerance is achieved between the applied bending moment at each cross section and the right-hand side of (2.118). When the curvature value is found the lateral deflection is calculated using $\kappa = \frac{d^2v}{dx^2}$, where v is the lateral deflection and x is measured along the beam axis. The integration constants in curvature-lateral deflection relationship are found by imposing the appropriate boundary conditions.

In the unloading phase, in the most general case the cross section may be divided into three regions. The material in the inner region with elastic response in loading ($y_{1t} < y < y_{1c}$) experiences elastic unloading. The outer regions with phase transformation in loading are divided into two regions during unloading; one with elastic unloading and the other one with reverse phase transformation in unloading. To obtain the boundaries of these regions consider a generic point in the cross section. If we denote the martensitic volume fraction at the end of loading for this point by ξ^*, the critical stress for the start of reverse phase transformation in unloading is given by replacing ξ^- in (2.97) or (2.98) by ξ^* and solving

the resulting equation for stress. Using the properties defined for the evolution equation (see below (2.98) for definitions), this critical stress is given by

$$\sigma_c = \frac{-(\ell_c\hat{\eta}+\hat{\omega}) + \ell_c\sqrt{(\ell_c\hat{\eta}+\hat{\omega})^2 - 2\Delta S_{11}\rho\Delta s_0(T-A_f) - \rho b^A\xi^*}}{\Delta S_{11}}. \tag{2.119}$$

During unloading, the elastic change of stress at a generic location is calculated by $\Delta\sigma = -(E^A + \xi^*\Delta E)(-\kappa^* y + \kappa_u y)$, where y is the distance of the point from the neutral axis. The parameters κ^* and κ_u are the curvature of the corresponding cross section at the end of the loading phase and the curvature in unloading, respectively. Now we can evaluate the start of reverse phase transformation by comparing the stress $\sigma_e = \sigma^* - \Delta\sigma$ (σ^* is the stress value at the end of loading phase) with σ_c. For $|\sigma_e| > |\sigma_c|$, the phase transformation in unloading has not started. In this case stress is equal to σ_e and $\xi = \xi^*$. If $|\sigma_e| \leq |\sigma_c|$, the reverse phase transformation has started. The stress and martensitic volume fraction are obtained from (2.97), (2.98), and (2.108) by considering the superscript "-" and the appropriate loading condition parameter $\ell_c = \pm 1$. For sake of brevity, the details of the bending moment-curvature relations and the process of finding the neutral axis position in unloading are not presented here. However, this procedure is very similar to the loading case.

For analyzing beams with circular cross sections a similar method is used where Ω is the area enclosed by the horizontal chords at y_{1t} and y_{2t}, and also the area between y_{1c} and y_{2c} in the cross section. In this case, we use a trapezoidal numerical integration method to obtain the bending moment-curvature relationship.

2.5.4 Numerical results

In this section, several case studies are presented for superelastic beams with circular and rectangular cross sections subjected to loading-unloading cycles. The results of both J_2 and $J_2 - I_1$ models are presented. The J_2-based solution is compared with a three-dimensional finite element model and the $J_2 - I_1$ results are presented to show the effect of taking into account the tension-compression asymmetry on the bending response of superelastic beams. Some experimental data for bending of a nickel-titanium micropillar are used to verify the applicability of the present method for modeling bending in the micro scale. The available

material response in compression and bending are used for extracting the material response in tension, which is very difficult to measure in experiments. The resulting tensile and compressive properties are compared with the nickel-titanium constitutive relations and it is shown that the predicted response in tension is in good agreement with the single-crystal theoretical response (see the end of §2.5.4.6).

2.5.4.1 The accuracy of the proposed approximations

In §2.5.2 we presented the exact stress distribution (2.104). Using this stress distribution needs a numerical integration for obtaining the bending moment-curvature relation. Using some assumptions an approximate stress distribution is given in (2.108), which can be used for calculating explicit expressions for the the bending moment-curvature relation. We used three different simplifying assumptions for calculating the bending moment as a function of curvature (see $\mathscr{I}^i$, $i = 1,\ 2,\ 3$ in (2.109)-(2.112)). In this section we compare the bending moment-curvature relationship obtained by the exact stress distribution and numerical trapezoidal integration with the results of the three approximations. A rectangular cross section with $h = 1$ cm and width $w = 1.5$ mm is considered. The J_2-based model is used for this comparison. The material properties for $Ni_{50}Ti_{50}$ [79] are used for obtaining the necessary constants in the constitutive relations (see Qidwai and Lagoudas [162] for details of extracting constitutive model constants from experimental data): $E^A = 72MPa$, $E^M = 30MPa$, $\nu^A = \nu^M = 0.42$, $\rho c^A = \rho c^M = 2.6 \times 10^6$ J/(m^{3}K), $H^t = 0.05$, $H^c = -0.035$, $(d\sigma/dT)^A_t = 8.4 \times 10^6$ J/(m^{3}K), $\rho \Delta s_0 = -H^t (d\sigma/dT)^A_t = -0.42 \times 10^6$ J/(m^{3}K), $A_f = 281.6K$, $A_s = 272.7K$, $M_f = 238.8K$, $M_s = 254.9K$. For implementing the J_2-based model, the constants in the transformation function are set to $\hat{\eta} = \aleph = H^t$, and $\hat{\omega} = 0$. The temperature is $T = T_0 = 300$ K and an isothermal loading-unloading process is assumed (see [128] for a detailed study of isothermal process and thermomechanical coupling in the response of SMAs). The bending moment-curvature relation is depicted in Figure 2.46. As it is seen, all the approximations are in good agreement with the solution obtained form the exact stress distribution even for large

curvature values. We use the approximation II (given in (2.111)) throughout the numerical results of this paper. We use the third approximation in a future communication for considering the large deflection effects.

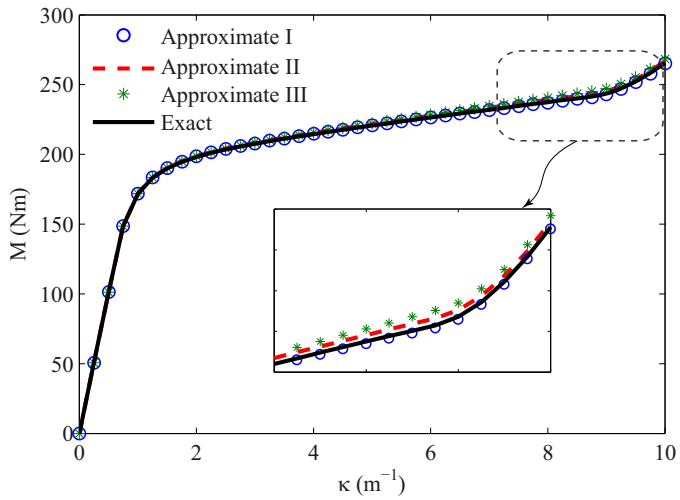

Figure 2.46: The bending moment-curvature relationship calculated by the exact stress distribution with trapezoidal integration, and three different approximate explicit integrals (2.109), (2.111), and (2.112) of §2.5.3.

2.5.4.2 J_2-based model

In this section the results of the J_2-based model are presented. We compare the analytical results obtained from the present formulation with those of a three-dimensional finite element simulation. The three-dimensional constitutive relations of §2.5.1 are used and an appropriate user subroutine (UMAT) is written by FORTRAN in the commercially available finite element program ABAQUS that enables this code to model SMA structures using solid elements and some two-dimensional elements. The details of implementing the constitutive equations in a displacement-based finite element formulation are given in [126]. The finite element framework is validated by comparing its results with many experimental tests and analytical solutions in [127, 129, 131]. An SMA cantilever with length $L = 10$ cm is considered in this section. The rectangular cross section has a height of $h = 1$ cm and width

$w = 1.5$ mm. Three-dimensional quadratic brick elements with reduced integration (element C3D20R in ABAQUS) are used in the finite element method. A convergence analysis is performed for choosing the appropriate number of elements by considering the normal stress distribution in the cross section and the load-displacement response as the convergence criteria. The stress distribution is considered to be converged when the maximum difference is smaller than 0.1MPa and the convergence criterion of the maximum difference for the load-displacement response is 10N. A total of 6000 elements are used for modeling the cantilever beam ($100 \times 20 \times 3$ elements in length, width, and thickness directions). All the finite element simulations are done using this mesh. The material properties are the same as the case study in §2.5.4.1. The temperature is $T = T_0 = 300$ K and the isothermal loading-unloading process is assumed. The superelastic cantilever is subjected to a transverse tip load. The load-tip deflection is calculated by the present analytical method and the results are compared with the numerical simulation results in Figure 2.47.

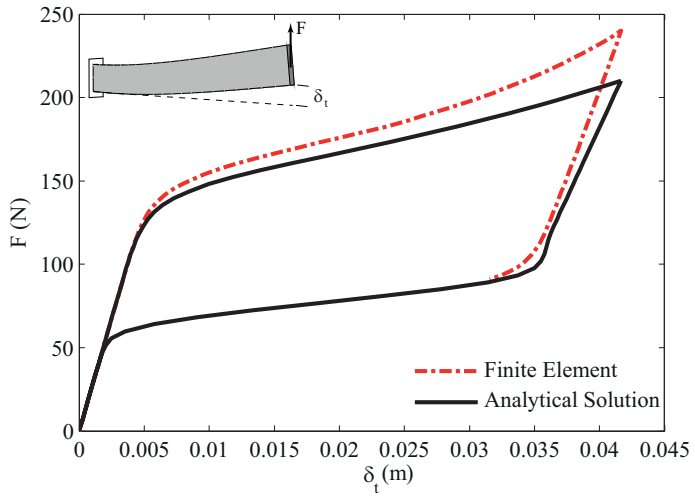

Figure 2.47: Force versus tip deflection for an SMA beam with rectangular cross section (b=1.5 mm, h=1 cm, and L=10 cm).

As it is shown, even for this relatively large deflection (the tip deflection is four times the height of the beam), the results are in good agreement (with a maximum 14% error).

The finite element results show stiffening at the end of loading phase as the slope of force-deflection increases while the analytical solution predicts an almost constant gradient. This difference is mainly caused by the nonlinear geometric effects that are ignored in the present solution and included in the numerical simulations. It is worth noting that the finite element simulation is completed in about two hours on a 2 GHz CPU with 2 GB RAM while the analytic solutions are obtained in a few seconds on the same system. Also as it is seen in Figure 2.47, the numerical simulation in unloading is not completed. This happens due to some convergence issues in most numerical simulations during unloading, especially in the case of large deflections or complicated geometries. While achieving convergence in the finite element simulation requires an excessive effort by refining the mesh size and modifying the numerical algorithms, the present analytic solution is a reliable method. The present method can also be used as a benchmark for validating the numerical simulations. In order to study the capability of the present formulation in calculating the stress and martensitic volume fraction distributions, the cross section of the superelastic cantilever at the clamped edge is considered. The stress distribution at the end of the loading phase is shown in Figure 2.48(a) and the martensitic volume fraction is shown in Figure 2.48(b). As it is shown the closed-form solution calculates both the stress and martensitic volume fractions accurately. It is worth noting that in the finite element simulation the outputs are averaged between integration points and this makes the results smooth compared to the analytical solution. As it is seen in these figures, the core remains austenite without phase transformation. By considering pure bending, the stress around the neutral axis is zero and there is always an austenite core without phase transformation even for large deflections. By considering the shear effect in bending, the stress at the core is nonzero which may cause phase transformation at the core as well. However, except for very thick beams the pure bending theory gives accurate results and this is reflected in comparison of the results with the finite element solution that considers the shear effect.

The contour plots of the stress and martensitic volume fraction distributions at the end of the loading phase obtained from the present closed-form solution are depicted in Figure 2.49 and compared with the finite element results. As it is shown, the deformed

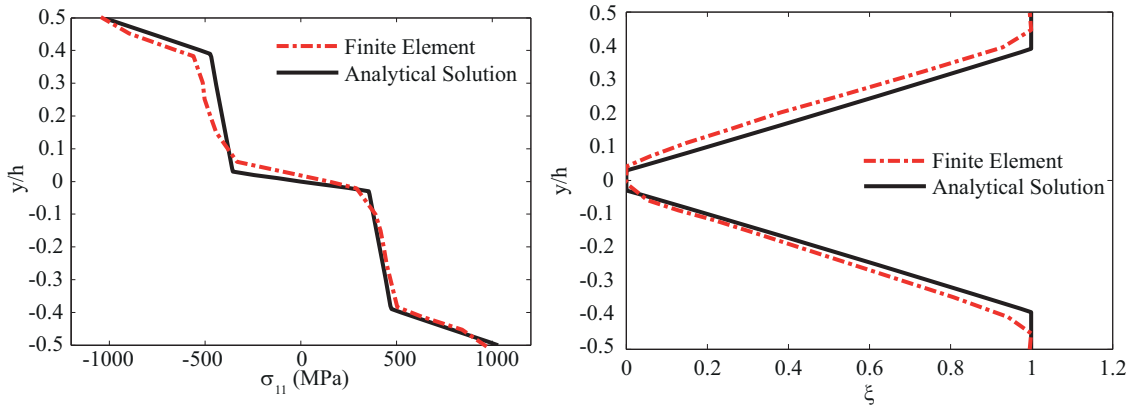

Figure 2.48: Comparison of the finite element and analytical results for (a) normal stress and (b) martensitic volume fraction distribution at the clamped edge of an SMA beam with rectangular cross section subjected to bending. The results correspond to the end of the loading phase (see Figure 2.47).

shape obtained by the present method is slightly different from the numerical simulation prediction. Also, the analytic solution (in this section we are using the J_2-based model) is predicting symmetric stress and martensitic volume fraction distributions, while the finite element results show a slight asymmetry along the beam axis. Note that in our solution the nonlinear geometry effects and the displacement along the beam axis direction are ignored while the numerical simulations show a minor deflection along the axis due to geometric nonlinearities. As shown in Figures 2.47-2.49, the present method gives accurate results even for the large deflection chosen in these case studies. It is worth nothing that the accuracy of the results based on small deflection assumption is geometry dependent. The geometry in the above case studies is chosen such that phase transformation starts in the cross section even for moderate tip deflections (in the order of thickness). If other geometries are chosen (e.g. the same beam in another direction with height $h = 1.5$ mm and width $w = 1$ cm), very large deflections are required for the phase transformation to start, and using the solutions based on the small deflection assumption leads to large errors in those cases. However, there are numerous applications for which the approach of this paper gives accurate results (e.g. the micropillar studied at the end of this section).

As another case study, consider a superelastic cantilever with circular cross section. The

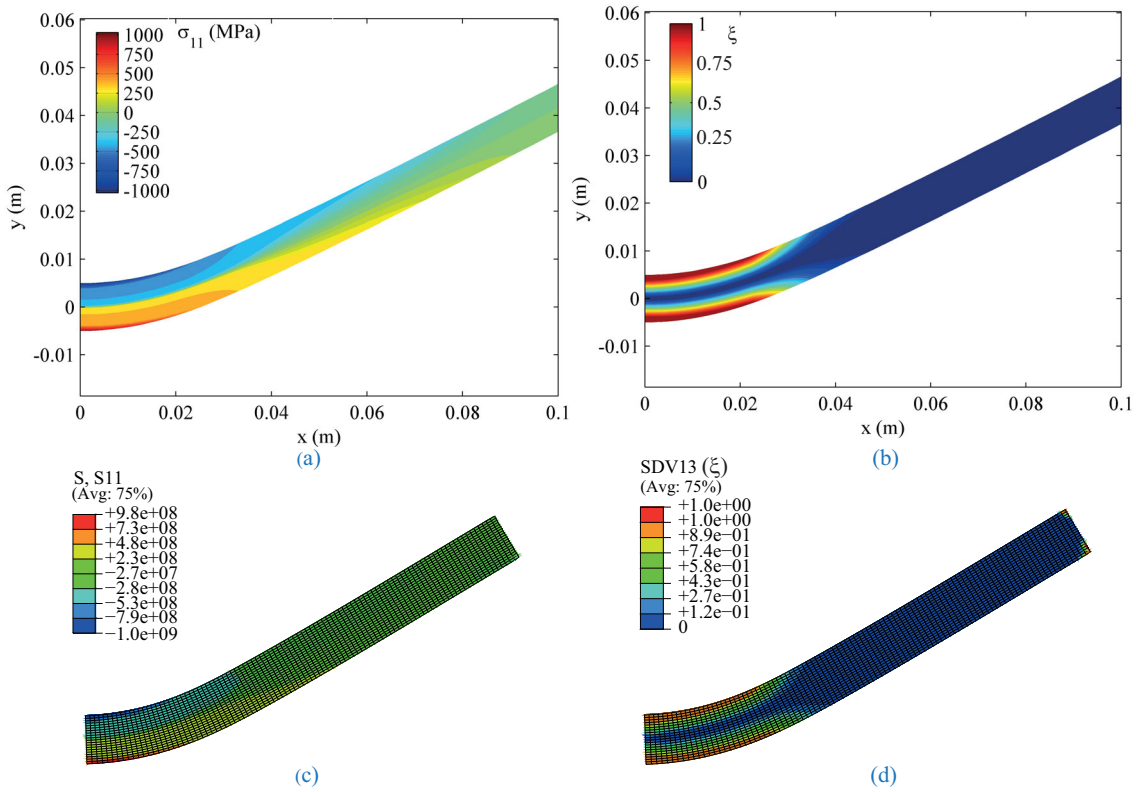

Figure 2.49: Contour plots of the normal stress (a and c) and the martensitic volume fraction distributions (b and d) obtained by the analytical solution (a and b), and the finite element solution (c and d) for a beam with rectangular cross section subjected to bending. The results correspond to the end of loading phase (see Figure 2.47).

material properties are the same as those of the previous case study and the dimensions are $R = 5$ mm and $L = 10$ cm, where R is the cross section radius. A total of 9600 three-dimensional quadratic brick elements with reduced integration (element C3D20R in ABAQUS) are used in the finite element model (a cross section of the mesh is shown in Figure 2.52). The cantilever is clamped at one end and a transverse load is applied at the other end as shown in Figure 2.50. The applied force versus the tip deflection obtained by the present analytical method is shown in Figure 2.50 and compared with the finite element results. As it is seen, the finite element results again suffer from convergence issues during the unloading phase and this causes the solution to terminate before completion. The results are in a good agreement (with a maximum 11% error) even for the relatively

large deflection (four times the bar diameter). The results for the calculated stress and

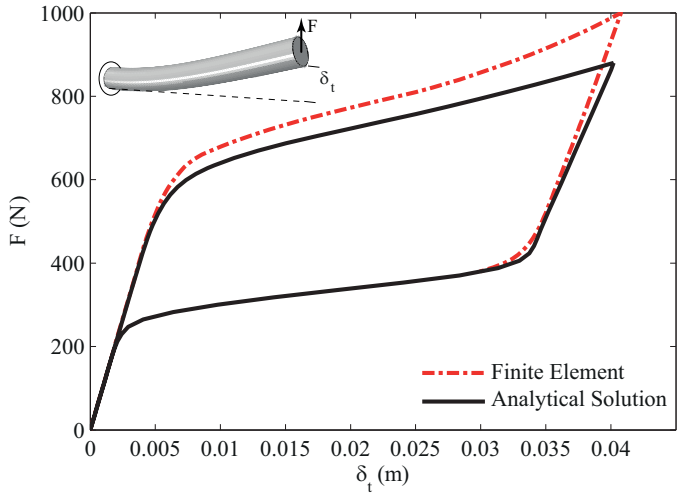

Figure 2.50: Force versus tip deflection for an SMA beam with circular cross section (R=5 mm, and L=10 cm).

martensitic volume fraction corresponding to the end of the loading phase at the clamped edge are compared in Figure 2.51. The results are depicted along a vertical path passing through the center of the cross section at the clamped edge.

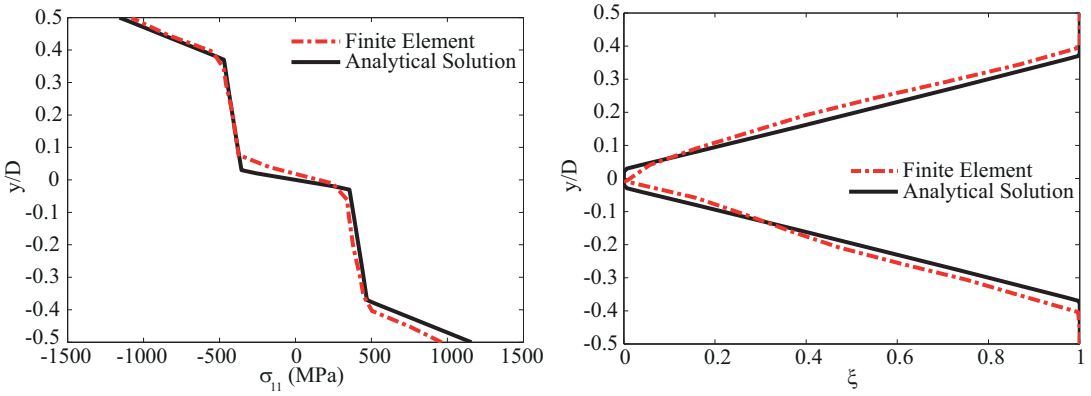

Figure 2.51: Comparison of the finite element and analytical results for (a) normal stress and (b) martensitic volume fraction distribution at the clamped edge of an SMA beam with circular cross section subjected to bending. The results correspond to the end of loading phase (see Figure 2.50).

The contour plots of the stress and martensitic volume fraction distributions are shown

in Figure 2.52. These contours are plotted for a vertical section passing through the axis of the bar (see Figure 2.50 for the geometry). As mentioned earlier, a slight difference in the deformed shape and the asymmetry of distributions observed in the finite element outputs both result from ignoring the geometric nonlinearities in the present formulation. In the

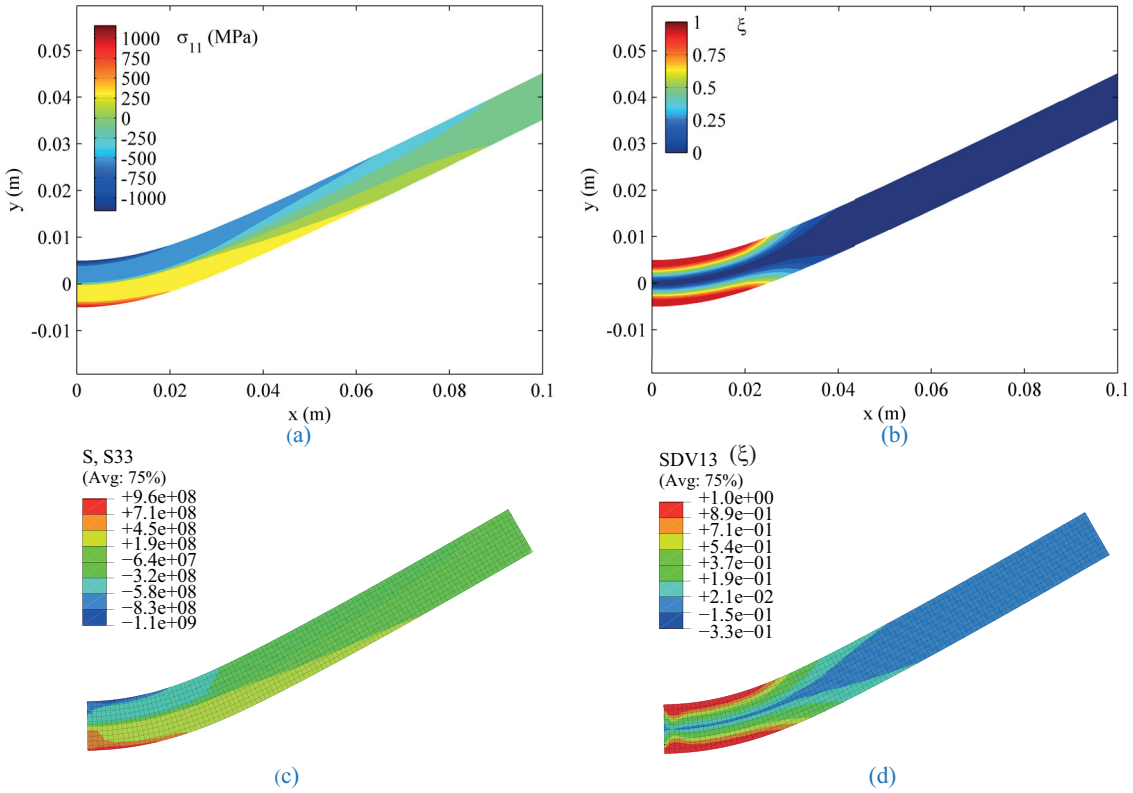

Figure 2.52: Contour plots of the normal stress (a and c) and the martensitic volume fraction distributions (b and d) obtained by the analytical solution (a and b), and the finite element solution (c and d) for a beam with circular cross section subjected to bending. The results correspond to the end of loading phase (see Figure 2.50).

results presented in this section, both the numerical simulations and the analytic solutions are based on the J_2 model. The effect of taking into account the tension-compression asymmetry on the response of SMAs is considered by using the $J_2 - I_1$-based model and the results are presented in the next section.

2.5.4.3 *Effect of tension-compression asymmetry on the bending response of SMAs*

Most shape memory alloys including NiTi exhibit significant different responses in tension and compression when subjected to uniaxial loading. Bending is readily affected by this phenomenon because the material is subjected to both tension and compression in bending. We presented a J_2-I_1-based model capable of modeling the tension-compression asymmetry in §2 and 3. The constitutive model parameters should be calibrated using the experimental data. Denoting the maximum transformation strain in tension and compression by H^t and H^c, respectively, the $J_2 - I_1$ model parameters are given by $\hat{\eta} = \eta = \frac{1}{2}(H^t + |H^c|)$, and $\hat{\omega} = \omega = \frac{1}{2}(H^t - |H^c|)$. We consider the material properties used in the previous section and modify the constitutive relations parameters by implementing the above modifications. The response of a NiTi alloy with these properties in uniaxial compression is calculated using both the J_2 and $J_2 - I_1$ models as shown in Figure 2.53. It is worth noting that the material response in tension is identical for both models and equivalent to the results of the J_2-based model in Figure 2.53 with positive stress and strain values. As it is shown in Figure 2.53, the $J_2 - I_1$-based model predicts the start of the phase transformation at larger absolute values of stress, and also predicts a lower compressive strain for completion of phase transformation compared to the J_2-based model. This phenomenon is in agreement with experimental data [59, 60]. The experimental data of Jacobus et al. [79] were used in [162] and the accuracy of the presented $J_2 - I_1$-based model was studied for modeling uniaxial loading. We are using the same constitutive model and material properties for studying bending of SMA beams.

Consider a cantilever superelastic beam with rectangular cross section with the same dimensions, temperature, and boundary conditions as those of the case study of §2.5.4.2. For comparison purposes we study the results of J_2 and $J_2 - I_1$-based models to analyze the effect of taking into account the tension-compression asymmetry on the bending response of superelastic beams. The tip deflection versus applied force is depicted in Figure 2.54. Two different case studies are solved with the J_2 model. In one case the beam is subjected to the same force as in the $J_2 - I_1$-based case study, and in the other one the tip deflections of both beams are equal. As it is shown, the tension-compression asymmetry significantly

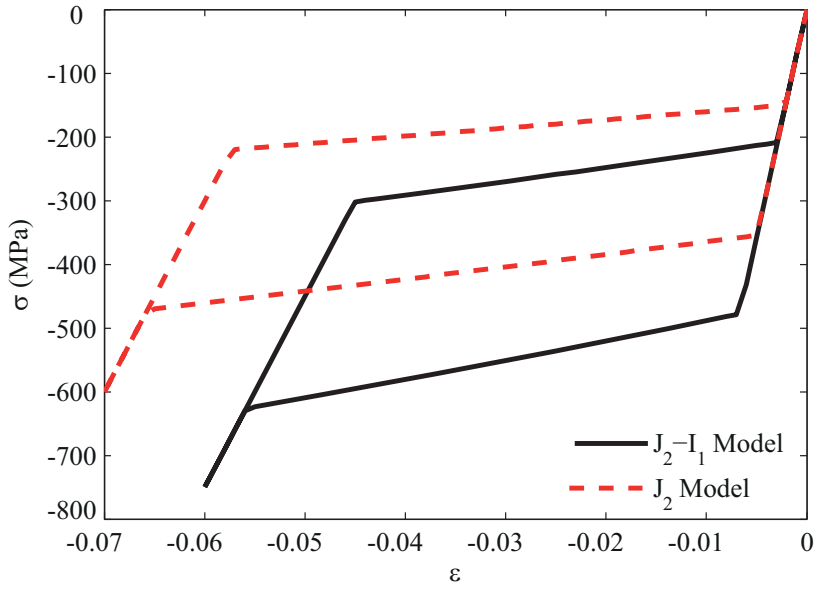

Figure 2.53: Axial stress versus axial strain for J_2 and $J_2 - I_1$ transformation functions under uniaxial compression loading-unloading.

affects the bending response. In the same deflection case, a maximum of 16% difference is seen in the applied force and in the same force case, the tip deflection differs by a maximum value of 41% at the end of the loading phase. The stress and martensitic volume fraction distributions at the clamped edge are shown in Figure 2.55 for this case study at the end of the loading phase. As it is seen in Figure 2.55(a), the $J_2 - I_1$ model predicts the zero stress above the cross section center (y=0). The non-symmetric martensitic volume fraction distribution is shown in Figure 2.55(b). It is worth noting that the minor symmetry observed in the FE results is caused by the effect of large deflections, mainly because the load at the tip is considered always vertical in the FE analysis (the load is not rotating as the tip rotates).

The zero stress point defines the neutral axis position that is found by solving (2.113) as explained in §2.5.3. As expected (see Figure 2.53), the absolute value of stress predicted by the $J_2 - I_1$-based model is larger compared to the predicted values by the J_2-based model. This phenomenon causes a larger force at the compression portion of the cross section, and the neutral axis is shifted up toward the compression part in order to satisfy

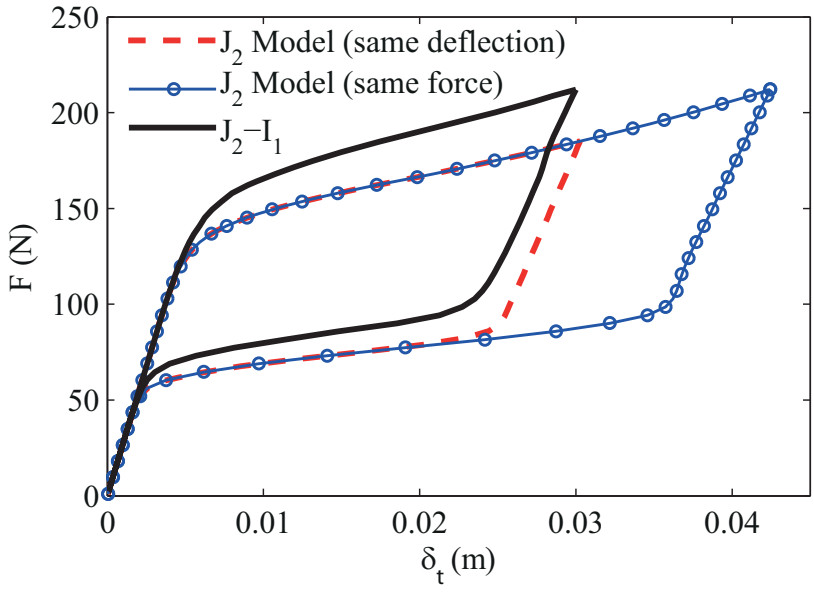

Figure 2.54: Comparison of the force-tip deflection response for an SMA beam calculated by the J_2 and $J_2 - I_1$ based models. Two different cases of equal tip deflection and equal applied force are presented (the cross section is rectangular with b=1.5 mm, h=1 cm, and L=10 cm).

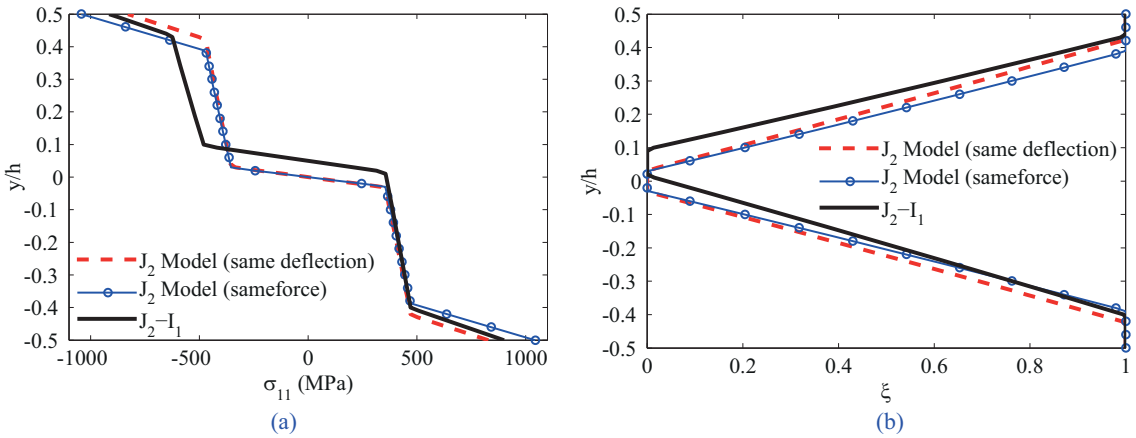

Figure 2.55: Comparison of the J_2 and $J_2 - I_1$-based model results for (a) normal stress and (b) martensitic volume fraction distribution at the clamped edge of an SMA beam with rectangular cross section subjected to bending. Two different cases of equal tip deflection and equal applied force are presented. The results correspond to the end of loading phase (see Figure 2.54).

equilibrium. It is worth noting that the height of the phase transformation area is smaller in the compression part due to smaller maximum compressive transformation strain (see Figure 2.53) and this causes a slight downward movement of the neutral axis towards the centerline as the phase transformation area (section II in Figure 2.45) is formed in the cross section. For having a detailed view of the neutral axis position with respect to the applied bending moment, this position is plotted along the axis of the beam (in which the bending moment is varying linearly) in Figure 2.56. As it is shown, in the regions far from the clamped edge in which the material responds elastically due to small bending moments, the neutral axis coincides with the centerline. Increasing the bending moment (decreasing x on the horizontal axis), the neutral axis distance from the centroid increases up to a specific bending moment value ($M = 17.5$ Nm at $x = 1.75$ cm in the present case study). By increasing the bending moment above this critical value, the neutral axis distance from the centroid decreases slightly due to spread of the fully transformed area.

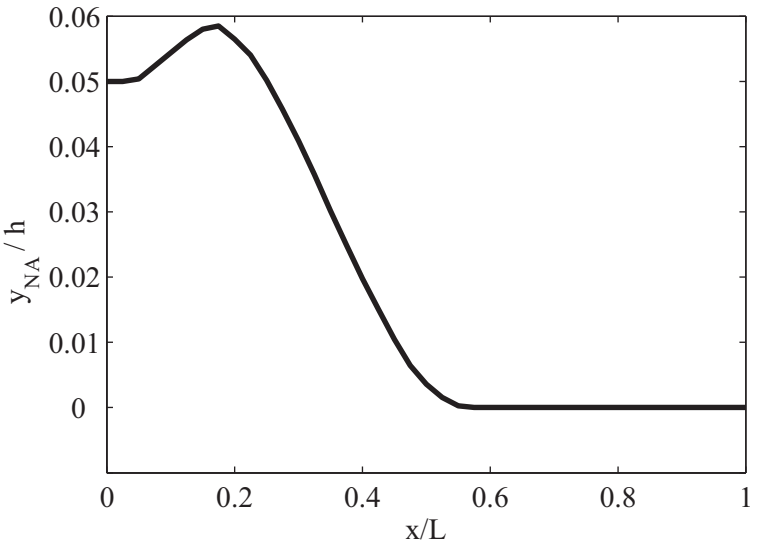

Figure 2.56: The location of neutral axis with respect to the cross section centroid along the length of an SMA beam subjected to bending.

The contour plots of martensitic volume fraction at the end of the loading phase near the clamped edge are shown in Figure 2.57 and the results are compared for the J_2 and $J_2 - I_1$ models (for case study with identical tip deflections). An asymmetric distribution

is clearly seen in Figure 2.57(a) and the neutral axis position is shown. As it is seen, the neutral axis coincides with the centerline in the regions far from the clamped edge where the phase transformation has not started. Figure 2.54 shows the significant effect of this asymmetry on the force-deflection response of the superelastic cantilever.

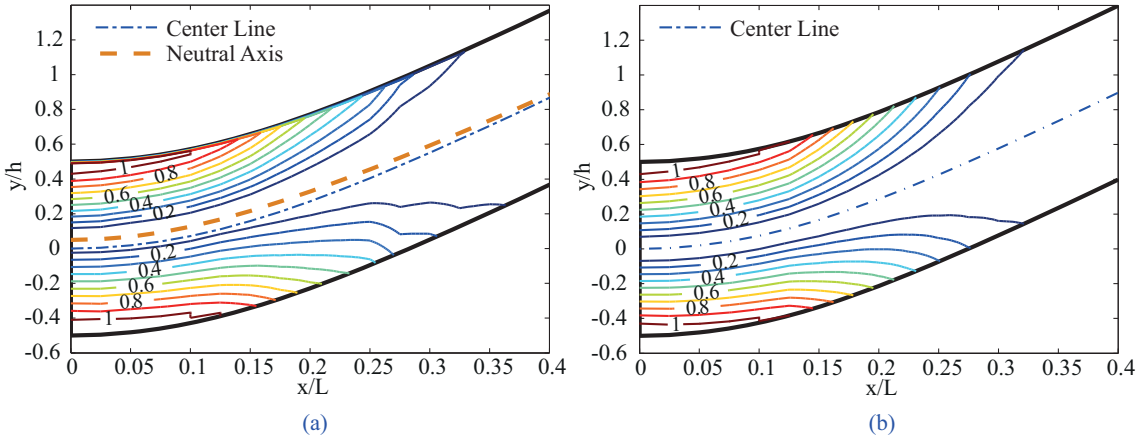

Figure 2.57: Contour plots of the martensitic volume fraction distribution near the clamped edge obtained by (a) $J_2 - I_1$ and (b) J_2 models for a beam with rectangular cross section subjected to bending. The results are for the equal tip deflection at the end of loading phase (see Figure 2.54).

2.5.4.4 Materials with large tension-compression asymmetries

It is shown in experiments that the material properties in shape memory alloys, particularly NiTi, are strongly affected by the deformation processing. Frick et al. [56] studied the properties of cast and deformation processed polycrystalline NiTi (Ti-50.9 at. pct Ni) bars. They have shown that while the material response for the cast NiTi samples is almost symmetric in tension and compression, a cast, hot rolled, then cold drawn material exhibits a very large asymmetry in tension-compression response. The maximum transformation strain in tension is reported more than two times the maximum transformation strain in compression for the hot rolled, then cold drawn material with a significant difference in the stress levels in the stress-strain plateau (see Figure 2.58). Such a large asymmetry in tension-compression response causes numerical instabilities in the finite element simulations. However, our closed-form solution does not suffer from such instabilities. In order to study

the applicability of our analytic solution for modeling bending of SMA beams with very large tension-compression asymmetry, a superelastic beam with rectangular cross section is considered. The geometry and boundary conditions are the same as those of the case studies in §2.5.4.2. The experimental results for the stress-strain response of the material is shown in Figure 2.58. The material properties in the constitutive model are calibrated as follows: $E^A = 63MPa$, $E^M = 35MPa$, $\nu^A = \nu^M = 0.3$, $H^t = 0.047$, $H^c = -0.02$, $(d\sigma/dT)_t^A = 6.4 \times 10^6$ J/(m^{3}K), $\rho\Delta s_0 = -H^t(d\sigma/dT)_t^A = -0.3008 \times 10^6$ J/(m^{3}K), $A_f = 300K$, $A_s = 273K$, $M_f = 218K$, $M_s = 254K$. We use the $J_2 - I_1$-based model for analyzing this problem by setting $\hat{\eta} = \eta = \frac{1}{2}(H^t + |H^c|)$ and $\hat{\omega} = \omega = \frac{1}{2}(H^t - |H^c|)$. The ambient temperature is $T = T_0 = 27°C$. The model prediction for the stress-strain response in uniaxial loading is compared with the experimental data in Figure 2.58. It is worth noting that the experimentally observed difference in the Young modulus in tension and cmpression is ignored in our solution. The difference of elastic modulus in tension and compression has been reported in Plietsch and Ehrlich [156] without explaining its origin. Frick et al. [56] used various experimental results and asserted that the asymmetry of the tensile and compressive response of the elastic modulus is caused by strain contributions related to the transformation, such as martensite interface motion, or pre-martensitic deformation modes such as the R-phase. These strain contributions are strongly affected by the texture of a polycrystalline SMA and a micromechanical model can be used to capture such effects, while phenomenological models ignore this asymmetry. Also, the smooth hardening observed at the end of stress-strain plateau can be simulated in phenomenological models by using higher degree polynomials or trigonometric hardening functions [92]. We have chosen the quadratic function (2.3), which ignores this effect, for obtaining a closed-form solution. A transverse load $F = 210$ N is applied to the superelastic cantilever (see Figure 2.47 for the geometry and loading). The martensitic volume fraction distribution in the cross section near the clamped edge is shown in Figure 2.59(a). Comparing this distribution with the results in the previous case study given in Figure 2.57(a), it is seen that for the material with the larger asymmetry, the neutral axis position moves further into the compression region, and the martensitic volume fraction distribution is considerably asymmetric with

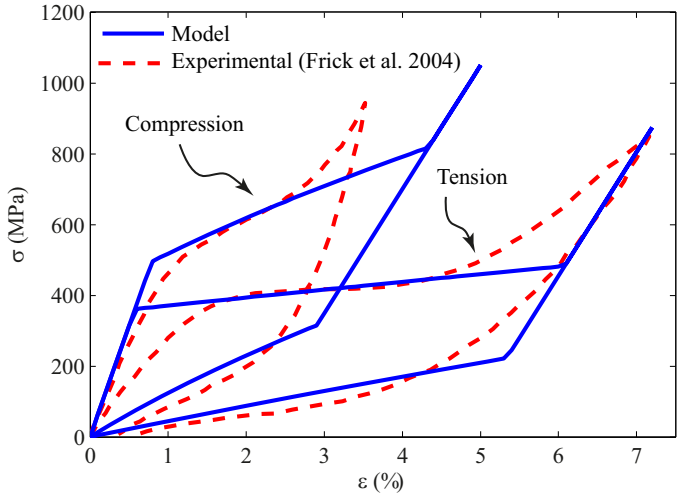

Figure 2.58: The stress-strain response in uniaxial loading for a cast, hot rolled, then cold drawn polycrystalline NiTi with a large tension-compression asymmetry [56].

respect to the centerline. The stress distribution in the cross section near the clamped edge of a beam made of this material with large tension-compression asymmetry is shown in Figure 2.59(b). As it is seen, the compression part is considerably smaller than the tension region. This is expected from the stress-strain response shown in Figure 2.58. The large asymmetry in the stress and martensitic volume fraction distributions clearly shows that using a symmetric constitutive model for this case leads to erroneous results. Our model is stable in modeling the bending of superelastic SMA beams made of materials with large asymmetries in tensile and compressive responses.

2.5.4.5 Three-point bending test of a NiTi beam

A NiTi shape memory alloy beam is used to compare the experimental and the corresponding theoretical results. A schematic of the setup for performing the three-point bending test is shown in Figure 2.60. The length of the SMA beam is $L = 170$ mm and the cross section is rectangular with w =7.5 mm and h =3 mm. The SMA beam is made of nearly equiatomic NiTi alloy and the material properties of $Ni_{50}Ti_{50}$ [79] as mentioned in §2.5.4.1 are used for developing the analytic solution. It is worth noting that thermal treatments and deformation processing may change the material properties slightly. However, in this

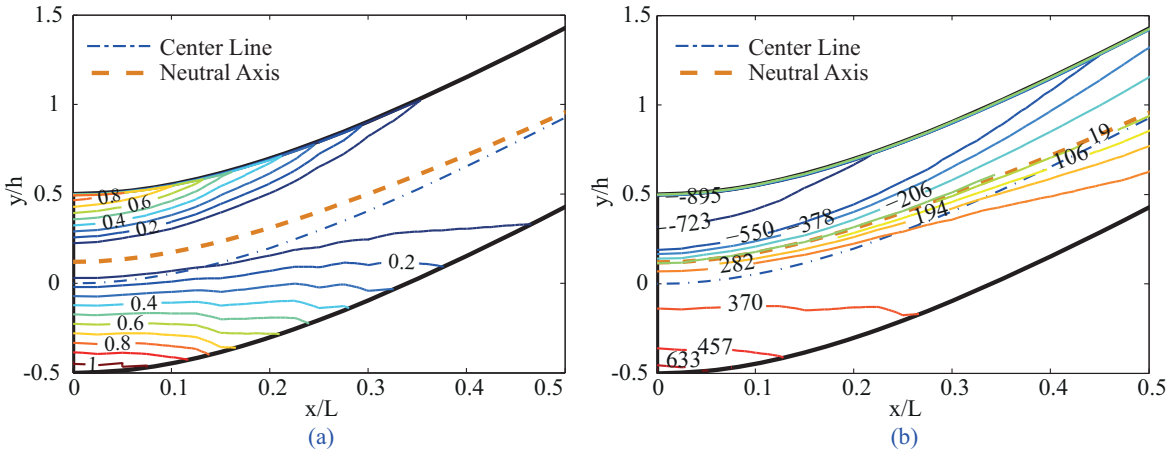

Figure 2.59: Contour plots of (a) the martensitic volume fraction distribution, and (b) the stress distribution near the clamped edge for a material with large tension compression asymmetry (see Figure 2.58).

case by performing a simple tension test on the sample, it was observed that using the same material properties predicts the response in tension with an acceptable accuracy (see Mirzaeifar et al. [129] for some examples of comparing the response of SMA samples in uniaxial tests with the results predicted by the present constitutive equations). A 250 kN MTS Universal Testing Machine is used for performing the three-point bending test with the setup shown in Figure 2.60. The maximum deflection of the center is set to δ =20 mm and the loading-unloading is performed slowly to ensure the isothermal condition. The

Figure 2.60: The experimental setup for the three-point bending test of an SMA beam.

non-dimensional load-deflection response of the beam obtained from the experiment is compared with the theoretical results in Figure 2.61. As it is shown in this figure, the loading response is accurately predicted by the $J_2 - I_1$-based model. However, the results in the unloading phase show a larger difference. This is because the constitutive equations used in this work (with the choice of polynomial hardening function) cannot predict the smooth stress-strain plateau in unloading and this difference is more when unloading starts before the material is fully transformed to martensite ($\xi < 1$). In the presented test, the thickness of the SMA beam is small and the phase transformation is not completed in most parts of the cross section (see the previous sections for some examples of SMA beams with larger thicknesses). By increasing the thickness, the error in the unloading phase is decreased remarkably. It is worth noting that by modifying the hardening function (2.3) the constitutive equation results improve in the unloading phase [92]. However, more complicated hardening functions are not suitable for developing closed-form solutions.

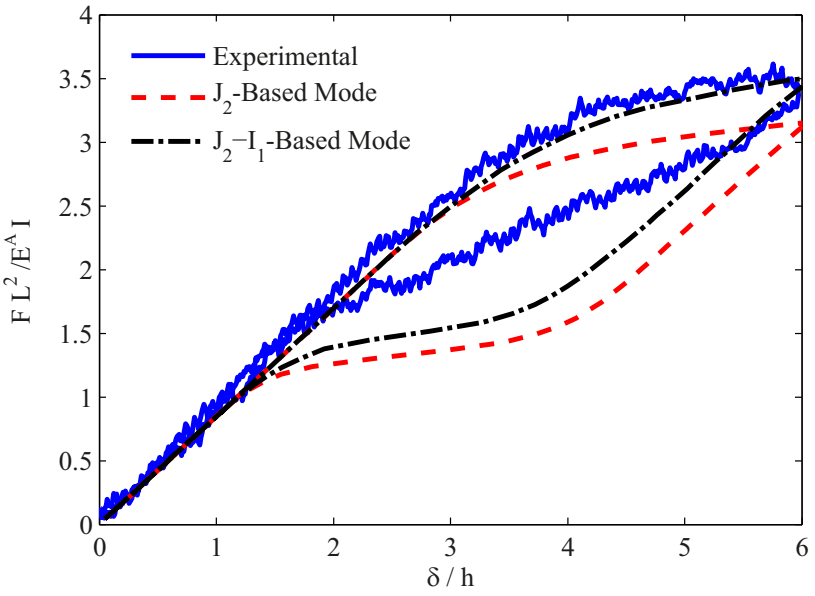

Figure 2.61: Comparison of the non-dimensional load-deflection response obtained from three-point bending test and theoretical solutions.

2.5.4.6 Bending of micropillars

As was mentioned earlier, one application of the presented analytic solution is the assessment of material properties in tension (compression) when the bending and compressive (tensile) responses are known but performing tension (compression) tests is practically difficult. The presented solution is developed based on the constitutive equations suitable for polycrystalline SMAs, and an example of such application for polycrystalline SMAs is to obtain the compressive response of tiny wires using the known bending and tensile test results. However, we will consider a different example in this section. Although the constitutive equations of this paper are developed for modeling polycrystalline SMAs, we will show that the analytical solution of this paper can also be used as an approximation for studying the single crystal NiTi micropillars with specific orientations with a significant hardening in the stress-strain response.

In this section we study the superelastic response of NiTi microscale pillars. Nickel-titanium nano to micro scale pillars have been extensively studied experimentally in recent years. In experiments on compressive loading of micropillars, it is observed that the [111] NiTi samples exhibit a significant hardening during phase transformation compared to [100] oriented samples (compare the stress-strain curves for [100] oriented crystals in [81, 165] with the response of [111] crystals in [57, 117]). This phenomenon is expected from the theory as well because the NiTi crystals of [111] orientation are hard under compression [59]. The hardening during phase transformation in the compressive response of [111] NiTi micropillars motivated us to implement the present formulation, which is capable of considering the stress hardening with arbitrary slope in the phase transformation plateau[20] (see Figure 2.53) for studying bending of micropillars. We show in this section that the material properties predicted by this method are in good agreement with the expected properties for NiTi single crystals as well. The experimental results on the bending of a micropillar reported by Clark et al. [40] are used in this section. They tested a [111] oriented NiTi pillar with a diameter

[20]The slope of stress-strain plateau for single crystal SMAs in some specific orientations, and also polycrystalline SMAs with particular heat treatments may be near zero. The material properties of the presented model cannot be calibrated for modeling a zero slope during the transformation. However, these properties can be calibrated for modeling a very small slope in the stress-strain plateau if needed.

of $D_t = 1.2\mu m$ at the top of pillar and length of $L = 3.8\mu m$. The undeformed micropillar and the deformed shape of the micropillar subjected to bending are shown in Figure 2.62. As mentioned in the pillar specifications, all the samples had an estimated taper angle of $\approx 3^\circ - 5^\circ$. We consider a 3° angle, which leads to a diameter of $D_t = 1.6\mu m$ at the pillar base. Among the material properties required for our constitutive model, the austenite finish tem-

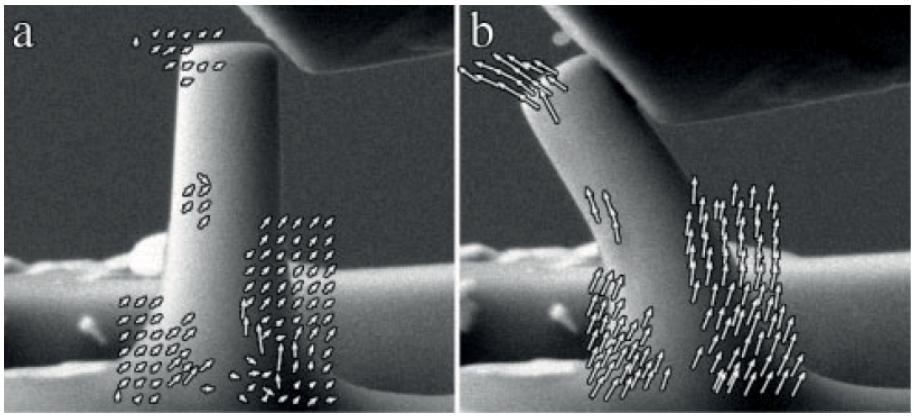

Figure 2.62: SEM images showing (a) the initial configuration and the inclined flat-tip punch, and (b) in situ bending of the pillar. Copyright (2010) Wiley. Used with publisher permission from (Clark *et. al.*, 2010. Size Independent Shape Memory Behavior of NiTi, Adv. Engng. Mat. 12: 808-815. Wiley).

peratures is reported as $A_f = 33^\circ C$. The other properties in compression can be calibrated by using a cyclic compressive test on the micropillar reported in [40]. These properties are obtained as follows (some of the properties are considered identical with the NiTi bulk material as given in the previous sections): $E^A = 55MPa$, $E^M = 50MPa$, $\nu^A = \nu^M = 0.3$, $\rho c^A = \rho c^M = 2.6 \times 10^6$ J/(m^{3}K), $H^t = 0.05$, $H^c = -0.03$, $(d\sigma/dT)_t^A = 11.4 \times 10^6$ J/(m^{3}K), $\rho \Delta s_0 = -H^t (d\sigma/dT)_t^A = -0.57 \times 10^6$ J/(m^{3}K), $A_f = 306K$, $A_s = 288K$, $M_f = 242K$, $M_s = 274K$. We use the $J_2 - I_1$-based model for analyzing this case study by setting $\hat{\eta} = \eta = \frac{1}{2}(H^t + |H^c|)$, and $\hat{\omega} = \omega = \frac{1}{2}(H^t - |H^c|)$. It is worth noting that for calibrating these properties, H_t, and $(d\sigma/dT)_t^A$ cannot be obtained only from the compression test; we have used an error and trial method for finding these properties for the best match in the theoretical and experimental results in bending as it will be discussed in the following. The material response in compression obtained from the experiments [40] and the present

model are compared in Figure 2.63 for two loading-unloading cycles with 3% and 5% axial strains[21]. The pillar is subjected to bending using an inclined indenter with the angle of

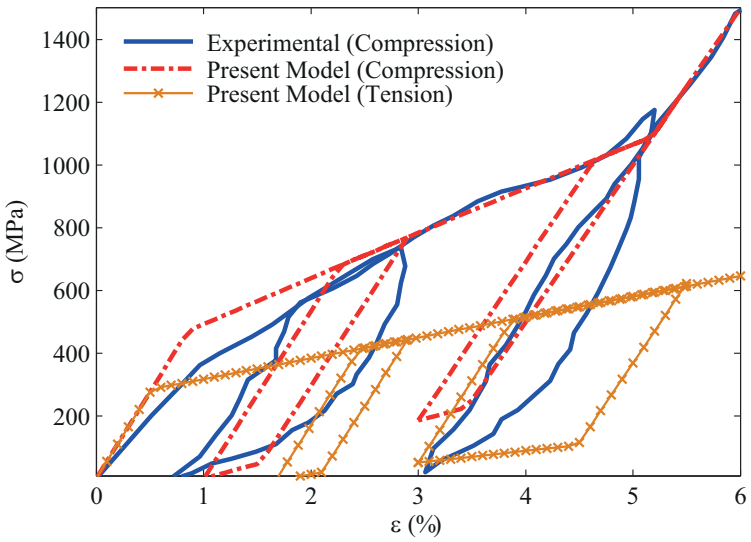

Figure 2.63: The compressive stress-strain response of [111] NiTi micro pillars obtained from experiments [40], and the compressive and tensile response obtained from the present model.

$\approx 60^\circ$ (see Figure 2.62). As mentioned in [40], the pillar slips on the indenter during loading and this releases the axial compressive load. It can be assumed that the pillar is subjected to a pure bending with the projection of force in the transverse direction[22]. The transverse force versus tip deflection obtained from the present formulation with the $J_2 - I_1$-based model is compared with the experimental results in Figure 2.64. As it is shown, the present model predicts the force-deflection in bending of the micropillar with a good accuracy. It is worth noting that the experiment contains loading further up to a tip deflection of near 1500 nm. However, as it is shown in Figure 2.64 for tip deflections larger than $\delta \approx 790$nm the force-deflection slope suddenly decreases (see Figure 2(e) in [40]). This is due to the

[21] In the compression response reported in [40], the initiation of loading was associated with a stress-strain plateau with a very small slope. It was assumed that the small Young modulus at the start of loading is due to the imperfect contact. We calibrated the austenite elastic modulus by ignoring the initial low elastic modulus in the response. This region is not shown in Figure 2.63 for the sake of clarity.

[22] The transverse force is $F = F_a \cos(60^\circ) = 0.5F_a$, where F_a is the actuation force reported in [40], and 60° represents the indenter angle (see Figure 1(b) in [40]).

start of plastic deformation of martensite that happens by further loading the material far beyond the completion of phase transformation. We are not considering the martensite plastic response in our model and restrict our comparison to the start of the plastic deformation. The dashed line in Figure 2.64 shows the model prediction for the unloading phase if the pillar was unloaded after the maximum tip deflection of $\delta \approx 790$nm. As it is shown, even by ignoring the plastic nonrecoverable response a residual deflection is observed in the model. This is due to the ambient temperature $T = 300$ K, which is slightly bellow A_f temperature. The present method can be used to calculate the stress distribution and the

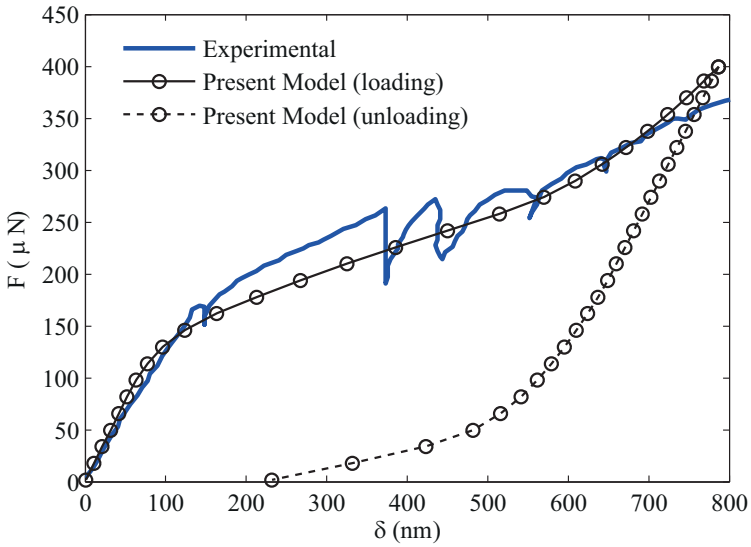

Figure 2.64: Comparison of the force-deflection response for micropillars obtained from experiments [40] and the present formulation.

intensity of phase transformation inside and at the surface of the micropillar (which are both extremely difficult to be measured experimentally). The martensitic volume fraction distribution, as a measure of the phase transformation intensity, is shown in Figure 2.65(a), and the stress distribution at the surface at the end of the loading phase is shown in Figure 2.65(b). As it is shown in Figure 2.65(b), the maximum stress at the surface is ≈ 2500 MPa. This is in agreement with our previous prediction of martensite plastic deformation start at this tip deflection. The reason is that the compression tests show the same stress for the start of martensite plastic deformation (see Figure 4 in [40]). Considering the fact

that the present model with the calibrated material properties is predicting the material response in both compression and bending with good accuracy, it can be concluded that the material properties in tension are also assumed accurately (these properties are guessed by considering the bending results for finding the best possible match). The predicted material response in tension for two loading-unloading cycles with 3% and 5% tensile strains is also shown in Figure 2.63. The predicted response in tension for this special geometry is valuable because it is practically very difficult to test a micropillar in tension. It is worth noting that there are several uncertainties in the experiment used in this section, including the non-uniform cross section of the pillar, the inclined indentor for bending, and the imperfect contact at the start of compressive loading that cause the observed error in the results. In order to obtain more accurate results, a specific experiment on a micropillar with uniform cross section subjected to bending with a sharp perpendicular indentor is required. Also, various length to thickness rations should be considered for studying the effect of shear deformation on the bending response of NiTi micropillars. However, as it will be shown in the following, the results of this section are in agreement with the theoretical expectations for single crystal NiTi shape memory alloys.

The predicted maximum transformation strains in tension and compression are in agreement with the response of [111] oriented NiTi single crystals. Considering the crystallographic data for 24 martensite correspondence variant pairs (CVPs) in NiTi (see Table 1 in [59]), and using the method described in detail by Gall and Sehitoglu [59], it can be shown that for a [111] oriented NiTi single crystal, CVP#2 with habit plane normal $\mathbf{n} = (-0.4044, -0.8889, -0.2152)$ and transformation direction $\mathbf{m} = (-0.4981, 0.4114, -0.7633)$ is the first CVP to satisfy the transformation criteria in tension, and the CVP#1 with habit plane normal $\mathbf{n} = (-0.8889, -0.4044, 0.2152)$ and transformation direction $\mathbf{m} = (0.4114, -0.4981, 0.7633)$ is the first CVP to satisfy the transformation criteria in compression. Using these directions and the magnitude of transformation $g = 0.13078$, the transformation strain for the kth variant is given by $\epsilon_{ij}^k = \frac{g}{2}(m_i^k n_j^k + m_j^k n_i^k)$ [59]. Calculating the transformation strain tensors for tension and compression with the given directions, the normal transformation strains in [111] direction are obtained as $\epsilon_t^t = 5.59\%$

and $\epsilon_c^t = 3.18\%$ in tension and compression, respectively. These transformation strains are in good agreement with the values obtained for $H_t = 5\%$ and $H_c = 3\%$ that represent the maximum transformation strains in our model. Using the transformation criteria for NiTi single crystals given in [59], the ratio of phase transformation start stresses in tension and compression is given by $|\hat{\sigma}_c|/\hat{\sigma}_t = \hat{\alpha}_t/|\hat{\alpha}_c|$, where $\hat{\sigma}$ is the critical stress at which phase transformation starts and $\hat{\alpha}$ is the normal component of the tensor $\boldsymbol{\alpha}$ on (111) plane with $\alpha_{ij} = \frac{1}{2}(m_i^k n_j^k + m_j^k n_i^k)$. This ratio is obtained as $|\hat{\sigma}_c|/\hat{\sigma}_t = 1.7578$ using the $\mathbf{m}$ and $\mathbf{n}$ directions given above, which is in agreement with the value predicted by our model $|\hat{\sigma}_c|/\hat{\sigma}_t = 477/275 = 1.7345$ (see Figure 2.63).

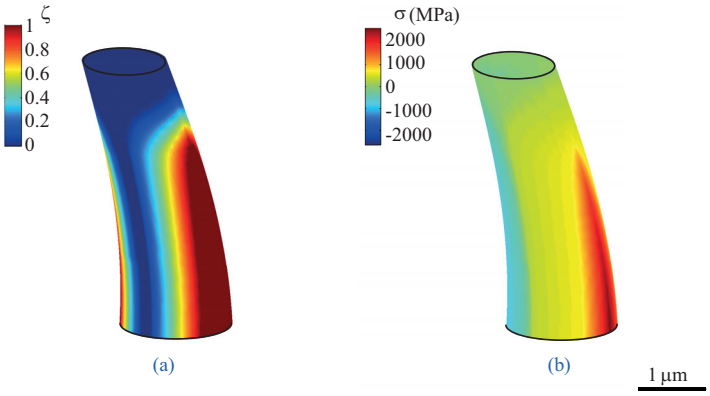

Figure 2.65: Distributions of (a) phase transformation intensity, and (b) stress at the surface of a micropillar subjected to bending obtained from the present closed-form solution.

CHAPTER III

THERMOMECHANICAL COUPLING IN THE RESPONSE OF SMAS

3.1 Introduction

In this chapter, a coupled thermomechanical framework considering the effect of generated (absorbed) latent heat during forward (reverse) phase transformation is presented for shape memory alloys. The governing equations are discretized for SMA bars and wires with circular cross sections by considering the non-uniform temperature distribution in the cross section. Appropriate convective boundary conditions are used for still and flowing air and also flowing water on slender and thick cylinders. The present formulation is capable of simulating the uniaxial thermomechanical response of SMA bars and wires by taking into account the effect of phase transformation-induced latent heat in various ambient conditions. In addition to the uniaxial case, the thermomechanical response of SMA bars subjected to pure torsion is also studied. The results of some experiments are used for evaluating the accuracy of the present formulation in modeling the rate dependency and temperature changes in uniaxial loading of SMA wires and bars. Several numerical examples are presented for studying the interaction between thermomechanical coupling, loading rate, ambient conditions, and size of the specimen in both uniaxial loading and pure torsion. It is shown that a loading being quasi static strongly depends on external conditions, e.g. the size and ambient conditions. Temperature distribution in the cross section is also studied for both loading cases and it is shown that the loading rate, ambient conditions, and size of the specimen affect the temperature distribution. The method of this section can be used for an accurate simulation of the material response of SMA devices in the presence of rate-dependency, size, and ambient condition effects. The present method can be exploited to analyze SMA bars with various cross sections. Our three-dimensional coupled-thermomechanical formulation can be used for studying other loadings, e.g. bending, and combined loadings.

3.2 The Rate-Dependent Coupled Thermomechanical Response of SMA Bars and Wires in Tension

In this section, the coupled thermomechanical response of shape memory alloy bars and wires in tension is studied. By using the Gibbs free energy as the thermodynamic potential and choosing appropriate internal state variables, a three-dimensional phenomenological macroscopic constitutive model for polycrystalline SMAs is derived. Taking into account the effect of generated (absorbed) latent heat during the forward (inverse) martensitic phase transformation, the local form of the first law of thermodynamics is used to obtain the energy balance relation. The three-dimensional coupled relations for the energy balance in the presence of the internal heat flux and the constitutive equations are reduced to a one-dimensional problem. An explicit finite difference scheme is used to discretize the governing initial-boundary-value problem of bars and wires with circular cross sections in tension. Considering several case studies for SMA wires and bars with different diameters, the effect of loading-unloading rate and different boundary conditions imposed by free and forced convections at the surface are studied. It is shown that the accuracy of assuming adiabatic or isothermal conditions in the tensile response of SMA bars strongly depends on the size and the ambient condition in addition to the rate-dependency that has been known in the literature. The data of some experimental tests are used for validating the numerical results of the present formulation in predicting the stress-strain and temperature distribution for SMA bars and wires subjected to axial loading-unloading.

3.2.1 Coupled thermomechanical governing equations for SMAs

For deriving the coupled thermomechanical governing equations for SMAs we start from the first law of thermodynamics in local form

$$\rho \dot{u} = \boldsymbol{\sigma} : \dot{\boldsymbol{\epsilon}} - \text{div } \boldsymbol{q} + \rho \hat{g}, \tag{3.1}$$

where ρ is mass density, u is the internal energy per unit mass, $\boldsymbol{\sigma}$ and $\boldsymbol{\epsilon}$ are the stress and strain tensors, respectively. The parameters $\boldsymbol{q}$ and $\hat{g}$ are the heat flux and internal heat generation. The dot symbol on a quantity ($\dot{}$) represents time derivative of the quantity.

The dissipation inequality reads

$$\rho\dot{s} + \frac{1}{T}\,\text{div}\,\boldsymbol{q} - \frac{\rho\hat{g}}{T} \geq 0, \tag{3.2}$$

where s is the entropy per unit mass. Substituting the Gibbs free energy

$$G = u - \frac{1}{\rho}\boldsymbol{\sigma} : \boldsymbol{\epsilon} - sT, \tag{3.3}$$

into the dissipation inequality, another form of the second law of thermodynamics is obtained as

$$-\rho\dot{G} - \dot{\boldsymbol{\sigma}} : \boldsymbol{\epsilon} - \rho s\dot{T} \geq 0. \tag{3.4}$$

Note that

$$\dot{G} = \frac{\partial G}{\partial \boldsymbol{\sigma}} : \dot{\boldsymbol{\sigma}} + \frac{\partial G}{\partial T}\dot{T} + \frac{\partial G}{\partial \boldsymbol{\chi}} : \dot{\boldsymbol{\chi}}, \tag{3.5}$$

where $\boldsymbol{\chi}$ is the set of internal state variables. Substituting (3.5) into (3.4) gives

$$-\left(\rho\frac{\partial G}{\partial \boldsymbol{\sigma}} + \boldsymbol{\epsilon}\right) : \dot{\boldsymbol{\sigma}} - \rho\left(\frac{\partial G}{\partial T} + s\right)\dot{T} - \rho\frac{\partial G}{\partial \boldsymbol{\chi}} : \dot{\boldsymbol{\chi}} \geq 0. \tag{3.6}$$

Assuming the existence of a thermodynamic process in which $\dot{\boldsymbol{\chi}} = 0$ and noting that (3.6) is valid for all $\dot{\boldsymbol{\sigma}}$ and $\dot{T}$ [162], the following constitutive equations are obtained

$$-\rho\frac{\partial G}{\partial \boldsymbol{\sigma}} = \boldsymbol{\epsilon}, \quad -\frac{\partial G}{\partial T} = s. \tag{3.7}$$

The constitutive relations (3.7) are valid everywhere at the boundary of the thermodynamic region as well [163]. Substituting (3.7) into (3.6), the dissipation inequality is expressed in a reduced form as

$$-\rho\frac{\partial G}{\partial \boldsymbol{\chi}} : \dot{\boldsymbol{\chi}} \geq 0. \tag{3.8}$$

In the present study, we consider the transformation strain $\boldsymbol{\epsilon}^t$ and the martensitic volume fraction ξ as the internal state variables[1]. The Gibbs free energy G for polycrystalline SMAs is given in (2.1). Another form of the first law of thermodynamics is obtained by

[1]The portion of strain that is recovered due to reverse phase transformation from detwinned martensite to austenite is considered as the transformation strain. See Patoor et al. [152] for a detailed description of the transformation strain and martensitic volume fraction.

substituting (3.7) and (3.5) into (3.1) and considering the set of internal state variables as $\boldsymbol{\chi} = \{\boldsymbol{\epsilon}^t, \xi\}$. This form is given by

$$\rho T \dot{s} = \rho \frac{\partial G}{\partial \boldsymbol{\epsilon}^t} : \dot{\boldsymbol{\epsilon}}^t + \rho \frac{\partial G}{\partial \xi} \dot{\xi} - \text{div}\boldsymbol{q} + \rho \hat{g}. \tag{3.9}$$

The constitutive relation $(3.7)_2$ is used for calculating the time derivative of the specific entropy as

$$\dot{s} = -\frac{\partial \dot{G}}{\partial T} = -\frac{\partial^2 G}{\partial \boldsymbol{\sigma} \partial T} : \dot{\boldsymbol{\sigma}} - \frac{\partial^2 G}{\partial T^2} \dot{T} - \frac{\partial^2 G}{\partial \boldsymbol{\epsilon}^t \partial T} : \dot{\boldsymbol{\epsilon}}^t - \frac{\partial^2 G}{\partial \xi \partial T} \dot{\xi}. \tag{3.10}$$

Substituting (2.1) into (3.10), the third term on the right hand side of (3.10) is zero and the rate of change of specific entropy is given by

$$\dot{s} = \frac{1}{\rho} \boldsymbol{\alpha} : \dot{\boldsymbol{\sigma}} + \frac{c}{T} \dot{T} + \left[\frac{1}{\rho} \Delta \boldsymbol{\alpha} : \boldsymbol{\sigma} - \Delta c \ln \left(\frac{T}{T_0} \right) + \Delta s_0 \right] \dot{\xi}. \tag{3.11}$$

Before substituting (3.11) into (3.9) for obtaining the final form of the first law, it is necessary to introduce a relation between the evolution of the selected internal state variables. By ignoring the martensitic variant reorientation effect, it can be assumed that any change in the state of the system is only possible by a change in the internal state variable ξ. The time derivative of the transformation strain tensor is related to the time derivative of the martensitic volume fraction as the flow rule $\dot{\boldsymbol{\epsilon}}^t = \boldsymbol{\Gamma} \dot{\xi}$. Substituting this flow rule into the first term in the right hand side of (3.9) and considering the Gibbs free energy in (2.1), the thermodynamic force conjugated to the martenstic volume fraction is calculated as

$$\rho \frac{\partial G}{\partial \boldsymbol{\epsilon}^t} : \dot{\boldsymbol{\epsilon}}^t + \rho \frac{\partial G}{\partial \xi} \dot{\xi} = \left(-\boldsymbol{\sigma} : \boldsymbol{\Gamma} + \rho \frac{\partial G}{\partial \xi} \right) \dot{\xi} = -\pi \dot{\xi}, \tag{3.12}$$

where π is given in (2.9). Introducing this new term (π) will remarkably simplify writing the constitutive and thermomechanical relations. Also, the second law of thermodynamics (3.8) can be written as $\pi \dot{\xi} \geq 0$. Substituting (3.12) and (3.11) into (3.9), the final form of the first law is obtained as

$$T \boldsymbol{\alpha} : \dot{\boldsymbol{\sigma}} + \rho c \dot{T} + \left[-\pi + T \Delta \boldsymbol{\alpha} : \boldsymbol{\sigma} - \rho \Delta c \; T \ln \left(\frac{T}{T_0} \right) + \rho \Delta s_0 T \right] \dot{\xi} = -\text{div}\boldsymbol{q} + \rho \hat{g}. \tag{3.13}$$

Let us now introduce the conditions that control the onset of forward and reverse phase transformations. Considering the dissipation inequality (3.8) as $\pi \dot{\xi} \geq 0$, a transformation function is obtained as expressed in (2.10).

The consistency during phase transformation guaranteeing the stress and temperature states to remain on the transformation surface is given by [162, 169]

$$\dot{\Phi} = \frac{\partial \Phi}{\partial \boldsymbol{\sigma}} : \dot{\boldsymbol{\sigma}} + \frac{\partial \Phi}{\partial T}\dot{T} + \frac{\partial \Phi}{\partial \xi} : \dot{\xi} = 0. \tag{3.14}$$

Substituting (2.9) and (2.10) into (3.14) and rearranging gives the following expression for the martensitic volume fraction rate

$$\dot{\xi} = -\frac{(\boldsymbol{\Gamma} + \Delta \mathbb{S} : \boldsymbol{\sigma}) : \dot{\boldsymbol{\sigma}} + \rho \Delta s_0 \dot{T}}{\mathscr{D}^{\pm}}, \tag{3.15}$$

where $\mathscr{D}^{+} = \rho \Delta s_0 (M_s - M_f)$ for the forward phase transformation ($\dot{\xi} > 0$) and $\mathscr{D}^{-} = \rho \Delta s_0 (A_s - A_f)$ for reverse phase transformation ($\dot{\xi} < 0$). The parameters A_s, A_f, M_s, M_f represent the austenite and martensite start and finish temperatures, respectively. Substituting (3.15) into (3.13) and assuming $\Delta\alpha = \Delta c = 0$ – valid for almost all practical SMA alloys – the following expression is obtained

$$[T\boldsymbol{\alpha} - \mathscr{F}_1(\boldsymbol{\sigma}, T)] : \dot{\boldsymbol{\sigma}} + [\rho c - \mathscr{F}_2(T)]\, \dot{T} = -\mathrm{div}\boldsymbol{q} + \rho \hat{g}, \tag{3.16}$$

where

$$\mathscr{F}_1(\boldsymbol{\sigma}, T) = \frac{1}{\mathscr{D}^{\pm}}(\boldsymbol{\Gamma} + \Delta \mathbb{S} : \boldsymbol{\sigma})(\mp Y + \rho \Delta s_0 T), \quad \mathscr{F}_2(T) = \frac{\rho \Delta s_0}{\mathscr{D}^{\pm}}(\mp Y + \rho \Delta s_0 T). \tag{3.17}$$

In (3.17) (+) is used for forward phase transformation and (-) is used for the reverse transformation. Equation (3.16) is one of the two coupled relations for describing the thermomechanical response of SMAs. The second relation is the constitutive equation obtained by substituting (2.1) into $(3.7)_1$ as (2.4)

3.2.2 Coupled thermomechanical relations in uniaxial tension

In this section we consider the uniaxial loading of a bar with circular cross section. Considering the cross section in the (r, θ)-plane and the bar axis along the z-axis, the only nonzero stress component is σ_z. Using $(2.6)_1$, the transformation tensor during loading (forward phase transformation) is written as

$$\boldsymbol{\Gamma}^{+} = H\ \mathrm{sgn}(\sigma_z) \begin{bmatrix} -0.5 & 0 & 0 \\ 0 & -0.5 & 0 \\ 0 & 0 & 1 \end{bmatrix}, \tag{3.18}$$

where sgn(.) is the sign function. Substituting (3.18) into (2.5) it is seen that if we denote the transformation strain along the bar axis by ϵ_z^t, the transformation strain components in the cross section are $\epsilon_r^t = \epsilon_\theta^t = -0.5\epsilon_z^t$ and the other components are zero during loading. This is equivalent to assuming that the phase transformation is an isochoric (constant-volume) process. Considering the same assumption (isochoric deformation due to phase transformation), the transformation tensor during reverse phase transformation is obtained as

$$\mathbf{\Gamma}^- = H\ \mathrm{sgn}(\epsilon_z^{tr}) \begin{bmatrix} -0.5 & 0 & 0 \\ 0 & -0.5 & 0 \\ 0 & 0 & 1 \end{bmatrix}. \tag{3.19}$$

Substituting (3.19) into (2.9) and (2.10) and using given relations between the constitutive model parameters in (2.14) the following explicit expressions for the martensitic volume fractions in direct and inverse phase transformation in the case of uniaxial loading are obtained:

$$\xi^+ = \frac{1}{\rho b^M} \left\{ H|\sigma_z| + \frac{1}{2}\sigma_z^2 \Delta S_{33} + \rho \Delta s_0 (T - M_s) \right\}, \tag{3.20}$$

$$\xi^- = \frac{1}{\rho b^A} \left\{ H\sigma_z\, \mathrm{sgn}(\epsilon_z^{tr}) + \frac{1}{2}\sigma_z^2 \Delta S_{33} + \rho \Delta s_0 (T - A_f) \right\}. \tag{3.21}$$

As the first step, we consider loading of a bar in tension ($\sigma_z \geq 0$). In this special case, substituting (3.18) into (2.5) and integrating the flow rule gives an explicit expression for transformation strain as $\epsilon_z^t = H\xi$, which after substitution into (2.4) gives the following one-dimensional constitutive equation

$$\epsilon_z = (S_{33}^A + \xi \Delta S_{33})\sigma_z + \alpha_A (T - T_0) + H\xi, \tag{3.22}$$

where $S_{33}^A = 1/E_A,\ \Delta S_{33} = 1/E_M - 1/E_A$ (E_A and E_M are the elastic muduli of austenite and martensite, respectively). Substituting the martensitic volume fraction (3.20) into (3.22), the stress-strain relation can be written as the following cubic equation

$$\sigma_z^3 + a\ \sigma_z^2 + (m\ T + n)\sigma_z + (p\ T + q) = 0, \tag{3.23}$$

where a, m, n, p, and q are constants given by

$$a = \frac{3H}{\Delta S_{33}}, \quad m = \frac{2\rho\Delta s_0}{\Delta S_{33}}, \quad n = -\frac{2\rho\Delta s_0 M_s}{\Delta S_{33}} + \frac{2H^2 + 2\rho b^M S^A_{33}}{\Delta S^2_{33}},$$
$$p = \frac{2H\rho\Delta s_0 + 2\rho b^M \alpha_A}{\Delta S^2_{33}}, \quad q = \frac{-2H\rho\Delta s_0 M_s - 2\rho b^M(\alpha_A T_0 + \epsilon_z)}{\Delta S^2_{33}}. \tag{3.24}$$

The cubic equation (3.23) is solved for σ_z as a function of temperature and strain. The constitutive equation obtained from solving (3.23) is coupled with (3.16). The set of coupled thermomechanical equations to be solved in the uniaxial loading a bar with circular cross section is given by (the cross section is considered in the (r, θ)-plane and the internal heat generation due to any source other than the phase transformation is ignored):

$$\begin{cases} \left[\alpha^A\ T - \tilde{\mathscr{F}}_1(\sigma_z, T)\right]\dot{\sigma_z} + \left[\rho c - \tilde{\mathscr{F}}_2(T)\right]\dot{T} = k\left(\frac{\partial^2 T}{\partial r^2} + \frac{1}{r}\frac{\partial T}{\partial r}\right), \\ \\ \sigma_z = \frac{1}{6}\mathscr{G}(T) - \frac{2mT + (2n - 2a^2/3)}{\mathscr{G}(T)} - \frac{a}{3}, \end{cases} \tag{3.25}$$

where

$$\tilde{\mathscr{F}}_1(\sigma_z, T) = \frac{1}{\mathscr{D}^{\pm}}(H + \Delta S_{33}\sigma_z)(\mp Y + \rho\Delta s_0 T), \quad \tilde{\mathscr{F}}_2(T) = \frac{\rho\Delta s_0}{\mathscr{D}^{\pm}}(\mp Y + \rho\Delta s_0 T),$$
$$\mathscr{G}(T) = \left[f_1 T + f_0 + 12\sqrt{g_3 T^3 + g_2 T^2 + g_1 T + g_0}\right]^{1/3}. \tag{3.26}$$

The coefficients f_i and g_i are constants given by

$$f_1 = 36ma - 108p, \ f_0 = 36na - 108q - 8a^3, \ g_3 = 12m^3,$$
$$g_2 = -54amp - 3a^2m^2 + 36m^2n + 81p^2,$$
$$g_1 = 12a^3p - 54amq - 6a^2mn + 36mn^2 + 162pq - 54anp,$$
$$g_0 = 81q^2 + 12a^3q + 12n^3 - 3a^2n^2 - 54anq. \tag{3.27}$$

In $(3.25)_1$, k is the thermal conductivity and Fourier's law of thermal conduction ($\boldsymbol{q} = -k\boldsymbol{\nabla}T$) is used for deriving the right hand side.

As it is shown, both temperature and stress fields are functions of time and radius r. As initial conditions for (3.25) one prescribes stress and temperature distributions at $t = 0$:

$$T(r, 0) = \hat{T}, \ \sigma_z(r, 0) = \hat{\sigma_z}. \tag{3.28}$$

As boundary conditions, temperature or heat convection on the outer surface can be given

$$\text{Convection}: \qquad k\frac{\partial T(r,t)}{\partial r}\Big|_{r=R} = h_\infty[T_\infty - T(R,t)] \tag{3.29}$$

$$\text{Constant Temperature}: \qquad T(R,t) = T_1, \tag{3.30}$$

where h_∞ is the heat convection coefficient and T_∞ is the ambient temperature. R is the bar radius and T_1 is the constant temperature of the free surface. Another condition is obtained at the center of bar using the axi-symmetry of temperature distribution in the cross section as

$$\frac{\partial T(r,t)}{\partial r}\Big|_{r=0} = 0. \tag{3.31}$$

The coupled differential equations (3.25) with the initial and boundary conditions (3.28), (3.29), and (3.31) constitute the initial-boundary value problem governing an SMA bar (wire) in uniaxial tension.

3.2.3 Finite difference discretization of the thermomechanical governing equations

A finite difference method is used for solving the coupled thermomechanical governing equations (3.25) with boundary conditions given in (3.29) and (3.31), and the initial conditions (3.28). For discretizing (3.25) we use an explicit finite difference method because we are dealing with two coupled highly nonlinear equations; solving such equations is computationally very expensive using implicit schemes. The radius of the bar is divided into $M-1$ equal segments of size Δr as shown in Figure 3.1.

The derivatives on the right hand side of $(3.25)_1$ are discretized using a central difference scheme as

$$\begin{aligned}\frac{\partial^2 T}{\partial r^2} + \frac{1}{r}\frac{\partial T}{\partial r} &= \frac{1}{r}\frac{\partial}{\partial r}\left(r\frac{\partial T}{\partial r}\right)\\ &= \frac{1}{r_i}\frac{(r\partial T\partial r)^n_{i+1/2} - (r\partial T\partial r)^n_{i-1/2}}{\Delta r}\\ &= \left(r_i + \frac{\Delta r}{2}\right)\frac{T^n_{i+1} - T^n_i}{r_i(\Delta r)^2} - \left(r_i - \frac{\Delta r}{2}\right)\frac{T^n_i - T^n_{i-1}}{r_i(\Delta r)^2},\end{aligned} \tag{3.32}$$

where the subscript i denotes the node number (see Figure 3.1) and the superscript n refers to the nth time increment. In explicit schemes, the first-order forward difference

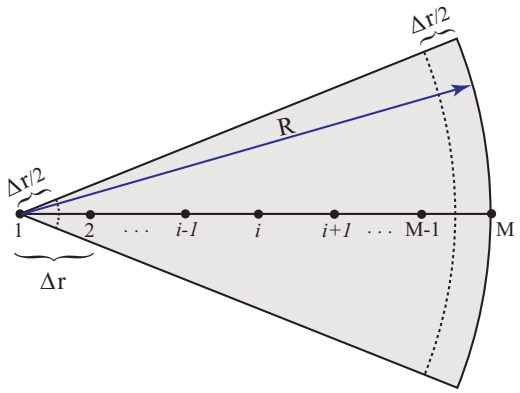

Figure 3.1: Internal and boundary nodes in the cross section for the finite difference discretization. The dashed lines are the boundaries of the control volumes attached to the central and boundary nodes used for deriving the finite difference form of the boundary conditions.

is used for approximating the time derivatives. The finite difference form of the coupled thermomechanical equations (3.25) using the explicit method is given by

$$\left[\alpha^A\, T_i^n - \frac{1}{\mathscr{D}^{\pm}}(H + \Delta S_{33}\sigma_{z,i}^n)(\mp Y + \rho\Delta s_0 T_i^n)\right]\frac{\sigma_{z,i}^{n+1} - \sigma_{z,i}^n}{\Delta t} + \left[\rho c - \frac{\rho\Delta s_0}{\mathscr{D}^{\pm}}(\mp Y + \rho\Delta s_0 T_i^n)\right]\frac{T_i^{n+1} - T_i^n}{\Delta t} = \left(r_i + \frac{\Delta r}{2}\right)\frac{T_{i+1}^n - T_i^n}{r_i(\Delta r)^2} - \left(r_i - \frac{\Delta r}{2}\right)\frac{T_i^n - T_{i-1}^n}{r_i(\Delta r)^2}, \tag{3.33}$$

$$\sigma_{z,i}^{n+1} = \frac{1}{6}\mathscr{G}(T_i^{n+1}) - \frac{2mT_i^{n+1} + (2n - 2a^2/3)}{\mathscr{G}(T_i^{n+1})} - \frac{a}{3}, \tag{3.34}$$

where $\sigma_{z,i}^n$ is the axial stress in the ith node at the nth time increment. For calculating the finite difference approximation of the boundary conditions for our problem that includes internal heat generation, energy balance for a control volume[2] should be considered. For the central node $i = 1$, consider a control volume with radius $\Delta r/2$ as shown in Figure 3.1. The finite difference approximation of the boundary condition in the central node is given by [141]

$$k\,\frac{T_2^n - T_1^n}{2} + \frac{1}{8}(\Delta r)^2\,\Re_1^n = \frac{1}{8}(\Delta r)^2\rho c\frac{T_1^{n+1} - T_1^n}{\Delta t}, \tag{3.35}$$

[2]To obtain the governing equations for the central and boundary nodes, a volume attached to these nodes (e.g. a region with width $\Delta r/2$ as shown in Figure 1) is considered and the energy balance is written for this control volume.

and for the outer node with the convection boundary condition, considering a control volume attached to the outer radius like that shown in Figure 3.1 with the dashed line, the energy balance gives

$$Rh_{\infty}(T_{\infty}-T_M^n)+k\left(R-\frac{\Delta r}{2}\right)\frac{T_{M-1}^n-T_M^n}{\Delta r}+\left[\frac{R\Delta r}{2}-\frac{(\Delta r)^2}{4}\right]\Re_M^n=\left[\frac{R\Delta r}{2}-\frac{(\Delta r)^2}{4}\right]\rho c\frac{T_M^{n+1}-T_M^n}{\Delta t}, \tag{3.36}$$

where the parameters $\Re_1^n$ and $\Re_M^n$ are the equivalent internal heat generation due to phase transformation calculated at the central ($i=1$) and outer ($i=M$) nodes. For calculating the equivalent internal heat generation, consider the diffusion equation in cylindrical coordinates for a transient problem with internal heat generation $\hat{g}$ as [11]

$$k\left(\frac{\partial^2 T}{\partial r^2}+\frac{1}{r}\frac{\partial T}{\partial r}\right)+\hat{g}=\rho c\frac{\partial T}{\partial t}. \tag{3.37}$$

Comparing $(3.25)_1$ with (3.37), we define an equivalent internal heat generation corresponding to the ith node as

$$\begin{aligned}\Re_i^n &= \left[\alpha^A\ T_i^n-\frac{1}{\mathscr{D}^{\pm}}(H+\Delta S_{33}\sigma_{z,i}^n)(\mp Y+\rho\Delta s_0 T_i^n)\right]\frac{\sigma_{z,i}^{n+1}-\sigma_{z,i}^n}{\Delta t}\\ &+ \left[-\frac{\rho\Delta s_0}{\mathscr{D}^{\pm}}(\mp Y+\rho\Delta s_0 T_i^n)\right]\frac{T_i^{n+1}-T_i^n}{\Delta t},\end{aligned} \tag{3.38}$$

where $\sigma_{z,i}^{n+1}$ is given in (3.34).

Considering the fact that at the nth loading increment stress and temperatures are known (these parameters are known from the initial condition (3.28) in the first time increment), for any of the nodes except the central and outer nodes, substituting (3.34) into (3.33) in the nth increment a nonlinear algebraic equation is obtained with only one unknown $T_i^{n+1}, i=2...M-1$. This equation is solved numerically [55] and the temperature at the (n+1)th time increment is calculated. Substituting the calculated temperature into (3.34) gives the stress for (n+1)th increment. For the central and outer nodes, a similar procedure is used considering (3.34), (3.35), (3.36), and (3.38).

3.2.4 Convection boundary conditions

In most practical applications, SMA devices are surrounded by air during loading-unloading. In cases in which the device is working in conditions with negligible air flow, a free convection

occurs around the device due to temperature changes caused by phase transformation. For all the outdoor structural applications of SMAs, the device is exposed to airflow and a forced convection boundary condition should be considered. For studying the effect of ambient on the thermomechanical response of SMAs, both free and forced convection boundary conditions are considered in this chapter and the convection coefficient is calculated by considering a vertical[3] SMA bar or wire in still or flowing air with different velocities.

3.2.4.1 Free convection for SMA Bars in still air

When airflow speed is negligible, a free convection boundary condition should be considered around the SMA device. Considering an SMA vertical cylinder in still air, it is shown by Cebeci [33] that the cylinder is thick enough to be considered a flat plate in calculating the convection coefficient with less than 5.5% error if $\mathsf{Gr}_L^{0.25} D/L \geq 35$, where $\mathsf{Gr}_x = g\beta(T_w - T_\infty)x^3/\upsilon^2$ is the Grashof number, $D = 2R$ is the cylinder diameter, g is the gravitational acceleration, β is the volume coefficient of expansion, i.e. $\beta = 1/T$ for ideal gasses, T_w is the wall temperature, T_∞ is the ambient temperature, υ is the kinematic viscosity of air, and x is a characteristic dimension, e.g. height or diameter of the cylinder. The Nusselt number for a flat plate with height L is given by [75, 159]

$$\mathsf{Nu}_{\mathrm{FP}} = 0.68 + \frac{0.67\ \mathsf{Ra}_L^{0.25}}{[1 + (0.49\ \mathsf{Pr})^{0.56}]^{0.44}}, \tag{3.39}$$

where $\mathsf{Ra}_L = \mathsf{Gr}_L\mathsf{Pr}$ is the Rayleigh number and Pr is the Prandtl number for air in the ambient temperature. Having the Nusselt number, the free convection coefficient for the cylinder is calculated by $\mathsf{Nu} = h_\infty x/k$, where x is the characteristic length (the height of cylinder in this case) and k is the air thermal conductivity at the ambient temperature. For studying slender cylinders with $\mathsf{Gr}_L^{0.25} D/L \leq 35$ or for avoiding the error in the case of considering thick cylinders, the following correction can be used [159]

$$\frac{\mathsf{Nu}_c}{\mathsf{Nu}_{\mathrm{FP}}} = 1 + 0.30\left[\sqrt{32}\ \mathsf{Gr}_L^{-0.25}\left(\frac{L}{D}\right)\right]^{0.91}. \tag{3.40}$$

The free convection coefficient around the cylinder is calculated by substituting (3.39) into (3.40) and using $\mathsf{Nu}_c = h_\infty L/k$.

[3] In forced convection, a vertical bar is perpendicular to the air flow. In free convection, the gravitational acceleration is parallel to the axis of a vertical bar.

3.2.4.2 Forced convection for SMAs in air and fluid flow

For calculating the average convection heat transfer coefficients for the flowing air across a cylinder, the experimental results presented by Hilpert [74] are used. The Nusselt number in this case can be calculated by [75]

$$\mathsf{Nu} = C\ \mathsf{Re}^{n}\ \mathsf{Pr}^{0.33}, \tag{3.41}$$

where $\mathsf{Re} = u_\infty D/\upsilon$ is Reynolds number and u_∞ is the airflow speed. The parameters C and n are tabulated in heat transfer books for different Reynolds numbers (*e.g.* see Chapter 6, Holman [75]). Note that the characteristic length in Nusselt number for this case is the cylinder diameter and forced convection coefficient is calculated using $\mathsf{Nu} = h_\infty D/k$. Experimental results presented by Knudsen and Katz [89] shows that (3.41) can be used for cylinders in fluids too. However, Fand [50] has shown that for fluid flow on cylinders, when $10^{-1} < \mathsf{Re} < 10^{5}$, the following relation gives a more accurate Nusselt number

$$\mathsf{Nu} = (0.35 + 0.56\ \mathsf{Re}^{0.52})\mathsf{Pr}^{0.3}. \tag{3.42}$$

3.2.5 Verification using experimental results

In order to verify our formulation for simulating the rate-dependent response of SMA bars and wires in simple tension, the experimental data previously reported by the second author [16] is used. The experiments were carried out using a commercial NiTi wire with circular cross section of radius $R = 0.5mm$. Since the alloy composition was unknown, simple tension tests were performed [16] and some basic material properties including the elastic moduli of austenite and martensite, the maximum transformation strain and the stress levels at the start and end of phase transformation process during loading and unloading were reported. These reported properties and the experimental results are used for calibrating the constants needed in the present constitutive equations. The material properties suitable for the constitutive relations of the present study are given in Table 3.1 as Material I.

In the experiments two different loading-unloading rates were considered. In the quasi-static test the total loading-unloading time is set to $\tau = 1000$ sec and the dynamic test was performed in $\tau = 1$ sec. Both tests were performed in the ambient temperature $T_\infty = 293K$.

Table 3.1: SMA material parameters for studying thermomechanical coupling

Material constants	Material I, [16]	Material II, [124]	Material III, [44]	A generic SMA (Material IV), [92]
E^A	31.0×10^9Pa	34.0×10^9Pa	34.0×10^9Pa	55.0×10^9Pa
E^M	24.6×10^9Pa	31.0×10^9Pa	31.0×10^9Pa	46.0×10^9Pa
$\nu^A = \nu^M$	0.3	0.33	0.33	0.33
α^A	22.0×10^{-6}/K	22.0×10^{-6}/K	22.0×10^{-6}/K	22.0×10^{-6}/K
α^{M}	22.0×10^{-6}/K	22.0×10^{-6}/K	22.0×10^{-6}/K	22.0×10^{-6}/K
ρc^A	3.9×10^6 J/(m^{3}K)	5.8×10^6 J/(m^{3}K)	5.8×10^6 J/(m^{3}K)	2.6×10^6 J/(m^{3}K)
ρc^M	3.9×10^6 J/(m^{3}K)	5.8×10^6 J/(m^{3}K)	5.8×10^6 J/(m^{3}K)	2.6×10^6 J/(m^{3}K)
k	18W/(mK)	18W/(mK)	18W/(mK)	18W/(mK)
H	0.041	0.036	0.038	0.056
$\rho\Delta s_0$	-0.52×10^6J/(m^{3}K)	-0.16×10^6J/(m^{3}K)	-0.29×10^6J/(m^{3}K)	-0.41×10^6J/(m^{3}K)
A_f	291.0 K	257.8 K	270.0 K	280.0 K
A_s	276.0 K	239.1 K	263.0 K	270.0 K
M_s	265.0 K	233.1 K	253.1 K	245.0 K
M_f	250.0 K	216.1 K	245.1 K	230.0 K

The experimental results for these two tests are depicted in Figure 3.3. In order to calculate the free convection coefficient, the method of the previous section for slender cylinders is used. The length of the wire is $L = 20cm$ and the properties of air at $T = 293K$ are extracted from standard tables [75]. The free convection coefficient is a function of the temperature difference between the wire and ambient $T_w - T_\infty$. Since T_w is unknown, it is difficult to satisfy the exact free convection boundary condition. But as it is depicted in Figure 3.2 (Case I), the free convection coefficient is almost constant for the range of temperature difference $0 < T_w - T_\infty < 40$. We will show in the sequel that this temperature difference range matches the maximum temperature difference that is observed in an adiabatic loading-unloading for a vast range of SMA bar geometries, material properties, and ambient conditions. Therefore, an average value of $h_\infty = 21\ W/m^2K$ is considered during the loading-unloading process in this case. In the following case studies a similar analysis will be carried out for finding an average free convection coefficient.

The stress-strain response for quasi static and dynamic loading-unloading obtained by the present coupled thermomechanical formulation is compared with the experimental results in Figure 3.3. As it is seen, the analytical formulation predicts both the change of

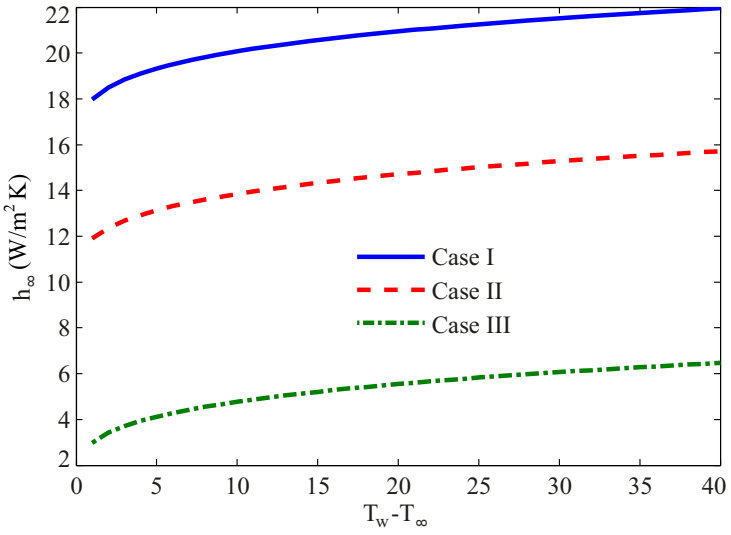

Figure 3.2: The free convection coefficient as a function of temperature difference calculated for a vertical SMA cylinder with (Case I): $d = 1mm,\ L = 20cm$ in still air with $T = 293K$, (Case II): $d = 2mm,\ L = 10cm$ in still air with $T = 328K$, and (Case III): $d = 5cm,\ L = 10cm$ in still air with $T = 328K$.

slope and change of hysteretic area in different loading-unloading rates. It is worth noting that the experimental loading-unloading curves in Figure 3.3 are stabilized cycles after a few initial cycles and a minor accumulated strain is observed at the beginning of loading that is ignored in the analytic results. In these experiments, the SMA temperature was not monitored. We will present a detailed study of the effect of ambient conditions and SMA bar geometry on the thermomechanical response of SMA bars with circular cross sections in uniaxial loading in the sequel. However, in order to validate the present formulation for simulating the thermomechanical response of SMAs, another experimental test is considered in this section.

The next experiment was performed by the second author on an SMA bar and the stress-strain response is reported in McCormick et al. [124]. In addition to the mechanical response, a pyrometer was used for monitoring the surface temperature of the SMA bar during loading-unloading. The specimen is made from a solid stock with a 12.7mm diameter. The specimen is subjected to a loading protocol with 20 cycles to 6% strain using a 250 kN hydraulic

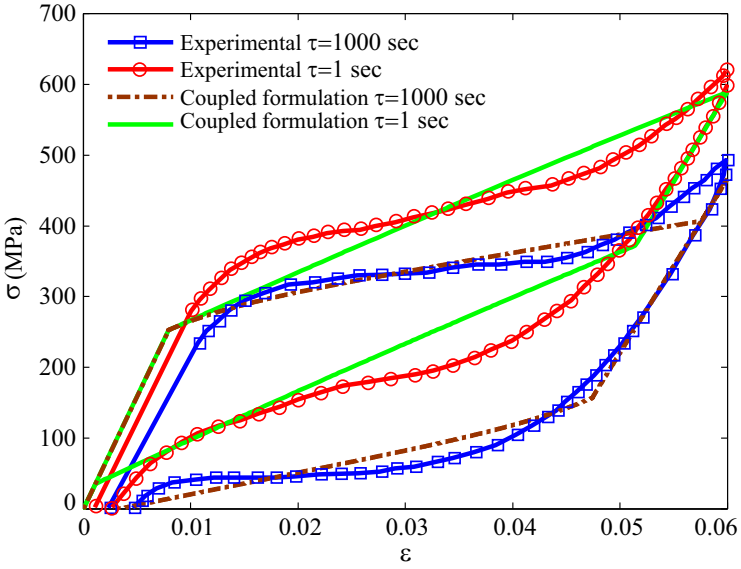

Figure 3.3: Comparison of the experimental and analytical results for the stress-strain response of an SMA wire (Material I) with $d = 1mm$ in quasi-static and dynamic loadings (τ is the total loading-unloading time).

uniaxial testing apparatus. During the initial loading-unloading cycles accumulated strain is observed but for the last five cycles the material stress-strain response is stabilized. Here we consider the $20th$ stabilized loading-unloading cycle by setting the strain at the beginning of this cycle to zero (an accumulated strain of $\epsilon = 0.0057$ is observed at the beginning of the last cycle). Some of the material properties of the NiTi alloy for this bar are presented in [186] and the remaining parameters are calibrated using the stress and strain values corresponding to start and completion of phase transformation in the stress-strain response of the bar in uniaxial loading-unloading.

These material properties are given in Table 3.1 as Material II. The initial temperature of the bar at the beginning of the last cycle is $\hat{T} = 304.6$K and the ambient temperature is $T_\infty = 301$K. The average free convection coefficient for the bar in this test is obtained using the method of the previous example and it is calculated as $h_\infty = 7.5\ W/m^2K$. The total loading-unloading time is $\tau = 114$ sec. The calculated temperature at the surface of the bar using the present formulation is compared with the experimental results in Figure

3.4(a). The experimental stress-strain response for the stabilized cycle is compared with the analytical results in 3.4(b). It is worth noting that the monitored temperature in the experimental data fluctuates and the smooth function in Matlab that uses a moving average filter is used to smoothen the data. As it is seen, the present formulation predicts the thermomechanical response of the bar with an acceptable accuracy.

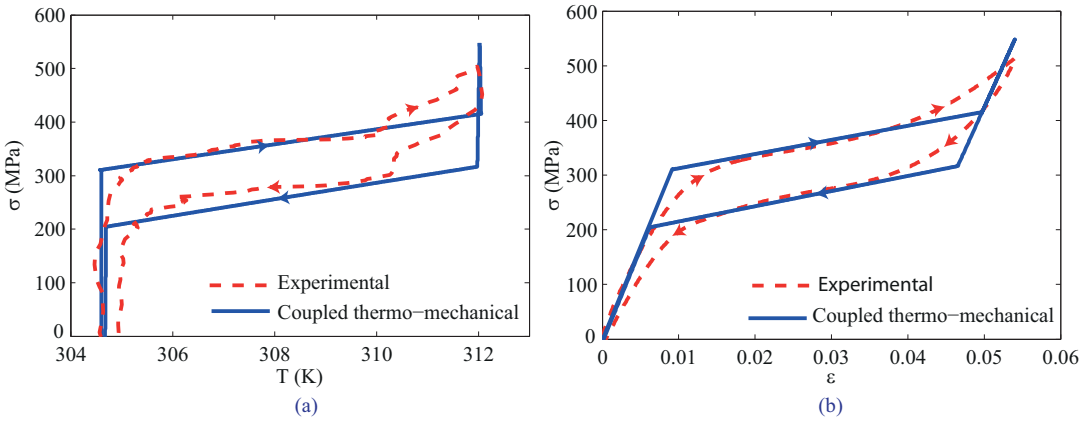

Figure 3.4: Comparison of the experimental and analytical results for (a) stress-temperature at the surface, and (b) the stress-strain response of an SMA bar (Material II) with $d = 12.7mm$ in quasi-static loading-unloading ($\tau = 114$ sec).

As another case study, the experimental results of the cyclic loading of an SMA bar with 7.1mm diameter is considered. The experiment was performed by the second author and the stress-strain response of the bar in this test is reported in DesRoches and Smith [44]. In this section we are considering the monitored surface temperature of the bar in addition to the stress-strain response. This bar is made of NiTi alloy with the material properties given in Table **??** as Material III (some of these properties are given by the material provider and the others are calibrated using the uniaxial test results). The initial temperature of the bar and the ambient temperature are $\hat{T} = T_\infty = 298$K. The average free convection coefficient for the bar in this test is obtained using the method of the previous example and it is calculated as $h_\infty = 8\ W/m^2K$. The SMA bar is subjected to a dynamic cyclic loading consisting of 0.50%, 1.0-5% by increments of 1%, followed by four cycles at 6%. Frequency

of the applied cyclic loading is 0.5Hz (2sec for each loading-unloading cycle). The stress-strain response of the bar obtained by the present coupled thermomechanical formulation is compared with the experimental results in Figure 3.5(a). It is seen that the analytical formulation predicts a slight upward movement of the hysteresis loop in the stress-strain response in each cycle. This phenomenon is also seen in the experimental results and is caused by the temperature increase during the fast loading-unloading cycles.

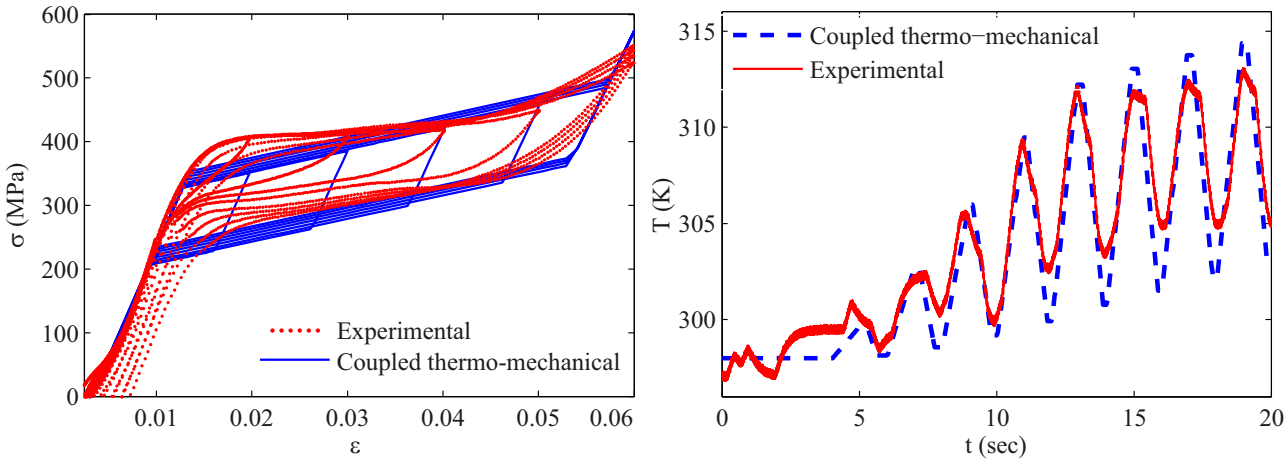

Figure 3.5: Comparison of the experimental and analytical results for (a) the stress-strain response, and (b) temperature-time at the surface of an SMA bar (Material III) with $d = 7.1mm$ in dynamic cyclic loading.

The experimentally monitored temperature at the surface of bar is shown in Figure 3.5(b) and compared with the analytical results. It is seen that the analytical results are following the cyclic temperature change of the material with an acceptable accuracy (the maximum error in the analytical results is 1.15%). Both the experimental and analytical results show an increase of temperature at the start of each loading-unloading cycle with respect to its previous cycle. This temperature increase is the reason for the upward movement of the stress-strain hysteresis loops in Figure 3.5(a). It is worth noting that the experimental results show an accumulation in the strain for cyclic loading, typically referred to as the fatigue effect. Developing constitutive relations capable of modeling this accumulated cyclic strain accurately is an active field of research [148, 164]. The present formulation is ignoring this effect. However, it is known that the constitutive equations

used in this chapter can be modified for accurate modeling of SMAs in cyclic loadings [93]. Modifying the present coupled thermomechanical formulation for taking into account the effect of accumulated strains in cyclic loading will be the subject of a future communication.

3.2.6 SMA wires with convection boundary condition

In this section we consider some numerical examples for studying the effect of the loading-unloading rate and ambient conditions on the response of SMA wires in uniaxial tension based on our coupled thermomechanical formulation. An SMA wire with circular cross section of radius $R = 1mm$ and length $L = 10cm$ is considered. A generic SMA material with properties given in Table 3.1 as Material IV is considered [92]. These material properties have been used in many numerical simulations of SMAs. An approximate solution for the adiabatic and isothermal response of an SMA wire with these properties by ignoring the nonuniformity of temperature distribution in the cross section and ambient conditions is presented in [92]. For comparison purposes, the initial temperature of the wire is considered equal to the value in Lagoudas [92], i.e. $\hat{T} = 328K$. The ambient temperature is assumed to be $T_\infty = 328K$. The method of §5.1 is used for calculating the free convection coefficient as a function of temperature difference in the range $0 < T_w - T_\infty < 40$. The change of free convection coefficient versus the temperature change is plotted in Figure 3.2 (Case II). As it is seen, the convection coefficient does not change much with the temperature difference; assuming a constant value $h_\infty = 14.04\ W/m^2K$ is a good approximation. The response of this SMA wire subjected to free convection in three different loading rates is modeled based on the present coupled thermomechanical formulation. Figure 3.6(a) shows the temperature changes during loading-unloading for three different rates in free convection. The stress-strain response in this case is shown in Figure 3.6(b). As the cross section diameter is small compared to its length, a uniform temperature distribution is observed in the cross section. Comparing these with those of the adiabatic solution by ignoring the ambient condition in Lagoudas [92], it is seen that the response of the SMA wire in total loading-unloading time of $\tau = 10$sec and exposed to a free convection boundary condition is identical with the adiabatic case. This is expected as the convection coefficient is low

and loading is applied fast and hence the material cannot exchange heat with the ambient. For the loading-unloading times of $\tau = 120$ and 900sec, as it is shown in Figure 3.6(a), although the temperature changes are less than that of $\tau = 10$sec, they cannot be ignored, i.e. assuming an isothermal process is not justified. As it is seen, for slow loading-unloading ($\tau = 120$ and 900sec), the temperature increase during the forward phase transformation is suppressed. After phase transformation completion, and also during the initial elastic unloading regime, when there is no phase transformation heat generation or absorption, the air cooling effect causes a decrease in temperature. This temperature decrease when accompanied by heat absorption during the reverse phase transformation, causes the material to be colder than the initial and ambient temperatures at the end of the unloading phase.

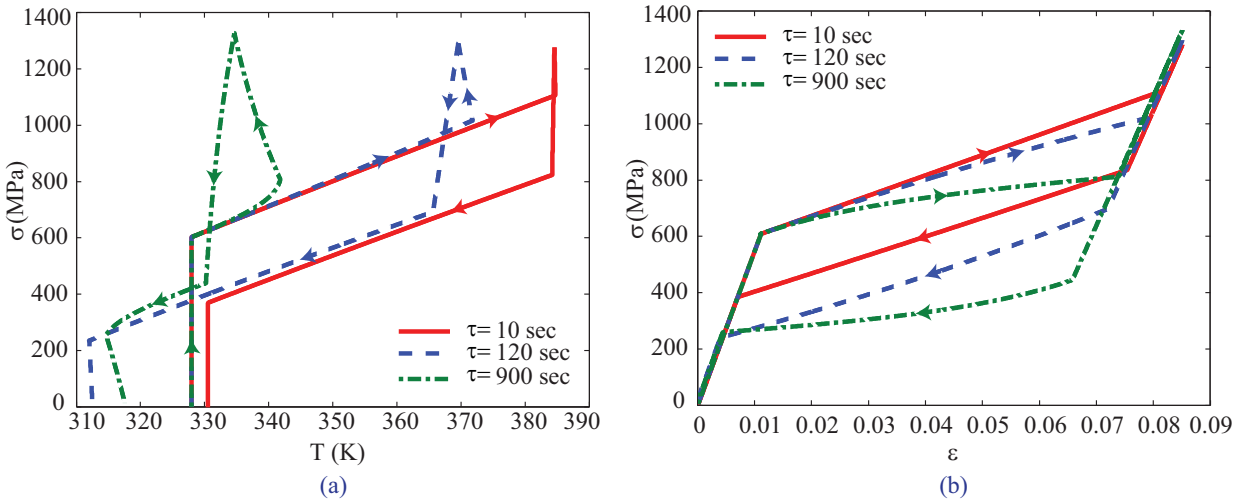

Figure 3.6: The effect of total loading-unloading time τ on (a) stress-temperature, and (b) stress-strain response of an SMA wire with $d = 2mm$ in free convection (still air with $h_\infty = 14.04 W/m^2K$).

The effect of ambient boundary condition on the response of SMA wires is studied in Figure 3.7. For this purpose a constant loading-unloading time of $\tau = 60$sec and different air flow speeds are considered. The method of §5.2 is used for calculating the forced convection coefficients for $U_\infty = 15$ and 50m/s and these values are obtained as $h_\infty = 269.05$ and $493.20 W/m^2K$, respectively. The free convection coefficient is the same as that of the previous example. Figure 3.7(a) shows the change of temperature versus stress for various

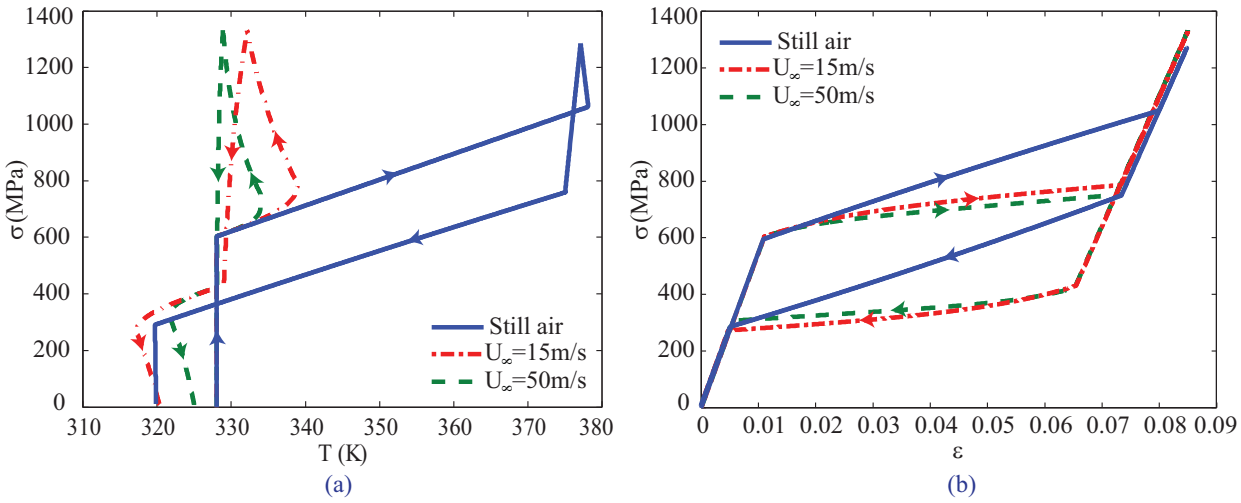

Figure 3.7: The effect of airflow speed U_∞ on (a) stress-temperature, and (b) stress-strain response of an SMA wire with $d = 2mm$ in free and forced convection (the total loading-unloading time is $\tau = 60$sec).

air flow speeds and the stress-strain response of SMA wires is shown in Figure 3.7(b). As it is seen, temperature is strongly affected by the ambient condition. The temperature at the end of unloading phase is lower than the ambient and initial temperatures. During loading, after the phase transformation completion, and also at the beginning of unloading, before the start of reverse phase transformation, the material is fully martensite and phase transformation does not occur. During these steps, the transformation heat is not generating and the material is cooling due to the high rate of heat exchange with the ambient. This temperature loss is followed by heat absorption during reverse phase transformation and causes the material to be colder than the initial and ambient temperatures at the end of unloading phase. As shown in Figure 3.7(b), temperature change affects the stress-strain response as well. By increasing the air flow speed, when the material response changes from adiabatic to isothermal, the slope of stress-strain curve decreases and the hysteresis area increases. As mentioned earlier, this change in the hysteresis area, caused by a change in temperature during loading-unloading has been observed in experiments (see §6.1, [124] and Auricchio et al. [16]).

3.2.7 SMA bars with convection boundary condition

In the previous section the response of SMA wires with small cross section diameters was studied. In this section SMA bars will be considered. In bars, in contrast with wires, the temperature distribution in the cross section is not uniform. It will be shown that for having a precise description of an SMA bar response in loading-unloading it is necessary to consider the coupled thermomechanical equations and the ambient conditions; assuming an isothermal response may cause considerable errors. An SMA bar with the material properties identical with those in the previous section is considered. The bar has a diameter of $d = 5$cm and length of $L = 20$cm. Using the method of §5.1, the free convection coefficient as a function of the temperature difference is calculated and plotted in Figure 3.2 as Case III. Similar to previous examples, it is seen that the free convection coefficient is almost constant and assuming an average value of $h_\infty = 5.86 W/m^2K$ is reasonable. The effect of the loading-unloading rate on the response of SMA bars is shown in Figure 3.8.

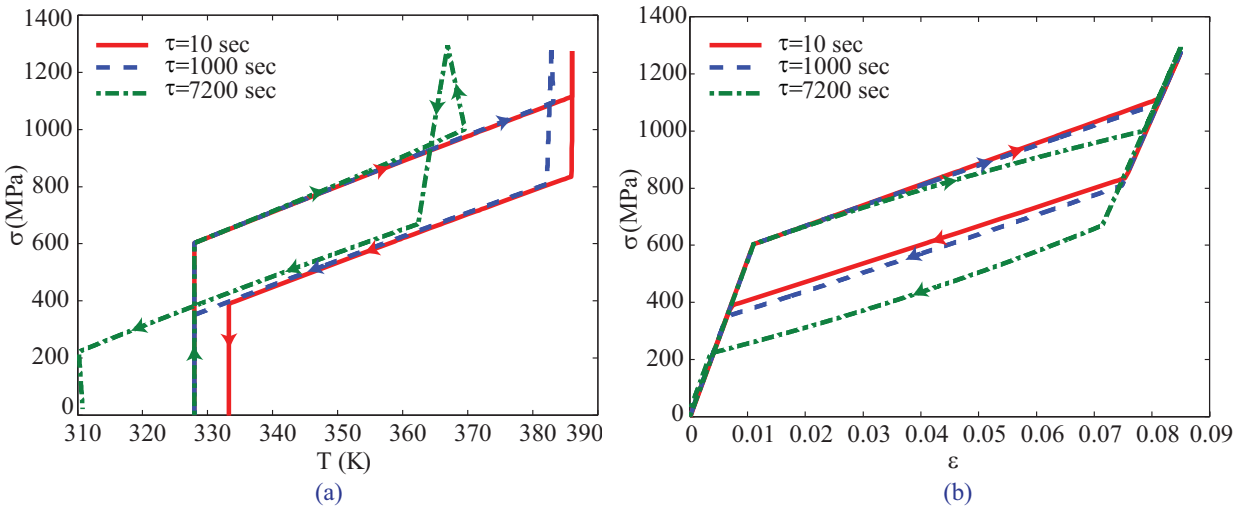

Figure 3.8: The effect of total loading-unloading time τ on (a) stress-temperature, and (b) stress-strain response at the center of an SMA bar with $d = 5cm$ in free convection (still air with $h_\infty = 5.86 W/m^2K$).

As it will be shown in the sequel, temperature has a nonuniform distribution in the cross section. Temperature at the center of the bar is plotted versus stress for various

total loading-unloading times in Figure 3.8(a). It is seen that the results for $\tau = 10$sec are similar to those presented by Lagoudas [92] which are obtained assuming adiabatic loading-unloading and ignoring the ambient condition and non-uniform temperature distribution in the cross section. It can be concluded that the response of the material is almost adiabatic for this fast loading rate. However, as it is seen in Figure 3.8(a), even for the total loading-unloading time of $\tau = 7200$sec, which is considered a quasi-static loading with isothermal response in the majority of the previously reported works, the temperature in the SMA bar of this example is far from that in either an isothermal or an adiabatic process. Also the final cooling as explained in the case of SMA wires is seen in slow loading-unloading rates. This example reveals the necessity of using a coupled thermomechanical formulation, especially for SMA bars with large diameters.

The stress-strain response at the center of the bar is shown in Figure 3.8(b). As it is seen in this figure, increasing the loading-unloading time decreases the stress-strain curve slope during the transformation and increases the hysteresis area. Comparing Figures 3.8 and 3.6 shows that increase of loading-unloading time affects the response of SMA wires more noticeably. This is expected because a wire has more potential for exchanging heat with the ambient air compared to a bar. The effect of air flow speed on the response of SMA bars in a constant loading-unloading time of $\tau = 300$sec is shown in Figure 3.9. The forced convection coefficients are calculated using the method of §5.2 as $h_\infty = 134.37$ and $234.79 W/m^2K$ for $U_\infty = 50$ and 100m/s, respectively. Temperature at the center of the bar versus stress is shown in Figure 3.9(a). As it is seen, even for the high air flow speed of $U_\infty = 100$m/s, the response of the SMA bar is not isothermal. Similar to SMA wires, cooling of material after completion of phase transformation and at the beginning of unloading causes the material to be in a lower temperature at the end of unloading compared to the initial temperature. The stress-strain response at the center of the bar for various air flow speeds is shown in Figure 3.9(b).

As mentioned earlier, for bars with large diameters, the temperature distribution in the cross section is not uniform because the heat transfer in regions near the surface differs from that in the central part. This non-uniformity in temperature distribution can be ignored

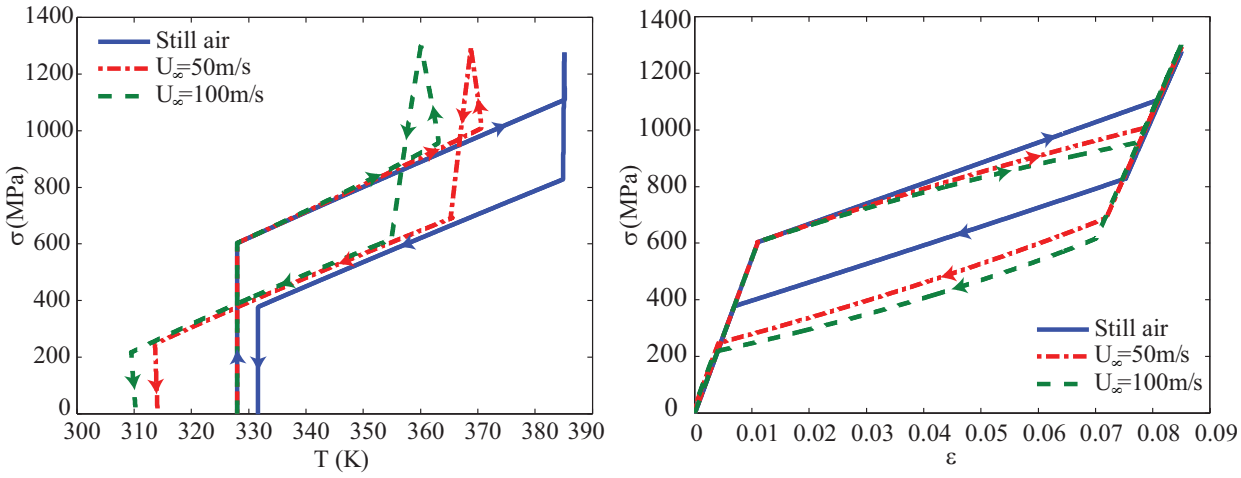

Figure 3.9: The effect of airflow speed U_∞ on (a) stress-temperature, and (b) stress-strain response in the center of an SMA bar with $d = 5cm$ in free and forced convection (the total loading-unloading time is $\tau = 300$sec).

for wires with small diameters but it is of more importance in bars with large diameters. Temperature distribution for the bar with $d = 5$cm diameter subjected to free and forced convection at the end of loading phase is shown in Figure 3.10. As it is seen, for the total loading-unloading time of $\tau = 300$sec, the temperature distribution is almost uniform for the free convection case and becomes non-uniform when the bar is subjected to air flow. In all the cases, temperature at the center of the bar is maximum. Increasing the air flow speed decreases temperature at every point of the cross section. Temperature non-uniformity increases for higher airflow speeds. It is worth emphasizing that in the free convection case and for very slow loading-unloading rates a non-uniform temperature distribution is seen for SMA bars with large diameters.

3.2.8 Non-uniform stress distribution in uniaxial tension of an SMA bar

As mentioned earlier, the generation (absorption) of latent heat during forward (reverse) phase transformation and the heat exchange with the ambient at the surface of bars causes a nonuniform temperature distribution in the cross section. The non-uniformity of temperature increases for larger diameters, slower loading-unloading rates, and larger convection

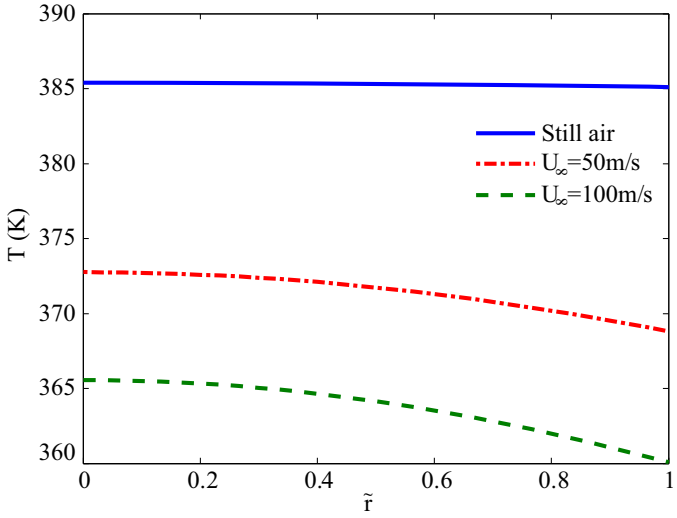

Figure 3.10: The effect of airflow speed U_∞ on the temperature distribution in the cross section of an SMA bar with $d = 5cm$ in forced convection. The total loading-unloading time is $\tau = 300$sec and the distribution is shown at the end of loading phase.

coefficients. Non-uniformity of temperature distribution is determined by the interaction of size, loading rate, and ambient conditions. Because of the strong coupling between the thermal and mechanical fields in SMAs temperature difference in the cross section causes a non-uniform stress distribution in the cross section. In other words, for uniaxial loading of an SMA bar, while the material in the cross section has a uniform strain distribution[4], stress distribution may be non-uniform. We will show that stress has a nonuniform distribution during the phase transformation and has different shapes for different loads. As an example, consider an SMA bar with diameter $d = 5$cm subjected to loading-unloading at total time of $\tau = 300$sec. The initial and ambient temperatures are $\hat{T} = T_\infty = 328K$ and air is flowing on the specimen with speed of $U_\infty = 100$ m/s that results in a forced convection coefficient of $h_\infty = 234.79 W/m^2K$. Material properties are given as Material IV in Table 3.1. Stress distributions corresponding to different uniform strains during the loading phase is shown in Figure 3.11.

[4]The uniform strain distribution is a boundary condition considered in this special case study. The formulation of this paper is general and can be used for modeling a bar with and arbitrary strain distribution in the cross section.

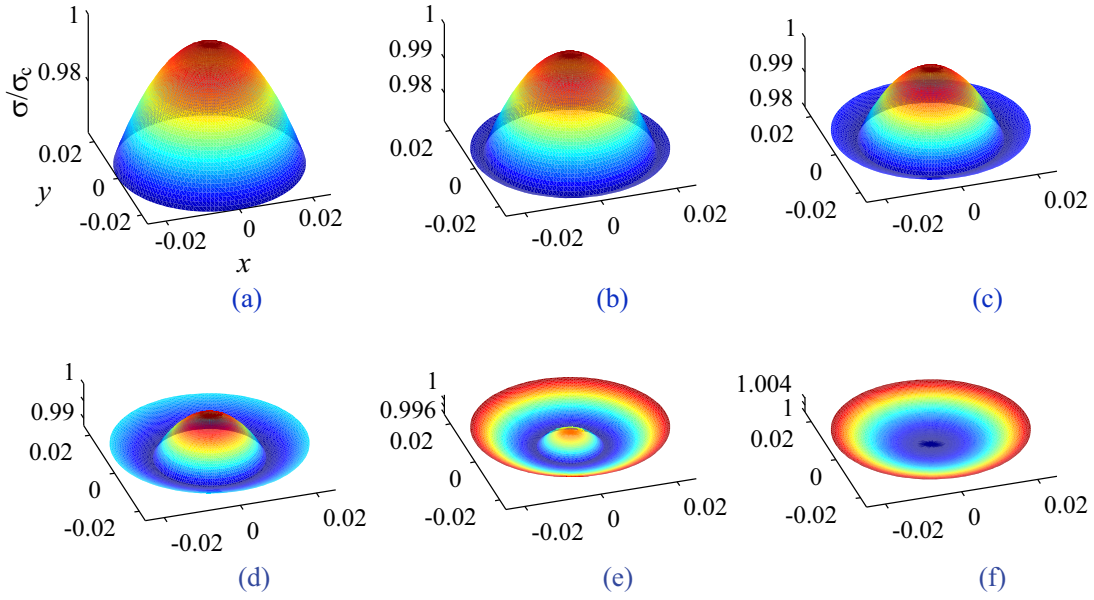

Figure 3.11: Non-uniform stress distribution in the cross section of an SMA bar subjected to uniform tensile strain at (a) $\epsilon = 0.0680$, $\sigma_c = 959.0$MPa, (b) $\epsilon = 0.0768$, $\sigma_c = 994.5$MPa, (c) $\epsilon = 0.0770$, $\sigma_c = 995.6$MPa, (d) $\epsilon = 0.0773$, $\sigma_c = 996.6$MPa, (e) $\epsilon = 0.0775$, $\sigma_c = 997.5$MPa, and (f) $\epsilon = 0.085$, $\sigma_c = 1296.0$MPa.

Before the phase transformation starts, no latent heat is generated; the whole cross section has uniform stress and temperature distributions. By the start of phase transformation from austenite to martensite, latent heat is generated inside the bar. The convective heat transfer at the surface results in lower temperatures for points closer to the surface compared to the center of the bar (see Figure 3.10). The non-uniform temperature distribution in the cross section results in the stress distribution shown in Figure 3.11(a). In each of the plots in Figure 3.11, the stress distribution is normalized with respect to stress at the center of the bar (σ_c) for a better visualization. Stress at the center of the bar corresponding to each strain is given in Figure 3.11. Stress distribution in the cross section remains "convex" until the start of phase transformation completion. The phase transformation completion starts from the surface of the bar due to the lower temperature at the surface as decreasing temperature remarkably decreases the threshold of phase transformation completion in

SMAs. Formation of martensite at the surface results in a decrease in stress with a sharper slope compared to the material at the inner region. The "convex" stress surface starts to invert from the outer radius as shown in Figure 3.11(b). By increase of load, the "convex" stress surface is inverted to a "concave" surface as shown in Figures 3.11(b) to 3.11(f). When the whole cross section is fully transformed to martensite stress distribution has the "concave" shape shown in Figure 3.11(f). As it is seen in Figures 3.11(a) to 3.11(f), the stress distribution nonuniformity (deviation of the normalized stress distribution surface from unity) decreases with the increase of strain and completion of phase transformation. It is worth mentioning that the strain corresponding to each stress distribution in Figure 3.11 is uniform.

3.2.9 SMA bars operating in water

The wide variety of applications of SMAs in recent years necessitates the analysis of SMA devices operating in various environments. It is now known that large scaled SMA bars and wires can be used as efficient elements for improving the seismic performance of bridges [43, 45, 142]. The SMA tendons in bridges may operate in water and hence it is necessary to have a precise analysis of the response of these wires and bars subjected to water flow. As a case study, an SMA bar with geometric and material properties given in §3.2.7 is considered. It is assumed that the SMA bar is operating as a tendon in a bridge in the water flow. The average water velocity in rivers varies from $0.1m/s$ to $3m/s$. Considering the flow velocity of $0.5m/s$ and the temperature of $T = 27^\circ$ for the water, the forced convection coefficient is calculated using (3.42) and is $h_\infty = 2529.3W/m^2K$. A loading-unloading cycle in $\tau = 10sec$ is considered. The temperature distribution in the cross section at the end of loading and unloading phases is shown in Figure 3.12(a). As it is seen, the excessive cooling of water at the surface causes a remarkable temperature gradient in the cross section at the end of loading phase. It is obvious that ignoring this temperature distribution in the cross section is not justified in the present case study. As it is shown in this figure at the end of unloading phase the outer parts of the cross section are in a temperature below the initial temperature while the inner core has a temperature slightly

above the initial temperature. This phenomenon was previously explained in Figures 3.6-3.9. The normalized stress distribution for various strain values during the loading phase are shown in Figure 3.12(b). As it is shown in this figure, the convex to concave transformation of the stress distribution shape is seen in this case study as well (this phenomenon was explained in detail in §3.2.8). Comparing the results of Figures 3.12(b) and 3.11 reveals that while the stress difference in the cross section of a bar cooling in flowing air is 4%, it increases to 14% in the present case study (SMA bar operating in water).

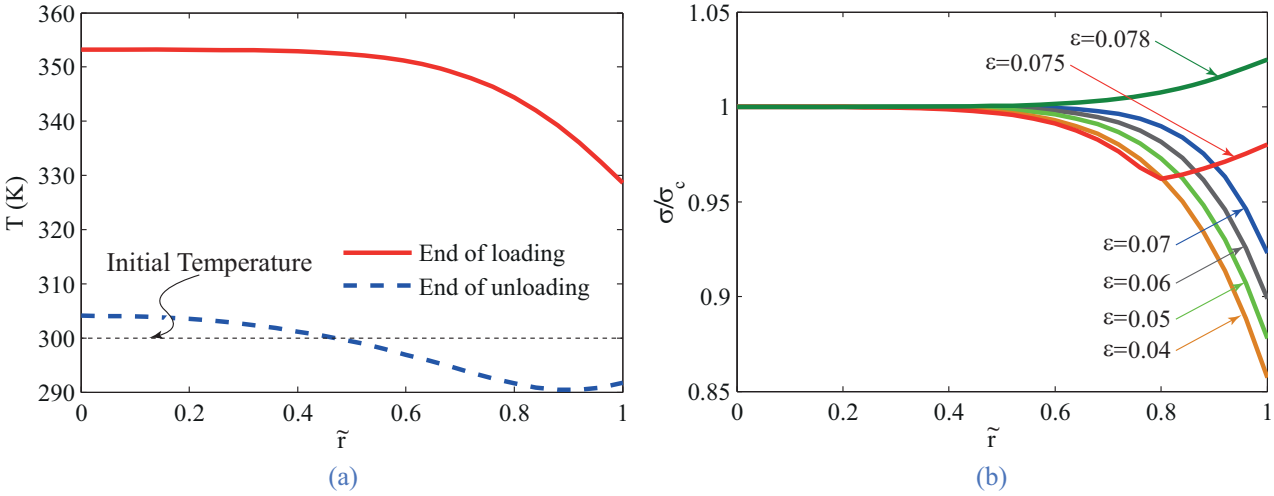

Figure 3.12: (a) Temperature distribution in the cross section, and (b) stress distribution in the loading phase for an SMA bar with $d = 5$cm operating in water. The stress at the center point for strain values $\epsilon = 0.04,\ 0.05,\ 0.06,\ 0.07,\ 0.075$, and 0.078 are $\sigma_c = 582.2,\ 631.6,\ 676.2,\ 722.5,\ 864.1$, and 958.2MPa, respectively.

3.2.10 Size, boundary condition, and loading rate effects on the temperature and stress gradients

As it was shown in the previous sections, the gradients of temperature and stress in the cross section are strongly affected by the ambient condition, diameter of the bar, and the loading-unloading rate. In this section we study the effect of these parameters on the maximum temperature and stress gradients in the cross section of SMA bars and wires subjected to uniaxial loading. For sake of brevity, we consider only the loading phase. The initial and ambient temperatures are assumed to be $T_0 = T_\infty = 300K$ for all the case studies

in this section. In each case, for studying the non-uniformity in stress and temperature distributions in the cross section, the difference between the value of these parameters at the center and surface of the bar is nondimensionalized by dividing by the value of the corresponding parameter at the surface. The maximum temperature and stress gradients versus the convection coefficient for four various loading rates are shown in Figure 3.13. A bar with $d = 5cm$ and material properties similar to the previous case study is considered and the range of convection coefficient is chosen to cover the free and forced convection of air, and water flow on the bar (see the case studies in §6.3 and 6.5). As it is shown in this figure for all the loading rates both the temperature and stress gradients increase for larger convection coefficients. However, for the slow loading rate $\tau = 300sec$, the increase of gradient is suppressed for convection coefficients larger than $h_\infty \simeq 1000W/m^2K$, since the material has enough time to exchange heat with the ambient. It is worth noting that for the slow loading rate τ =300 sec the trend of the gradient change is different from the other (fast) loading rates. We will study the effect of changing the loading rate on the gradients in the following case study and will find the critical time corresponding to this change of trend for some sample ambient conditions. It is shown in Figure 3.13 that the temperature and stress gradients in the cross section are more excessive for larger convection coefficients for all the loading rates.

The effect of changing the loading rate on the maximum temperature and stress nonuniformity in the cross section for three different convection coefficients is shown in Figure 3.14. The results are presented for the total loading-unloading times $1 \leq \tau \leq 3600sec$. As it is shown, larger convection coefficients lead to more nonuniformity for both the stress and temperature distributions. Also, it is shown that for all the convection coefficients the temperature and stress gradients are negligible for very fast and very slow loading rates, and peaks at an intermediate loading rate ($\tau = 140sec$ for $h_\infty = 134W/m^2K$, $\tau = 100sec$ for $h_\infty = 234W/m^2K$, and $\tau = 30sec$ for $h_\infty = 2529W/m^2K$). This is expected because for very fast loadings the material at the surface does not have enough time to exchange the latent heat with the ambient and the temperature and stress distributions are almost uniform. For very slow loadings, the latent heat in the whole cross section has enough

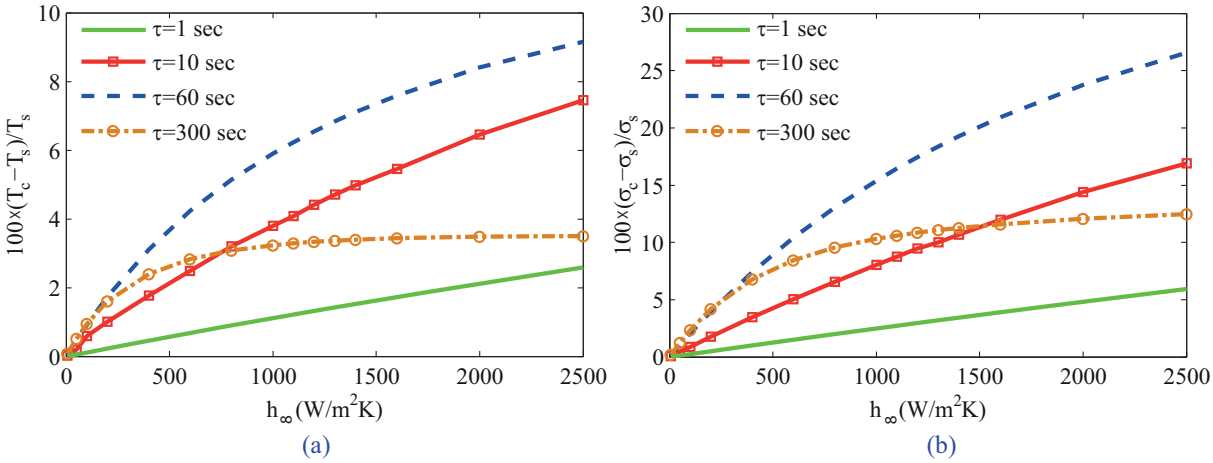

Figure 3.13: (a) The maximum temperature gradient, and (b) the maximum stress gradient versus the convection coefficient for four different loading rates. The subscripts s and c denote the value measured at the surface and center of the bar, respectively. The diameter of the bar is $d = 5cm$.

time to be exchanged with the ambient and the temperature and stress distributions are almost uniform in the cross section. For an intermediate loading rate the temperature and stress distribution nonuniformity is maximum. Also it is worth mentioning that the loading rate corresponding to the maximum nonuniformity decreases by increasing the convection coefficient.

The size effect on the temperature and stress nonuniformity is studied for three different ambient conditions in Figure 3.15 (the total loading-unloading time is $\tau = 10sec$). As explained in §5, the convection coefficient depends on the bar diameter and for obtaining the results presented in Figure 3.15 the appropriate convection coefficient for each diameter and ambient condition is calculated using the formulation of §5. As it is shown in Figure 3.15, in the case of water flow the temperature and stress nonuniformities are more pronounced compared to those of the air flow ambient condition. For the forced convection by air the temperature and stress gradients increase for larger diameters. However, in the case of water flow, the gradients have a peak at $d \simeq 25mm$.

The results presented in Figures 3.13-3.15 clearly describe the complicated effect of size, ambient condition, and loading rate on the coupled thermomechanical response of SMA

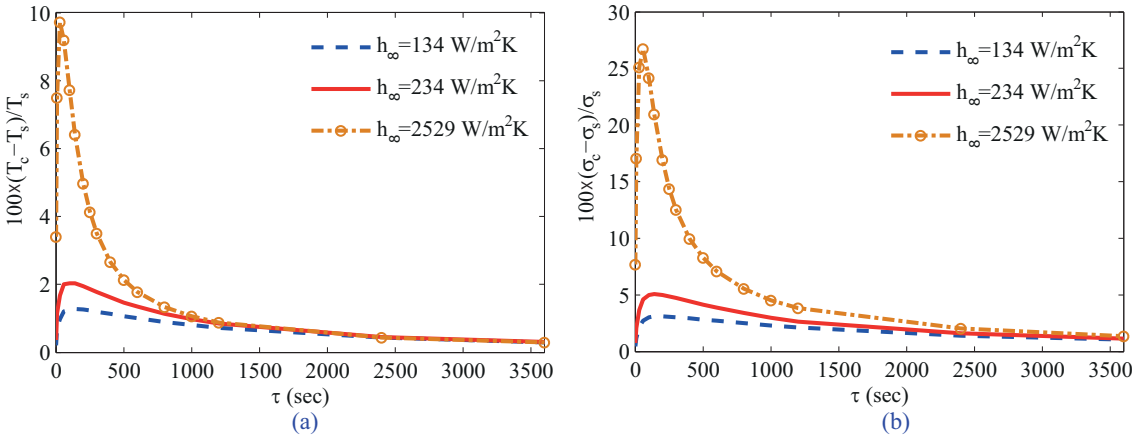

Figure 3.14: (a) The maximum temperature gradient and (b) the maximum stress gradient versus the loading rate for three various convection coefficients. The subscripts s and c represent the value measured at the surface and center of bar respectively. The diameter of bar is d=5cm.

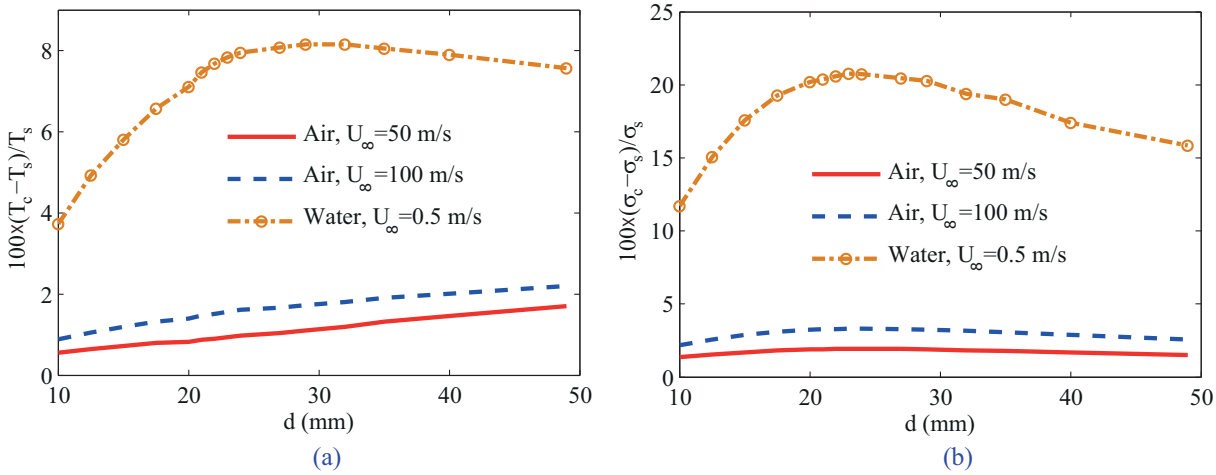

Figure 3.15: (a) The maximum temperature gradient and (b) the maximum stress gradient versus the bar diameter for three various ambient conditions. The subscripts s and c represent the value measured at the surface and center of bar, respectively. The total loadig-unloading time is τ =10 sec.

bars. These figures can be used by a designer to decide whether a coupled thermomechanical formulation with considering the heat flux in the cross section is necessary or using simpler lumped models is enough. It is worth mentioning that although for the uniaxial loading of bars and wires the simpler models assuming lumped temperature in the cross section can be used with an error, there are numerous cases for which the present formulation is the only analysis option. An example is torsion of circular SMA bars for which shear stress has a complicated nonuniform distribution in the cross section [127]. It would be incorrect to consider a lumped temperature in the cross section for torsion problems. Considering the effect of phase transformation latent heat in torsion of SMA bars is the subject of a future communication. We have been able to show that ignoring the heat flux and the temperature nonuniformity in the cross section of SMA bars subjected to torsion leads to inaccurate results. It is also worth nothing that all the numerical simulations presented in this section are performed on a 2 GHz CPU with 2 GB RAM. Since the presented explicit finite difference formulation needs a variable minimum time increment for guarantying numerical stability for various dimensions and material properties [141], the computational time varies for different case studies. However, by considering an average of 30 nodes (for smaller diameters fewer nodes are used) in the cross section and using the material properties in Table 3.1, the most time consuming case studies (examples with large number of nodes in the cross section and large loading-unloading times) are all completed in less than 20 minutes.

3.3 Coupled Thermomechanical Analysis of SMA Circular Bars in Pure Torsion

Shape memory alloys (SMAs) in recent applications are usually subjected to combined loadings in contrast with the early devices that were mostly designed based on using the uniaxial deformation of SMA wires operating as tendons. The recent interest in using sophisticated SMA devices reveals the necessity of analyzing these materials subjected to complicated loadings. To our best knowledge, there is no reported work in the literature on studying the coupled thermomechanical response of SMA bars in torsion. In this section, we present the heat balance equation by considering the phase transformation latent heat and the heat flux effects for bars in pure torsion. This relation is coupled with the exact solution

for pure torsion of SMA bars that we presented previously assuming that the SMA bar is under torsion in a constant temperature. The generation and absorption of latent heat due to phase transformation and its flux toward the other parts of the cross section in which the material is responding elastically is taken into consideration. Boundary conditions at the outer surface of the bar caused by free or forced convection of air or fluid flow are carefully enforced. For verification purposes the results of the present coupled thermomechanical formulation are compared with the experimental data for a thin-walled NiTi tube subjected to pure torsion.

Since the heat conduction inside the SMA bar and the convection with the ambient both are strongly affected by the loading rate, it is shown that the response of SMA bars in torsion is rate dependent. Several case studies are considered and the effect of loading rate and ambient conditions on the torsional response of SMA bars is studied in detail. In each case, the results are compared with the solution obtained by ignoring the thermomechanical coupling and it is shown that the special characteristics of torsion in SMA bars leads to a significant difference between the isothermal and coupled thermomechanical results. It is worth noting that although some simplified lumped temperature methods can be used for studying the coupled thermomechanical response of SMA bars subjected to uniaxial loading in particular conditions (when there are no propagating transformation fronts along the length, the Biot number is sufficiently small, and thermal boundary conditions at the ends are insulated), due the nonuniform distribution of shear stress in the cross section of SMA bars subjected to torsion, the effect of temperature nonuniformity and the flux of latent heat is more evident compared to the simple tension without propagating phase fronts.

3.3.1 Coupled thermomechanical governing equations for SMAs in pure torsion

Deriving the three-dimensional coupled thermomechanical governing equations for SMAs is explained in details in the previous section. Starting from the first law of thermodynamics in local form and using the second law of thermodynamics, the coupled energy balance equation is obtained as expressed in (3.13). It is worth noting that, although the constitutive relations are capable of modeling finite strains [162], we consider the small strains assumption and

the formulation is not affected by the stress measure in use.

The exact solution for pure torsion of shape memory alloy circular bars ignoring the effect of phase transformation latent heat, and assuming the isothermal condition was given in Section 2.2. In this section we modify the solution for the pure torsion of circular bars considering the coupled thermomechanical governing equations for SMAs as presented in the previous section. In the new formulation, we study the coupled thermomechanical torsion problem in the presence of the phase transformation induced heat generation/absorption and the heat flux effect in the cross section. A finite difference formulation is used to solve the governing coupled thermomechanical equations.

The closed form solution of pure torsion was given as a function of the radius, twist angle and temperature, $\tau_{\theta z} = \wp^{\pm}(r, \theta, T)$ in Section 2.2. This equation will replace the constitutive equation in the set of coupled equations. The reduction of the other equation (3.16) for pure torsion is obtained by substituting (2.11) and (2.13) into (3.16). The set of coupled thermomechanical governing equations read

$$\begin{cases} -\tilde{\mathscr{F}}_1(\tau_{\theta z}, T)\ \dot{\tau_{\theta z}} + \left[\rho c - \tilde{\mathscr{F}}_2(T)\right] \dot{T} = k \left(\frac{\partial^2 T}{\partial r^2} + \frac{1}{r}\frac{\partial T}{\partial r}\right), \\ \\ \tau_{\theta z} = \wp^{\pm}(r, \theta, T), \end{cases} \tag{3.43}$$

where

$$\tilde{\mathscr{F}}_1(\tau_{\theta z}, T) = \frac{1}{\mathscr{D}^{\pm}}(\sqrt{3}H + 4\Delta S_{44}\ \tau_{\theta z})(\mp Y + \rho \Delta s_0 T), \qquad \tilde{\mathscr{F}}_2(T) = \frac{\rho \Delta s_0}{\mathscr{D}^{\pm}}(\mp Y + \rho \Delta s_0 T). \tag{3.44}$$

In $(3.43)_1$, k is the thermal conductivity and Fourier's law of thermal conduction ($\boldsymbol{q} = -k\boldsymbol{\nabla} T$) is used for deriving the right-hand side. The explicit expression for $(3.43)_2$ can be found in Mirzaeifar et al. [127]. Temperature and stress distributions at $t = 0$ are given as the initial conditions, $T(r, 0) = \hat{T},\ \tau_{\theta z}(r, 0) = \hat{\tau}_{\theta z}$. The following boundary conditions are given at the outer surface and the center of the circular bar

$$k\frac{\partial T(r,t)}{\partial r}\Big|_{r=R} = h_{\infty}[T_{\infty} - T(R,t)], \qquad \frac{\partial T(r,t)}{\partial r}\Big|_{r=0} = 0, \tag{3.45}$$

where h_{∞} is the heat convection coefficient, T_{∞} is the ambient temperature, and R is the bar outer radius.

3.3.2 Finite difference discretization of the governing equations

Considering axisymmetric stress and temperature distributions in the circular bar, the set of coupled thermomechanical equations (3.43) and the boundary conditions (3.45) are discretized by dividing the bar into N_r annuli of equal size Δr and using an explicit finite difference method. The finite difference form of the coupled thermomechanical equations (3.43) for pure torsion is given by (see Section 3.2 for details of deriving similar relations in the uniaxial case)

$$\begin{aligned}\left[-\frac{1}{\mathscr{D}^{\pm}}(\sqrt{3}\ H+4\Delta S_{44}\tau^{n}_{\theta z,i})(\mp Y+\rho\Delta s_0 T^{n}_{i})\right]\frac{\tau^{n+1}_{\theta z,i}-\tau^{n}_{\theta z,i}}{\Delta t}\\ +\left[\rho c-\frac{\rho\Delta s_0}{\mathscr{D}^{\pm}}(\mp Y+\rho\Delta s_0 T^{n}_{i})\right]\frac{T^{n+1}_{i}-T^{n}_{i}}{\Delta t}\\ =\left(r_i+\frac{\Delta r}{2}\right)\frac{T^{n}_{i+1}-T^{n}_{i}}{r_i(\Delta r)^2}-\left(r_i-\frac{\Delta r}{2}\right)\frac{T^{n}_{i}-T^{n}_{i-1}}{r_i(\Delta r)^2},\end{aligned}\tag{3.46}$$

$$\tau^{n+1}_{\theta z,i}=\wp^{\pm}(r,\theta^{n+1},T^{n+1}),\tag{3.47}$$

where the subscript i denotes the ith node in the cross section and the superscript n refers to the nth time increment. For calculating the finite difference approximation of the boundary conditions that include internal heat generation, energy balance for a volume attached to boundary nodes should be considered. For the central node $i=1$, consider a cylindrical volume with radius $\Delta r/2$. The axis of this volume coincides with the bar axis. The finite difference approximation of the boundary condition in the central node is given by (3.35) and for the outer node with the convection boundary condition, considering a cylindrical volume attached to the outer node (Mth node) with inner radius $R-\Delta r/2$ and outer radius R, the energy balance gives the boundary condition as expressed in (3.36), where the parameters $\Re^{n}_{1}$ and $\Re^{n}_{M}$ are the equivalent internal heat generation due to phase transformation calculated at the central ($i=1$) and outer ($i=M$) nodes of a bar subjected to torsion as

$$\begin{aligned}\Re^{n}_{i} &= \left[-\frac{1}{\mathscr{D}^{\pm}}(\sqrt{3}H+4\Delta S_{44}\tau^{n}_{\theta z,i})(\mp Y+\rho\Delta s_0 T^{n}_{i})\right]\frac{\tau^{n+1}_{\theta z,i}-\tau^{n}_{\theta z,i}}{\Delta t}\\ &+ \left[-\frac{\rho\Delta s_0}{\mathscr{D}^{\pm}}(\mp Y+\rho\Delta s_0 T^{n}_{i})\right]\frac{T^{n+1}_{i}-T^{n}_{i}}{\Delta t}.\end{aligned}\tag{3.48}$$

The solution procedure is as following: the stress and temperature in all nodes are known

at the nth loading increment (from the initial conditions if n=0, and from the completed solution in the previous increment if n≠0). For any of the nodes except the central and outer nodes, substituting (3.47) into (3.46) a nonlinear algebraic equation is obtained with only one unknown: $T_i^{n+1}, \quad i = 2...M-1$. This equation is solved numerically [55] and the temperature at the (n+1)th time increment is calculated. Substituting the calculated temperature into (3.47) gives the stress for the (n+1)th increment. For the central and outer nodes, a similar procedure is used considering (3.47), (3.35), (3.36), and (3.48).

We previously reported the exact solution for SMA straight bars with circular cross sections in torsion and SMA helical springs by using the torsion of straight and curved SMA bars. In the previous section we showed that considering an isothermal process in uniaxial loading-unloading of SMA bars and wires gives accurate results only for wires with small diameters subjected to loadings applied with a very slow rate. To consider the effect of ambient condition, loading rate, and size accurately, it is necessary to solve the coupled thermomechanical equations. In this section we study the pure torsion of SMA circular bars using the coupled thermomechanical equations. The present formulation has the capability of considering an accurate convection boundary condition on the bar surface. The details of calculating the convection coefficient on the surface of a cylindrical bar in free air, flowing air, and fluid flow is presented in Section 3.2.

3.3.3 Verification using experimental results

There are some reported experiments in the literature for the torsion of prismatic solid SMA bars [47]. However, although these works report the results of torsion tests, the material properties needed in our constitutive model are not presented. Also, the temperature is not measured in these tests. In order to verify our coupled thermomechanical formulation the experimental data reported by Lim and McDowell [108] is used. Lim and McDowell [108] performed experiments on thin-wall tubes of pseudoelastic NiTi subjected to pure torsion. During loading-unloading the change of temperature due to latent heat generation/absorption during phase transformation was measured using four thermocouples attached to the specimen and temperature versus shear strain was reported. The specimen

was made of a NiTi alloy with the near equiatomic composition and was subjected to a heat treatment after machining from bar stock. In [108] only the austenite finish temperature is reported and the other material properties are not measured. However, the results of several uniaxial loading tests are reported that can be used for calibrating the required material constants in the the constitutive relation that we are using in this section. The experimental date in [108, 109] are used for obtaining the following properties (see [162] for details of calibrating the model using experimental data): $E^A = 72$ GPa, $E^M = 30$ GPa, $\nu^A = \nu^M = 0.42$, $H = 0.05$, $\rho\Delta s_0 = -0.57 \times 10^6$ J/(m^{3}K), $A_f = 273.1$ K, $A_s = 265.7$ K, $M_f = 231.8$ K, $M_s = 247.9$ K. Since the thermal conductivity and the specific heat are not reported for this material, we use the previously reported values in the literature for $Ni_{50}Ti_{50}$ [92]: $k = 18$ W/(mK), $\rho c^A = \rho c^M = 3.9 \times 10^6$ J/(m^{3}K). Both the inner and outer surfaces of the tube are subjected to free convection by air. In the numerical simulations, both the inner and outer nodes are considered as the boundary nodes and the boundary condition (3.36) is imposed for both these nodes. The thickness is divided into 20 sections. The free convection coefficient for both surfaces is $h_\infty = 5.2$W/m^{2}K (see §5 in [128] for calculation details). The initial and ambient temperatures are $\hat{T} = T_\infty = 287$ K. The loading rate is $\dot{\epsilon}_{\rm eq} = 5 \times 10^{-4}$s^{-1}, where $\epsilon_{\rm eq} = \gamma/\sqrt{3} = 2\epsilon_{\theta z}/\sqrt{3}$ is the Mises equivalent strain. The specimen was subjected to five loading cycles with the equivalent strains between $\pm 3\%$. We use the results of the second loading-unloading cycle, in which the material response is stabilized, for verification purposes (due to the unknown thermal condition between the specimen and the grips, the simulation results may be inaccurate for the final cycles and the second cycle is chosen because the material response is stabilized while the effect of head exchange between the grips and the specimen is minimum). The equivalent shear stress versus the equivalent shear strain at the outer surface obtained from the present formulation is compared with the experimental results in Figure 3.16(a). The temperature versus the equivalent shear strain is calculated using the method of this paper and compared with the experimental results in Figure 3.16(b). It is worth noting that due to the small thickness (t=1.95 mm), the temperature gradient in the cross section is negligible. We present a detailed study of the effect of size on the temperature gradient in the sequel. As it is shown,

the results are in an acceptable agreement. The differences in the strain-stress response is due to the formation of R-phase in phase transformation that is not considered in our formulation. The differences in temperature distribution originated from the difference in the stress distribution, and also by considering the special specimen shape. The specimen has two thick bars attached to the ends for being mounted into the grips, and the heat transfer between the tube gage section and the attached parts to the tube at the ends is ignored in our theoretical modeling (see Figure 1 in [108] for details of the specimen shape). As it is seen in Figure 3.16(b), the specimen temperature immediately reaches the ambient temperature at the start of unloading, while this is not seen in the numerical simulations. This phenomenon may be caused by the high heat exchange between the specimen and the grips (that are in the same temperature with the ambient) that is ignored in the theoretical modeling.

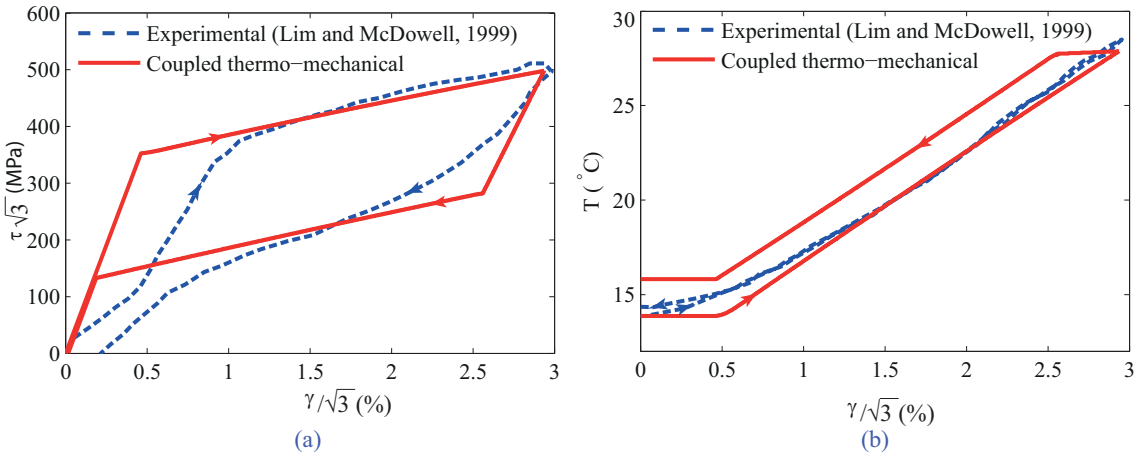

Figure 3.16: Comparison of the experimental and analytical results for (a) equivalent shear stress versus equivalent shear strain, and (b) temperature versus equivalent shear strain at the outer surface of a thin-walled SMA tube subjected to pure torsion.

3.3.4 Thermomechanical analysis of solid SMA bars subjected to pure torsion

As the first case study for analyzing the coupled thermomechanical response of solid SMA bars under torsion, consider an SMA bar with circular cross section of radius $R = 2.5$ cm and length $L = 20$ cm. The bar is made of a NiTi alloy with the following material properties:

$E^A = 72$ GPa, $E^M = 30$ GPa, $\nu^A = \nu^M = 0.42$, $\rho c^A = \rho c^M = 2.6 \times 10^5$ J/(m^{3}K), $H = 0.05$, $\rho \Delta s_0 = -0.42 \times 10^6$ J/(m^{3}K), $A_f = 281.6$ K, $A_s = 272.7$ K, $M_f = 238.8$ K, $M_s = 254.9$ K. These properties are extracted for the phenomenological constitutive equations by Qidwai and Lagoudas [162] using the experimental date reported by Jacobus et al. [79] for a $Ni_{50}Ti_{50}$ alloy. The thermal conductivity is not reported for this material and we use $k = 18$ W/(mK), which is reported in the literature for $Ni_{50}Ti_{50}$ [92]. The SMA bar is fixed at one end and the other end is twisted to the maximum twist angle per unit length of $\theta = 5$ rad/m and then unloaded to the initial configuration at rest. The total loading-unloading time is assumed to be $\tilde{\tau} = 10$ sec. It is assumed that the whole bar is initially at the temperature $\hat{T} = 300$ K and it is surrounded by still air with temperature $T_\infty = 300$ K. The SMA specimen is vertical and surrounded by air with negligible flow speed. For calculating the free convection coefficient of a vertical cylinder, the empirical and numerical relations for the Nusselt number are used (See section §5.1, and Figure 2, Case III in [128], and also [75, 159] for more details). By considering an average temperature difference of 15 K between the bar surface and the surrounding air, free convection coefficient for this case study is $h_\infty = 4.5$W/m^{2}K (see Figure 2, Case III in [128]). The number of grid points is M =50. The minimum time increment for having a stable solution in the explicit formulation is a function of the radius in each case study [141]. It is observed that in practice a convergence study is not required because the stable solution (with appropriate choice of time increment) always converges to the same stress and temperatures at the selected points and the only criterion is obtaining a smooth distribution that is acceptable by choosing 50 grid points. The results of this case study are depicted in Figure 3.17. The shear stress distribution in the cross section of the bar in loading is shown in Figure 3.17(a) for various twist angles.

Figure 3.17(b) shows the shear stress distribution in the cross section for various twist angles in unloading. The observed spark in the shear stress distribution for $\theta = 4$ rad/m is caused by the arrangement of different regions that experience phase transformation during loading and unloading. A detailed study of this phenomenon, along with some graphs showing the martensitic volume fraction distribution in the cross section are presented in

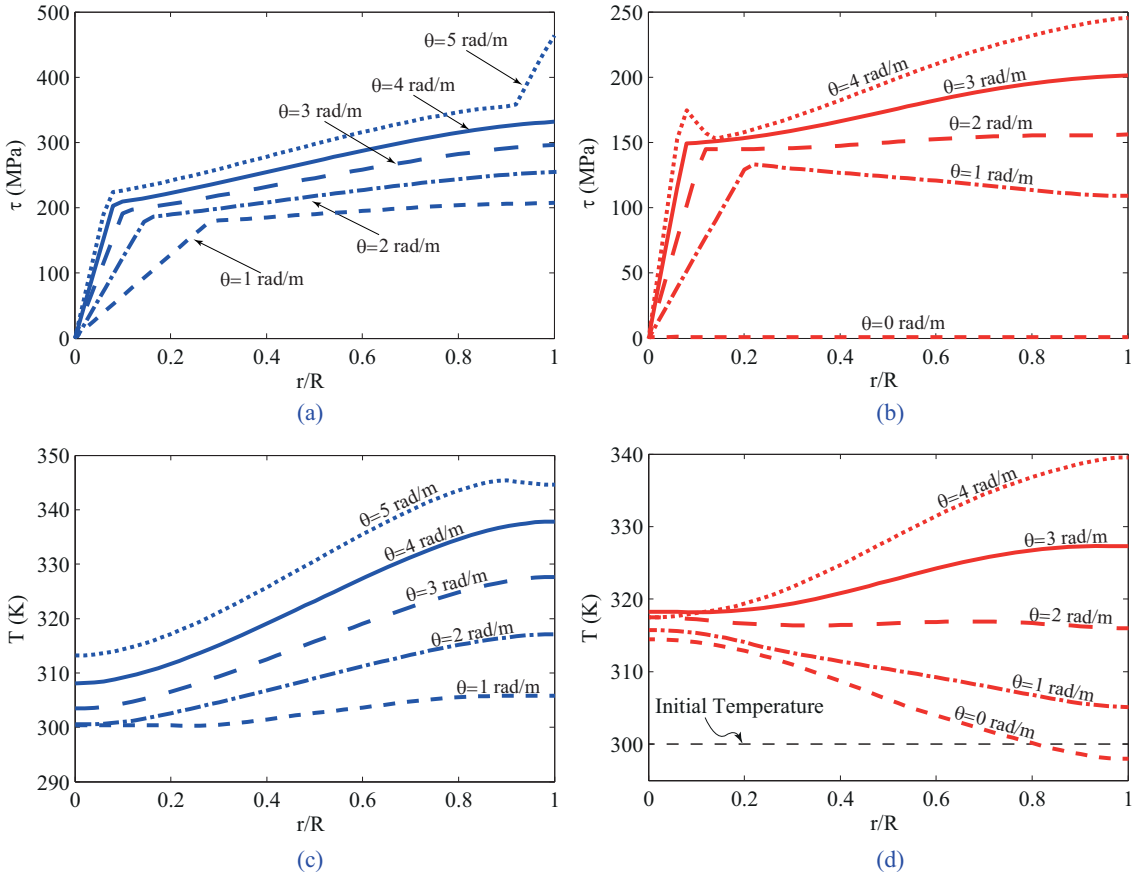

Figure 3.17: Distributions of (a) shear stress during loading, (b) shear stress during unloading, (c) temperature during loading, and (d) temperature during unloading in the cross section of an SMA bar in free convection. The total loading-unloading time is $\tilde{\tau} = 10$ sec.

[127]. Since the temperature of the bar in the parts that experience phase transformation is above the austenite finish temperature during loading-unloading, there is no residual stress in the cross section at the end of unloading. It is worth noting that, temperature distribution in the cross section is affected by a set of parameters, e.g. the loading rate, size of the bar, and the ambient condition. Temperature may be lower than the initial temperature in some cases (see Mirzaeifar et al. [128] and the following case studies in this section). For having zero residual stress at the end of unloading, $\hat{T} > A_f$ is not an adequate condition and the complete history of temperature distribution in the cross section during loading-unloading should be considered. Figure 3.17(c) shows the temperature distribution in the cross section of the bar during loading for various twist angles per unit length. There

are some important observations regarding the temperature distribution worth explaining. As it is shown in Figure 3.17(a), during loading for each twist angle the SMA bar has an austenite core surrounding the bar axis (characterized by a linear shear stress distribution in the cross section). Since there is no phase transformation inside this core, consequently no heat is generated in this region while the temperature of the material outside this austenite core is increasing due to forward phase transformation. During loading, the temperature inside the austenite core is increasing by the hot material in the outer region due to thermal conduction. Because the temperature change inside this austenite core during loading and unloading is solely caused by the heat exchange with the outer material, as it will be shown in the sequel, temperature is strongly affected by the rate of loading and a complicated interaction between the loading rate and the core temperature is observed. This phenomenon will be studied in detail in the following case studies. The temperature distribution in the region attached to the outer radius at the end of loading phase ($\theta = 5$ rad/m) in Figure 3.17(c) shows that the slope of temperature distribution changes at a specific point and temperature starts to decrease slightly in an annular ring attached to the outer surface. By looking at Figure 3.17(a), it is seen that the material in this region is fully transformed to martensite (the linear part of shear stress distribution for the regions near $r/R = 1$). Since after completion of phase transformation there is no heat generation, the material in this region loses temperature due to heat exchange with the colder ambient at the surface. This negative slope in temperature distribution for the outer region is seen with more intensity for slower loading rates and higher convection coefficients as we will show in the following case studies. The temperature distribution during unloading in the cross section is depicted in Figure 3.17(d) for various twist angles. As it is expected, the heat absorption during reverse phase transformation from martensite to austenite causes a temperature decrease in the cross section during unloading. The significance of the results in this figure is in predicting the temperature distribution in some regions at the end of unloading to be lower than the initial and ambient temperatures. This phenomenon is also observed in the uniaxial loading-unloading of SMA bars and a detailed study of this phenomenon in tension is presented in [128]. As it will be shown in the following case studies, temperature in the

whole cross section may drop below the initial temperature for very slow loadings and high convection coefficients. This phenomenon will be further discussed in the sequel. It is worth noting that the thermomechanical coupled response is strongly affected by the strain history. The results presented in this section correspond a monotonic increase and decrease of twist angle. Any other loading or unloading history, e.g. a sinusoidal or impulsive loading, should be studied separately.

Another case study is considered in order to demonstrate the effect of loading rate on the response of SMA bars. The geometry, material properties, the initial condition, and the boundary conditions are the same as those of the previous example. The response of the bar is studied for four different loading rates $\tilde{\tau}$ =1, 10, 60, and 600 sec ($\tilde{\tau}$ is the total loading-unloading time). For comparison purposes, the results of the exact solution of SMA bars assuming the whole material at a constant initial temperature during loading-unloading are also presented in this section. The shear stress distribution at the end of loading phase (SMA bar is twisted to $\theta = 5$ rad/m and then unloaded) in the cross section of the bar is shown in Figure 3.18(a). As it is seen, the stress distribution is strongly affected by the loading rate. The slope of stress distribution in the region with $0 < \xi < 1$ is increased by increasing the loading rate.

The applied torque versus the twist angle for different loading rates is shown in Figure 3.18(b). The loading rate does not have a significant influence on the applied torque for different loading rates for the present case in which the bar is subjected to free convection by air. We will show in the following examples that the effect of loading rate on the applied torque depends also on the boundary conditions and different results are observed for higher convection coefficients. Figures 3.18(a) and (b) reveal a remarkable difference between both the stress distribution and applied torque of the present analysis and those obtained by considering the isothermal loading-unloading assumption. It is shown in these figures that considering the bar in the constant initial temperature during loading-unloading is unrealistic even for the slow loading cycle with $\tilde{\tau}$=600 sec. We will show in the next example that slow loading rate is not an adequate measure of the isothermal response of SMA bars in torsion; the ambient condition should be considered as well to justify the

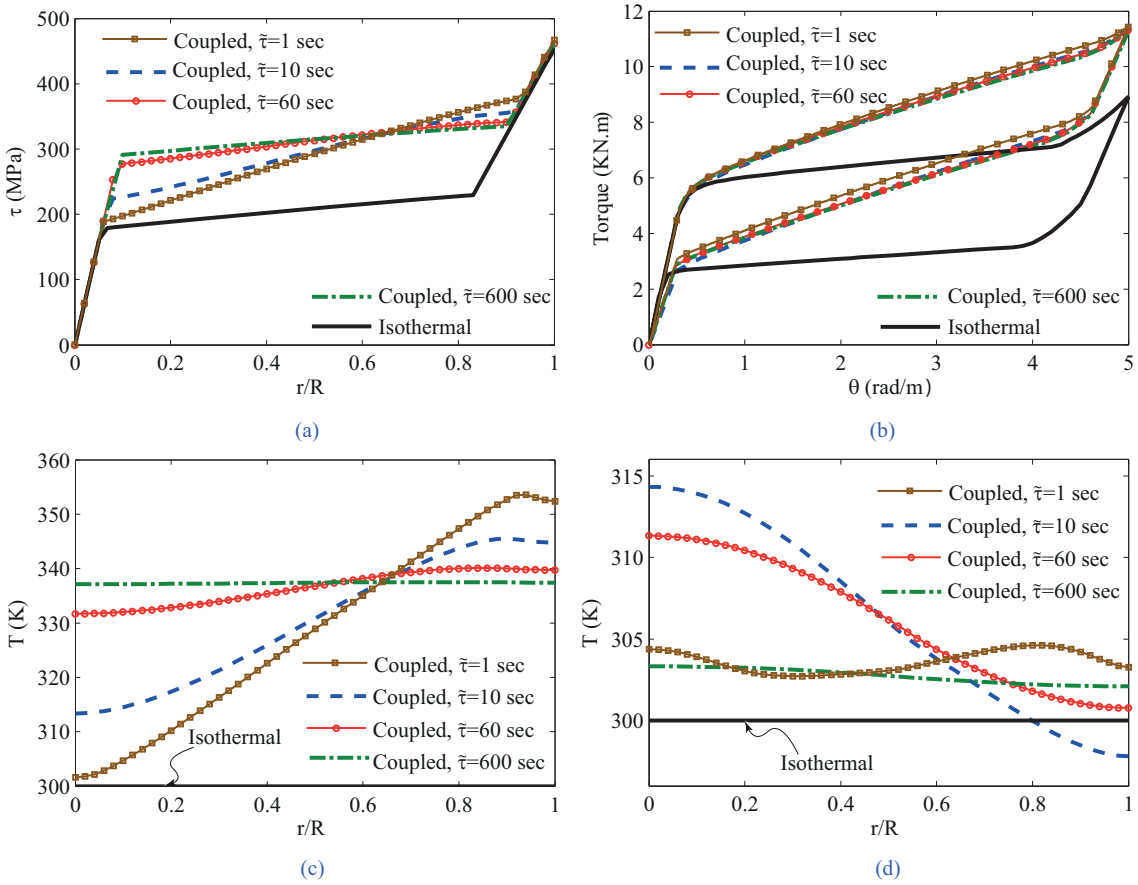

Figure 3.18: The effect of loading rate on (a) shear stress distribution at the end of loading, (b) applied torque versus twist angle, (c) temperature distribution at the end of loading, and (d) temperature distribution at the end of unloading in the cross section of an SMA bar in free convection ($h_\infty = 4.5$ W/m^{2}K).

accuracy of assuming a constant temperature during loading-unloading. The temperature distribution in the cross section at the end of the loading phase is depicted in Figure 3.18(c). As it is shown, the slope of temperature distribution decreases for slower loading rates. This is expected because as explained earlier the temperature in the central austenite core, with no phase transformation heat generation, increases by the heat flux conducted from the outer region. For very fast loading (e.g. see $\tilde{\tau}$=1 sec in Figure 3.18(c)), the generated heat in the outer regions does not have enough time to warm the central austenite core and hence the temperature at the center remains close to the initial temperature. For the slow loading $\tilde{\tau}$=600 sec, the temperature distribution is almost uniform. However, it is

worth mentioning that this uniform temperature is not the same as that of an isothermal loading process (compare the temperature by assuming an isothermal loading with the slow loading in Figures 3.18(c)). Temperature distribution in the cross section at the end of unloading phase is shown in Figures 3.18(d). It is seen that the effect of loading rate on the temperature at the end of unloading is more complicated compared to the previous cases. Temperature distributions for $\tilde{\tau}$=1 and 600 sec are similar. This seems surprising at first. This figure clearly shows the complexity of the coupling between various parameters, e.g. loading rate and boundary conditions on the response of bars in torsion. For having a more precise understanding of the temperature changes during a loading-unloading cycle, and explaining the non-trivial results shown in Figures 3.18(d), the history of temperature at the center of the bar is shown in Figure 3.19.

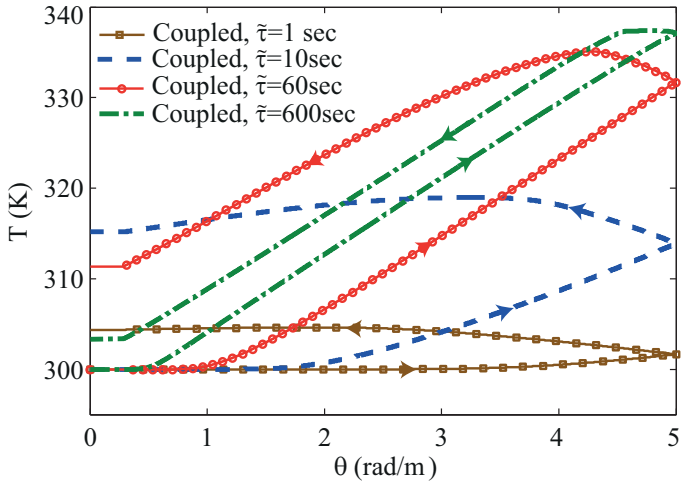

Figure 3.19: The history of temperature at the center of an SMA bar subjected to pure torsion with free convection boundary condition for different loading rates.

Looking at Figure 3.19 and also Figures 3.18(c) and (d) leads to some important conclusions. As it is seen in Figure 3.19, and as explained earlier, during fast loading the material at the center is not warmed by the outer material, and at the end of loading temperature at the center is remarkably lower than those of the outer parts (see Figures 3.18(c)). The heat flux from the outer material toward the center in this case, causes a slight temperature increase at the center during unloading as it is shown in Figure 3.19. The whole process

leads to a temperature slightly above the initial temperature at the end of unloading in fast loading. However, as shown in Figure 3.19, for the slow loading rate of $\tilde{\tau} = 600$ sec, there is enough time for the heat flux to warm the internal austenite core of the bar and the temperature at the center increases significantly during loading. At the end of loading the whole cross section is in an almost uniform high temperature (see Figures 3.18(c)). During slow unloading, temperature of the material in the outer parts decreases due to reverse phase transformation heat absorption and because unloading is slow there is enough time for the heat flux to cool down the material in the central parts of the cross section. As shown in Figure 3.19 temperature at the end of unloading is slightly above the initial temperature and close to the final temperature in fast loading. Considering the four graphs presented in Figure 3.19, it is seen that decreasing the loading rate from $\tilde{\tau} = 1$ sec to $\tilde{\tau} = 600$ sec, the slope of temperature changes during loading and unloading increases. Also it is seen that the area of the hysteretic temperature history increases from $\tilde{\tau}$ =1 sec to $\tilde{\tau} = 60$ sec and then decreases from $\tilde{\tau} = 60$ sec to $\tilde{\tau} = 600$ sec. For extremely fast and slow loadings, the hysteresis areas will be zero (based on the above-mentioned explanation for relatively fast and slow loadings $\tilde{\tau} = 1$ and 60 sec).

In order to study the effect of various ambient conditions on the coupled thermomechanical response of SMA bars subjected to pure torsion, consider an SMA bar with the same initial conditions, material properties, and geometry as the previous case studies. The total loading-unloading time is $\tilde{\tau} = 600$ sec and various ambient conditions are considered. For comparison purposes, the results of the exact solution assuming isothermal loading-unloading are also presented here. In recent years SMA devices have been used in various structures ranging from buildings and bridges to aerospace structures [43, 45, 70]. The SMA devices in these structural applications are exposed to various ambient conditions, e.g. the slow air flow in buildings, fast air flow in aerospace structures, and water flow in bridges. In this case study we consider the free convection by air, forced convection by air flow with speed of $U_\infty = 20$ m/s, and water flow with the speed of $U_\infty = 0.5$ m/s, which is a common value for the speed of water in rivers (the average water velocity in rivers varies from 0.1m/s to 3m/s). Temperature of both air and water flows are assumed

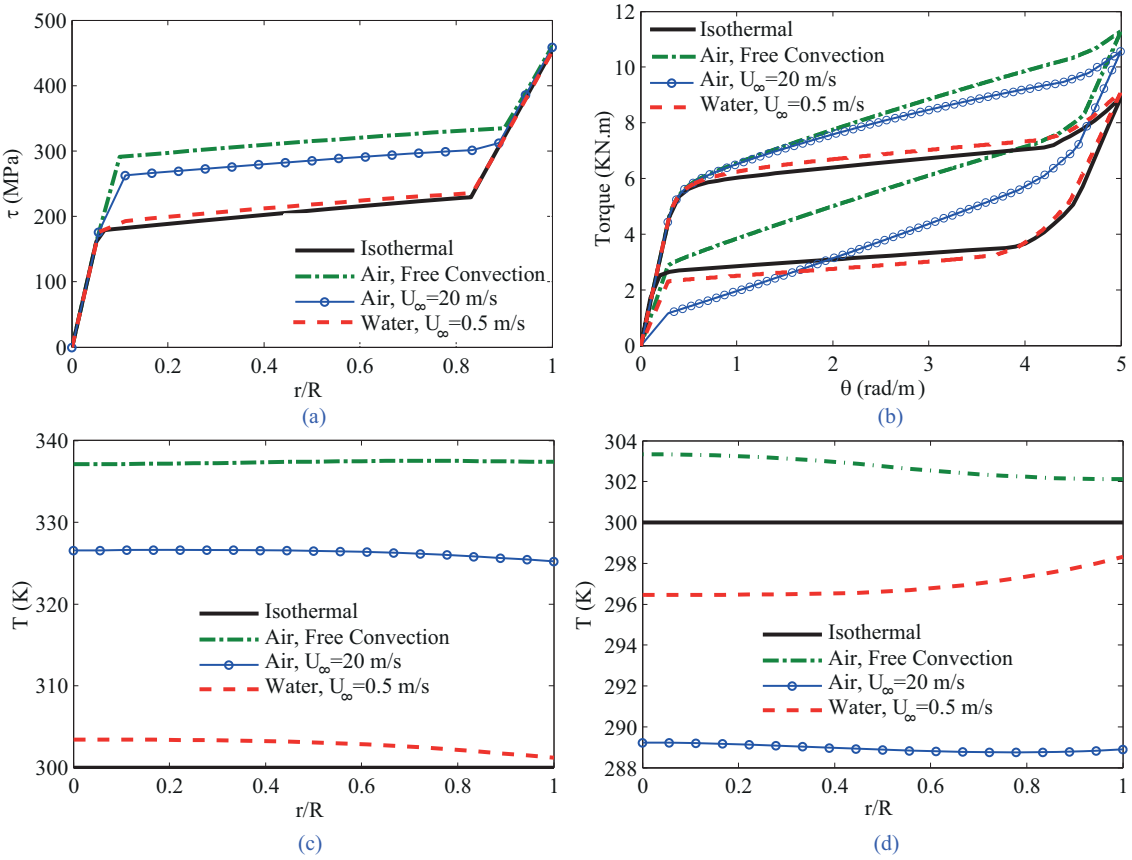

Figure 3.20: The effect of ambient condition on (a) shear stress distribution at the end of loading, (b) applied torque versus twist angle, (c) temperature distribution at the end of loading, and (d) temperature distribution at the end of loading in the cross section of an SMA bar. The total loading-unloading time is $\tilde{\tau}$ =600 sec.

to be $T_\infty = 300$ K. Using the empirical relations for the forced convection (see Mirzaeifar et al. [128] for details), the convection coefficients are obtained as $h_\infty = 91.71\text{W/m}^2\text{K}$ for air flow and $h_\infty = 2529.3\text{W/m}^2\text{K}$ for water flow. The convection coefficient for free air is $h_\infty = 4.5\text{W/m}^2\text{K}$ as explained in the previous case studies. The SMA bar is twisted from rest (fully austenite material) to $\theta = 5$ rad/m and unloaded. The shear stress distribution in the cross section of the bar for different ambient conditions is shown in Figure 3.20(a). It is seen that changing the boundary conditions causes moving of the shear stress plateau without a significant change in the slope (the slope of shear stress distribution varies by changing the loading rate as shown in Figure 3.18(a)).

The applied torque versus the twist angle of the SMA bar is shown in Figure 3.20(b). The most important observation in these figures is the deviation of the results corresponding to each ambient condition from the isothermal results. It is seen that although the loading-unloading is applied in 10 min, only the water flow ambient with a very large convection coefficient is giving similar results to those obtained by assuming a constant temperature during loading-unloading. We will study the effect of various parameters on the validity of isothermal assumption in §5. Temperature distribution at the end of loading is shown in Figure 3.20(c). It is clearly seen that only for the SMA bar operating in water flow the temperature distribution remains constant and close to the initial temperature. For the other cases, although the temperature distribution is almost constant, it is remarkably higher than the initial temperature in the whole cross section. Both the temperature uniformity and temperature change with respect to the initial conditions are studied in §5 for various size, loading rate, and ambient conditions. The temperature distribution at the end of the unloading phase is depicted in Figure 3.20(d). Two important observations are made: temperature in the whole cross section is lower than the initial and ambient temperatures for both the air and water flows, and temperature of the SMA bar exposed to air flow is lower than that of the bar exposed to water flow. These observations can be explained by studying the history of temperature during loading-unloading. The history of temperature at the outer surface of the bar is shown in Figure 3.21. Temperature versus shear stress is shown in this figure to specify the different parts of loading-unloading phases before, during, and after phase transformation. In Figure 3.21, the end of forward phase transformation is denoted by A and the start of reverse phase transformation is marked by the symbol B in all the graphs. We will use these special points in the sequel to explain more details of the material response during loading and unloading.

Starting from $T = \hat{T} = 300$ K the vertical part with no temperature change corresponds to the response of material at the surface before the start of forward phase transformation. This vertical plateau is proceeded by a temperature increase during forward phase transformation. The forward phase transformation continues up to the point A on all the

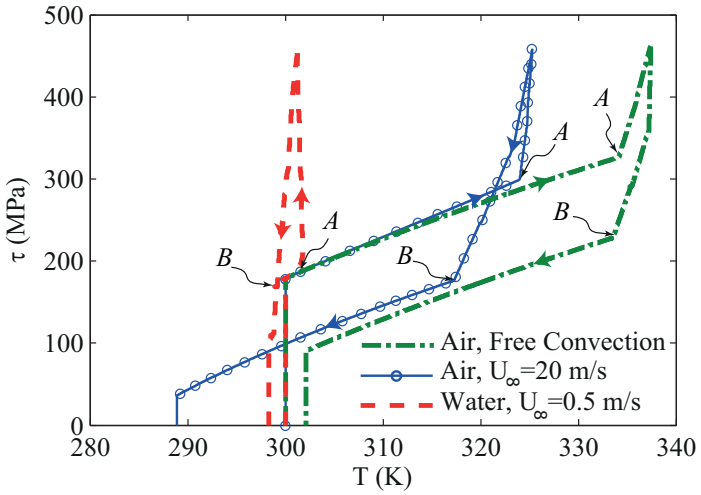

Figure 3.21: Temperature versus shear stress at the surface of an SMA bar subjected to pure torsion for different ambient conditions. The total loading-unloading time is $\tilde{\tau}$ =600 sec.

graphs. As it is seen, with free convection boundary condition, temperature increases remarkably during phase transformation, while with the water flow boundary condition it remains almost constant during this phase. The amount of temperature increase during phase transformation at the surface of the SMA bar in air flow is between the other two boundary conditions. After point A, the phase transformation at the surface is completed and the material is fully transformed to martensite. With further loading, there is no phase transformation heat generation at the surface. At this stage of loading (from the end of phase transformation at A to the end of loading), the material at the surface loses temperature due to cooling by the ambient, and gaining heat by conduction from the inner parts that are experiencing forward phase transformation. For the free and forced convection of air, the conduction from inner parts is dominant and the temperature at the surface increases, while for the water flow, cooling by the ambient is dominant and temperature at the surface decreases slightly. The unloading phase starts with an elastic stage up to point B. In this stage, the reverse phase transformation does not occur. On the other hand, the material is exposed to an ambient that is cooling the bar. In all the cases, temperature decreases at the surface during this stage of unloading. For the free convection boundary

condition, temperature deceases slightly while temperature at the surface of the bar exposed to force convection by air decreases much more. Temperature of bars exposed to water flow does not change much during this stage because the material is not heated too much during loading and the temperature is almost equal to the ambient temperature. This elastic unloading stage is proceeded by the reverse phase transformation from martensite to austenite at the surface and is accompanied by heat absorption. For the free convection case for which the temperature drop during the elastic unloading phase was negligible, the heat absorption during reverse phase transformation returns the temperature near the initial temperature at the end of unloading. However, for the forced air convection for which temperature dropped remarkably, the reverse phase transformation heat absorption causes the material to be at a lower temperature compared to the initial and ambient temperatures at the end of unloading. For the water flow, the high convection coefficient keeps the material temperature close to the ambient temperature during the whole unloading phase (heat flux is from the ambient to the material for overcoming the heat absorption during the reverse phase transformation). Temperature distributions at the end of unloading depicted in Figure 3.20(d) are now clearly understood and temperature history shown in Figure 3.21 explains the reason for observing the lowest temperature for the forced air flow convection. A detailed study of the effect of ambient condition on the temperature history during loading-unloading and a precise study of the conditions required for observing a temperature distribution below the initial temperature is presented by the authors for SMA bars and wires subjected to uniaxial tension in [128].

The presented results clearly show the necessity of using a coupled thermomechanical forrmulation for analyzing torsion of SMA bars. Even for relatively slow loadings, considering the whole material in a constant temperature is not a realistic assumption (see Figures 3.18(a) and (b), and also §5 for a detailed study of the effect of various parameters on the maximum temperature gradient). As it is shown in [127, 129], in general, the cross section of a bar in pure torsion is divided into three regions during both loading and unloading. During loading, the inner region is fully austenite, the outer region is fully transformed into martensite, and the phase transformation is happening in the intermediate region. During

unloading, the inner austenite region unloads elastically and the rest of cross section is divided into two regions. In one of these two regions, the material has been partially transformed to martensite during loading but the reverse phase transformation has not started yet and in the other region the material has experienced both forward and reverse phase transformations [127]. Note that phase transformation occurs in only one of these three regions. Consequently, heat is generated or absorbed in only one region. As a result, a complicated thermomechanical problem should be solved considering the heat flux between these three regions and also the ambient condition. Existence and interaction of these three regions in the cross section causes a more complex temperature distribution in the cross section compared to that of the uniaxial case. This nonuniform temperature distribution is the origin of the significant differences in the stress distributions that are observed between the coupled thermomechanical and isothermal torsion solutions.

3.3.5 Effect of Size, boundary conditions, and loading rate on the temperature distributions in the cross section

The main effect of thermomechanical coupling is reflected in the temperature changes, although this temperature change affects the other parameters including the stress and martensitic volume fraction as well. In order to study the thermomechanical coupling effects, two different parameters are considered in this section: the maximum temperature difference between the surface and center in the cross section, and the maximum temperature change with respect to the initial temperature. We will consider only the loading phase in this section, and the maximum is calculated by comparing all the increments during loading. In some cases the temperature distribution is excessively nonuniform as seen in Figures 3.17 and 3.18. In some other cases, the temperature distribution in the cross section may be approximately uniform, while the temperature in the hole cross section is remarkably different from the initial temperature (e.g. the case shown in Figure (3.20). As shown in the previous sections, the accuracy of assuming an isothermal loading-unloading for SMA bars subjected to torsion strongly depends on the ambient conditions, size, and loading rate. In this section we consider the maximum temperature difference between the surface and center in the cross section, and the maximum temperature change with respect to the the

initial temperature as a measure of the thermomechanical coupling effect on the response of the bar. In other words, when both these parameters are small, the bar subjected to torsion can be assumed isothermal during loading-unloading with an acceptable accuracy.

As the first case study in this section, the effect of convection coefficient and diameter on the temperatures is studied in Figure 3.22. In this case study, the total loading-unloading time is τ=10 sec. Both the considered parameters increase with a steep slope by increasing the diameter. Figure 3.22(a) shows that for large diameters, increasing the convection coefficient decreases the temperature gradient between the surface and center. However, as shown in 3.22(b), the temperature is much higher than the initial temperature even for large convection coefficients for large diameters. It can be concluded that for this loading rate, the isothermal assumption is valid only for small diameters, i.e. SMA wires.

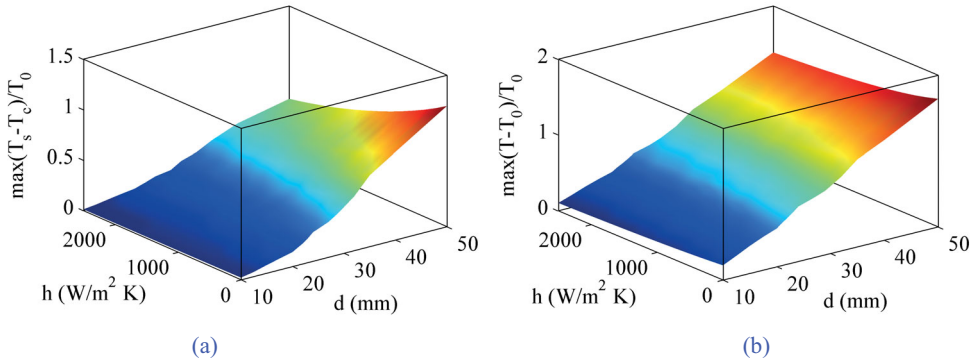

Figure 3.22: The normalized maximum temperature difference between the surface and center (a), and the normalized maximum temperature increase with respect to the initial temperature (b) versus the convection coefficient and diameter (T_0=27°C). The subscripts s and c represent the values measured at the surface and center of the bar, respectively.

The effect of loading rate and diameter on the temperature distribution in loading phase is studied in Figure 3.23 for a bar subjected to free convection of air. The maximum temperature difference between the surface and center during loading is small for slow loading rates even for large bars (Figure 3.23(a)). However, as shown in Figure 3.23(b), the maximum temperature increase with respect to the initial temperature is negligible only for small diameters.

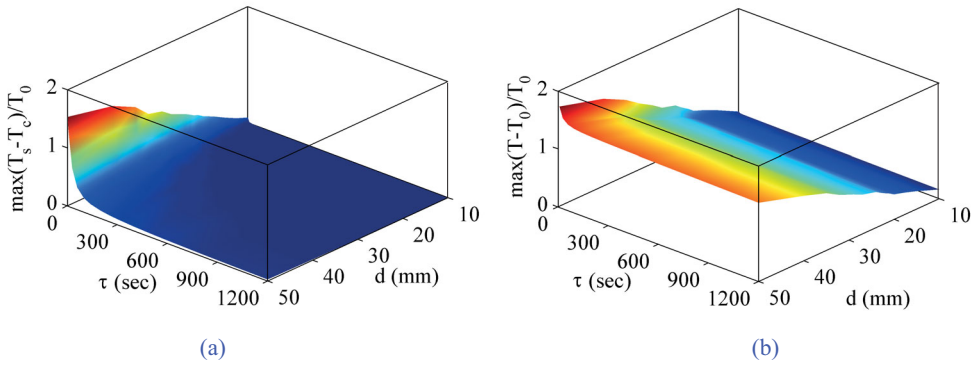

Figure 3.23: The normalized maximum temperature difference between the surface and center (a), and the normalized maximum temperature increase with respect to the initial temperature (b) versus the loading rate and diameter (T_0=27°C). The subscripts s and c represent the values measured at the surface and center of the bar, respectively.

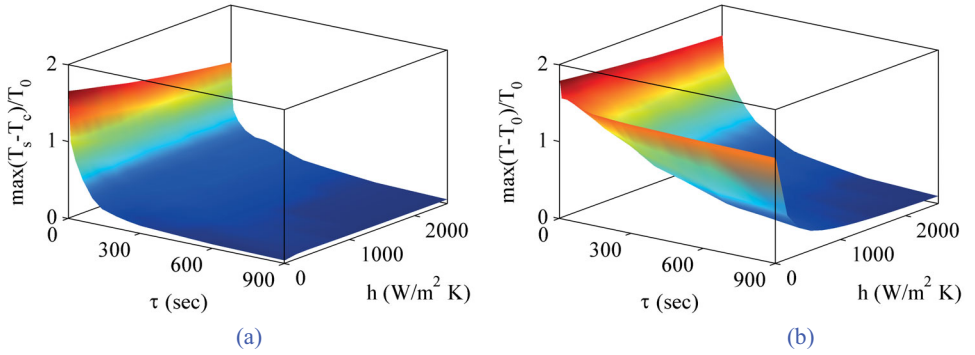

Figure 3.24: The normalized maximum temperature difference between the surface and center (a), and the normalized maximum temperature increase with respect to the initial temperature (b) versus the loading rate and convection coefficient (T_0=27°C). The subscripts s and c represent the values measured at the surface and center of the bar, respectively.

The effect of loading rate and convection coefficient on the temperature distributions is studied in Figure 3.24 for a thick bar (d=5 cm). As shown in Figure 3.24(a), the maximum temperature difference between the surface and center during the loading phase uniformly decreases by decreasing the loading rate for all the convection coefficients. Figure 3.24(b) shows that the maximum temperature difference with respect to the initial temperature is negligible only when both loading time and convection coefficient are large enough.

CHAPTER IV

MICROMECHANICAL ANALYSIS OF TEXTURED AND UNTEXTURED POLYCRYSTALLINE NITI SHAPE MEMORY ALLOYS

4.1 Introduction

In this chapter a micromechanical model that incorporates single crystal constitutive relationships is used for studying the pseudoelastic response of polycrystalline shape memory alloys (SMAs). In the micromechanical framework, the stress-free transformation strains of the possible martensite twinned structures, correspondence variant pairs (CVPs), obtained from the crystallographic data of NiTi are used, and the overall transformation strain is obtained by defining a set of martensitic volume fractions corresponding to active CVPs during phase transformation. The local form of the first law of thermodynamics is used and the energy balance relation for the polycrystalline SMAs is obtained. Generalized coupled thermomechanical governing equations considering the phase transformation latent heat are derived for polycrystalline SMAs. A three-dimensional finite element framework is used and different polycrystalline samples are modeled based on Voronoi tessellations. By considering appropriate distributions of crystallographic orientations in the grains obtained from experimental texture measurements of NiTi samples, the effects of texture, and the tension-compression asymmetry in polycrystalline SMAs are studied. The interaction between the stress state (tensile or compressive), number of grains, and the texture on the mechanical response of polycrystalline SMAs is studied. It is found that the number of grains (or size) affects both the stress-strain response and the phase transformation propagation in the material. In addition to tensile and compressive loadings, textured and untextured NiTi micropillars with different sizes are also studied in bending. The coupled thermomechanical framework is used for analyzing the effect of loading rate and the phase transformation latent heat on the response of both textured and untextured samples. It is shown that the

temperature changes due to the heat generation during phase transformation can affect the propagation of martensite in samples subjected to high strain rates.

4.2 Micromechanical-Based Constitutive Modeling

In recent years, several different classes of constitutive models have been introduced for studying SMAs. Some of these models are developed for studying the macroscopic behavior of polycrystalline SMAs. Phenomenological macroscopic constitutive models are derived by using the Gibbs free energy as the thermodynamic potential and choosing an appropriate set of internal state variables to describe a measure of phase transformation. In these models evolution equations are postulated for the internal variables (i.e. the martensitic volume fraction and the transformation strain) and the second law of thermodynamics is used in order to find thermodynamic constraints on the material constitutive equations [103, 162, 180]. In this work, we consider a micromechanical model in which the transformation strain is related to the crystallographic data. Experimental and theoretical data are used to find the stress free transformation strain of martensite variants exactly [31, 121]. The macroscopic transformation strain is considered as a sum of different active transforming martensite variants and the contribution of each variant is related to the total strain by the volume fraction of that specific variant [59, 110, 119, 120]. The general micromechanical framework is briefly discussed next. It is worth noting that the austenite to martensitic phase transformation in the constitutive framework of this paper is rate-independent in nature and possible effects of strain rate on the transformation are ignored. However, the thermomechanical coupling and the effect of phase transformation latent heat causes the material response to be rate dependent which is not directly caused by the rate dependency of the martensitic transformation.

4.2.1 The Micromechanical Framework

We use the micromechanical framework of Patoor et al. [153]. This model was used by Gall and Sehitoglu [59] to study the the role of texture in tension-compression asymmetry

in polycrystalline NiTi using an averaging scheme. It was also implemented in a three-dimensional finite element formulation for studying the the cyclic thermomechanical behavior of polycrystalline pseudoelastic shape memory alloys [110] based on a simplified model of the grains in the microstructure. The stress-free transformation strain corresponding to the nth martensite variant is given by

$$\hat{\epsilon}_{ij}^n = \frac{1}{2} g(l_i^n d_j^n + d_i^n l_j^n), \tag{4.1}$$

where d is the transformation direction, l is the habit plane normal, and g is the transformation magnitude. We consider the $B2 \rightarrow B19'$ martensitic transformation for NiTi. Theoretically, there are 192 possible variants in NiTi by considering type I and type II twins [110] and this number is even larger when considering the compound twinning in NiTi [69, 193]. However, it has been observed that type II-1 is by far the most prominent twinning mode in NiTi [137] and calculating the transformation strain by considering the active CVPs of this type results in a very good agreement between experimental observations and theoretical predictions [49, 59, 110, 167]. In this case, the number of martensite variants for transformation is $1 \leq n \leq 24$ and the habit plane and transformation direction components are obtained from the crystallographic data (i.e. see Table 1 in [59]). The transformation magnitude for this case is $g = 0.1308$. The total transformation strain in a single grain is the sum of transformation strains from all martensite variants. By defining a martensitic volume fraction corresponding to each variant, the volume averaged transformation strain is given by[1]

$$\epsilon_{ij}^t = \sum_{n=1}^{24} \hat{\epsilon}_{ij}^n \xi^n, \tag{4.2}$$

where ξ^n is the volume fraction of the nth martensite variant. The total martensitic volume fraction is $\xi = \sum_{n=1}^{24} \xi^n$. The total volume fraction and the volume fraction of each variant are always between 0 and 1. For a single crystal, several free energy functions have

[1] Although the phase transformation induced deformation is inhomogeneous at the microscale, it can be assumed that the deformation is averaged over a sufficiently large element that guaranties a smooth response during phase transformation [182].

been reported in the literature [5, 49, 59, 151]. In this section, we use the Gibbs free energy G for developing the coupled thermomechanical constitutive framework for studying polycrystalline SMAs. For obtaining this function, we use the appropriate terms from the complementary free energy Ψ ($\Psi = -G$) introduced by Patoor et al. [151], and the appropriate terms for the thermal free energy given by Anand and Gurtin [5] in the Helmholtz free energy $\hat{\psi}$ for polycrystalline SMAs. The Gibbs free energy is given by:

$$G(\boldsymbol{\sigma}, T, \xi^n) = -\frac{1}{2}\boldsymbol{\sigma} : \mathbb{S} : \boldsymbol{\sigma} - \boldsymbol{\sigma} : \sum_{n=1}^{24} \hat{\boldsymbol{\epsilon}}^n \xi^n + \beta(T - T_0) \sum_{n=1}^{24} \xi^n - \boldsymbol{\sigma} : \boldsymbol{\alpha}(T - T_0)$$
$$+ \rho c \left[(T - T_0) - T \ln\left(\frac{T}{T_0}\right) \right] + \sum_{m,n=1}^{24} H_{nm} \xi^n \xi^m, \tag{4.3}$$

where, $\mathbb{S}$, $\boldsymbol{\sigma}$, T, T_0, $\hat{\boldsymbol{\epsilon}}^n$ and ξ^n are the compliance tensor, local stress tensor, temperature, reference temperature, transformation strain and martensitic volume fraction on the nth variant, respectively. The parameter β is a material constant, $\boldsymbol{\alpha}$ is the thermal expansion coefficient tensor, and c is the specific heat.[2] The last term in (4.3) is an approximation that accounts for martensite variant interactions by introducing an interaction matrix H [151, 153]. The terms in this matrix represent the interaction energy due to the formation of multiple interacting martensite CVPs. The incompatible CVPs are mutually transformed with a higher interaction energy compared to the compatible CVPs. Compatible CVPs have a smaller net intrinsic shear strain compared to incompatible CVPs and the crystallographic data can be used for finding the compatible and incompatible pairs. However, we use a simplified method based on the strain compatibility equation as expressed in detail by Gall and Sehitoglu [59]. Also, the interaction energies for the compatible and incompatible CVPs are assumed constant and temperature independent (Gall and Sehitoglu [59], Table 2) which is shown to give accurate results compared to the experimental measurements [49, 59, 110, 151]. The interface energies are ignored in this model. This is justifiable as the interface energies between the twin-related variants can be ignored because of the

[2]The parameters $\boldsymbol{\alpha}$ and c may be considered as functions of the martensitic volume fraction. However, for the SMAs used in practical applications these parameters are independent of the volume fraction and we have considered them constant throughout this paper, e.g. $\boldsymbol{\alpha} = \boldsymbol{\alpha}^A = \boldsymbol{\alpha}^M$ [128, 162].

compatibility at the interface. The austenite-martensite interface energy is remarkably small compared to the other terms in the energy and can be ignored [78, 111, 155]. However, it should be noted that although these energies can be ignored at the microscale, they play an important role at the nanoscale [85, 101].

By defining a deriving force f_n for each variant as

$$f_n = -\frac{\partial G}{\partial \xi_n} = \boldsymbol{\sigma} : \hat{\boldsymbol{\epsilon}}^n - \sum_{m=1}^{24} H_{nm}\xi^m - \beta(T - T_0), \tag{4.4}$$

the criteria for forward transformation of austenite to the nth martensite variant is given by $f_n = f^{am}$, and the condition for reverse transformation of the nth martensite variant to austenite is expressed as $f_n = f^{ma}$, where f^{am} and f^{ma} are critical energies for A to M and M to A transformations, respectively. During the forward and reverse phase transformations, the consistency condition $\dot{f}_n = 0$ is written as

$$\frac{\partial f_n}{\partial \boldsymbol{\sigma}} : \dot{\boldsymbol{\sigma}} + \frac{\partial f_n}{\partial T} : \dot{T} + \sum_{m=1}^{24} \frac{\partial f_n}{\partial \xi^m}\dot{\xi^m} = 0. \tag{4.5}$$

By substituting (4.4) into (4.5), the consistency condition can be rewritten as

$$\dot{\boldsymbol{\sigma}} : \hat{\boldsymbol{\epsilon}}^n - \sum_{m=1}^{24} H_{nm}\dot{\xi}^m - \beta\dot{T} = 0. \tag{4.6}$$

The condition (4.6) will be used in the next section for finding the incremental change of volume fraction of all the active variants during the phase transformation. It is worth noting that $\dot{\xi}$ is nonzero only for the active variants that satisfy the forward or reverse transformation conditions for the deriving force (4.4) and it is computationally more efficient to write the summations only on the active variants in developing the numerical algorithm.

4.2.2 The Mechanical and Thermal Jacobians

We use a finite element framework for modeling polycrystalline SMAs. For developing an incremental displacement based finite element, in addition to the constitutive relations given in the previous section, the tangent stiffness (mechanical Jacobian) and thermal moduli tensors are also needed. In order to obtain these tensors, the constitutive model of the SMA material should be linearized and represented as an incremental form. Deriving the

mechanical Jacobian is given briefly in the sequel. More details of deriving the Jacobians are given in [110].

For an infinitesimal time increment, Δt, the time rate of each parameter $\mathscr{P}$ can be approximated by $\dot{\mathscr{P}} = \Delta\mathscr{P}/\Delta t$. Using this approximation, (4.6) can be written as a set of q simultaneous equations ($1 \leq q \leq 24$ is the number of variants that satisfy the transformation conditions (4.4))

$$\Delta\boldsymbol{\sigma} : \hat{\boldsymbol{\epsilon}}^n = \sum_{m=1}^{24} H_{nm}\Delta\xi^m + \beta\Delta T. \tag{4.7}$$

Using this approximation, the stress increment is related linearly to the increment of temperature and the martensitic volume fraction of active variants. It can be shown that the martensitic volume fraction increment is also related to the strain increment linearly [110]. The stress increment can be approximated by

$$\Delta\boldsymbol{\sigma} = \frac{\partial\Delta\boldsymbol{\sigma}}{\partial\Delta\boldsymbol{\epsilon}} : \Delta\boldsymbol{\epsilon} + \frac{\partial\Delta\boldsymbol{\sigma}}{\partial\Delta T}\,\Delta T, \tag{4.8}$$

where $\partial\Delta\boldsymbol{\sigma}/\partial\Delta\boldsymbol{\epsilon}$ is the mechanical Jacobian. The stress increment can be written as

$$\Delta\boldsymbol{\sigma} = \mathbb{S}^{-1} : \left(\Delta\boldsymbol{\epsilon} - \sum_{m=1}^{24} \boldsymbol{\Delta}\epsilon^m\right), \tag{4.9}$$

where $\boldsymbol{\epsilon}^i$ is the contribution of transformation strain from the ith martensite variant that is related to the stress free transformation strain of the corresponding variant through the volume fraction as $\boldsymbol{\epsilon}^i = \hat{\boldsymbol{\epsilon}}^i\xi^i$. Substituting (4.9) into (4.7) one obtains

$$\mathbb{S}^{-1} : \left(\Delta\boldsymbol{\epsilon} - \sum_{m=1}^{24} \hat{\boldsymbol{\epsilon}}^m\Delta\xi^m\right) : \hat{\boldsymbol{\epsilon}}^n = \sum_{m=1}^{24} H_{nm}\Delta\xi^m + \beta\Delta T. \tag{4.10}$$

By defining a transformation matrix Γ and a driving force vector F as

$$\Gamma_{mn} = \hat{\boldsymbol{\epsilon}}^m : \mathbb{S}^{-1} : \hat{\boldsymbol{\epsilon}}^n + H_{mn}, \quad F_m = \hat{\boldsymbol{\epsilon}}^m : \mathbb{S}^{-1} : \Delta\boldsymbol{\epsilon} - \beta\Delta T, \tag{4.11}$$

the set of q simultaneous equations (4.10) can be rewritten in the matrix form as

$$[\Gamma]\{\Delta\xi\} = \{F\}, \tag{4.12}$$

where the size of vectors and the transformation matrix depends on the number of active variants (q) and $\{\Delta\xi\}$ is a vector containing the incremental change of volume fraction of all the active variants. This set of equations will be used for calculating the incremental change of volume fractions.

For deriving the mechanical Jacobian, the incremental stress-strain relation (4.9) is differentiated with respect to the strain increment as

$$\frac{\partial \Delta\boldsymbol{\sigma}}{\partial \Delta\boldsymbol{\epsilon}} = \mathbb{S}^{-1} : \left(\mathbb{I} - \sum_{m=1}^{24} \frac{\partial \Delta\boldsymbol{\epsilon}^m}{\partial \Delta\boldsymbol{\epsilon}} \right), \tag{4.13}$$

where $\mathbb{I}$ is the identity tensor. The derivative of the transformation strain with respect to the total strain can be written as

$$\frac{\partial \Delta\boldsymbol{\epsilon}^m}{\partial \Delta\boldsymbol{\epsilon}} = \frac{\partial \Delta\boldsymbol{\epsilon}^m}{\partial \Delta\xi^m} \otimes \frac{\partial \Delta\xi^m}{\partial \Delta\boldsymbol{\epsilon}} = \boldsymbol{\epsilon}^m \otimes \Gamma^{-1}_{mn} \frac{\partial F^n}{\partial \Delta\boldsymbol{\epsilon}}, \tag{4.14}$$

where $\otimes$ denotes the tensor product, and the last term is derived using the inverse of (4.12). Substituting (4.14) into (4.13) gives the mechanical Jacobian to be implemented in the finite element formulation. The thermal Jacobian is obtained by differentiating (4.9) with respect to the temperature increment as

$$\frac{\partial \Delta\boldsymbol{\sigma}}{\partial \Delta T} = \mathbb{S}^{-1} : \left(- \sum_{m=1}^{24} \frac{\partial \Delta\boldsymbol{\epsilon}^m}{\partial \Delta T} \right), \tag{4.15}$$

where the derivative of the transformation strain with respect to temperature is calculated using the chain rule as

$$\frac{\partial \Delta\boldsymbol{\epsilon}^m}{\partial \Delta T} = \frac{\partial \Delta\boldsymbol{\epsilon}^m}{\partial \Delta\xi^m} \frac{\partial \Delta\xi^m}{\partial \Delta T} = \hat{\boldsymbol{\epsilon}}^m \Gamma^{-1}_{mn} \frac{\partial F^n}{\partial \Delta T}. \tag{4.16}$$

Substituting (4.16) into (4.15) gives the thermal Jacobian. Details of implementing the calculated Jacobians and the constitutive equations into the user subroutine (UMAT) in the finite element program is given in Lim and McDowell [110] as a computational step-by-step algorithm. For algorithmic details of the time integration procedure for a rate-independent single-crystal constitutive model for SMAs the readers are referred to [182], which is based on the algorithm developed by Anand and Kothari [4] for rate-independent crystal plasticity.

4.3 Thermomechanical Coupling

We generalize the thermomechanical framework presented by Lim and McDowell [110] in this section by considering a comprehensive description of the energy balance equation for obtaining the thermal coupled equations. It will be shown that the method of relating the latent heat linearly to the rate of change of martensitic volume fraction is a simplification of this general model by ignoring some terms in the energy balance equation. We use a similar method as used previously by the authors for obtaining the governing thermomechanical equations based on phenomenological constitutive models for SMAs [128, 130].

The coupled thermomechanical governing equations for SMAs are derived by considering the first law of thermodynamics in local form (3.1). Using the definition of the Gibbs free energy for a polycrystal (4.3), the time derivative of G is given by

$$\dot{G} = \frac{\partial G}{\partial \boldsymbol{\sigma}} : \dot{\boldsymbol{\sigma}} + \frac{\partial G}{\partial T}\dot{T} + \sum_{n=1}^{24} \frac{\partial G}{\partial \xi^n} : \dot{\xi^n}. \tag{4.17}$$

Substituting (4.17) into (3.4) gives

$$-\left(\frac{\partial G}{\partial \boldsymbol{\sigma}} + \boldsymbol{\epsilon}\right) : \dot{\boldsymbol{\sigma}} - \left(\frac{\partial G}{\partial T} + \rho s\right)\dot{T} - \sum_{n=1}^{24} \frac{\partial G}{\partial \xi^n} : \dot{\xi^n} \geq 0. \tag{4.18}$$

The energy balance equation is obtained by substituting (3.7) and (4.17) into (3.1) as

$$\rho T \dot{s} = -\sum_{n=1}^{24} \frac{\partial G}{\partial \xi^n}\dot{\xi^n} - \mathrm{div}\boldsymbol{q} + \rho\hat{g}. \tag{4.19}$$

The constitutive relation $(3.7)_2$ is used for calculating the time derivative of the specific entropy as

$$\rho\dot{s} = -\frac{\partial \dot{G}}{\partial T} = -\frac{\partial^2 G}{\partial \boldsymbol{\sigma}\partial T} : \dot{\boldsymbol{\sigma}} - \frac{\partial^2 G}{\partial T^2}\dot{T} - \sum_{n=1}^{24} \frac{\partial^2 G}{\partial \xi^n \partial T}\dot{\xi^n}, \tag{4.20}$$

which after substituting (4.3) into (4.20) gives the rate of change of specific entropy as

$$\rho\dot{s} = \boldsymbol{\alpha} : \dot{\boldsymbol{\sigma}} + \frac{\rho c}{T}\dot{T} - \beta\sum_{n=1}^{24} \dot{\xi^n}. \tag{4.21}$$

Substituting (4.21) into (4.19), the final form of the first law is obtained as

$$\rho c\dot{T} = \sum_{n=1}^{24} \left(-\frac{\partial G}{\partial \xi^n} + \beta T\right)\dot{\xi^n} - T\boldsymbol{\alpha} : \dot{\boldsymbol{\sigma}} - \mathrm{div}\boldsymbol{q} + \rho\hat{g}. \tag{4.22}$$

The energy balance (3.13) is used for finding the volumetric heat generation in SMAs as

$$\mathcal{R} = \sum_{n=1}^{24} \left(-\frac{\partial G}{\partial \xi^n} + \beta T \right) \dot{\xi^n} - T\boldsymbol{\alpha} : \dot{\boldsymbol{\sigma}} = \sum_{n=1}^{24} \left(f_n + \beta T \right) \dot{\xi^n} - T\boldsymbol{\alpha} : \dot{\boldsymbol{\sigma}}, \tag{4.23}$$

where the term f_n is defined in (4.4). It is worth noting that during the phase transformation the consistency condition implies that $f_n = f^{\pm}$, where $f^+ = f^{am}$ for the forward phase transformation and $f^- = f^{ma}$ for the reverse transformation. Comparing (4.23) with the expression assumed by Lim and McDowell [110], it is observed that (4.23) can be simplified to the volumetric heat generation obtained in Lim and McDowell [110] by ignoring the second term that corresponds to the heat generation related to the rate of change of stress and also ignoring the temperature dependency of the coefficient that relates the heat generation to the rate of change of martensitic volume fraction.

The volumetric heat generation $\mathcal{R}$ is given to the finite element model in a user subroutine (UMAT). The numerical solution needs the derivatives of the volumetric heat generation with respect to the temperature and strain. For calculating the derivative of $\mathcal{R}$, we use the variation of the volumetric heat generation, which after some manipulations is expressed as

$$\begin{aligned} \delta\mathcal{R} = \frac{1}{\Delta t} \left[\beta \sum_{n=1}^{24} \xi^n - \boldsymbol{\alpha} : \Delta\boldsymbol{\sigma} - \boldsymbol{\alpha} : \frac{\partial \Delta\boldsymbol{\sigma}}{\partial \Delta T} T + (f^{\pm} + \beta T) \sum_{n=1}^{24} \frac{\partial \Delta \xi^n}{\partial \Delta T} \right] \delta T \\ + \frac{1}{\Delta t} \left[(f^{\pm} + \beta T) \sum_{n=1}^{24} \frac{\partial \Delta \xi^n}{\partial \boldsymbol{\epsilon}} - \boldsymbol{\alpha} : \frac{\partial \Delta \boldsymbol{\sigma}}{\partial \Delta \boldsymbol{\epsilon}} T \right] \delta \boldsymbol{\epsilon}, \end{aligned} \tag{4.24}$$

where $\partial\Delta\boldsymbol{\sigma}/\partial\Delta T$ and $\partial\Delta\boldsymbol{\sigma}/\partial\Delta\boldsymbol{\epsilon}$ are the thermal and mechanical Jacobians given in (4.15) and (4.13), respectively. The terms $\partial\Delta\xi^n/\partial\Delta T$ and $\partial\Delta\xi^n/\partial\Delta\boldsymbol{\epsilon}$ are given in $(4.16)_2$ and $(4.14)_2$, respectively. Substituting these parameters into (4.24) gives the derivatives of the volumetric heat generation with respect to temperature and strain as

$$\begin{aligned} \partial\Delta\mathcal{R}/\partial\Delta T &= \beta \sum_{n=1}^{24} \xi^n - \boldsymbol{\alpha} : \Delta\boldsymbol{\sigma} - \boldsymbol{\alpha} : \mathbb{S}^{-1} : \left(- \sum_{m=1}^{24} \frac{\partial \Delta \boldsymbol{\epsilon}^m}{\partial \Delta T} \right) T \\ &+ (f^{\pm} + \beta T) \sum_{m,n=1}^{24} \Gamma^{-1}_{nm} \frac{\partial F^m}{\partial \Delta T}, \end{aligned} \tag{4.25}$$

$$\partial\Delta\mathcal{R}/\partial\Delta\boldsymbol{\epsilon} = (f^{\pm} + \beta T) \sum_{m,n=1}^{24} \Gamma^{-1}_{nm} \frac{\partial F^m}{\partial \Delta \boldsymbol{\epsilon}} - \boldsymbol{\alpha} : \mathbb{S}^{-1} : \left(\mathbb{I} - \sum_{m=1}^{24} \frac{\partial \Delta \boldsymbol{\epsilon}^m}{\partial \Delta \boldsymbol{\epsilon}} \right) T. \tag{4.26}$$

It is worth noting that in the numerical algorithm the summations with the volume fraction

increment in (4.23), (4.25), and (4.26) are only written on the q active variants for which the volume fraction is changing during the current increment.

4.4 Finite Element Modeling

The constitutive equations, the mechanical and thermal Jacobians, the volumetric heat generation, and the derivatives of volumetric heat generation with respect to temperature and strain are implemented in an appropriate user subroutine (UMAT) in the finite element program ABAQUS. The subroutine is written in a local coordinate system. In the finite element model, a separate local orientation is assigned to the elements in each grain. Details of assigning the crystal orientations for textured and untextured samples are given in §4.4.2. All the orientation-dependent parameters are transformed to the local coordinate before passing them into the subroutine, and transformed back to the global coordinate when the subroutine results are given to the finite element code. We use the material properties given by Lim and McDowell [110]. These properties are obtained from DSC tests and manufacturer data for a commercial SMA used in the experiments by Lim [109]. The elastic constants (Lamé parameters) are $\lambda = 69.2$ GPa, and $\mu = 46.2$ GPa. The critical transformation energies are $f^{am} = 17 \times 10^6 \mathrm{Jm}^{-3}$ and $f^{ma} = 7 \times 10^6 \mathrm{Jm}^{-3}$. The mass density is $\rho = 6500 \mathrm{Kgm}^{-3}$ and the chemical energy coefficient is $\beta = 0.6 \times 10^6 \mathrm{Jm}^{-3}\ {}^{\circ}C^{-1}$. The thermal expansion coefficient is $\alpha_{ij} = \alpha\delta_{ij},\ \alpha = 22 \times 10^{-6}/\mathrm{K}$ [92].[3]

4.4.1 Grain-Scale Modeling Based on Voronoi Tessellations

In the previously reported works in the literature that study polycrystalline SMAs using micromechanical based models, the polycrystal structure was designed for resembling the microstructure as closely as possible to the actual structure (see Figure 2 in [110] and Figure 5 in [182]). In these works hexagonal prisms and cubes are used for modeling the geometry of each grain which is far from the actual grains shape. We use a more realistic microstructure in the finite element model for simulating polycrystal SMAs.

[3]The compliance and thermal expansion tensors are anisotropic for single crystal monoclinic martensite NiTi. However, experimentally measured values for the anisotropic material properties of NiTi are not available and these properties can be assumed isotropic with an acceptable accuracy, particularly when the inelastic response is studied [182].

Voronoi tessellations are widely accepted to model polycrystalline aggregates as they provide a realistic approximation of the actual microstructure of non-uniform grain shapes [26, 58, 171, 192]. Voronoi cells are constructed from a set of randomly positioned points (called the generators or Poisson points) in the given domain. Each Voronoi cell is the set of all points in the given set whose distance to the corresponding generator is not greater than their distance to the other generators. Recently, novel frameworks have been introduced for developing FE models based on Voronoi tessellations to generate polycrystalline grain structures for micromechanics simulations [170, 171]. We use four different Voronoi tessellations for modeling polycrystalline samples subjected to uniaxial loading and bending in this section. The microstructure and finite element meshes of these models are shown in Figure 4.1.

The cubic model shown in Figure 4.1(a) consists 100 grains. Each side of this cube is $a = 250$ μm which after considering the number of grains along each side results in a mean grain size of 50 μm that is consistent with the optical micrographs of NiTi [62]. We use two models with different number of grains as shown in Figures 4.1(b) and (c) for studying the uniaxial tension and also bending. The polycrystal structure in Figure 4.1(b) is $38 \times 75 \times 250$ μm and contains a total of 26 grains. The polycrystalline sample in Figure 4.1(c) is $150 \times 300 \times 1000$ μm and constructed by 357 grains. Another sample with circular cross section is also used for studying the uniaxial tension as shown in Figure 4.1(d). This model is constructed by 172 grains with a length and radius of $L = 1000$ and $r = 70$ μm. The selected dimensions in all these models result in a mean grain size of 50 μm. Linear solid tetrahedral elements are used for constructing the FE model (C3D4 and C3D4T). The finite element meshes of the beams are shown in Figure 4.1. Periodic boundary conditions are not used in this section. For nodes lying on the back face perpendicular to the loading direction ($z = 0$) the axial component of displacement is constrained and one node at the corner is fixed in all directions for preventing the rigid body motion. For the bending studies, the nodes in the clamped surface are constrained in all directions.

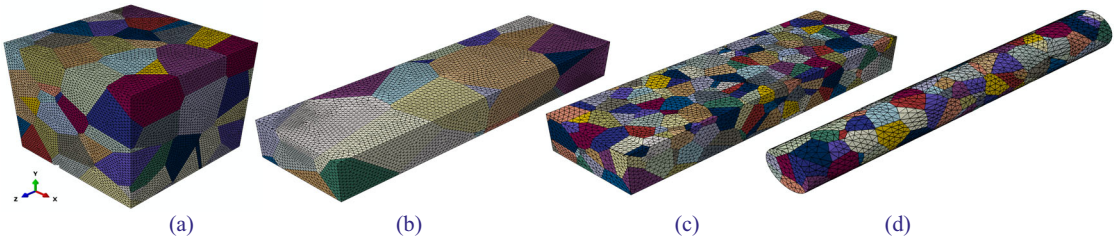

Figure 4.1: The finite element mesh of polycrystalline SMAs with (a) 100 grains, (b) 26 grains, (c) 357 grains, and (d) 172 grains.

4.4.2 FE Modeling of Textured and Untextured Samples

In order to study the effect of texture on the bending response of NiTi, we consider two different distributions of crystal orientations in the grains. For modeling the untextured material, a random orientation is assigned to each grain. For modeling the textured material, the results of texture analysis on a drawn bar using an X-ray diffraction are used [59, 62]. The experimental pole figures resulting from the X-ray analysis show that the [111] directions of the crystal lattice among all the grains are dominantly parallel to the axial direction (z direction in Figure 4.1), while the [001] directions of the crystal lattice are randomly distributed [59, 110]. In the finite element model, for modeling the textured material, all the elements in each grain are assigned an orientation such that the [111] direction of all the orientations is scattered along the axis based on a Gaussian distribution with standard deviation of 10°, while the [001] directions are randomly distributed. In order to verify the distribution of crystal orientations in the microstructure, we used the orientations in all the grains and calculated the orientation distribution functions (ODFs) for plotting the pole figures corresponding to each sample. These pole figures are compared with the experimental data to make sure that the modeled texture is in agreement with the measured data. As an example, the pole figures obtained from the crystal orientations in all the grains for the sample with 357 grains (Figure 4.1(c)) is shown in Figure 4.2. Comparing these figures with the experimental data presented in Gall and Sehitoglu [59] shows that the texture in the material is modeled accurately in the microstructure.

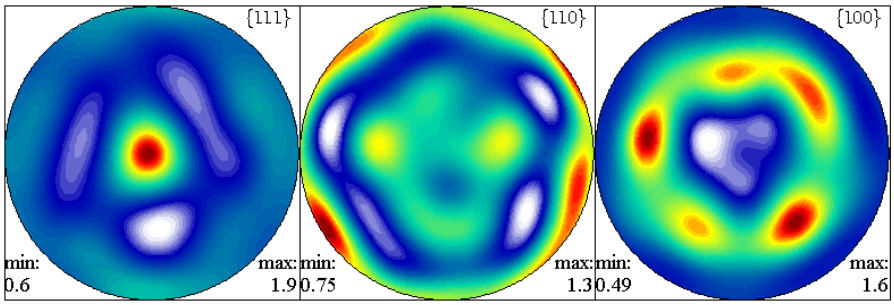

Figure 4.2: The {111}, {110}, and {100} pole figures obtained from the crystal orientations in the grains of the sample shown in Figure 4.1(c).

4.5 Numerical Results

Several different case studies are presented in this section for analyzing various aspects of the mechanical and thermomechanical response of polycrystalline NiTi shape memory alloys. In sections 4.5.1 through 4.5.3 we ignore the thermomechanical coupling by neglecting the effect of phase transformation latent heat. In these sections the loading and unloading processes are assumed isothermal. It is shown that neglecting the latent heat and assuming an isothermal process is valid when the material has enough time for exchanging the generated or absorbed heat with the ambient. This is the case for slow loadings or ambient conditions with high convection coefficients at the surfaces [128]. The thermomechanocal coupling is studied in §4.5.4. It will be shown that the latent heat generated by the phase transformation causes a rate dependency in the response of polycrystalline SMAs. It is also shown that the latent heat affects the martensite propagation between the grains of a polycrystalline NiTi shape memory alloy.

4.5.1 The Role of Texture

In this section the role of texture on the mechanical response of polycrystalline SMAs is studied. As mentioned earlier, the role of texture on tension-compression asymmetry has been studied extensively in the literature. The uncoupled constitutive model of this paper was used by Gall and Sehitoglu [59] for studying the stress-strain behavior of textured and untextured polycrystalline NiTi subjected to tension versus compression. Microstructure of

the polycrystal is not modeled in this work and the constitutive equations are solved for a cluster of 2000 grains with different crystallographic orientations by calculating the transformation strain corresponding to each orientation and summing the transformation strains for all the relevant orientations. With this method, only the global stress-strain response is modeled, and the distribution of solution parameters in a polycrystal cannot be studied. However, by using several experiments Gall and Sehitoglu [59] showed the capability and accuracy of this micromechanical model for studying the role of texture on the tension-compression asymmetry of polycrystalline SMAs. Gall et al. [62] and Lim and McDowell [110] used finite element modeling for studying textured polycrystalline NiTi shape memory alloys. In these works, a simplified geometry was chosen for modeling the microstructure by assuming identical hexagonal prisms as grains in the polycrystal. The role of texture, and also the rate dependency based on a simplified thermomechanical coupled model were studied. Thamburaja and Anand [182] studied the effect of crystallographic texture on the response of polycrystalline SMAs using a crystal-mechanics-based constitutive model and the finite element simulation. The microstructure in the polycrystal is modeled by assuming all the grains as cubes. In this section we use the polycrystalline models based on the Voronoi tessellations for studying the rule of texture on the mechanical response of NiTi shape memory alloys. As the first step the effect of texture on the tension-compression asymmetry is studied by considering a polycrystalline sample shown in Figure 4.1(a). Details of the finite element simulation and modeling the crystal orientations for textured and untextured samples are given in §4.4. The stress-strain responses for textured and untextured NiTi in tension and compression are given in Figure 4.3. The stress-strain response for a single grain (modeled using one cubic element with periodic boundary conditions) with the [111] crystal orientation along the loading direction is also shown in Figure 4.3(b) for comparison purposes.

As shown in Figure 4.3, while the tension-compression response is almost symmetric for the polycrystalline NiTi with random distribution of grain orientations, the response is significantly asymmetric for the textured polycrystal. It is observed that the phase transformation is slightly more favorable in compression compared to tension for the untextured

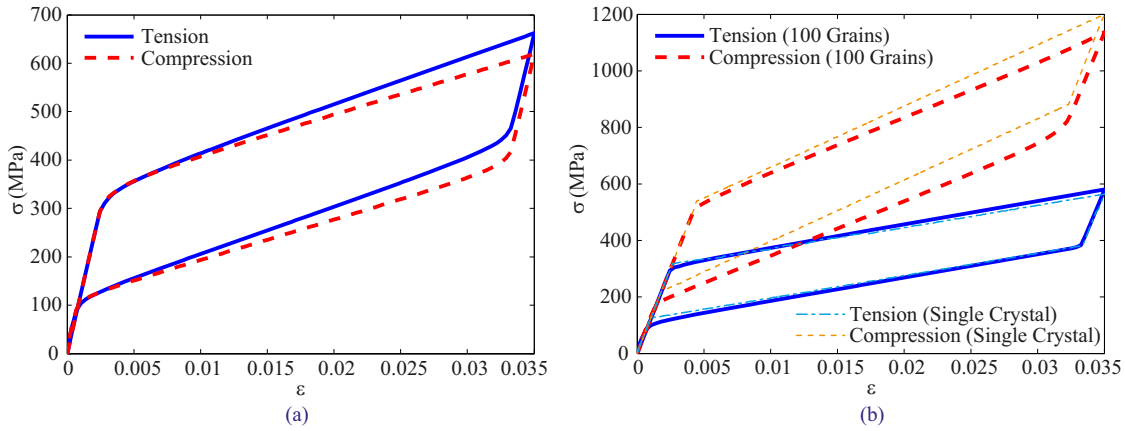

Figure 4.3: Comparison of the stress-strain response in tension and compression for (a) untextured and (b) textured NiTi polycrystal model with 100 grains as shown in Figure 4.1(a).

material as shown in Figure 4.3(a). This result is in agreement with the previously reported studies of polycrystalline SMAs based on Taylor models [138], self-consistent models [59], and micromechanical models in conjunction with simplified finite element simulations [62]. The stress-strain curves for a textured polycrystal and a [111] oriented single crystal are shown in Figure 4.3(b). As observed earlier, the crystallographic texture is the origin of tension-compression asymmetry in polycrystalline SMAs and this phenomenon is reflected in the similarity between the single crystal and textured polycrystalline responses [63] as shown in Figure 4.3(b). The tension-compression asymmetry for the [111] oriented single crystal can be explained theoretically by considering the Schmid factors of the most favorably oriented martensite variant for uniaxial compression and tension directions, which are 0.27 and 0.39, respectively [60, 153]. It is worth noting that in modeling the textured polycrystalline SMAs in Gall et al. [62], the [111] crystallographic direction of the grains are randomly wobbled around the loading direction within tolerances of 0-5 degrees or 0-10 degrees. However, as explained in §4.4.2, in the present work we use a Gaussian distribution for modeling the textured polycrystal. This is more realistic and has the capability of modeling different textures more accurately by changing the standard deviation in the distribution. By using a Gaussian distribution with a relatively small standard deviation

(10° in the present work) for the crystallographic directions, the stress-strain curves of the polycrystal are more similar to the response of a single [111] oriented crystal compared to a random distribution between 0 and 10 degrees. This happens because in the Gaussian distribution with small standard deviations most of the orientations are aligned near the [111] direction while for a random distribution they are freely distributed between 0 and 10 degrees. Comparing the results of the present work with those of Gall et al. [62] we observe that the difference between the response of a single crystal and a polycrystal is more significant in Gall et al. [62]. However, the present model is capable of modeling various textures accurately by choosing appropriate standard deviations in the Gaussian distribution.

Comparing the simulation results in Figure 4.3(b) with the experimentally measured stress-strain curves for polycrystal and single crystal NiTi reported by Gall et al. [63] it is clear that the present model is predicting the key features of the response accurately. Consistent with the experiments, the model predicts a slight decrease in the critical transformation stress for the polycrystal compared to the single crystal. Decreasing the stress levels for a polycrystal is more prominent in compression, which is consistent with the experimental observations. This can also be explained based on transformation Schmid factor arguments [62, 153]. It is worth noting that a similar study was presented by Gall et al. [62] and the stress-strain curves for a single crystal and a polycrystal were compared. As mentioned earlier, the structure of grains in the polycrystal is modeled assuming a uniform shape for all the grains. The simulation results in Gall et al. [62] show that the stress-strain curves are not sensitive to the number of grains and the results are not affected by increasing the number of grains. This finding was also used by Lim and McDowell [110] for concluding that a single mesh and microstructure is adequate for studying the general response of polycrystalline SMAs. However, we will show in the present work that the rapid convergence of results by increasing the number of grains in the previous works is due to the assumption of uniformity of the grains shapes. We will show in the next section that for the accurate microstructure representation used in this section, the material response is highly affected by the number of grains, which can be understood as a size effect.

4.5.2 The Size Effect

In this section, the effect of size (or the number of grains) on the response of textured and untextured polycrystalline SMAs is studied. The stress-strain curves for a cubic polycrystal shown in Figure 4.1(a) are presented in §4.5.1. In this section we study the uniaxial tension and compression for the polycrystal models shown in Figures 4.1(b) and (c). As mentioned in §4.4.1 the model of Figure 4.1(b) contains a total of 26 grains and by considering a mean grain size of 50 μm the size of this model is $38 \times 75 \times 250$ μm. The polycrystal model in Figure 4.1(c) is $150 \times 300 \times 1000$ μm and contains 357 grains. The results in this section can also be compared with the curves in the previous section for a cubic model with 100 grains. However, one should notice that the number of grains along the loading axis and in the cross section for the models of this section are different from the cubic model in the previous section and the results cannot be compared directly. We will also study the response of a single crystal with [111] direction along the loading axis for comparison purposes.

The stress-strain curves for the uniaxial loading of polycrystalline SMAs in tension and compression are shown in Figure 4.4. The uniaxial stress-strain curves for untextured models are shown in Figure 4.4(a). It is observed that the difference between tensile and compressive responses is more prominent for the larger model with 357 grains. Comparing the results in this figure with those of Figure 4.3(a) shows that the difference between tensile and compressive responses is remarkably larger for the rectangular cuboid models of Figures 4.1(b) and (c) compared to the cubic model of Figure 4.1(a). This shows that not only the number of grains in the micromechanical model but also the shape of the sample can affect the mechanical response of polycrystalline SMAs.

The stress-strain curves for the textured polycrystalline samples are shown in Figure 4.4(b). Similar to the cubic model with 100 grains, for both sizes considered in this section the difference between the tensile and compressive responses is remarkably larger for NiTi polycrystal with a dominant $< 111 >$ fiber texture compared to the polycrystal with a random distribution of orientations. Figure 4.4(b) for textured polycrystal NiTi shows that

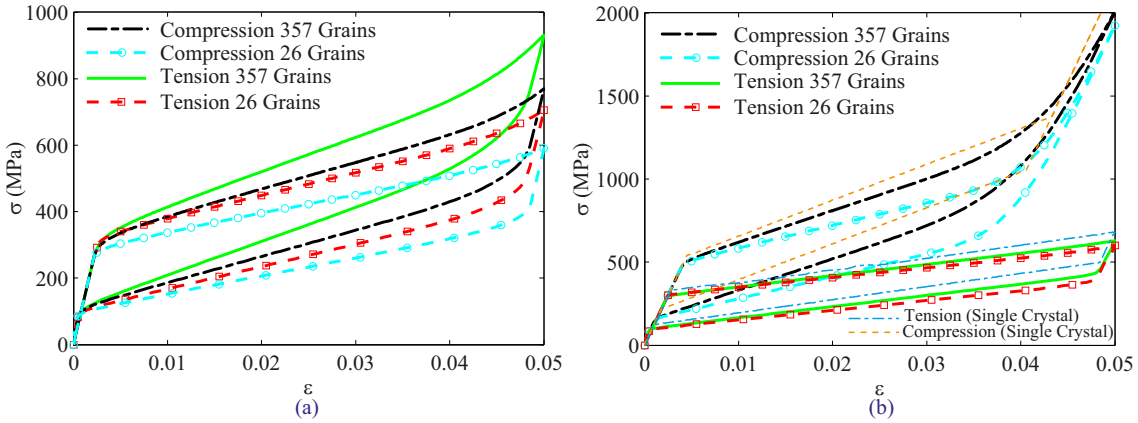

Figure 4.4: The effect of size on the stress-strain response in tension and compression for (a) untextured and (b) textured NiTi polycrystal models with 26 and 357 grains as shown in Figures 4.1(c) and (d).

while the tensile response is not highly affected by the size, the compressive response is remarkably different for the small and large textured polycrystal samples. This phenomenon can be explained by considering the stress-strain curves for a single [111] oriented crystal (shown with thin lines in the figure). As discussed in the previous section, the Schmid factor arguments explain the effect of adding more grains with [111] orientations around the loading direction on increasing the difference in tensile and compressive responses. As seen in Figures 4.4(a) and (b), in the model with 26 grains, the textured polycrystal contains a small number of grains with [111] orientation and the response is slightly moved from an untextured sample toward the single [111] oriented crystal. However, adding a large number of grains with [111] orientation along the loading axis in the model with 357 grains leads to a stress-strain curve similar to that of the single crystal. The important observation is that the compressive response is more sensitive to the size (or the number of grains) compared to the tensile response. It is worth noting that we are not considering the thermomechanical coupling in this section and the size effect studied here is not originated from the size dependence of exchanging the latent heat with the ambient that was previously studied at the macrosclae [128]. Also, it should be noted that periodic boundary conditions are not imposed and our simulations correspond to the mechanical response of

NiTi micropillars with free surfaces. Conducting experiments on some NiTi micropillars for studying the size effect and validating the theoretical observations will be the subject of a future communication.

To further understand the effect of size and texture on the response of polycrystalline SMAs, the distribution of martensitic volume fraction is also studied. The initiation and propagation of martensite during forward phase transformation (austenite to martensite) is studied for small and large models with 26 and 357 grains in tension and compression. In each case, both random and textured distributions of crystallographic orientations are studied. In order to label the contour plots in this section we use a three-letter code in which the first letter stands for texture (U for untextured and T for textured crystallographic orientations), the second letter defines the size (L for the larger model with 357 grains and S for smaller model with 26 grains), and the third letter represents the loading (T for tension and C for compression). For comparison purposes, a uniform color coding is selected in all the contour plots in Figures 4.5 and 4.6 in which red represents martensite and blue shows austenite. The propagation of martensitic volume fractions in large polycrystalline NiTi samples for strains between 3 and 5% are shown in Figure 4.5. The same results for the smaller model with 26 grains are shown in Figure 4.6.

Comparing the contour plots in Figures 4.5 and 4.6 shows that the martensitic volume fraction is strongly affected by the texture, the number of grains and the stress state. Comparing the first two rows in Figure 4.5 shows that while the phase transformation initiates from a large number of grains distributed in the sample for the large polycrystal subjected to tension with random orientation of grains (ULT), in the large textured sample subjected to tension (TLT) the phase transformation initiates in a limited number of grains with more favorable crystallographic directions for phase transformation in tension. Comparing tensile and compressive responses of these models in Figure 4.5 reveals an important effect of texture on the martensite propagation in polycrystalline SMAs. Comparing the tensile and compressive responses for the untextured large samples (ULT and ULC) shows that the phase transformation propagates similarly for both stress states. However, the same comparison for the textured samples (TLT and TLC) shows that the spatial spread

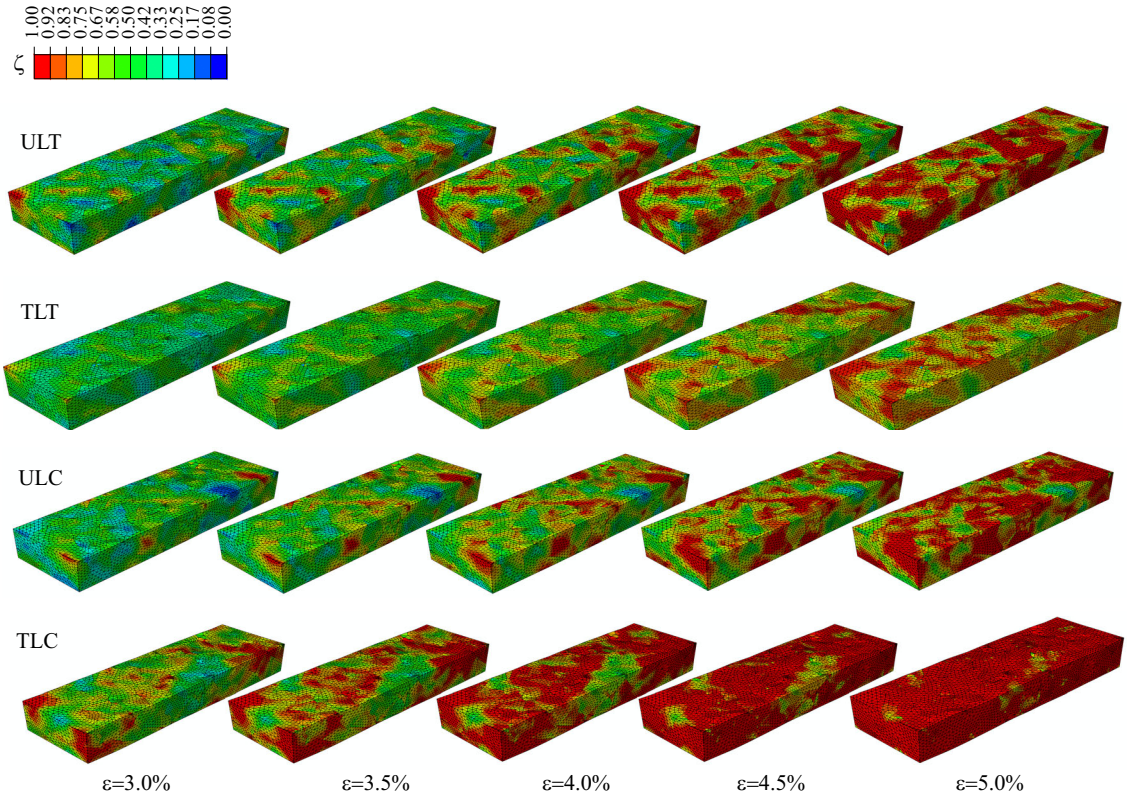

Figure 4.5: The initiation and propagation of martensite in textured and untextured NiTi polycrystalline model with 357 grains subjected to 5% tensile and compressive strain. The three-letter labels stand for texture (U for untextured and T for textured), size (L for large and S for small model), and loading (T for tension and C for compression), respectively.

of phase transformation is remarkably more rapid under compression. It is worth noting that the spatial spread of phase transformation initiation in textured polycrystal samples is more rapid in tension compared to compression as shown by Gall et al. [62]. They studied the phase transformation initiation (at least 0.05% martensite was assumed as the initiation of phase transformation) and it was observed that the number of grains in which the phase transformation has been started is larger in tension compared to compression at equal strains. This is consistent with the stress-strain response shown in Figure 4.4 because the phase transformation initiation occurs at lower strain values for tensile loading. However, we are studying the contour plots of the martensitic volume fraction and as shown in this section, the spatial spread of grains with a full transformation from austenite to martensite (shown with red in the contour plots) is more rapid in compression. This result is also

consistent with the stress-strain curves shown in Figure 4.4 where the phase transformation is completed for smaller strains in compression compared to tension. As shown in Figure 4.4(a), the compressive and tensile responses for the untextured material are similar. This is the reason for observing a similar propagation of martensitic volume fractions in ULT and ULC models (Figure 4.5). The martensitic volume fraction distributions for smaller samples (with 26 grains) are shown in Figure 4.6. The grain boundaries are distinguished more clearly in this figure (see Figure 4.1(b) for a better view of the grain boundaries).

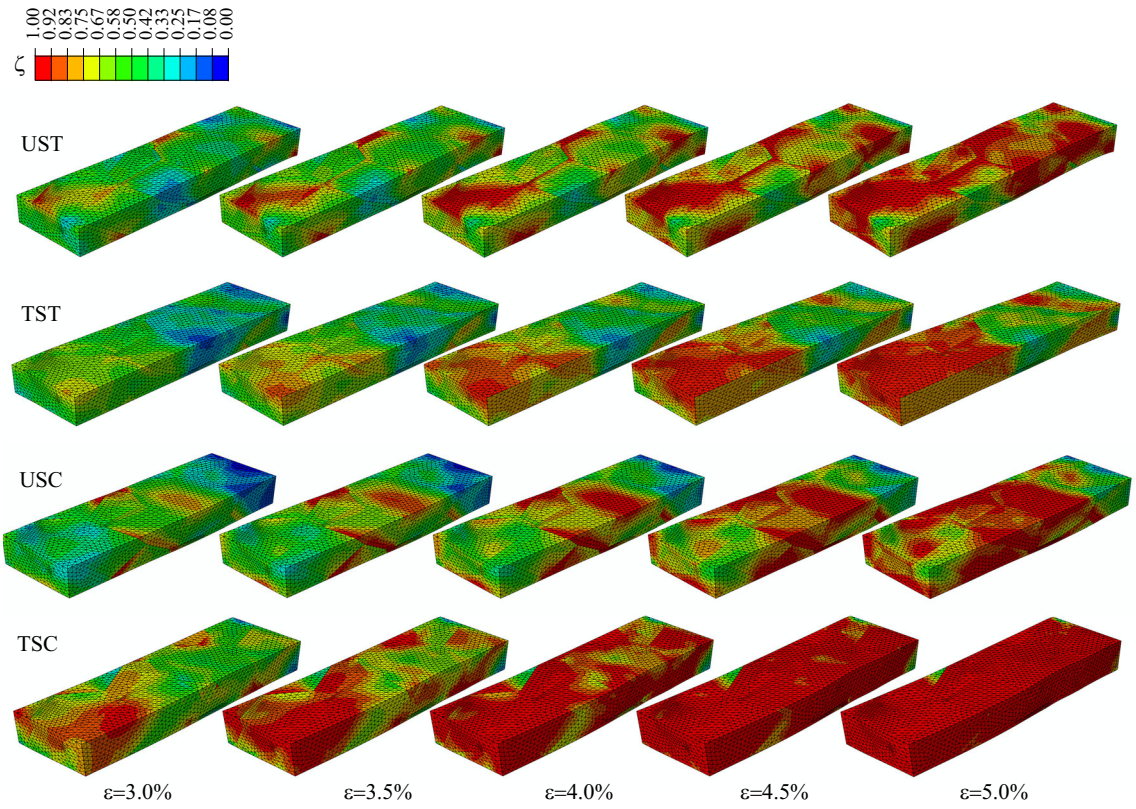

Figure 4.6: The initiation and propagation of martensite in textured and untextured NiTi polycrystalline model with 26 grains subjected to 5% tensile and compressive strain. The three-letter labels stand for texture (U for untextured and T for textured), size (L for large and S for small model), and loading (T for tension and C for compression), respectively..

Comparing the untextured and textured small samples in tension (UST and TST in Figure 4.6) shows that the phase transformation initiates from more grains in the untextured material. Also, it is observed that in the untextured samples (both UST and USC in

Figure 4.6) the phase transformation initiation from the grain boundaries is more prominent compared to the textured polycrystal samples. This happens because in the untextured samples there are several boundaries between grains with a large mismatch between the crystallographic orientations, while in the textured samples the orientations in adjacent grains are more likely similar. It can be concluded that the initiation of phase transformation from the grain boundaries plays a more important rule in the untextured material compared to the textured case. Comparing the tensile and compressive responses for the textured and untextured samples shows that the spatial distributions of phase transformation are similar for the large and small samples.

Comparing the results in Figures 4.5 and 4.6 shows that the number of grains (or size) has a strong effect on the phase transformation propagation in polycrystalline SMAs. As shown in these figures, the role of phase transformation initiation at the grain boundaries is more prominent in the small samples and the spread of the fully transformed regions is affected by the number of grains. This difference in the phase transformation propagation is related to the size effect observed in the stress-strain responses (Figure 4.4).

4.5.3 Bending Analysis of Microscaled Beams

In this section the numerical results for bending analysis of textured and untextured polycrystalline SMA beams are presented. The FE models are shown in Figures 4.1(b) and (c). All the nodes in one end are constrained in all directions and a transverse displacement is applied to the nodes in the other end. The final transverse deflection δ is set such that δ/h=2 for both beams, where h is the thickness. The loading phase is then followed by an unloading phase that is modeled by setting the deflection to zero. The geometrical nonlinearity is considered in the FE solution for studying both the transverse and in-plane deflections. The reaction forces at the clamped nodes are computed and summed for obtaining the total reaction force during loading-unloading. The force-deflection response of the beams with 26 and 357 grains are shown in Figures 4.7(a) and (b), respectively. In both cases of coarse and fine grains, the texture effect is studied by comparing the response of a beam with texture versus an untextured beam with random crystal orientations.

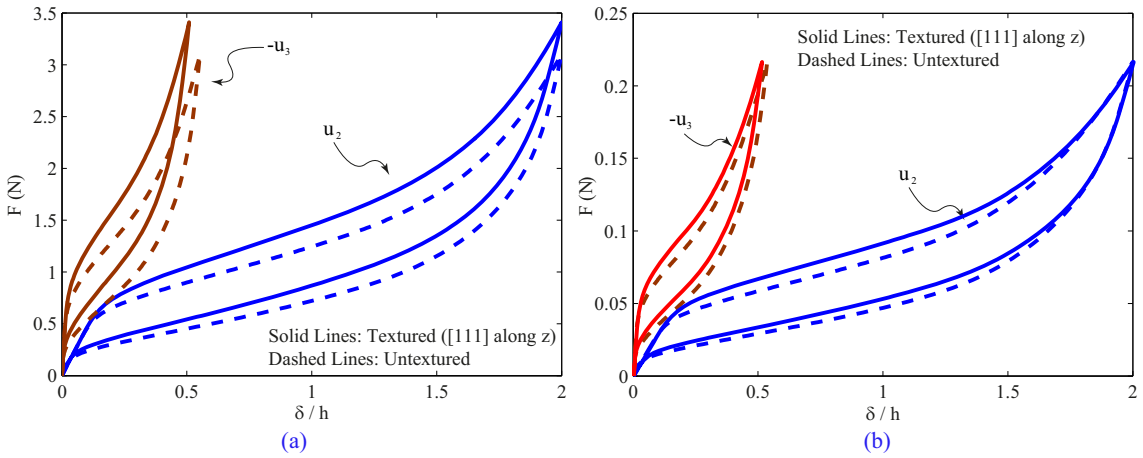

Figure 4.7: In-plane and transverse tip deflection for a polycrystal beam subjected to bending. The response of textured and untextured beams are compared for polycrystal structures with (a) 26 grains, and (b) 357 grains.

Comparing Figures 4.7(a) and (b) shows that the effect of texture on the force-deflection response is more significant in the polycrystalline beam with large number of grains. The force-deflection response for the smaller beam with 26 grains is almost identical for the textured and untextured crystal orientations. We consider the polycrystal structure with 357 grains for studying the stress and martensitic volume fraction distribution in the beams subjected to bending in the following. All the distributions correspond to the loading phase with δ/h=1.5. The martensitic volume fraction (summation of volume fraction of all active martensite variants) is shown in Figure 4.8. The volume fraction distributions in textured and untextured beams are shown in Figures 4.8(a) and (b), respectively. Comparing the volume fraction distribution near the clamped edge in these figures shows the asymmetric distribution of matrensite volume fraction in the textured beam. It was previously shown that while an untextured NiTi polycrystalline response is smei-symmetric in tension-compression, the tensile and compressive responses are remarkably different in a textured polycrystal [59]. As mentioned in §4.5.1, this happens because in the textured material, the majority of grains are oriented along the [111] crystallographic direction, which is soft under tensile loading and hard under compression. In the untextured samples the crystallographic directions are randomly distributed and that leads to an almost symmetric response

in tension-compression. As shown in Figure 4.8(a), the neutral axis position (marked with a red arrow on the figure) is shifted towards the compressive part of the cross section for the textured beam, while it is near the center line for the untextured beam due to the symmetry in tension-compression response. The response of macro SMA beams subjected to bending was studied previously by the authors based on phenomenological constitutive frameworks [**?**]. Comparing the results of this section with those presented in **?**] shows that the J_2-based phenomenological models are suitable for modeling the response of untextured polycrystalline materials and $J_2 - I_1$-based models can be used for studying the textured polycrystal SMAs in bending with an acceptable accuracy.

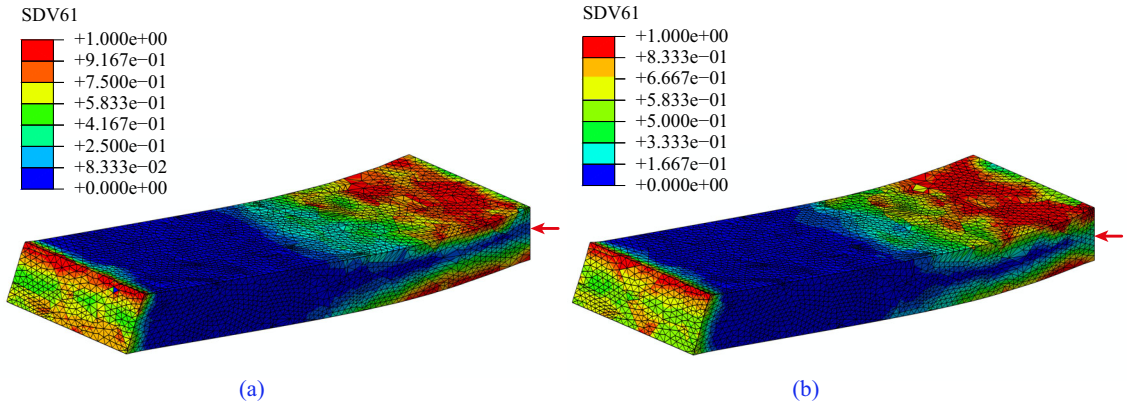

Figure 4.8: Martensitic volume fraction distribution in a polycrystal beam with 357 grains subjected to bending with (a) textured and (b) untextured crystal orientations.

The normal stress distribution is compared for the textured and untextured beams in Figures 4.9(a) and (b). An asymmetry in the stress distribution for the textured material is observed. Also it is observed that the maximum compressive stress is remarkably larger than the maximum tensile stress in the textured beam, which is consistent with the stress-strain curves obtained in §4.5.1.

4.5.4 Thermomechanical Coupling in Polycrystalline SMAs

In this section the effect of phase transformation latent heat is considered and the thermomechanical response of textured and untextured polycrystalline SMAs is studied. In the previous numerical case studies, an isothermal loading-unloading process was assumed,

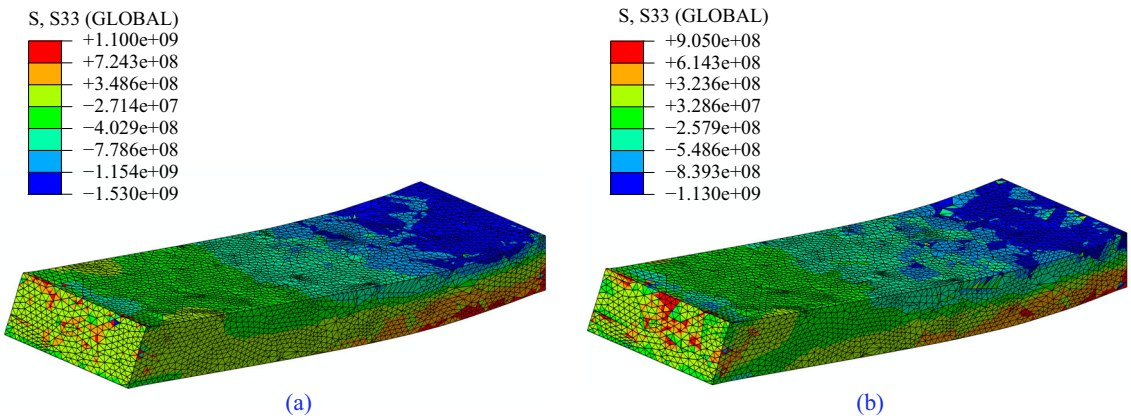

Figure 4.9: Normal stress distribution in a polycrystal beam with 357 grains subjected to bending with (a) textured and (b) untextured crystal orientations.

which is valid when the phase transformation latent heat can be exchanged with the ambient and the material temperature is constant during the whole process. In this section we consider the latent heat effect and also the temperature changes due to generation or absorption of latent heat in forward or reverse phase transformation as explained in §4.3. As mentioned earlier, our model considers a more accurate description for the rate of latent heat generation and its derivatives with respect to strain and temperature compared to the simplified works previously reported in the literature [49, 110]. Also, the more accurate micromechanical model based on Voronoi tessellations sheds some light on the effect of thermomechanical coupling on the the propagation of phase transformation in polycrystalline NiTi.

In this section, a polycrystalline model with circular cross section is used. This model with 172 grains is shown in Figure 4.1(d). The details of the finite element model and mechanical boundary conditions are similar to the previous case studies in §4.4. Continuous solid tetrahedral elements with added temperature degrees of freedom (C3D4T) are used. The initial temperature is $T_0 = 293$K and the material is austenite initially. Free convection with heat transfer coefficient $h_\infty = 10\ W/m^2K$ is considered at the sides of the sample. Two different loading rates of $\dot{\epsilon} = 10^{-4}$ and $10^{-1}\ s^{-1}$ are studied for simulating the near isothermal and near adiabatic cases, respectively. The polycrystal average stress-strain

curves for these two loading rates are shown in Figure 4.10 for untextured and textured samples.

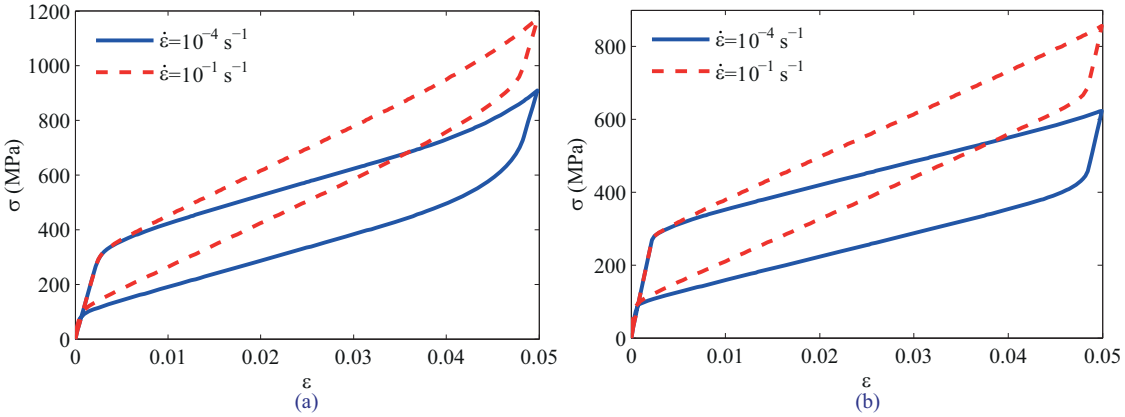

Figure 4.10: The effect of loading rate by considering the thermomechanical coupling on the stress-strain response of (a) untextured and (b) textured polycrystalline NiTi samples (the micromechanical model is shown in Figure 4.1(d)).

As shown in Figure 4.10, in the vicinity of thermomechanical coupling, the loading rate has a significant effect on the mechanical response of both samples with textured and random distributions of crystal orientations. Comparing the stress-strain curves for slow and fast loadings in each case shows that the maximum stresses at the end of the loading phase are increased by 29.8% and 37.8% in fast loading for untextured and textured samples, respectively. For the fast loading, $\dot{\epsilon} = 10^{-1}\ s^{-1}$, the slope of stress-strain curve is increased and the hysteresis area is slightly decreased for both untextured and textured samples. These observations are both consistent with similar responses at the macroscale NiTi samples studied by a phenomenological constitutive framework by ignoring the micromechanical structure [128], and also experimental results for large polycrystalline SMA samples [16]. The average temperature of the polycrystal during loading-unloading is studied in Figure 4.11. The temperature at all the integration points is averaged for calculating the parameter T in this figure.

As it is expected, the temperature change in slow loading is negligible while a significant temperature change is observed in fast loading $\dot{\epsilon} = 10^{-1}\ s^{-1}$. Figure 4.11 shows that during

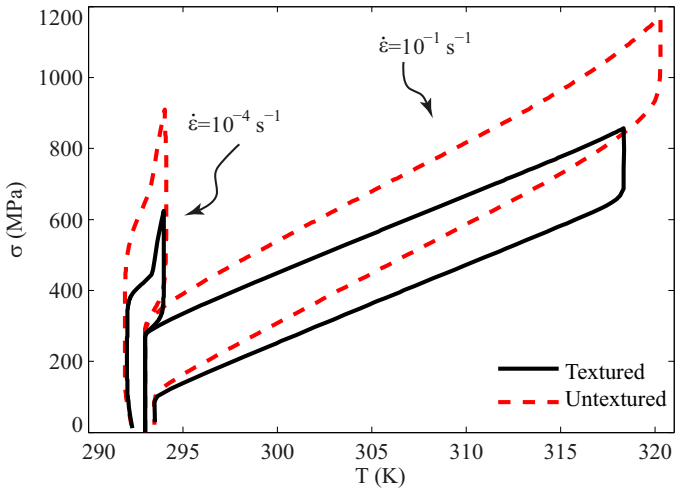

Figure 4.11: Average temperature of untextured and textured polycrystalline NiTi samples subjected to slow and fast loadings.

loading for the strain rate $\dot{\epsilon} = 10^{-1}\ s^{-1}$, the temperature increase in the textured material is larger at a specific stress (the temperature increases form 297 to 309K at $\sigma = 800$MPa in the untextured sample while the temperature increases to 316K at the same stress level in the textured sample). However, the temperature change in the untextured sample is larger at the same strain compared to the textured material (at the end of loading with $\epsilon = 0.05$ the temperature is increased to 318K in the textured material, while the temperature in the untextured sample is 320K). The temperature changes are consistent with the results obtained from phenomenological constitutive equations for polycrystalline SMAs at large scales [128]. As shown in Figure 4.11, the average temperature of the sample is lower than the initial temperature at the end of loading for the slow loading rate. This phenomenon is also observed in the calculations based on the phenomenological constitutive equations. This effect can be explained as follows [128]. As shown in Figure 4.10, at the beginning of unloading, before the start of reverse phase transformation, phase transformation does not occur. During this step, the phase transformation heat is not generated and the material is cooling due to convective heat exchange with the ambient. This temperature loss is followed by heat absorption during reverse phase transformation and causes the material to be colder than the initial and ambient temperatures at the end of the unloading phase.

The effect of thermomechanical coupling and the latent heat on the propagation of phase transformation in the polycrystalline material is studied next. We consider the textured sample subjected to slow and fast loadings. The stress-strain curves for this sample are shown in Figure 4.10(b). The martensitic volume fraction distributions at the end of the loading phase in the textured polycrystalline SMA samples are shown in Figure 4.12.

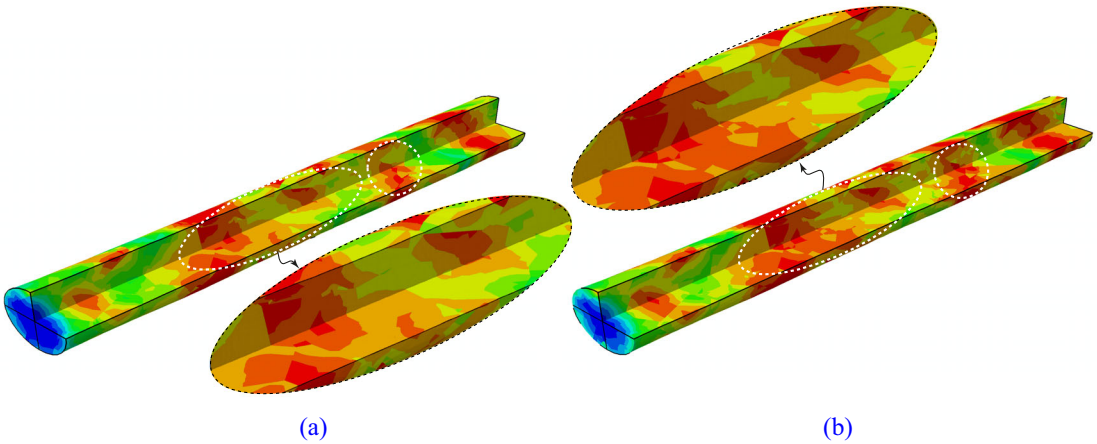

Figure 4.12: The martensitic volume fraction distributions at the end of the loading phase in the textured polycrystalline SMA samples subjected to (a) fast and (b) slow loadings (the stress-strain curves are shown in Figure 4.10(b)).

Distribution of the martensitic volume fraction in the sample subjected to fast loading is shown in Figure 4.12(a). Two cuts along the length of the sample are used to show the distribution inside the sample (the micromechanical model is shown in Figure 4.1(d)). Figure 4.12(b) shows the same results for the slow loading rate. Two sample regions with the highest martensitic volume fraction values are marked by dashed white lines in both figures. For comparison purposes, a larger view of one of these regions is also shown for both fast and slow loading rates. It is clear that the loading rate affects the distribution of phase transformation. In both marked regions in the figure, the phase transformation is distributed in a larger area in the sample subjected to slow loading.

4.5.5 Texture Development in Polycrystalline NiTi

The mutivariant micromechanical framework of this chapter can also be used for studying the texture development during the martensitic phase transformation in polycrystalline NiTi alloys. The drastic orientation dependency in the response of single crystal NiTi reveals the importance of texture on the thermomechanical behavior of available commercial polycrystalline Nitinol specimens. Texture evolution during martensitic phase transformation plays an important role on the macroscopic mechanical response. Studying texture development by the theoretical frameworks and comparing the obtained predictions against the experimental data can also be considered as a powerful method for validating the multivariant micromechanical models, which is obviously more reliable compared to the usual method of exclusively comparing the macroscopic predictions.

Measuring the texture evolution during the phase transformation in NiTi faces numerous challenges in practice due to complicated phase transformation from a cubic phase to a combination of various variants of a monoclinic phase. A more practical study can be done on martensite reorientation in NiTi samples bellow M_f temperature that a reorientation between martensite variants happens instead of an austenite to martensite phase transformation. Stebner et al. [174] reported the experimental data for texture developments during martensite reorientation in polycrystalline NiTi parallelepiped specimens subjected to multiaxial stress states. Ex situ neutron diffraction measurements at critical points of the loading sequences have been used for studying the texture evolution in this work. The obtained experimental results have been compared against the theoretical predictions of a simplified multivariant solution in Gao et al. [65]. In modeling the polycrystal, the microstructure of grains was not constructed and an averaging scheme was used in this work. It was shown that the theoretical multivariant model predicts the texture developments during reorientation with a good accuracy. In this section we use the presented micromechanical framework and the accurate polycrystal structure for studying the texture development during the austenite to martensite phase transformation in NiTi alloys. The methodology of measuring the texture evolution is similar to what used in [65] for analyzing the reorientation. However, since we are studying the phase transformation, appropriate modifications

are implemented on the method for tracking the evolution of texture corresponding to the austenite and martensite phases in the material during the transformation. In this method the volume fraction of all active martensite pairs is calculated in all the elements at each stress state. The volume fraction of active pair i is composed of two variants that form the twin in that pair. The crystallographic data for these pairs, the two composing variants in each pair and also the fraction of each variant (one of the variants is the major with a larger volume fraction compared to the minor variant) are given in Buchheit and Wert [31] and Miyazaki et al. [132]. This experimental crystallographic data contains the rotation matrices to transform a vector inside each martensite variant to the relative vector in the parent austenite lattice coordinates. Also, the initial texture data is used for rotating this vector to the global coordinate system by considering the orientation assigned to the elements in each grain as explained in Section 4.4.2. For calculating a specific pole, the corresponding vector is weighted according to the the volume fraction of martensite pairs. Each weighted vector is transformed to the austenite lattice coordinates, and then to the global coordinates. The contribution of each variant to the texture is measured by placing this transformed value in a standard pole figure grid. Clearly, the contribution of the vector related to the portion of the material that is in austenite phase is only transformed from the austenite lattice to the global coordinated through the orientation obtained from the texture. By this method, at each state two different textures are calculated; one related to the martensite phase and another one corresponding to the parent austenite phase. It is obvious that at the start of phase transformation when the material is pure austenite, the texture only corresponds to the parent phase. However, by starting the phase transformation the martensite texture starts evolving while the austenite texture resolves until the whole material is transformed to martensite.

In order to study the texture evolution during phase transformation a cubic polycrystalline specimen as shown in Figure 4.1(a) is considered. The initial texture is identical with the case explained in Section 4.4.2. The specimen is loaded in both tension and compression to $\epsilon = \pm 0.035$ (see Figure 4.3). Evolution of the texture for the austenite and martensite phase in tensile loading is shown in Figure 4.13.

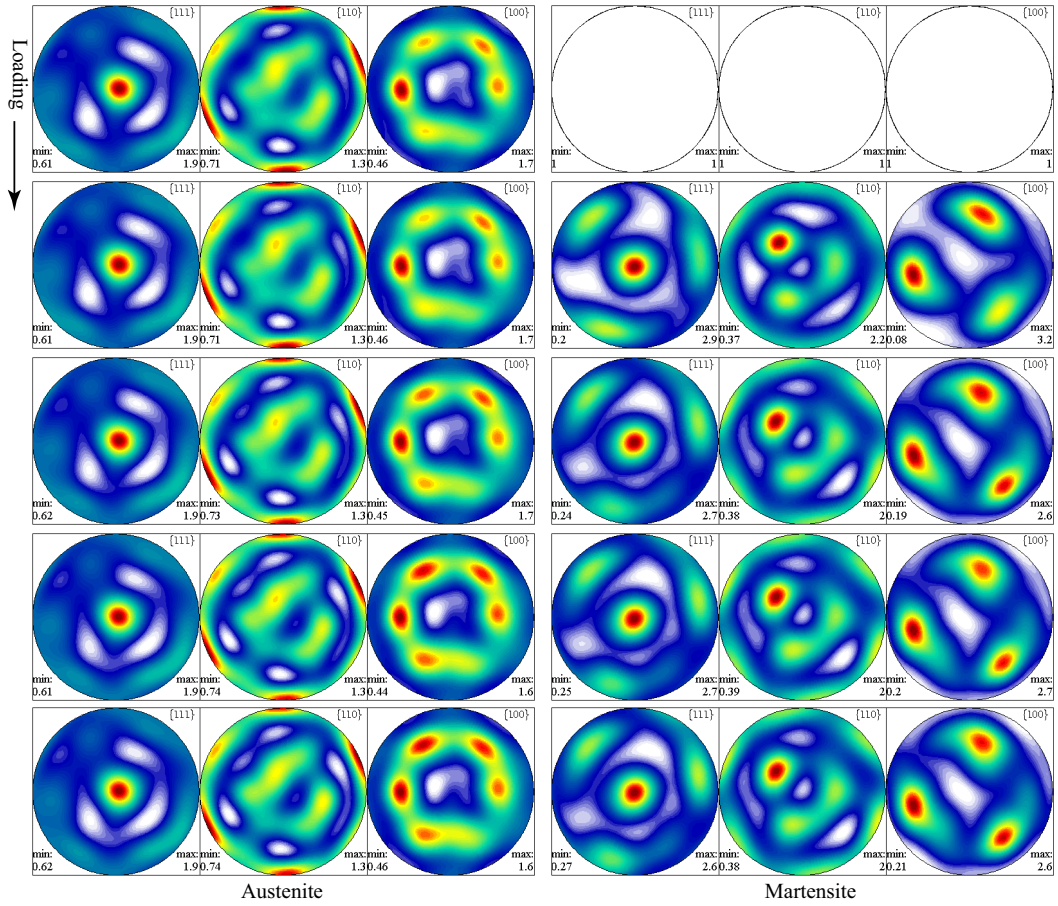

Figure 4.13: Evolution of the texture for the austenite (left column) and martensite (right column) phases during tensile loading of a polycrystalline NiTi sample.

The left column in Figure 4.13 corresponds the austenite phase while the right column shows the evolution of martensite phase texture during loading. It is observed that the austenite phase texture is almost kept constant during loading with a high [111] texture along the loading axis consistent with the initial texture. This phenomenon is expected since the applied strain is not adequate for transformation the majority of the material to martensite. Loading the material to higher strain levels faces computational difficulties in the model due to very high stresses in the grain boundaries and regions with a concentrated phase transformation. The texture of martensite in the right column shows the formation and evolution of the new phase during the loading. Interestingly the transformed martensite shows a [111] texture along the loading axis in tensile loading. The texture evolution in

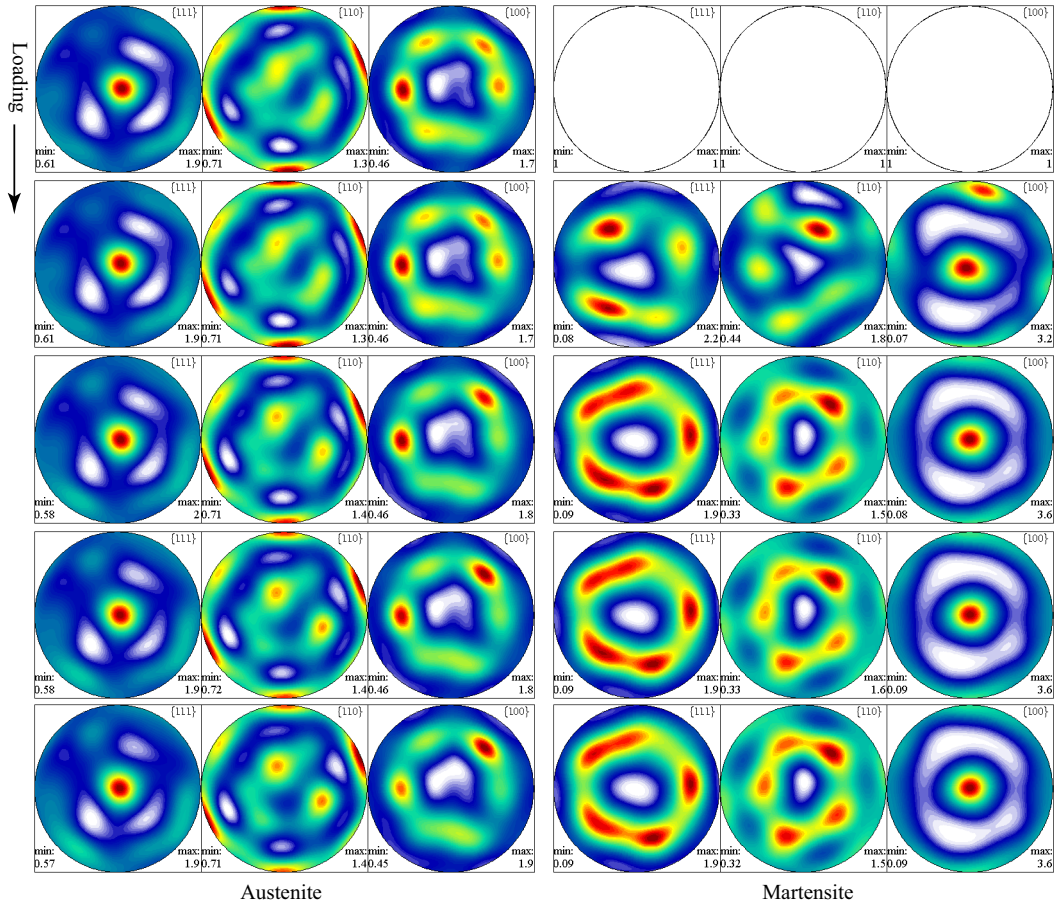

Figure 4.14: Evolution of the texture for the austenite (left column) and martensite (right column) phases during compressive loading of a polycrystalline NiTi sample.

compression is also shown in Figure 4.14. Similar to the tension case, it is observed that the austenite texture is not strongly affected by the phase transformation. The texture evolution corresponding to the transformed martensite in compressive loading is shown in the right column in Figure 4.14. It is observed that in compression, the formed martensite has a [100] texture along the loading axis. Performing experimental measurements of texture evolution during phase transformation and comparing the observations with the presented results can shed light upon some details of the twinning mechanisms in polycrystal NiTi and can be used for remarkably improving the multivariant models by appropriately modifying the considered possible twining systems in developing these models. This research is suggested as a possible future extension of this work in Chapter 6.

CHAPTER V

NANOSCALE STUDY OF NITI SHAPE MEMORY ALLOYS

5.1 Introduction

Several aspects of the SMAs thermomechanical properties cannot be studied neither by the phenomenological constitutive models nor by the micromechanical models. Both the mentioned models rely on the properties of the SMAs at the atomistic scale, and studying the martensitic phase transformation in nanoscale can shed light upon many unknown properties of these materials in the macroscopic level. In this chapter, molecular dynamics (MD) simulations are used for studying the thermomechanical response of NiTi shape memory alloys in various cases.

The thermomechanical loading of NiTi alloys causes a complicated set of transformations between various phases including B2, B19, B19', R and BCO [76, 139]. Also several type-I, type-II and compound twinning modes have been observed in NiTi systems [137, 139]. Zhong et al. [196] performed atomistic simulations to study the structure and geometrical limit of nanoscale twins in NiTi shape memory alloys. In this work the atomic-level details of nanotwinned structures is studied by combining the crystallographic theory and atomistic simulations. Recently, Zhong et al. [196] used molecular dynamics simulations to study the atomistic mechanisms governing the pseudoelasticity and shape memory in NiTi nanostructures. In this work a [110] oriented nanopillar subjected to compressive loading-unloading is studied. It is observed that either a pseudoelastic or shape memory response happens during compressive loading, depending on the applied strain and temperature that control the reversibility of phase transformation and deformation twinning. It is shown that in nanopillars subjected to compressive loading, irreversible twinning arises owing to the dislocation pinning of twin boundaries, while hierarchically twinned microstructures facilitate the reversible twinning. To our best knowledge, a comprehensive study of the pseudoelasticity and shape memory in NiTi nanostructures under tensile loading is not reported in

the literature. In most of the reported works on this topic, an unrealistic temperature of 0 K is considered and molecular statics simulations are used for studying the phase transformation at this temperature [166]. Although this assumption remarkably simplifies the simulation, it will strongly affect the obtained results since the B2 phase is only stable at high temperatures. Mutter and Nielaba [135] studied the temperature-driven diffusionless structural phase transitions in equiatomic and nearly equiatomic ordered NiTi alloys. In this paper a new stable phase is observed at low temperatures (called $\overline{B19'}$ in the paper) and it is shown that by heating an initial B19' system to a high temperature, a B19'→ B2 transformation occurs but upon cooling the obtained B2 structure to low temperatures, instead of transforming back to B19' crystal structure, the system transforms to a slightly different phase, denoted by $\overline{B19'}$, which is not observed to exist experimentally. Mutter and Nielaba [136] considered this new stable state and studied the mechanical response of NiTi nanoparticles subjected to axial tensile loading in a multi variant martensitic ground state. In this chapter we study the temperature induced phase transformation and also the stress induced transformation in various NiTi systems at different temperatures. It is observed that besides the B2↔B19' transformation that occurs in large systems representing the bulk material (simulated as supercells with periodic boundary conditions), a B2↔B19 transformation also may happen in some special cases, particularly in NiTi nanowires that the surface-to-volume ratio is extremely high. A similar phenomenon is recently reported by Zhong and Zhu [194] for NiTi thin films. They performed Monte Carlo simulations and it was shown that a B2 initial structure at high temperatures transforms to B19 phase upon cooling and martensitic nanotwins are formed during this transformation. We observed a similar patterning of martensitic nanotwins in NiTi nanowires using MD simulations as explained in the following sections.

5.2 Methods

5.2.1 EAM Potential

In this study, for the atomic interaction, a many-body interatomic potential for the NiTi binary system is used. The embedded atom potential (EAM), was originally developed by

Lai and Liu [97]. It is confirmed that this EAM has structural stability and lower potential energy for both parent and martensite phases. This potential was later improved by Zhong et al. [195] with a smooth cutoff behavior to avoid the diverging forces in simulations involving large atomic displacements. This Finnis-Sinclair potential [53] computes pairwise interactions for the alloy using a generalized form of EAM potentials. The total energy of the system is expressed as [195]:

$$E = \sum_i \left\{ \sum_{j \neq i} A_{\alpha\beta} \; exp\left[-p_{\alpha\beta} \left(\frac{r_{ij}}{d_{\alpha\beta}} - 1 \right) \right] - \sqrt{\sum_{j \neq i} F(r_{ij})} \right\}, \tag{5.1}$$

where

$$F(r_{ij}) = \xi_{\alpha\beta}^2 \; exp\left[2q_{\alpha\beta} \left(\frac{r_{ij}}{d_{\alpha\beta}} - 1 \right) \right]. \tag{5.2}$$

The parameters α and β represent the element types (here Ni and Ti) of atoms i and j. The distance between atoms i and j is denoted by r_{ij}. The parameters in this potential for describing a NiTi alloy (i.e. values for Ni-Ni, Ti-Ti, and Ni-Ti interaction) have been fitted to the properties of a cubic NiTi system at 0k by Lai and Liu [97]. Since the function $F(r_{ij})$ and its derivative about r_{ij} are nonzero at the cutoff radius $r_c = 4.2\mathring{A}$, we use a modified form of this function proposed by [195] which is more suitable for an MD simulation as:

$$F(r_{ij}) = \begin{cases} \xi_{\alpha\beta}^2 \; exp\left[2q_{\alpha\beta} \left(\frac{r_{ij}}{d_{\alpha\beta}} - 1 \right) \right], & r_{ij} \leq r_1, \\ c_{3,\alpha\beta}(r_{ij} - r_1)^3 + c_{2,\alpha\beta}(r_{ij} - r_1)^2 + c_{1,\alpha\beta}(r_{ij} - r_1) + c_{0,\alpha\beta}. & r_1 < r_{ij} \leq r_c, \end{cases} \tag{5.3}$$

Four coefficients $c_{i,\alpha\beta},\ i = 1, 2, 3, 4$ in (5.3) are determined by imposing the continuity conditions on $F(r_{ij})$ and its first derivative at r_1 and r_c. The potential parameters are given in Table I in [195] with $r_1 = 4.0\mathring{A}$ and $r_c = 4.2\mathring{A}$. As it is shown in Table II in [195], the modified potential removes the discontinuities at r_c, and also improves the predicted lattice constant and various phases energies of NiTi compared to the *ab initio* calculations.

5.2.2 Analysis Framework

The MD simulation package LAMMPS is used in this work [158]. Different starting structures are considered; cubic B2 for modeling the austenite system and monoclinic B19 and

B19' structures for modeling the martensite phase (see Figure 5.1 for a schematic of different phases and the martensitic PT in NiTi alloys).

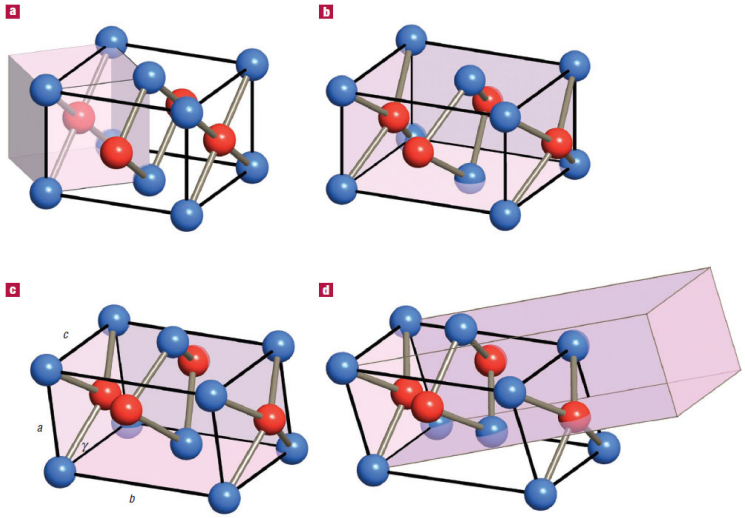

Figure 5.1: Martensitic phase transformation in NiTi (blue atoms are Ti). (a) the austenite phase with B2 cubic structure (shaded box) and the undistorted tetragonal B19 cell. (b) The orthorhombic B19 structure. (c) The distortion to the stress-stabilized monoclinic B19' structure. (d) The Base-centered orthorhombic (BCO) structure shown as the shaded box [76].

Different crystal orientations are also considered in the following case studies by aligning the x direction along various crystallographic directions of the B2 lattice. The input scripts for all the following case studies are run using the Jan 2012 version of LAMMPS [1]. For the case of considering austenite B2 phase as the starting structure, different simulation cells are generated for modeling NiTi nanowires and supercells with periodic boundary conditions. Some sample models with B2 phase as the starting structure are shown in Figure 5.2. The "orient" option is used to align the loading direction along various crystallographic directions of the cubic B2 structure. In the case of considering the martensite (B19 or B19') as the starting structure, we use the crystallographic theory of phase transformation to construct the structure by calculating the position of the atoms [21].

For studying nanowires, periodic boundary conditions are applied in the axial direction and the sidewalls are free surfaces with zero traction. In studying periodic supercells the

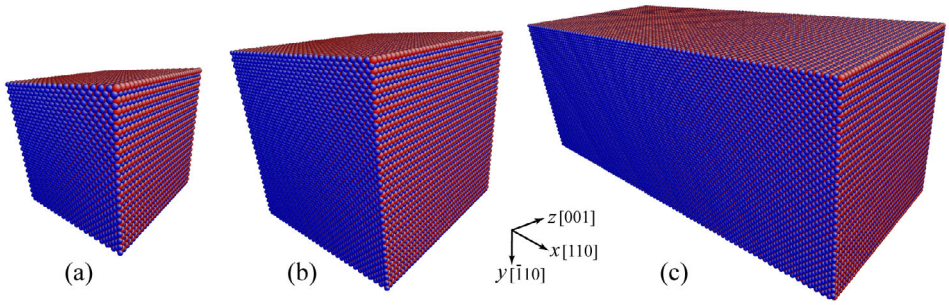

Figure 5.2: Some of the initial configurations in the ordered B2 phase considered in this paper: (a) $8.5nm \times 8.5nm \times 9nm$ periodic supercell, (b) 12.8nm × 12.8nm × 13.5nm periodic supercell, and (c) $34nm \times 12.8nm \times 13.5nm$ nanowire (the dimensions correspond the unrelaxed structure).

system is subjected to periodic boundary condition in all directions. In cases that the initial structure is the ordered B2 phase, the temperature is set to 500 K by thermal equilibration and system is relaxed to zero stresses for 50ps through 100,000 MD time steps (the time step is set to 0.5 fs for all the following cases studies). The temperature is kept constant at 500 K during the relaxation. This stage is performed by time integration on Nose-Hoover style non-Hamiltonian equations of motion which are designed to generate positions and velocities sampled from the isothermal-isobaric ensembles. This is achieved by adding some dynamic variables which are coupled to the particle velocities (thermostatting) and simulation domain dimensions (barostatting). The equilibration stage allows the lattice to expand or contract to an initial temperature with a pressure of 0 bar at each simulation cell face. For modeling the uniaxial tension-compression at lower temperatures (250 K to 300 K) the system is then cooled to the specified temperature with a rate of 2K per picosecond (i.e. through 200,000 MD steps of 0.5 fs each for cooling from 500 K to 300 K). After cooling the system is equilibrated for another 50 ps.

After the equilibration stage, the simulation cell is loaded by applying a strain controlled deformation in the x-direction (see Figure 5.2). Different strain ranges are considered for various case studies. In all the simulations a constant loading or unloading rate of $1 \times 10^9\ s^{-1}$ is considered (i.e. a 10% strain is applied through 200,000 MD steps of 0.5 fs each). In

cases studies with unloading phase, at the end of loading phase the NiTi system is relaxed at a constant temperature for 20 ps and the supercell is unloaded to the initial length at the same loading rate after this equilibration. This relaxation process results in obtaining a macroscopic equilibrium configuration at the prescribed strain and allows the structural changes to occur [106]. Several MD simulations have been performed with different initial distributions of randomly assigned atomic velocities for each case study to explore the possibly different phase transformation mechanisms. Except some of the very small systems, all the case studies are performed parallel on 8 CPUs. The major results and discussions on the reorientation of martensite variants and austenite to martensite phase transformation observed in NiTi systems are given in the following sections.

5.3 B2↔B19 Phase Transformation

As mentioned in Section 5.1, in addition to the B2↔B19' transformation which is mostly associated with twinning in large MD systems representing the bulk material (simulated as supercells with periodic boundary conditions), a B2↔B19 transformation is observed in some cases, particularly in NiTi nanowires that the surface-to-volume ratio is extremely high, and also in periodic supercells with special boundary conditions. The B2↔B19 transformation and also the reorientation between two different B19 variants will be studied in the following sections. However, in order to better understand this phase transformation, we study the temperature-driven B2↔B19 transformation in this section to analyze the transformation temperatures. The effect of free surfaces and size on this transformation is also studied in the sequel.

A schematic of the B2, B19, B19' and BCO phases in NiTi is shown in Figure 5.1. Readers are referred to [139] for a detailed review of various phases and the transformation mechanisms in NiTi systems. For a detailed study of using MD simulations for studying the B2, B19' and BCO phases in NiTi and calculation of relaxed lattice constants and energies per atom corresponding to these three phases see the work by Zhong et al. [195]. We will focus on studying the B19 phase in this section.

Huang et al. [76] used first-principles calculations based on density functional theory

(DFT) and showed that the energy of B19 phase is lower than B2 and the R phase. However, since the B19 phase in NiTi is not observed in experiments, they have proposed that B19 is mechanically unstable against a monoclinic distortion to the B19' structure (or BCO which is shown also to be stable in their work) due to a negative elastic modulus. However, we will show in the sequel that in some cases in vicinity of the surface anergies and also in presence of constrains due to high stresses (i.e. in a nanowire) the B19 phase may also be stable. A similar phenomenon is recently reported by Zhong and Zhu [194] for NiTi thin films based on Monte Carlo simulations. Figure 5.3 shows a schematic of a B2 unit cell (left) and two possible B19 equivalent variants (right).

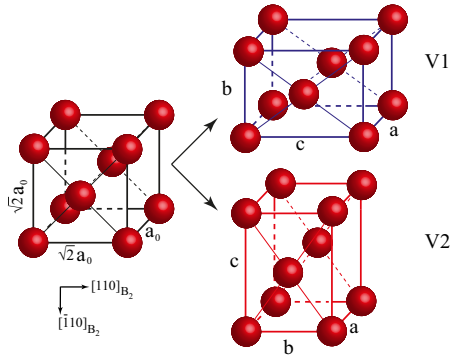

Figure 5.3: Schematic of the parent B2 (left), and two variants of B19 unit cells (right) viewed form [001] direction (The unit cell deformation is exaggerated for increasing the geometric contrast between the two B19 variants).

A comprehensive study of lattice parameters and the energy per atom for the B2 and B19 cells is given in Table 1 in Huang et al. [76]. The lattice constant of the B2 phase is $a_0 \simeq 3.008\mathring{A}$ (as obtained form *ab initio* calculations and also predicted by the FS-potential used in this work). In the selected coordinates shown in Figure 5.3 the parent B2 phase has equal cell edges of length $\sqrt{2}a_0$ in both $[110]_{B2}$ and $[\bar{1}10]_{B2}$ directions. In order to find the lattice parameters of the B19 phase, several periodic simulation boxes are relaxed by the stress-controlled conjugate gradient energy minimization. The average parameters for this phase are obtained as: Energy per atom=-5.0428 eV, a=3.107$\mathring{A}$, b=4.017 $\mathring{A}$, c=4.38$\mathring{A}$. It is observed that the results are in agreement with the *ab initio* calculations and the

experimental data [76].

In the next step, temperature-driven B2↔B19 phase transformation at zero stress is studied (see Zhong et al. [195] for a similar study on the B2↔B19' Transformation). In order to simulate the properties of bulk NiTi, we start by studying periodic supercells by considering two different simulation boxes. The small periodic supercell contains 1152 atoms (2.4nm × 2.4nm × 2.6nm) and the large call contains 9216 atoms (4.8nm × 4.8nm × 5.2nm). The initial system is B19 phase equilibrated at 100 K. The system is then heated to 450 K and then cooled back to 100 K with the simulation details explained in Section 5.2. It is observed that during the heating the B19→B2 is phase transformation mechanism. However, during the cooling a B2↔B19' transformation is dominant in the periodic system. Since we are interested in modeling the B2↔B19 transformation in this example, a special boundary condition is imposed on the system in which only the normal components of stress are relaxed. By this method the forward and reverse B2 to B19 phase transforation in the system with periodic boundary conditions is guaranteed.

The temperature-driven B2↔B19 phase transformation in bulk NiTi is shown in Figure 5.4(a). In order to distinguish the B2 and B19 phases, the changes in the dimensions of the unit cell can be studied in this simple case study. However, in order to study the phase transformation in more complicated cases in the sequel and particularly for studying the patterning of martensite variants in the sequel, an order parameter is defined based on lattice constants in the MD system.

The detecting method used in this work is similar to that used by Sato et al. [166] with some improvements. In our method for each atom the nearest neighbors that form a unit cell are found in the system (the cell is constructed by eight atoms of the same type as shown in Figure 5.3). The lattice constants a, b, and c are calculated by considering 12 edges in the cell. Each lattice constant is obtained by averaging the four values obtained form this calculation. For studying the B19 phase, the angels in the cell are not used. However, the criteria is also capable of calculating the unit cell angels for detecting B19' and BCO phases. A more simple criteria can also be developed by considering only three neighbors around each atom which also reduces the computational time remarkably (as

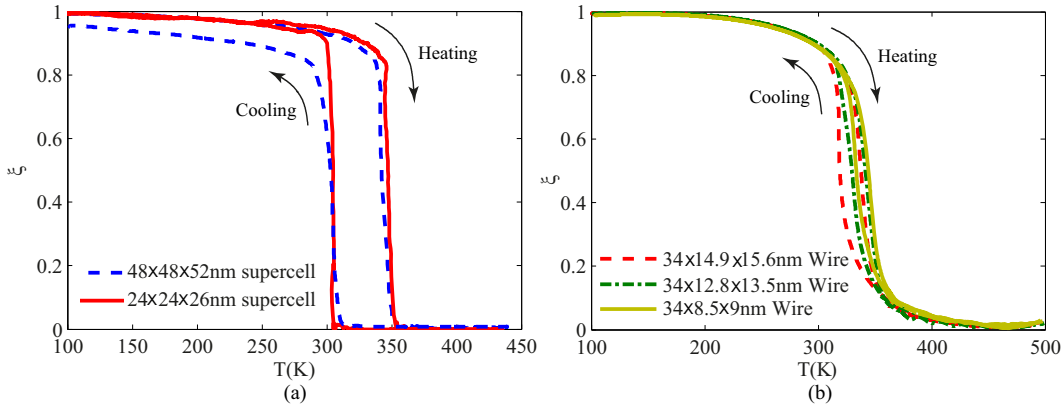

Figure 5.4: MD simulation of temperature induced B2↔B19 phase transformation for (a) periodic supercells and (b) nanowires with different sizes. The order parameter ξ changes between 1 for B19 structure and 0 for B2 structure.

used in Sato et al. [166]). We have studied both the methods and although the results were similar it was observed that the averaging improved the accuracy of the detecting scheme. After calculating the lattice constants with the method explained above, two different B19 variants are detected if the following conditions are satisfied for an atom: $b < 4.02\mathring{A}, c > 4.35\mathring{A}, c/a > 1.4$. As another choice, the parameters a, b, and c can also be monitored and used in the detection criterion. It is observed that the results are very similar by using these three parameters instead of a, b, and c. The defined order parameter ξ is set to zero for the B2 phase and the two different B19 variants are denoted by $\xi = +1$ and -1 for the variants shown with blue and red colors in Figure 5.3, respectively. This color coding will be used in the following sections for detecting the reorientation in multivariant martensite systems.

The change of order parameter ξ for two different simulation boxes with periodic boundary conditions is shown in Figure 5.4. This Figure is used for calculating the transformation temperatures in bulk NiTi for the B2↔B19 phase transformation. It is observed that the size effect is negligible on the transformation temperatures. However, while the small supercell is fully recovered to B19 phase during cooling, the larger cell is partially recovered. This is consistent with the case of B2↔B19' transformation and can be explained by considering the geometrical constraints as studied in detail by Zhong et al. [195].

In the next step, the B2↔B19 phase transformation is studied in NiTi nanowires with free surfaces. Four different sizes of nanowires are considered (the largest wire contains ∼600,0000 atoms). The same procedure is used for studying the temperature-driven phase transformation. However, it is observed that despite the supercell with periodic boundary conditions, the B2→B19 transformation is always dominant in the cooling phase instead of a B2→B19' transformation. A similar simulation is also perfomed on all the nanowires by considering a wire in B2 phase at 450 K as the starting structure, cooling this system to 100 K and then heating back the wire to 450 K. It was observed that upon cooling and heating a B2→B19→B2 transformation happens in all the nanowires with the same transformation temperature obtained from the simulations with B19 phase as the starting structure. The order parameter ξ during the heating-cooling cycle for the NiTi nanowires is shown in Figure 5.4(b). It is obvious that the transformation temperatures are strongly affected by the geometry due to the presence of surface energies in nanowires.

5.4 Martensite Reorientation and Austenite to Martensite Phase Transformation

5.4.1 NiTi Nanowires

In this section NiTi nanowires subjected to axial loading are studied. It will be shown that at temperatures below M_f a martensite reorientation is the dominant transformation mode for NiTi nanowires. Several case studies are presented for analyzing the mechanism of this martensite reorientation at different conditions. The simulation method is explained in detail in Section 5.2. As the first case study consider a NiTi nanowire with dimensions 34 nm × 12.8 nm × 13.5 nm in x,y, and z directions (Figure 5.2(c)) subjected to an axial load at 275 K. The system contains ∼500,0000 atoms and the initial structure is ordered B2 at high temperature (500 K). The axial direction of nanowire is aligned with the $[110]_{B2}$ and periodic boundary conditions are imposed only in the axial direction. At the start of simulation, the temperature is set to 500 K by thermal equilibration and the system is relaxed to zero stresses for 50ps through 100,000 MD time steps of 0.5 fs each. The temperature is kept constant at 500 K during the relaxation. The system is then cooled to 275 K through 225,000 MD steps of 0.5 fs each (2 K per picosecond). As previously shown

in Figure 5.4(b), B2 phase transforms to B19 during this cooling since 275 K is bellow the $M_f \simeq 320K$ for this wire. After cooling the system is equilibrated for another 50 ps at constant temperature T=275 K. The equilibrated structure at 275 K is considered as the initial state for applying the mechanical loading ($\epsilon = 0$). Using the martensite detecting method expressed in the previous section, it is observed that during the cooling from 500 K to 275 K, the nanowire is transformed to the B19 variant with the smaller lattice constant b along the axis of wire (variant 2 in Figure 5.3). This initial state is shown in Figure 5.5 at $\epsilon = 0$. The atoms with a variant 2 of B19 phase are shown with red color in this figure. The equilibrated wire is subjected to a 10% axial strain through 200,000 MD steps of 0.5 fs each by applying a strain controlled deformation in the x-direction (see Figure 5.2). It is observed that a reorientation from variant 2 to variant 1 happens during the axial loading of the wire with a pattern shown in Figure 5.5 for some strain intervals.

As shown in this figure, the reorientation initiates in the from of a narrow nanotwin oriented $\sim 45^\circ$ with respect to the loading direction. This phenomenon is shown with $\epsilon = 0.015$ in Figure 5.5 (variants 1 and 2 are shown with blue and red, respectively). The formation of this narrow multivariant nanotwin is associated with an abrupt change in the slope of stress-strain curves of the wire as will be studied in the following section. The reorientation process continues during the axial loading by propagation of variant 1 inside variant 2 and the initial narrow region of variant 1 broadens to cover the whole nanowire at $\epsilon = 0.1$ as shown in Figure 5.5. A similar study on the same wire at a higher temperature (300 K) is performed and the initiation and propagation of martensite variants at this temperature are shown in Figure 5.6.

It is observed that at this temperature the wire is transformed to variant 2 at the end of cooling step of loading $\epsilon = 0$ similar to the wire at 275 K. Then the reorientation initiates at two equivalent directions as shown in Figure 5.6 ($\epsilon = 0.02$). By applying the axial strain one of these two directions become dominant and variant 1 propagates through the wire until the reorientation from variant 2 to variant 1 is completed at $\epsilon = 0.1$. The effect of temperature on the stress-strain response of the wire during the martensite reorientation will be studied in the next section. The reorientation of a smaller wire is studied as the

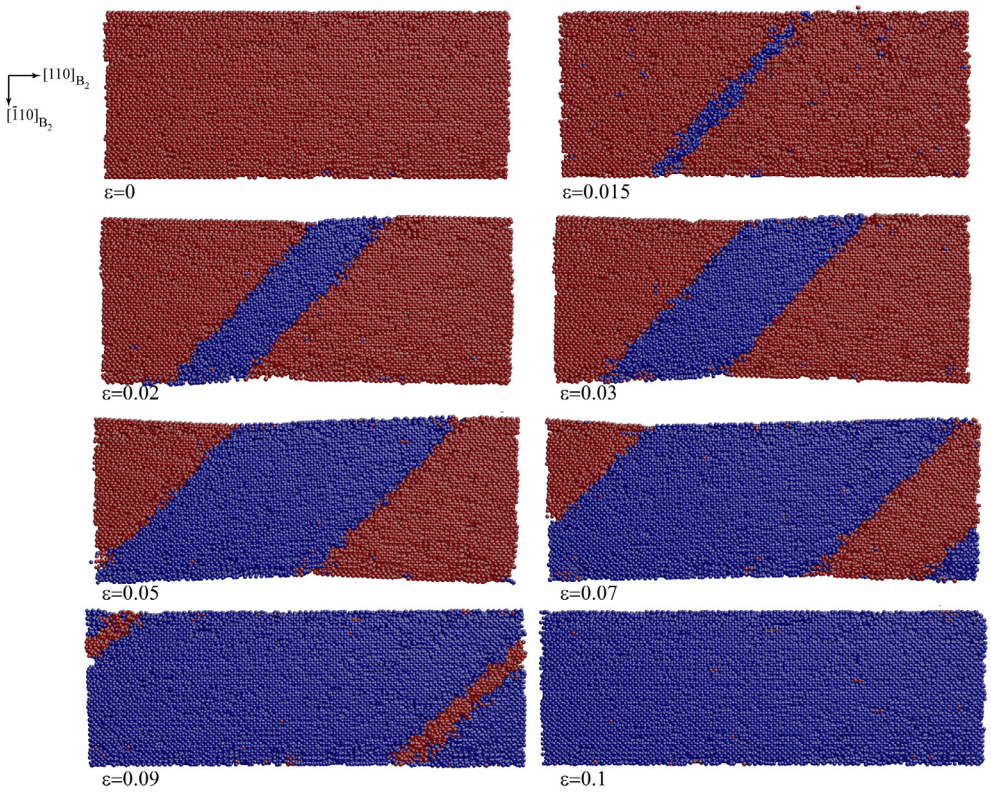

Figure 5.5: Martensite reorientation in a 34nm × 12.8nm × 13.5nm nanowire subjected to axial tensile load at T=275K. Blue and red represent two different martensite variants as shown in Figure 5.3.

next case study. In this example a 34 nm × 8.5 nm × 9 nm NiTi nanowire is studied at 275 K. Similar to the previous two case studies the wire with initial B2 structure at high temperature is cooled to 275 K. The martensite variant 2 is formed during this cooling as shown in Figure 5.7($\epsilon = 0$). An interesting initiation and propagation of reorientation is observed in this wire. As shown in ($\epsilon = 0.02$), variant 1 forms as three nanotwins in three regions aligned in the equivalent $\sim \pm 45^\circ$ directions with respect to the loading direction. Applying axial strain causes all the three nanotwins broadening, although the propagation of reorientation in one of the regions is prominent. As observed in Figure 5.7($\epsilon = 0.07$), branching happens inside the twins and a new twin in formed inside the existing twins. The reorientation continues until the whole wire is transformed to variant 1 at the end of loading ($\epsilon = 0.1$).

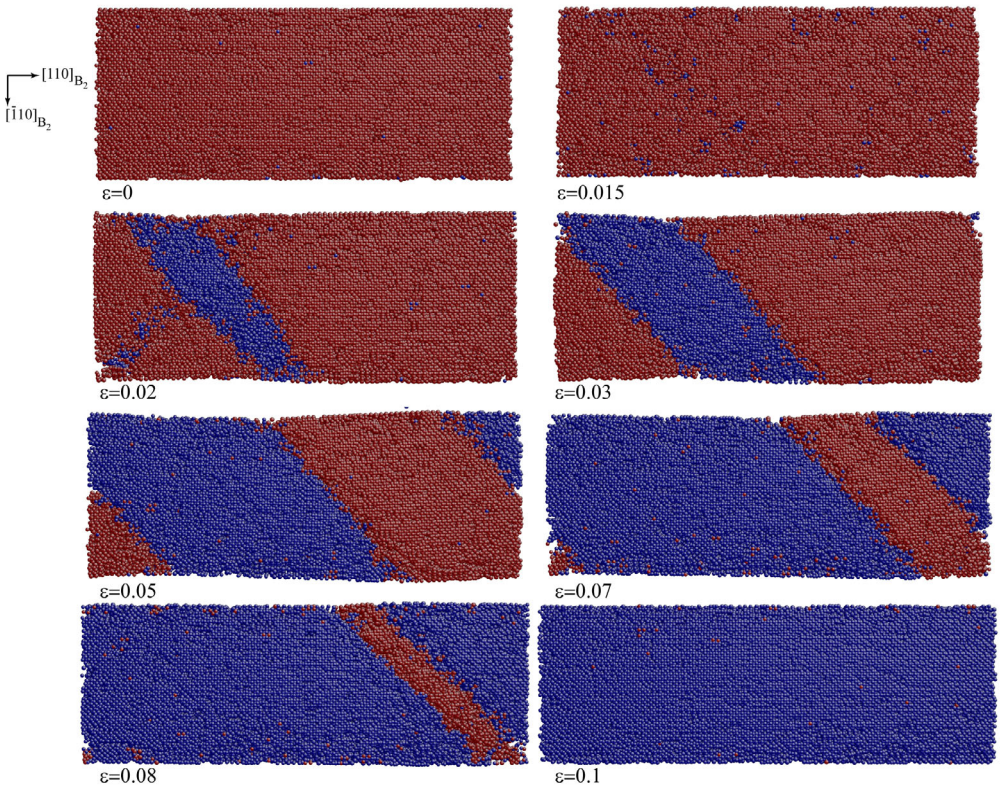

Figure 5.6: Martensite reorientation in a 34nm × 12.8nm × 13.5nm nanowire subjected to axial tensile load at T=300K. Blue and red represent two different martensite variants as shown in Figure 5.3.

5.4.2 Temperature Effect on the Reorientation Stress-Strain Curves of NiTi Nanowires

The effect of temperature on the reorientation stress-strain response of a 34 nm × 12.8 nm × 13.5 nm nanowire is studied in this section. The wire is studied in a loading-unloading cycle. Figure 5.8 shows the stress-strain response for this wire subjected to a 10% axial strain and then unloaded to the initial length. The response is studied at three different temperatures 250, 275, and 300 K.

It is worth noting that all the curves correspond to the loading-unloading of wires that are initially cooled from an equilibrated B2 structure to lower temperatures and the B2↔B19 transformation was observed at all the temperatures as explained in the previous sections (see Figure 5.9 for the change of order parameter during cooling from 500 to 300,

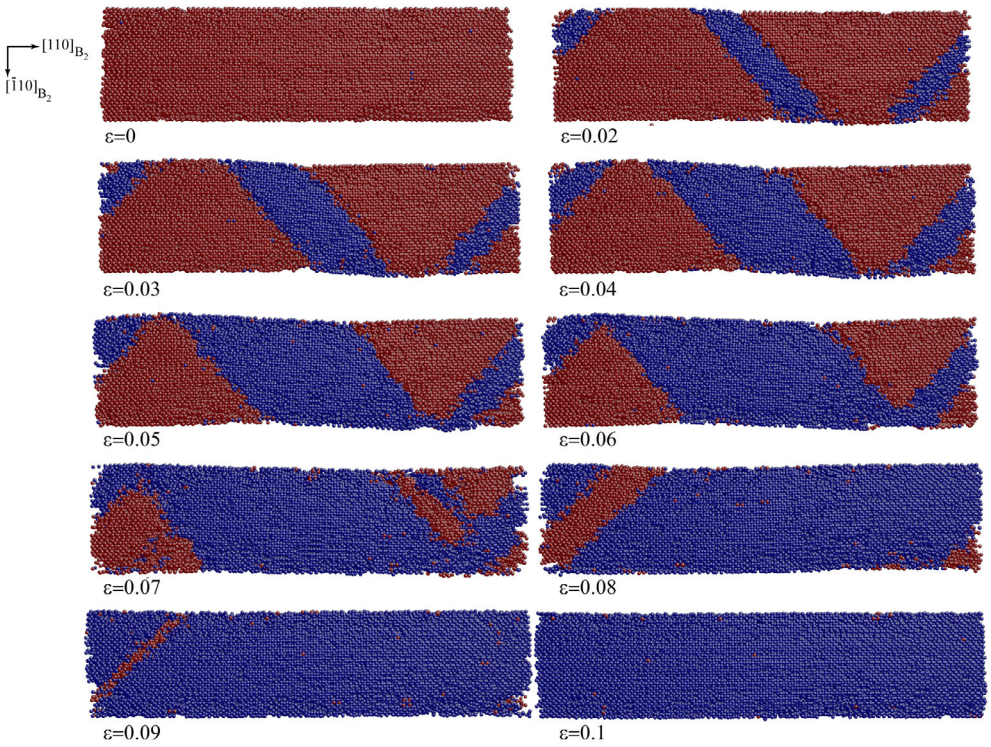

Figure 5.7: Martensite reorientation in a 34nm × 8.5nm × 9nm nanowire subjected to axial tensile load at T=300K. Blue and red represent two different martensite variants as shown in Figure 5.3.

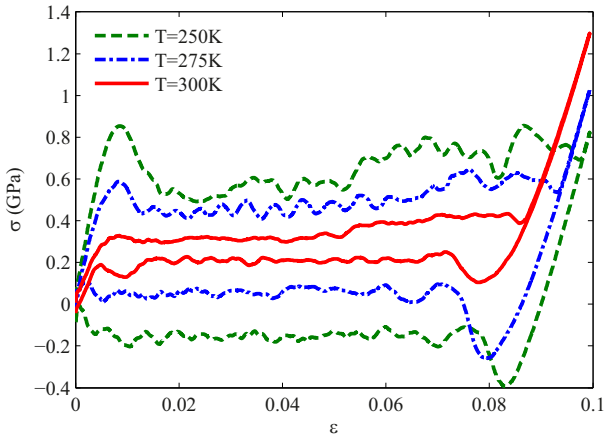

Figure 5.8: The stress-strain curves corresponding to martensitic reorientation at three different temperatures for a 34nm × 12.8nm × 13.5nm nanowire subjected to axial tensile loading-unloading.

275, and 259 K in this wire).

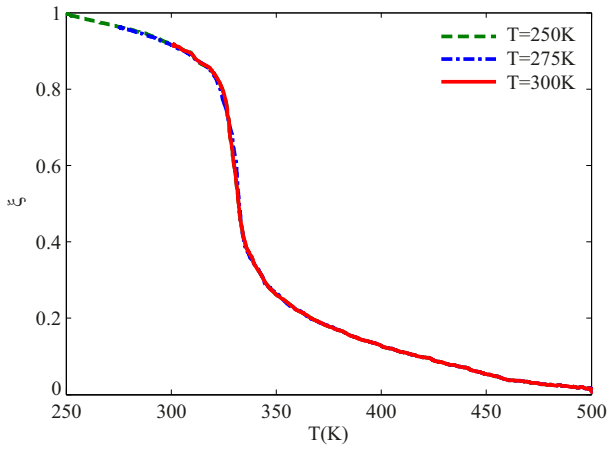

Figure 5.9: Change of the order parameter ξ during the initial cooling of nanowires. The stress-strain response of the wires subjected to axial loading after the initial cooling is shown in Figure 5.8.

Studying Figure 5.8 shows that the temperature has a significant effect on the mechanical response and reveals many important properties of temperature effect on the response of NiTi nanowires bellow M_f. Some of the major findings are summarized in the following:

1. The slope of the initial elastic response of the nanowire is affected by the change of temperature. The initial linear response at the beginning of loading at all temperatures corresponds to the elastic deformation of variant 2 before starting the reorientation. Interestingly, it is observed that this elastic response is affected by the temperature and the slope of stress-strain curved decreases by increasing the temperature.

2. The temperature affects the initial stress overshoot at the start of reorientation. As it is shown in Figure 5.8, the start of reorientation is associated with a stress overshoot at T=250 K while the stress-strain response is smooth at the initiation of reorientation at higher temperature T=300 K.

3. The martensite reorientation completes at lower strains by increasing the temperature. The completion of reorientation is identified by an abrupt change in the slope of stress-strain curves during loading.

4. The hysteresis area is decreased by increasing the temperature.

5. The stress value during reorientation is decreased by increasing the temperature. It is worth noting that the phase transformation critical stress increases by increasing the temperature at high temperatures above A_f. However, our results in Figure 5.8 show that bellow M_f the reorientation critical stress decreases by increasing the temperature in NiTi nanowires. This phenomenon is consistent with the bulk NiTi as reported experimentally [61, 140].

5.4.3 Bulk NiTi

In this section the stress-induced phase transformation is studied for bulk NiTi by simulating MD supercells with periodic boundary conditions. The simulation method is explained in detail in Section 5.2. As the first case study consider a NiTi periodic box with dimensions 12.8 nm $\times$ 12.8 nm $\times$ 13.5 nm in x,y, and z directions (Figure 5.2(b)) subjected to a tensile load in x direction at 300 K. The initial structure is B2 at high temperature T=500 K. The loading direction is aligned with the $[110]_{B2}$ and periodic boundary conditions are imposed in all directions. At the start of simulation, the temperature is set to 500 K by thermal equilibration and the system is relaxed to zero stresses for 50ps through 100,000 MD time steps of 0.5 fs each. The temperature is kept constant at 500 K during the relaxation. The system is then cooled to T=300 K through 200,000 MD steps of 0.5 fs each (2 K per picosecond). As previously shown in Zhong et al. [195] B2 phase transforms to B19' during this cooling. However since 300 K is very close to the M_f for bulk NiTi (M_f is reported $\simeq 300K$ in [195]), an equilibration stage in necessary after the completion of cooling to stabilize the obtained structure. The system is equilibrated for 50 ps at constant temperature T=300 K. The equilibrated structure at 300 K is considered as the initial state for applying the mechanical loading ($\epsilon = 0$).

As shown in Figure 5.10 during the equilibration stage the B2$\rightarrow$B19' transformation initiates in the structure. It is observed that the martensite variants tend to self-accommodate their shear deformation by forming nanotwins. Applying axial strain to this system magnifies the B19' martensite twinning in the system with a lattice angle $\gamma \simeq 98^\circ$ (see $\epsilon = 0.05$ in

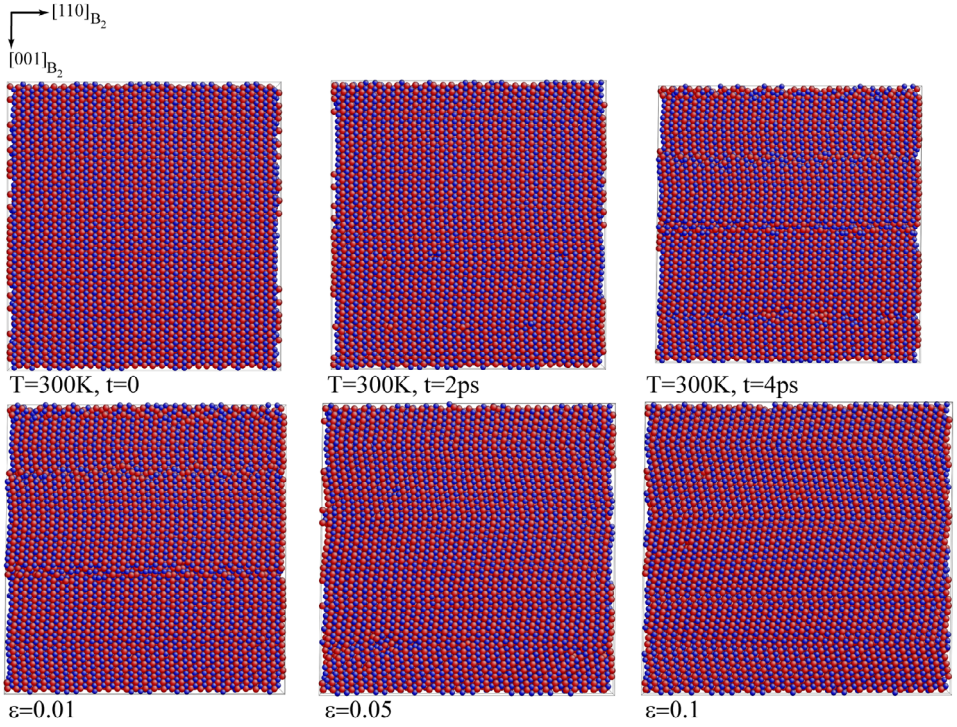

Figure 5.10: $[\bar{1}10]$ view of a 12.8nm × 12.8nm × 13.5nm supercell with periodic boundary conditions subjected to tensile loading at 300K. The supercell is cooled from initial B2 structure at 500K to 300K, equilibrated at 300K (first row), and then loaded in [110] direction (second row). All the pressure components are relaxed during cooling and equilibration stages.

Figure 5.10). Further increasing the axial strain causes formation of BCO nanotwins with a lattice angle $\gamma \simeq 108^\circ$ (see $\epsilon = 0.1$ in Figure 5.10).

As another example, we studied the same supercell with periodic boundary conditions but this time only the normal strass components are relaxed during the cooling and equilibrating stages in order to stimulate the B2→B19 transformation in bulk material. Using the martensite detecting method expressed in the previous section the B19 variants are studied in the system. The results of this case study are shown in Figure 5.11.

Since the temperature T=300 K is very close to the M_f, the phase transformation during cooling is completed at the equilibration stage after the cooling. The top row in Figure 5.11 shows that the B19 variants are formed as patterned nanotwins in order to self-accommodate the transformation strains in x and y directions.

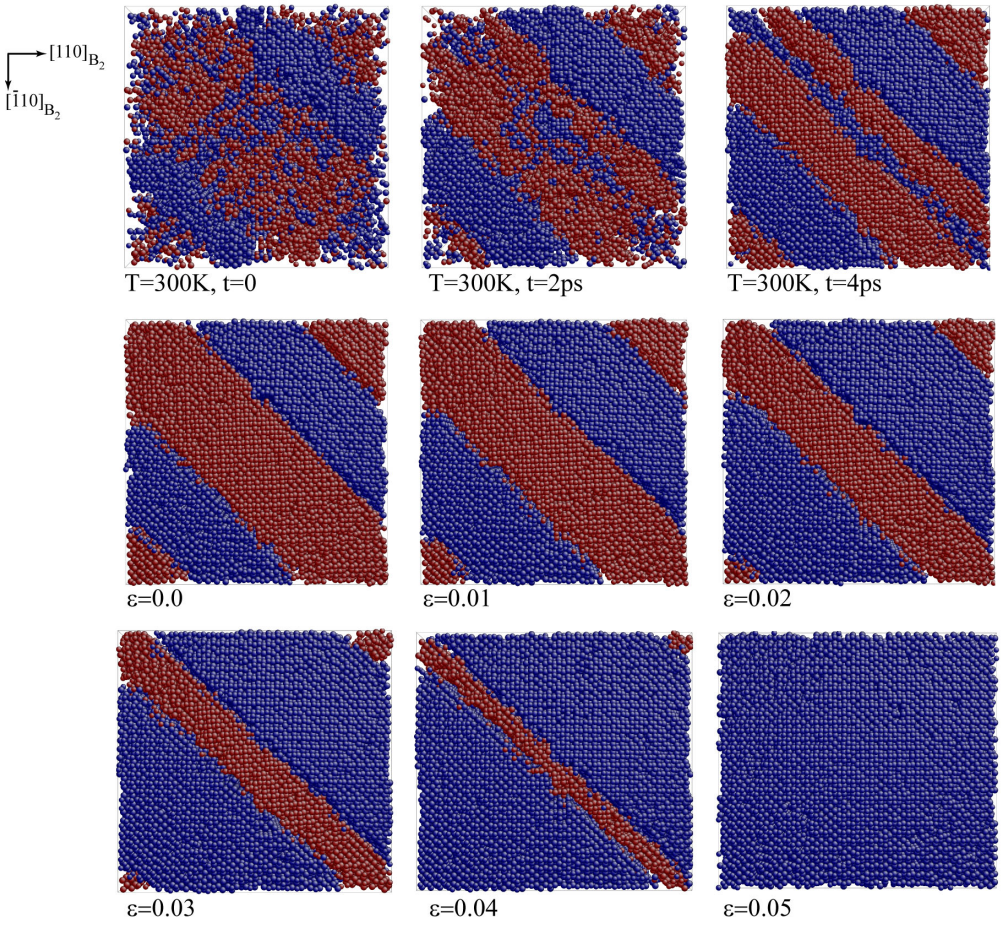

Figure 5.11: [001] view of a 12.8nm × 12.8nm × 13.5nm supercell with periodic boundary conditions subjected to tensile loading at 300K. The supercell is cooled from initial B2 structure at 500K to 300K, equilibrated at 300K (first row), and then loaded in [110] direction (second and third rows). Only the normal pressure components are relaxed during cooling and equilibration stages.

Comparing this results with those obtained from analyzing NiTi nanowires (i.e. see Figure 5.6) reveals that the surface energies and the free boundaries at the sidewalls causes the formation of a single variant B19 system in the wire, while a self-accommodated pattern is formed in a system with geometrical constraints uses in this section. The initial state after cooling and equilibrating the system is shown in Figure 5.11($\epsilon = 0$). The equilibrated system is then subjected to a 10% axial strain through 200,000 MD steps of 0.5 fs each by applying a strain controlled deformation in the x-direction (see Figure 5.2). It is observed that in the multivariant pattern at the start of loading, the regions of variant 1 start propagating while variant 2 is resolved by increasing the axial strain. This phenomenon is expected because variant 1 is more favorable in the strained material since the larger lattice constant in this variant is aligned with the loading direction. Figure 5.11($\epsilon = 0.1$) shows that the whole system is transformed to variant 1 at the end of loading phase.

The same simulation is also performed to study the thermomechanical response of bulk NiTi at a lower temperature T=250 K. The results for the supercell with relaxing all the stress components are shown in Figure 5.12. It is observed that the results are similar to the case of T=300 K, except for the cooling stage. While the transformation is not completed during cooling at T=300 K, the top row in Figure 5.13 shows that the phase transformation completes during cooling to T=250 K since this temperature is remarkably bellow the M_f.

The simulation at 250 K is also repeated by only relaxing the normal stress components in the periodic supercell. The results of this simulation are shown in Figure 5.13. A self-accommodated B19 multivariant pattern is formed during the cooling stage in this example as shown in the first row in Figure 5.13. Comparing the results obtained for 300 K in Figure 5.11 with those obtained for 250 K in Figure 5.13 shows a refinement in martensite nanotwins at lower temperatures. This observation is in agreement with the Monte Carlo simulations by Zhong and Zhu [194].

In order to study the effect of size on the martensite patterns during B2→B19 transformation, two sizes of supercells with periodic boundary conditions are analyzed in the next case study. The normal pressure components are relaxed during the cooling and relaxation stages to stimulate the B2→B19 transformation and the initial B2 systems are cooled to 275

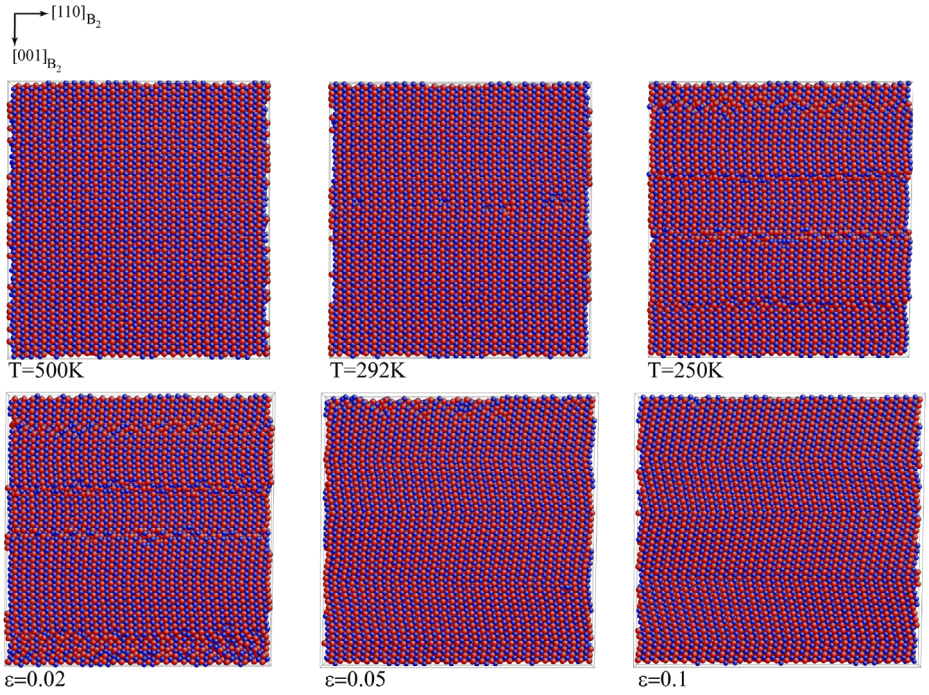

Figure 5.12: $[\bar{1}10]$ view of a 12.8nm × 12.8nm × 13.5nm supercell with periodic boundary conditions subjected to tensile loading at 250K. The supercell is cooled from initial B2 structure at 500K to 250K (first row), equilibrated at 250K, and then loaded in [110] direction (second row). All the pressure components are relaxed during cooling and equilibration stages.

K before applying the uniaxial strain. The larger simulation box is 17nm × 17nm × 18nm and the smaller one has the dimensions 12.8nm × 12.8nm × 13.5nm in x, y, and z directions. The mutivariant pattern of nanotwins are shown in Figures 5.14 and 5.15 for these case studies.

It is observed that the formation and propagation of mutivariant martensite nanotwins is very similar in both cases which shows that the size effect is negligible in this study and the results are representing a bulk material with an acceptable accuracy.

The stress strain response of bulk NiTi at during martensite reorientation and phase transformation is studied in Figure 5.16 for different temperatures. The stress-strain curves shown in Figure 5.16(a) correspond the supercells with periodic boundary conditions in all directions in which the all the pressure components are relaxed during cooling and equilibration. The stress-strain curve starts with a smooth change of slope during loading

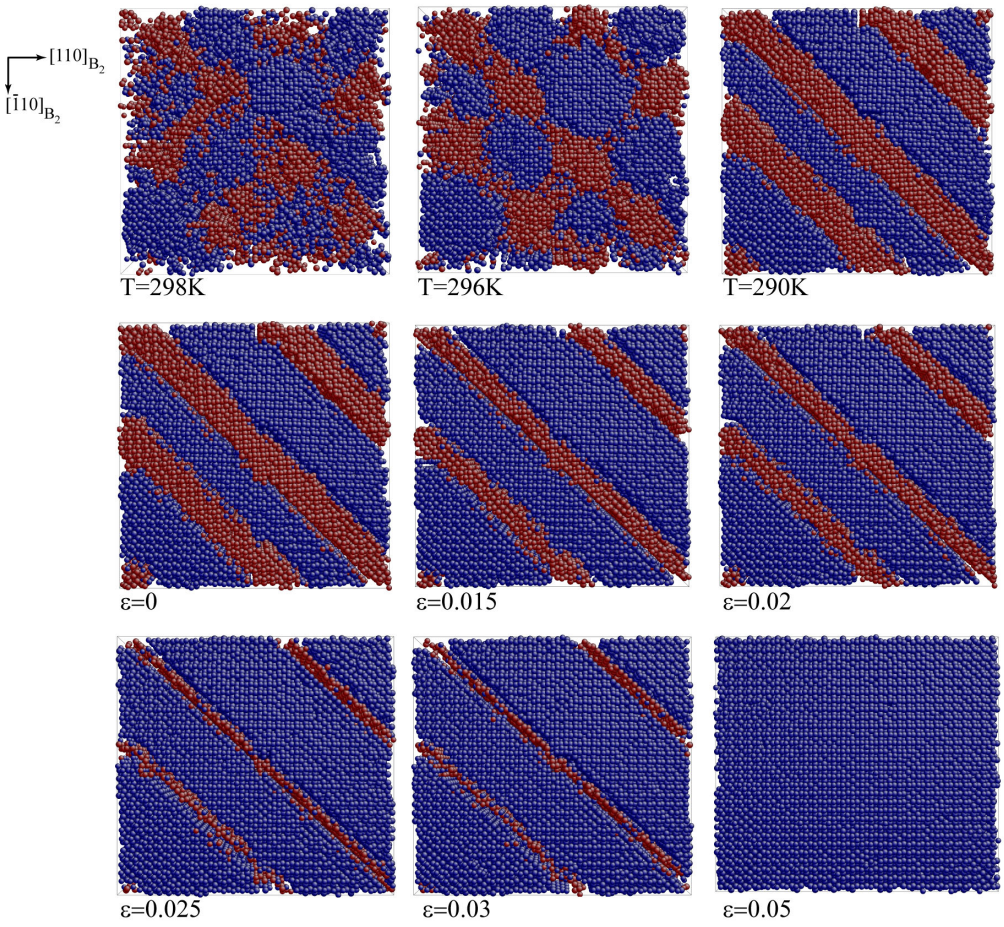

Figure 5.13: [001] view of a 12.8nm × 12.8nm × 13.5nm supercell with periodic boundary conditions subjected to tensile loading at 250K. The supercell is cooled from initial B2 structure at 500K to 250K (first row), equilibrated at 250K, and then loaded in [110] direction (second and third rows). Only the normal pressure components are relaxed during cooling and equilibration stages.

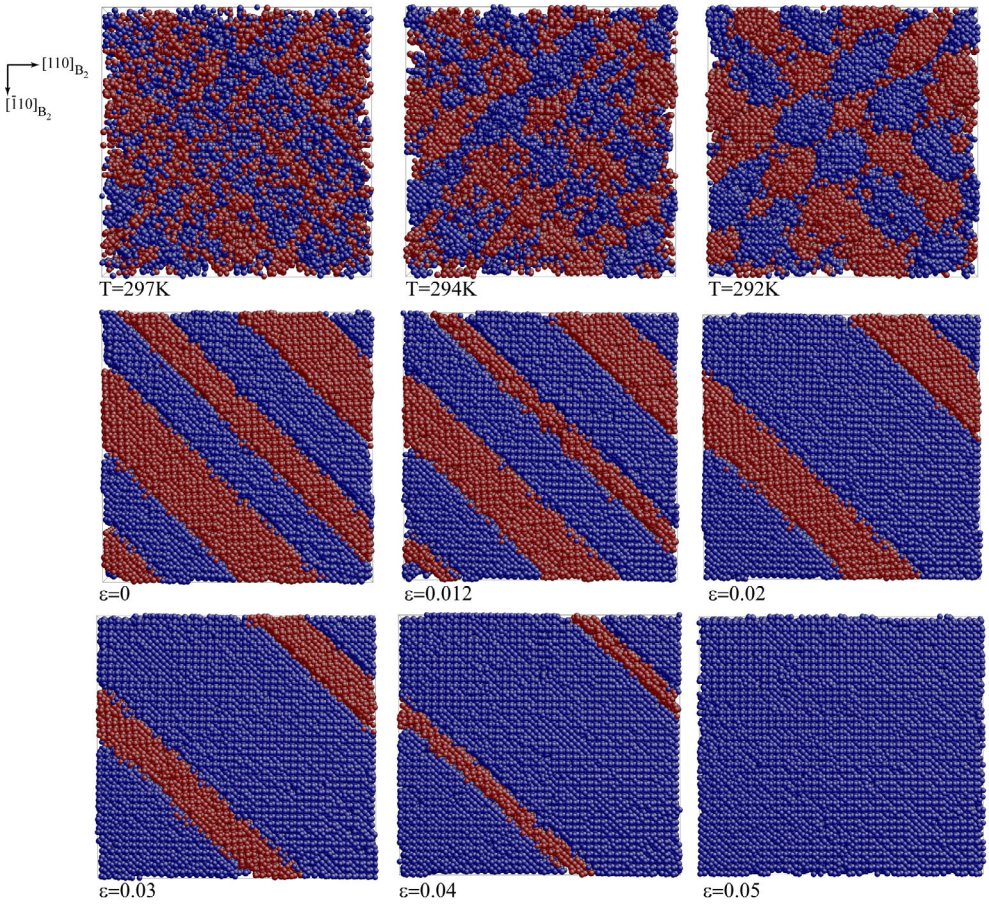

Figure 5.14: [001] view of a 17nm × 17nm × 18nm supercell with periodic boundary conditions subjected to tensile loading at 275K. The supercell is cooled from initial B2 structure at 500K to 275K (first row), equilibrated at 300K, and then loaded in [110] direction (second and third rows). "Only the normal pressure components are relaxed during cooling and equilibration stages".

during the propagation of B19' nanotwins in the system. The curve is followed by an abrupt change in the slope by the formation of BCO nanotwins in the material. Figure 5.16(b) shows the stress-strain curves for the systems in which only the normal pressure components were relaxed and the B2→B19 transformation was stimulated. It is observed that the curves contain several parts with a negative slope during loading. This local peaks in the curves correspond to the propagation of martensite variants which is associated with resolving the other variant in the system.

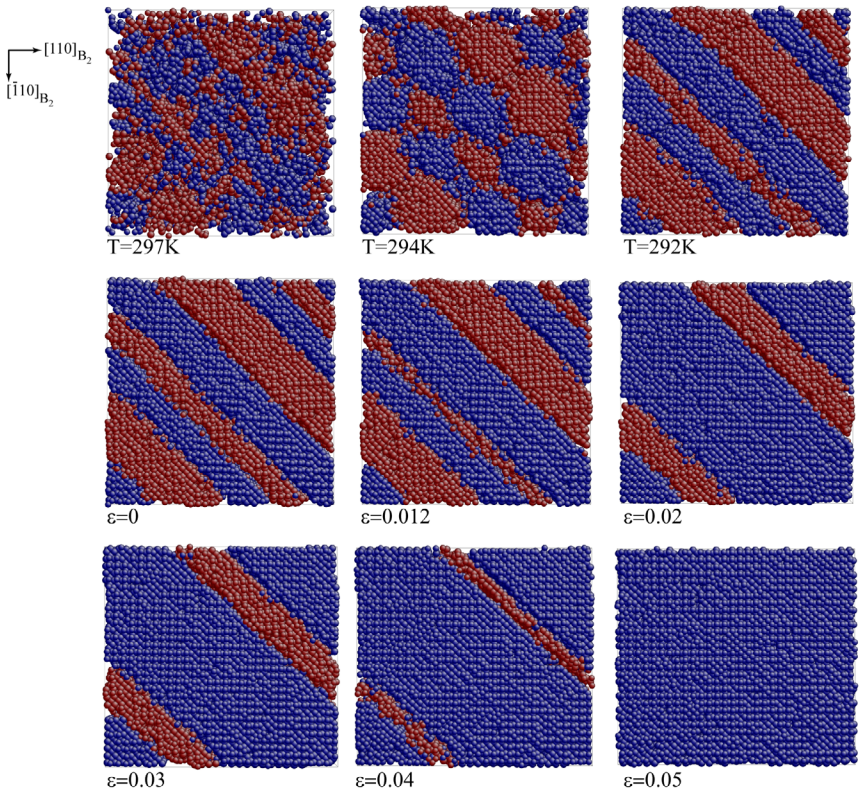

Figure 5.15: [001] view of a 12.8nm × 12.8nm × 13.5nm supercell with periodic boundary conditions subjected to tensile loading at 275K. The supercell is cooled from initial B2 structure at 500K to 275K (first row), equilibrated at 300K, and then loaded in [110] direction (second and third rows). "Only the normal pressure components are relaxed during cooling and equilibration stages".

5.5 Twinning in NiTi nanowires Subjected to High Tensile Strains

In Section 5.4 we studied the response of NiTi nanowires at temperatures bellow M_f subjected to a 10% strain in the axial direction. In this section we study the response NiTi nanowires when subjected to high axial strains. The method is similar to that used in Section 5.4. Different sizes of nanowires are studied at various temperatures. The initial structure for all the cases in B2 at high temperature T=500 K and the system is cooled to lower temperatures 250, 275, and 300 K before applying the mechanical loading. An axial strain of 20% is applied after equilibrating the cooled wire. It was shown in Section 5.4 that the single variant 2 formed at temperatures bellow M_f is reoriented by propagation of variant 1 in the form of multivariant nanotwins with a $\sim 45°$ orientation. Further loading

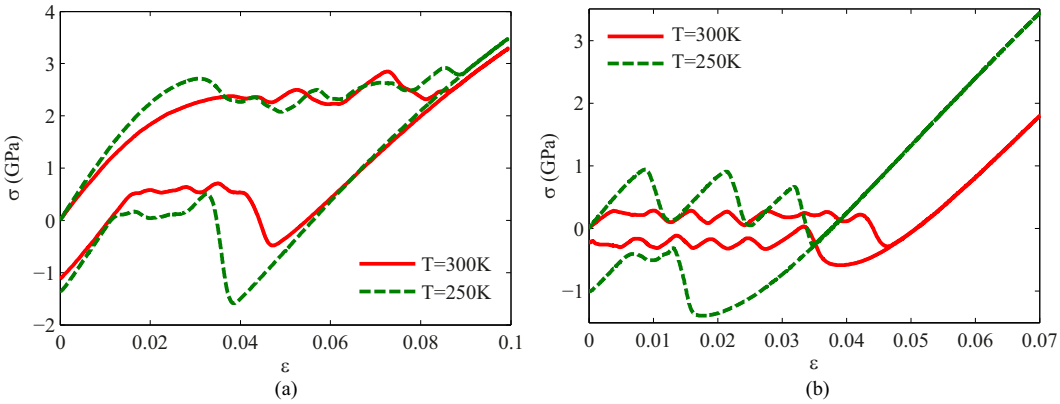

Figure 5.16: The stress-strain curves for a 12.8nm×12.8nm×13.5nm supercell with periodic boundary conditions subjected to axial tensile loading-unloading when (a) all the pressure components are relaxed during cooling and equilibration stages, and (b) only the normal pressure components are relaxed during cooling and equilibration stages.

this single variant of B19 phase is associated with an elastic response of this phase (the stress-strain curves are studied in detail in the next section). However at a specific strain, an abrupt change in the crystal structure is observed and several self-accommodated nanotwins are formed. Figure 5.17 shows the $[\bar{1}10]$ view of a 34nm × 12.8nm × 13.5nm nanowire subjected to 20% axial strain at 300K. It is observed that up to a strain level of $\epsilon \simeq 0.14$ the crustal structure is variant 1 of B19 phase. However, by further loading this nanowire, as shown for the strain values 0.18 and 0.2, several nanotwins are formes in the system. The BCO crystal structure is most prominent in these nanotwins.

Formation of these $[\bar{1}10]$ nanotwins can be explained by considering the Poisson effect. As the axial strain increases, the Poisson effect causes an increase in the lateral compression in the wire. At a critical lateral compression, the large compressive strain promotes strain accommodation by formation of multiple twinning. The twinning was previously reported for nanopillars subjected to an axial compression by Zhong et al. [196]. In the nanopillars subjected to axial compression, the twinning was observed at lower strain levels $\sim 5\%$ which is consistent with our results since the compressive lateral strain in tension is roughly one third the axial strain.

As another example consider a 34 nm × 8.5 nm × 9 nm nanowire subjected to 20% axial

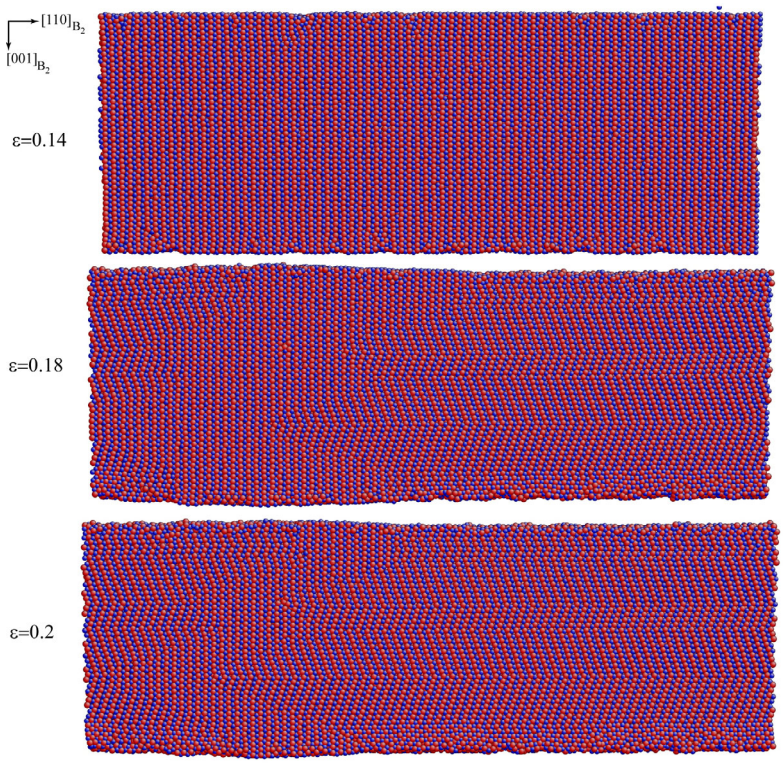

Figure 5.17: Formation of nanotwins in a 34nm × 12.8nm × 13.5nm nanowire subjected to 20% axial strain at 300K. The nanowire is viewed from $[\bar{1}10]$ direction.

strain at 275K. The response of this wire at 10% strain is studied in Section 5.4. Figure 5.18 shows the $[\bar{1}10]$ view of this wire when subjected to high axial strains.

It is observed that the self-accommodating nanotwins are formed at the high strain levels and comparing different strain values in Figure 5.18 reveals the initiation and propagation of these twins that initiates from the wire end and propagated toward the middle regions. Comparing the results given for small and large wires at different temperatures in Figures 5.17 and 5.18 shows that both the temperature and size affect the response of nanowires. Both these effects are more studied in the following section.

The [001] view of this wire is also shown in Figure 5.19. At $\epsilon = 0.05$ the wire is deformed due to the formation of several B19 multivariant nanotwins (see Figure 5.7). The whole wire is transformed to variant 1 which is more favorable by increasing the strain to 0.1. By increasing the strain, compressive strains promote formation of lateral nanotwins in the

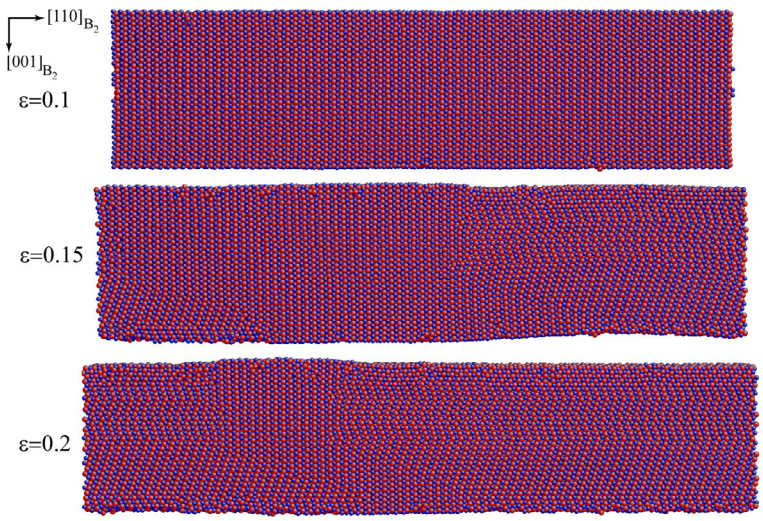

Figure 5.18: Formation of nanotwins in a 34nm × 8.5nm × 9nm nanowire subjected to 20% axial strain at 275K. The nanowire is viewed from $[\bar{1}10]$ direction.

wire. The size and temperature effects are more studied in the next section.

5.6 Size and Temperature Effects on the Response at High Strains

In this section the effect of size and temperature on the stress-strain response of NiTi nanowires subjected to high strains is studied. The simulation details are given in Section 5.5. As the first case study a NiTi nanowire with dimensions 34nm × 12.8nm × 13.5nm in x, y, and z directions is considered (See Figure 5.2(c)). The initial structure is B2 at high temperature T=500 K and the wire is cooled to three different temperatures T=300, 275, and 250 K. The wires are then loaded to a 20% axial strain in axial direction as expressed in Section 5.5. Figure 5.20(a) shows the stress-strain response of these nanowires at different temperatures (see Section 5.4.2 for a study on the effect of temperature on the stress-strain response corresponding the reorientation for strains bellow 10%).

Studying the stress-strain responses in Figure 5.20(a) shows that the formation of martensite lateral nanotwins in the wire is associated with an abrupt drop in the stress value which is consistent with the observed response in nanopillars subjected to an axial compression [196]. Also it is observed that the temperature slightly changes the critical

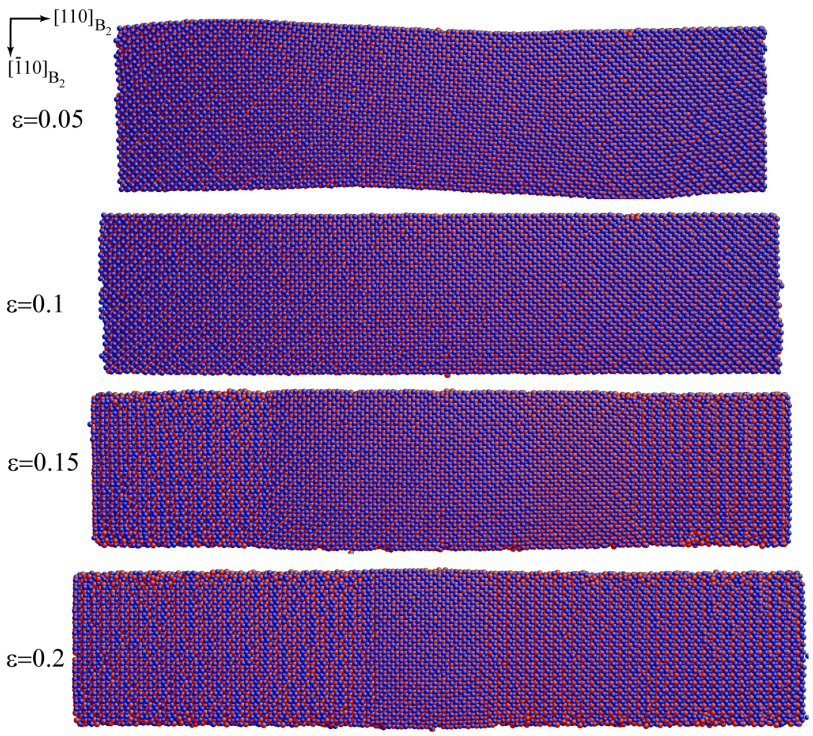

Figure 5.19: [001] view of 34nm × 8.5nm × 9nm nanowire subjected to 20% axial strain at 275K. Figures 5.7 and 5.18 show the reorientation of martensite at 10% strain and the formation of nanotwins at 20% strain for this wire, respectively. Blue and red atoms are Ni and Ti, respectively

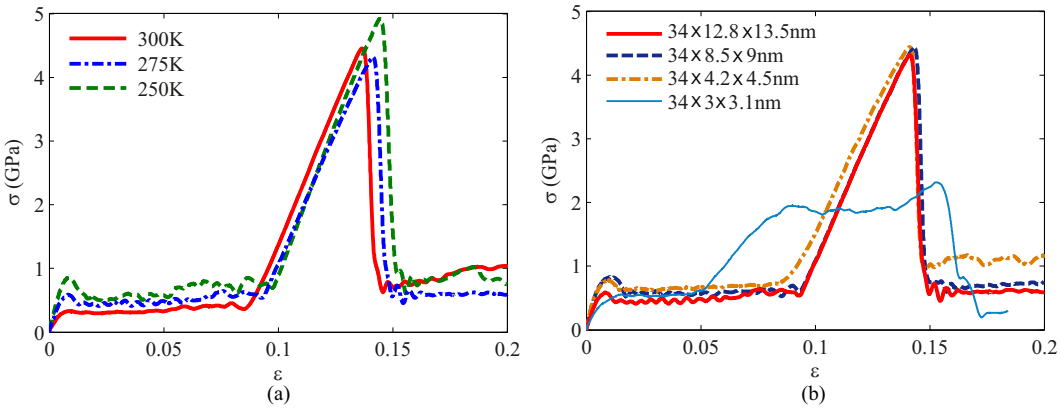

Figure 5.20: The effect of (a) temperature and (b) size on the stress-strain response of NiTi nanowires subjected to 20% axial strain

stress corresponding the start of twinning. Figure 5.20(b) shows the effect of size on the stress-strain response of wires. Four different cross section sizes are selected while the axial length of the wire is kept constant. All the wires are studied at T=275 K. It is observed that the mechanical response is very similar for three sizes while the response of the smallest wire with a 3nm $\times$ 3.1nm cross section is different. This phenomenon is due to the different transformation mechanism in the small wire as studied in Figure 5.21.

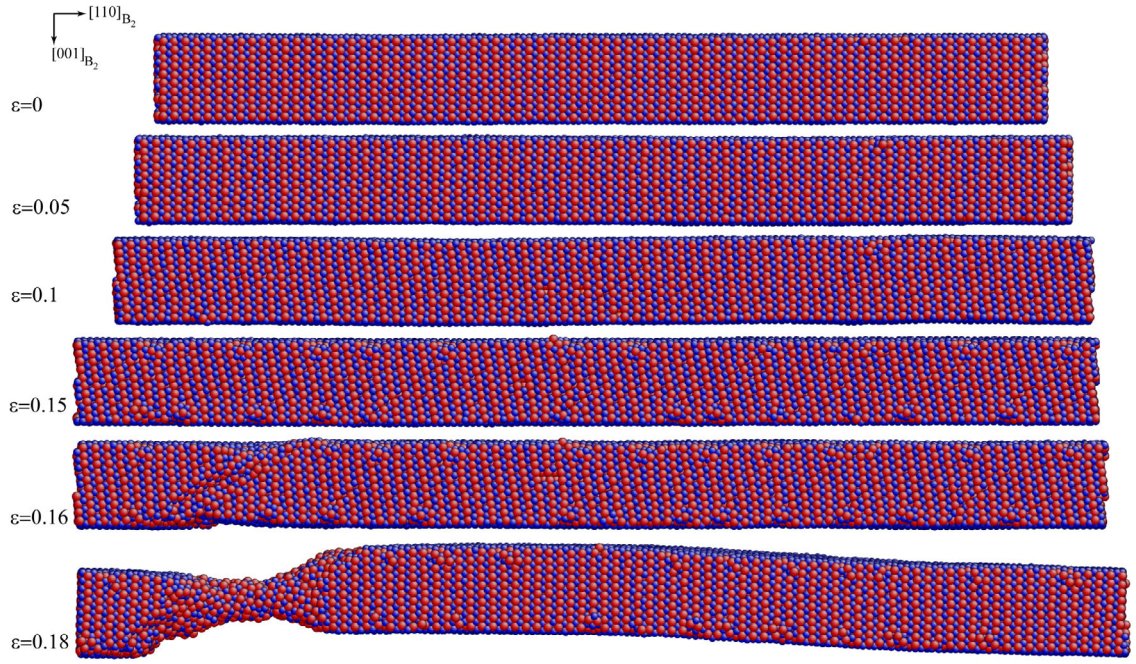

Figure 5.21: Phase transformation mechanism in a 34nm$\times$3nm$\times$3.1nm nanowire subjected to 18% axial strain at 275K. The nanowire is viewed from $[\bar{1}10]$ direction.

The initial configuration after cooling from a high temperature to T=275 K is shown in Figure 5.21($\epsilon = 0$). In contrast with the larger wires (i.e. Figure 5.5) the B2$\rightarrow$B19 transformation happens in the whole wire almost simultaneously in this thin wire instead of a nanotwin propagation that was observed in larger wires. This transformation is completed at lower strain levels ($\epsilon \simeq 0.05$). Further loading the wire in axial direction stimulates a B2$\rightarrow$B19' transformation in the whole wire (see $\epsilon = 0.05$ and 0.15 in Figure 5.5). The transformation mechanism in this stage is different from the larger wires in which self-accommodated nanotwins were formed in lateral direction (i.e. Figure 5.17). Plastic

deformation is observed at higher strain levels $\epsilon \simeq 0.16$ and the wire starts necking after this strain level as shown in Figure 5.21.

CHAPTER VI

CONCLUSIONS AND RECOMMENDED FUTURE RESEARCH

6.1 Summary and Conclusions

This research program introduces a multiscale analysis for SMAs, particularly Nickel-Titanium alloys (NiTi). SMAs are studied in a variety of length scales ranging from macroscale to nanoscale. Appropriate experiments are also performed for studying the mechanical and thermomechanical response of NiTi shape memory alloys at large scales. The research covers the following four major topics at different scales:

Phenomenological macroscale modeling: Large polycrystalline SMAs are studied in this work using a phenomenological macroscopic framework. Micromechanical properties are used for obtaining the macroscopic free energy potential, and the phenomenological constitutive equations are derived using this energy potential. The macroscopic phenomenological constitutive models are usually implemented in a numerical framework, particularly the finite element method, for simulating the mechanical response of SMA polycrystallines. However, numerical simulations have many drawbacks in modeling SMAs, including the convergence issues and the time consuming iterative simulations. In this research, closed-form solutions are presented for studying various SMA devices subjected to different types of loading, including uniaxial loads, torsion, bending, and also thick-walled SMA cylinders subjected to internal pressure. The results of introduced closed-form solutions are validated by performing various experiments on some large SMA elements.

Thermomechanical coupling in SMAs: The martensitic phase transformation in SMAs is associated with generation or absorption of latent heat in forward (austenite to martensite) and reverse (martensite to austenite) transformations. the effect of phase transformation induced latent heat is added to the solutions obtained based on the phenomenological constitutive framework and the coupled thermomechanical response

of SMAs is also studied. It is shown that the thermomechanics can be considered as the origin of rate and size dependency in SMAs. The thermomechanical response is studied experimentally as well by measureing the temperature changes due to the phase transformation latent heat at the surface of SMA specimens subjected to various loadings. The theoretical coupled thermomechanical models is calibrated using the experimentally measured temperatures at the surface. The calibrated model is then used for calculating the temperature distribution inside the device (which is practically difficult to be measured in tests). The obtained full temperature distribution is the basis for studying the complex effects of size, loading rate, and ambient condition on the response of SMA devices.

Micromechanical modeling: The phenomenological macroscopic frameworks are not capable of studying many important phenomena related to thermomechanical response of SMAs, including the texture effect and the intergranular effects in polycrystalline SMAs. In order to overcome these shortages, a micromechanical framework with a realistic modeling of the grains in a polycrystal SMA is used. A constitutive model based on the micromechanics of single crystals of SMAs is used for studying the pseudoelastic response of polycrystalline SMAs subjected to uniaxial and bending loads. By introducing a set of martensitic volume fractions corresponding to each active variant, the total transformation strain is obtained as a function of stress-free transformation strains of 24 correspondence variant pairs (CVPs) obtained from the crystallographic data for NiTi. Compared to the available micromechanical-based models in the literature, an improved coupled thermomechanical framework is introduced for polycrystalline SMAs by coupling the energy balance equation obtained from the first law of thermodynamics to the mechanical constitutive equations. The microstructure of polycrystalline SMAs is simulated accurately by using Voronoi tessellations in a three-dimensional finite element model and various samples with different number of grains and shapes are modeled for studying various aspects of the thermomechanical response of polycrystalline NiTi shape memory alloys. The effect of crystallographic texture on the thermomechanical response of NiTi is studied by assigning appropriate

crystallographic orientations in the grains. The interaction between the stress state (tensile or compressive), size (modeled by considering samples with different number of grains), and the crystallographic texture on the mechanical response and phase transformation propagation in polycrystalline SMAs is analyzed. The bending response of polycrystalline micropillars is also studied and the effect of size and crystallographic texture on the bending response is analyzed. Using the coupled thermomechanical framework for polycrystalline SMAs, the effect of loading rate and the phase transformation latent heat on the response of textured and untextured NiTi samples is studied. It is shown that the temperature changes due to the heat generation during phase transformation can affect the propagation of martensite in samples subjected to high strain rates.

Nanoscale study: Several aspects of the thermomechanical properties of SMAs cannot be studied neither by the phenomenological constitutive models nor by the micromechanical models. Both the mentioned models rely on the properties of the SMAs in atomistic scale, and studying the the martensitic phase transformation in nanoscale can shed light upon many unknown properties of these materials in the macroscopic level. In this research the temperature induced phase transformation and also the stress induced transformation in various NiTi systems at different temperatures is studied. The reorientation in martensite at lower temperatures is also studied. It is observed that besides the B2↔B19' transformation that occurs in large systems representing the bulk material (simulated as supercells with periodic boundary conditions), a B2↔B19 transformation also may happen in some special cases, particularly in NiTi nanowires that the surface-to-volume ratio is extremely high similar to the phenomenon which is recently reported by Zhong and Zhu [194] for NiTi thin films based on performing Monte Carlo simulations. By considering different simulation boxes and various temperatures, the size and temperature effects on the pseudoelastic response of NiTi alloys are studied. Several new aspects of the austenite-martensite phase transformation and reorientation of martensite variants are introduced in Chapter 5.

6.2 Recommended Future Research

Some areas of potential future work are as follows:

- Studying the large strain effects in bending analysis of SMA superelastic beams is an important extension of the work presented in Section 2.5, which can be obtained using the approximation III in this section. This approximation can also be used for developing a closed-form solution based on higher-order beam theories.

- Adding the thermomechanical coupling effect to the present solution for studying bending enables it to consider the phase transformation latent heat effect on the superelastic bending of SMA beams. This improvement leads to a comprehensive solution capable of modeling the rate dependency, ambient condition effects, and size effect in the response of superelastic SMA beams in bending.

- Performing in-situ texture measurements on NiTi samples during phase transformation and comparing the obtained results with the theoretical solutions calculated by the micromechanical framework of Chapter 4.

- Using efficient computational tools for modeling larger polycrystalline samples with larger number of grains in order to study the behavior of bulk material. Imposing periodic boundary conditions, which is challenging in models based on Voronoi tessellations can also improve the numerical results of the micromechanical model.

- The micromechanical model can be improved by considering a more comprehensive combination of twinning systems in NiTi based on experimental data.

- The nanoscale study can be improved by performing a detailed analyze on the structures with various crystal orientations. Many aspects of martensitic phase transformation can be studied by scrutinizing the thermomechanical response of NiTi nanowires and periodic supercells at different orientations.

- The stress induced martensitic phase transformation at high temperatures can be added to the nanoscale study of this research.

- This research can be used for designing experimental tests on NiTi naowires. The results can shed light to expectations from such a test because all the analyzes of this research are on NiTi at near room temperatures that would be the environment temperature if an in-situ test is designed for NiTi nanowires.

Bibliography

[1] http://lammps.sandia.gov (accessed may 26, 2013).

[2] Abramowitz, M. and Stegun, I. A. *Handbook of Mathematical Functions with Formulas, Graphs and Mathematical Tables.* National Bureau of Standards Applied Mathematics, Washington, 1964.

[3] Airoldi, G., Riva, G., Rivolta, B., and Vanelli, M. Dsc calibration in the study of shape memory alloys. *Journal of Thermal Analysis and Calorimetry*, 42:781–791, 1994.

[4] Anand, L. and Kothari, M. A computational procedure for rate-independent crystal plasticity. *Journal of the Mechanics and Physics of Solids*, 44(4):525–558, 1996.

[5] Anand, L. and Gurtin, M. E. Thermal effects in the superelasticity of crystalline shape-memory materials. *Journal of the Mechanics and Physics of Solids*, 51(6):1015 – 1058, 2003.

[6] Ancker, C. J. and Goodier, J. N. Pitch and and curvature corrections for helical springs. *Transactions of the ASME-Journal of Applied Mechanics*, 25:466–470, 1958.

[7] Ancker, C. J. and Goodier, J. N. Theory of pitch and curvature corrections for the helical springs-I (tension). *Transactions of the ASME-Journal of Applied Mechanics*, 25:471–483, 1958.

[8] Ancker, C. J. and Goodier, J. N. Theory of pitch and curvature corrections for the helical springs-II (torsion). *Transactions of the ASME-Journal of Applied Mechanics*, 25:484–495, 1958.

[9] Andrawes, B. and DesRoches, R. Comparison between shape memory alloy seismic restrainers and other bridge retrofit devices. *Journal of Bridge Engineering*, 12 (6):700–709, 2007.

[10] Andrawes, B. and DesRoches, R. Sensitivity of seismic applications to different shape memory alloy models. *ASCE Journal of Engineering Mechanics*, 134(2):173–183, 2008.

[11] Arpaci, V. S. *Conduction heat transfer*. Addison-Wesle: Reading.

[12] Atanackovic, T. and Achenbach, M. Moment-curvature relations for a pseudoelastic beam. *Continuum Mechanics and Thermodynamics*, 1:73–80, 1989.

[13] Auricchio, F. and Sacco, E. A temperature-dependent beam for shape-memory alloys: constitutive modelling, finite-element implementation and numerical simulations. *Computer Methods in Applied Mechanics and Engineering*, 174:171–190, 1999.

[14] Auricchio, F., Taylor, R. L., and Lubliner, J. Shape-memory alloys: macromodelling and numerical simulations of the superelastic behavior. *Computer Methods in Applied Mechanics and Engineering*, 146:281–312, 1997.

[15] Auricchio, F., Fugazza, D., and DesRoches, R. Numerical and experimental evaluation of the damping properties of shape-memory alloys. *Journal of Engineering Materials and Technology-Transactions of the ASME*, 128(3):312–319, 2006.

[16] Auricchio, F., Fugazza, D., and Desroches, R. Rate-dependent thermomechanical modelling of superelastic shape-memory alloys for seismic applications. *Journal of Intelligent Material Systems and Structures*, 19(1):47 – 61, 2008.

[17] Auricchio, F., Reali, A., and Stefanelli, U. A macroscopic 1D model for shape memory alloys including asymmetric behaviors and transformation-dependent elastic properties. *Computer Methods in Applied Mechanics and Engineering*, 198(17-20): 1631 – 1637, 2009.

[18] Auricchio, F. and Sacco, E. Thermo-mechanical modelling of a superelastic shape-memory wire under cyclic stretchingbending loadings. *International Journal of Solids and Structures*, 38(34-35):6123 – 6145, 2001.

[19] Auricchio, F., Morganti, S., Reali, A., and Urbano, M. Theoretical and experimental study of the shape memory effect of beams in bending conditions. *Journal of Materials Engineering and Performance*, 20(4-5):712 – 718, 2011.

[20] Bernardini, D. and Vestroni, F. Non-isothermal oscillations of pseudoelastic devices. *International Journal of Non-Linear Mechanics*, 38:1297–1313, 2003.

[21] Bhattacharya, K. *Microstructure of Martensite: Why It Forms and How It Gives Rise to the Shape-Memory Effect*. Oxford University Press, 2003.

[22] Bhattacharya, K. and James, R. The material is the machine. *Science*, 307(5706): 53–54, 2005.

[23] Birman, V. Review of mechanics of shape memory alloy structures. *Applied Mechanics Reviews*, 50(1):629–645, 1997.

[24] Birman, V. Analysis of an infinite shape memory alloy plate with a circular hole subjected to biaxial tension. *International Journal of Solids and Structures*, 36:167–178, 1999.

[25] Bo, Z. and Lagoudas, D. C. Thermomechanical modeling of polycrystalline smas under cyclic loading, part I: theoretical derivations. *International Journal of Engineering Science*, 37(9):1089 – 1140, 1999.

[26] Boots, B. The arrangement of cells in random networks. *Metallography*, 15(1):53 – 62, 1982.

[27] Boresi, A. P. and Schmidt, R. J. *Advanced mechanics of materials. 6th ed.* John Wiley and Sons, Hoboken, USA, 2003.

[28] Boyd, J. G. and Lagoudas, D. C. Thermodynamical constitutive model for shape memory materials. part I. the monolithic shape memory alloy. *International Journal of Plasticity*, 12(6):805 – 842, 1996.

[29] Brinson, L. C. One-dimensional constitutive behavior of shape memory alloy: thermomechanical derivation with non-constant material functions and redefined martensite internal variable. *Journal of Intelligent Material Systems and Structures*, 4:229–42, 1993.

[30] Brook, G. B. Applications of Titanium-Nickel shape memory alloys. *Materials and Design*, 4(4):835–840, 1983.

[31] Buchheit, T. E. and Wert, J. A. Modeling the effects of stress state and crystal orientation on the stress-induced transformation of NiTi single crystals. *Metallurgical and Materials Transactions A-physical Metallurgy and Materials Science*, 25:2383–2389, 1994.

[32] Cardano, G., Witmer, T. R., and Ore, O. *The Rules Of Algebra: (ars Magna)*. Dover Publications, 2007.

[33] Cebeci, T. Laminar free convective heat transfer from the outer surface of a vertical slender circular cylinder. *Proc. 5th Int. Heat Transfer Conference*, 3:15–19, 1974.

[34] Chang, B. C., Shaw, J., and Iadicola, M. Thermodynamics of shape memory alloy wire: Modeling, experiments, and application. *Continuum Mechanics and Thermodynamics*, 18:83–118, 2006.

[35] Chang, L. C. and Read, T. A. Plastic deformation and diffusionless phase changes in metals-the Gold-Cadmium beta-phase. *Transactions of the American Institute of Mining and Metallurgical Engineering*, 191(1):47–52, 1951.

[36] Chang, L. C. and Read, T. A. Experimental evidence of relaxation diffusionless phase changes of single crystal beta-AU-CD alloys containing 47.5 atomic percent CD. *Physical Review*, 82(5):770–770, 1951.

[37] Chen, T. A homogeneous elliptical shaft may not warp under torsion. *Acta Mechanica*, 169:221–224, 2004.

[38] Chen, Y. C. and Lagoudas, D. C. Impact induced phase transformation in shape memory alloys. *Journal of the Mechanics and Physics of Solids*, 48(2):275–300, 2000.

[39] Chung, J. H., Heo, J. S., and Lee, J. J. Modeling and numerical simulation of the pseudoelastic behavior of shape memory alloy circular rods under tension-torsion combined loading. *Smart Materials and Structures*, 15:1651–1660, 2006.

[40] Clark, B. G., Gianola, D. S., Kraft, O., and Frick, C. P. Size independent shape memory behavior of nickel-titanium. *Advanced Engineering Materials*, 12(8): 808 – 815, 2010.

[41] Coulomb, C. A. Recherches théoriques et expérimentales sur la force de torsion, et sur l'élasticité des fils de métal. *Mémoires of the Académie Royale des Sciences*, 1784: 229–69.

[42] DesRoches, B. A. R. Effect of hysteretic properties of superelastic shape memory alloys on the seismic performance of structures. *Structural Control and Health Monitoring*, 14:301–320, 2007.

[43] DesRoches, R. and Delemont, M. Seismic retrofit of simply supported bridges using shape memory alloys. *Engineering Structures*, 24(3):325–332, 2002.

[44] DesRoches, R. and Smith, B. Shape memory alloys in seismic resistant design and retrofit: a critical review of their potential and limitations. *Journal of Earthquake Engineering*, 8:415–29, 2004.

[45] DesRoches, R., Taftali, B., and Ellingwood, B. R. Seismic performance assessment of steel frames with shape memory alloy connections. part I analysis and seismic demands. *Journal of Earthquake Engineering*, 14(4):471–486, 2010.

[46] Diao, J. K., Gall, K., and Dunn, M. L. Surface-stress-induced phase transformation in metal nanowires. *Nature Materials*, 2(10):656–660, 2003.

[47] Dolce, M. and Cardone, D. Mechanical behaviour of shape memory alloys for seismic applications 1. martensite and austenite niti bars subjected to torsion. *International Journal of Mechanical Sciences*, 43(11):2631 – 2656, 2001.

[48] Dong, Y., Boming, Z., and Jun, L. A changeable aerofoil actuated by shape memory alloy springs. *Materials Science and Engineering A*, 485:243 – 250, 2008.

[49] Entemeyer, D., Patoor, E., Eberhardt, A., and Berveiller, M. Strain rate sensitivity in superelasticity. *International journal of plasticity*, 16(10):1269 – 1288, 2000.

[50] Fand, R. M. Heat transfer by forced convection from a cylinder to water in crossflow. *International Journal of Heat and Mass Transfer*, 8(7):995–1010, 1965.

[51] Feng, X. Q. and Sun, Q. P. Shakedown analysis of shape memory alloy structures. *International Journal of Plasticity*, 23(2):183–206, 2007.

[52] Feng, X. Q. and Sun, Q. P. In situ profilometry for non-uniform strain field measurement of NiTi shape memory alloy microtubing under complex stress states. *Smart Materials and Structures*, 16(1):S179–S186, 2007.

[53] Finnis, M. W. and Sinclair, J. E. A simple empirical N-body potential for transition metals. *Philosophical Magazine A*, 50(1):45–55, 1984.

[54] Flor, D. L. S., Urbina, C., and Ferrando, F. Asymmetrical bending model for niti shape memory wires: Numerical simulations and experimental analysis. *Strain*, 47(3):255 – 267, 2011.

[55] Forsythe, G. E., Malcolm, M. A., and Moler, C. B. *Computer methods for mathematical computations.* Prentice-Hall, 1976.

[56] Frick, C. P., Ortega, A. M., Tyber, J., Gall, K., and Maier, H. J. Multiscale structure and properties of cast and deformation processed polycrystalline niti shape-memory alloys. *Metallurgical and Materials Transactions A: Physical Metallurgy and Materials Science*, 35 A(7):2013 – 2025, 2004.

[57] Frick, C., Orso, S., and Arzt, E. Loss of pseudoelasticity in nickel-titanium sub-micron compression pillars. *Acta Materialia*, 55(11):3845 – 3855, 2007.

[58] Fritzen, F., Böhlke, T., and Schnack, E. Periodic three-dimensional mesh generation for crystalline aggregates based on voronoi tessellations. *Computational Mechanics*, 43:701–713, 2009.

[59] Gall, K. and Sehitoglu, H. The role of texture in tension-compression asymmetry in polycrystalline NiTi. *International journal of plasticity*, 15(1):69–92, 1999.

[60] Gall, K., Sehitoglu, H., Chumlyakov, Y., and Kireeva, I. Tension-compression asymmetry of the stress-strain response in aged single crystal and polycrystalline NiTi. *Acta Materialia*, 47(4):1203 – 1217, 1999.

[61] Gall, K., Sehitoglu, H., Chumlykov, Y., Kireeva, I., and Maier, H. The influence of aging on critical transformation stress levels and martensite start temperatures in NiTi: Part II-discussion of experimental results. *Transactions of the ASME. Journal of Engineering Materials and Technology*, 121(1):28–37, 1999.

[62] Gall, K., Lim, T. J., McDowell, D. L., Sehitoglu, H., and Chumlyakov, Y. I. The role of intergranular constraint on the stress-induced martensitic transformation in textured polycrystalline NiTi. *International Journal of Plasticity*, 16(10 - 11):1189 – 1214, 2000.

[63] Gall, K., Sehitoglu, H., Anderson, R., Karaman, I., Chumlyakov, Y. I., and Kireeva, I. V. On the mechanical behavior of single crystal NiTi shape memory alloys and related polycrystalline phenomenon. *Materials Science and Engineering A*, 317(1-2):85 – 92, 2001.

[64] Gao, X., Huang, M., and Brinson, L. A multivariant micromechanical model for smas part 1. crystallographic issues for single crystal model. *International Journal of Plasticity*, 16(1011):1345 – 1369, 2000.

[65] Gao, X., Stebner, A., Brown, D. W., and Brinson, L. C. Neutron diffraction studies and multivariant simulations of shape memory alloys: Concurrent verification of texture development and mechanical response predictions. *Acta Materialia*, 59(15): 5924 – 5937, 2011.

[66] Gillet, Y., Patoor, E., and Berveiller, M. Calculation of pseudoelastic elements using a non-symmetrical thermomechanical transformation criterion and associated rule. *Journal of Intelligent Material Systems and Structures*, 9:366–378, 1998.

[67] Goldberg, D. E. *Genetic algorithms in search, optimization, and machine learning*. Addison-Wesley, London, 1989.

[68] Goo, B. C. and Lexcellent, C. Micromechanics-based modeling of two-way shape memory effect of a single crystalline shape memory alloy. *Acta Metallurgica et Materialia*, 45(2):727–737, 1997.

[69] Hane, K. and Shield, T. Microstructure in the cubic to monoclinic transition in titaniumnickel shape memory alloys. *Acta Materialia*, 47(9):2603 – 2617, 1999.

[70] Hartl, D. J. and Lagoudas, D. C. Aerospace applications of shape memory alloys. *Proceedings of the Institution of Mechanical Engineers, Part G: Journal of Aerospace Engineering*, 221(4):535 – 552, 2007.

[71] He, X. and Rong, L. Dsc analysis of reverse martensitic transformation in deformed tininb shape memory alloy. *Scripta Materialia*, 51(1):7 – 11, 2004. ISSN 1359-6462.

[72] He, Y. J. and Sun, Q. P. Scaling relationship on macroscopic helical domains in niti tubes. *International Journal of Solids and Structures*, 46:4242–4251, 2009.

[73] Higgins, T. J. A comprehensive review of saint-venant's torsion problem. *American Journal of Physics*, 10(5):248 – 259, 1942.

[74] Hilpert, R. Wärmeabgabe yon geheizten drähten und rohern im lufstrom. *Forsch. Geb. Ingenieurw*, 4:215–224, 1933.

[75] Holman, J. *Heat transfer. 7th ed.* McGraw-Hill: New York, 1990.

[76] Huang, X. Y., Ackland, G. J., and Rabe, K. M. Crystal structures and shape-memory behaviour of NiTi. *Nature Materials*, 2(5):307–311, 2003.

[77] Iadicola, M. A. and Shaw, J. A. Rate and thermal sensitivities of unstable transformation behavior in a shape memory alloy. *International Journal of Plasticity*, 20: 577–605, 2004.

[78] Idesman, A., Levitas, V., Preston, D., and Cho, J.-Y. Finite element simulations of martensitic phase transitions and microstructures based on a strain softening model. *Journal of the Mechanics and Physics of Solids*, 53(3):495 – 523, 2005.

[79] Jacobus, K., Sehitoglu, H., and Balzer, M. Effect of stress state on the stress-induced martensitic transformation in polycrystalline Ni-Ti alloy. *Metallurgical and Materials Transactions A*, 27:3066–3073, 1996.

[80] Jee, K. K., Hana, J. H., and Jang, W. Y. A method of pipe joining using shape memory alloys. *Materials Science and Engineering A*, 438-440:1110–1112, 2006.

[81] Juan, J. S., No, M. L., and Schuh, C. A. Nanoscale shape-memory alloys for ultrahigh mechanical damping. *Nature Nanotechnology*, 4(7):415–419, 2009.

[82] Kahn, H., Huff, M. A., and Heuer, A. H. The TiNi shape-memory alloy and its applications for MEMS. *Journal of Micromechanics and Microengineering*, 8(3): 213–221, 1998.

[83] Kastner, O. Molecular-dynamics of a 2D model of the shape memory effect-part I: Model and simulations. *Continuum Mechanics and Thermodynamics*, 15:487–502, 2003.

[84] Kastner, O. Molecular-dynamics of a 2D model of the shape memory effect-Part II: Thermodynamics of a small system. *Continuum Mechanics and Thermodynamics*, 18:63–81, 2006.

[85] Kastner, O. and Ackland, G. J. Mesoscale kinetics produces martensitic microstructure. *Journal of the Mechanics and Physics of Solids*, 57(1):109 – 121, 2009.

[86] Kim, C., Jang, D. H., and Choi, H. S. An externally pressurized elliptic composite cylinder stiffened with activated SMA strips. In *43rd AIAA/ASME/ASCE/AHS/ASC Structures Structural Dynamics, and Materials Conference*, pages 22–25, Denver, Colorado, April 2002.

[87] Kim, J.-Y. and Greer, J. R. Tensile and compressive behavior of gold and molybdenum single crystals at the nano-scale. *Acta Materialia*, 57(17):5245 – 5253, 2009.

[88] Kim, J.-Y., Jang, D., and Greer, J. R. Insight into the deformation behavior of niobium single crystals under uniaxial compression and tension at the nanoscale. *Scripta Materialia*, 61(3):300 – 303, 2009.

[89] Knudsen, J. G. and Katz, D. L. *Fluid Dynamics and Heat Transfer*. McGraw-Hill, New York, 1958.

[90] Krulevitch, P., Lee, A., Ramsey, P., Trevino, J., Hamilton, J., and Northrup, M. Thin film shape memory alloy microactuators. *Journal of Microelectromechanical Systems*, 5(4):270 – 282, 1996.

[91] Kuribayashi, K., Tsuchiya, K., You, Z., Tomusb, D., Umemotob, M., Ito, T., and Sasaki, M. Self-deployable origami stent grafts as a biomedical application of Ni-rich TiNi shape memory alloy foil. *Materials Science and Engineering A*, 419: 131–137, 2006.

[92] Lagoudas, D. C. *Shape memory alloys: modeling and engineering applications.* Springer: New York, 2008.

[93] Lagoudas, D. C. and Entchev, P. B. Modeling of transformation-induced plasticity and its effect on the behavior of porous shape memory alloys part I: constitutive model for fully dense smas. *Mechanics of Materials*, 36(9):865–892, 2004.

[94] Lagoudas, D. C., Ravi-Chandar, K., Sarh, K., and Popov, P. Dynamic loading of polycrystalline shape memory alloy rods. *Mechanics of Materials*, 35(7):689 – 716, 2003.

[95] Lagoudas, D. C., Entchev, P. B., Popov, P., Patoor, E., Brinson, L. C., and Gao, X. Shape memory alloys, part ii: Modeling of polycrystals. *Mechanics of Materials*, 38(5-6):430 – 462, 2006.

[96] Lagoudas, D. C., Bo, Z., and Qidwai, M. A. Unified thermodynamic constitutive model for sma and finite element analysis of active metal matrix composites. *Mechanics of composite materials and structures*, 3(2):153 – 179, 1996.

[97] Lai, W. S. and Liu, B. X. Lattice stability of some Ni-Ti alloy phases versus their chemical composition and disordering. *Journal of Physics: Condensed Matter*, 12(5): L53, 2000.

[98] Langelaar, M. and Keulen, F. V. Modeling of a shape memory alloy active catheter.

[99] Leclercq, S. and Lexcellent, C. A general macroscopic description of the thermomechanical behavior of shape memory alloys. *Journal of the Mechanics and Physics of Solids*, 44(6):953 – 980, 1996.

[100] Leea, C. Y., Zhuob, H. C., and Hsu, C. W. Lateral vibration of a composite stepped beam consisted of sma helical spring based on equivalent euler-bernoulli beam theory. *Journal of Sound and Vibration*, 324:179–193, 2009.

[101] Levitas, V. I., Idesman, A. V., and Preston, D. L. Microscale simulation of martensitic microstructure evolution. *Phys. Rev. Lett.*, 93:105701, 2004.

[102] Li, Z. Q. and Sun, Q. P. The initiation and growth of macroscopic martensite band in nano-grained NiTi microtube under tension. *International Journal of Plasticity*, 18:1481–1498, 2002.

[103] Liang, C. and Rogers, C. A. The multi-dimensional constitutive relations of shape memory alloys. *Journal of Engineering Mathematics*, 26:429–443, 1992.

[104] Liang, C. and Rogers, C. A. Design of shape memory alloy springs with applications in vibration control. *Journal of Intelligent Material Systems and Structures*, 8 (4):314–322, 1997.

[105] Liang, W. and Zhou, M. Atomistic simulations reveal shape memory of fcc metal nanowires. *Phys. Rev. B*, 73:115409, 2006.

[106] Liang, W., Zhou, M., and Ke, F. Shape memory effect in cu nanowires. *Nano Letters*, 5(10):2039 – 2043, 2005.

[107] Liew, K. M., Kitipornchai, S., Ng, T. Y., and Zou, G. P. Multi-dimensional superelastic behavior of shape memory alloys via nonlinear finite element method. *Engineering Structures*, 24:51–57, 2002.

[108] Lim, T. J. and McDowell, D. L. Mechanical behavior of an Ni-Ti shape memory alloy under axial-torsional proportional and nonproportional loading. *Journal of Engineering Materials and Technology-Transactions of the ASME*, 121(1):9–18, 1999.

[109] Lim, T. *Behavior of a NiTi shape memory alloy under cyclic proportional and nonproportional loading*. Ph.D. Thesis, Georgia Institute of Technology, Atlanta, Georgia, 1999.

[110] Lim, T. and McDowell, D. Cyclic thermomechanical behavior of a polycrystalline pseudoelastic shape memory alloy. *Journal of the Mechanics and Physics of Solids*, 50(3):651 – 676, 2002.

[111] Liu, J.-Y., Lu, H., Chen, J.-M., and Zhang, Z. Finite element simulation of martensitic transition based on thermo-mechanical model. *Materials Science and Engineering: A*, 448(1-2):204 – 209, 2007.

[112] Liu, N. and Huang, W. M. DSC study on temperature memory effect of NiTi shape memory alloy. *Transactions of Nonferrous Metals Society of China*, 16:s37–s41, 2006.

[113] Liu, Y., Xie, Z., Humbeeck, J. V., and Delaey, L. Asymmetry of stress-strain curves under tension and compression for niti shape memory alloys. *Acta Materialia*, 46(12):4325 – 4338, 1998.

[114] Lu, Z. and Weng, G. A self-consistent model for the stressstrain behavior of shape-memory alloy polycrystals. *Acta Materialia*, 46(15):5423 – 5433, 1998.

[115] Machado, L. G. and Savi, M. A. Medical applications of shape memory alloys. *Brazilian Journal of Medical and Biological Research*, 36:683–691, 2003.

[116] Mahapatra, D. R. and Melnik, R. V. N. Finite element approach to modelling evolution of 3D shape memory materials. *Mathematics and Computers in Simulation*, 76:141–148, 2007.

[117] Manjeri, R. M., Qiu, S., Mara, N., Misra, A., and Vaidyanathan, R. Superelastic response of [111] and [101] oriented niti micropillars. *Journal of Applied Physics*, 108(2):023501, 2010.

[118] Marfia, S., Sacco, E., and Reddy, J. N. Superelastic and shape memory effects in laminated shape-memory-alloy beams. *AIAA Journal*, 41(1):100–109, 2003.

[119] Marketz, F. and Fischer, F. A micromechanical study on the coupling effect between microplastic deformation and martensitic transformation. *Computational Materials Science*, 3(2):307 – 325, 1994.

[120] Marketz, F. and Fischer, F. Modelling the mechanical behavior of shape memory alloys under variant coalescence. *Computational Materials Science*, 5(1-3):210 – 226, 1996.

[121] Matsumoto, O., Miyazaki, S., Otsuka, K., and Tamura, H. Crystallography of martensitic transformation in Ti-Ni single crystals. *Acta Metallurgica*, 35(8):2137 – 2144, 1987.

[122] McCormick, J. and DesRoches, R. The effect of training, pre-straining, and loading history on the properties of NiTi shape memory alloys for protective systems

in civil engineering. In *Proceedings of the ASCE Structures Congress*, St. Louis MO, 2006.

[123] McCormick, J., DesRoches, R., Fugazza, D., and Auricchio, F. Seismic vibration control using superelastic shape memory alloys. *Journal of Engineering Materials and Technology-Transactions of the ASME*, 128(3):294–301, 2006.

[124] McCormick, J., Tyber, J., DesRoches, R., Gall, K., and Maier, H. J. Structural engineering with niti. ii: Mechanical behavior and scaling. *Journal of Engineering Mechanics*, 133(9):1019 – 1029, 2007.

[125] Messner, C. and Werner, E. A. Temperature distribution due to localised martensitic transformation in SMA tensile test specimens. *Computational Materials Science*, 26:95–101, 2003.

[126] Mirzaeifar, R., Shakeri, M., and Sadighi, M. Nonlinear finite element formulation for analyzing shape memory alloy cylindrical panels. *Smart Materials and Structures*, 18(3):035002, 2009.

[127] Mirzaeifar, R., Desroches, R., and Yavari, A. Exact solutions for pure torsion of shape memory alloy circular bars. *Mechanics of Materials*, 42(8):797 – 806, 2010.

[128] Mirzaeifar, R., Desroches, R., and Yavari, A. Analysis of the rate-dependent coupled thermo-mechanical response of shape memory alloy bars and wires in tension. *Continuum Mechanics and Thermodynamics*, 23(4):363–385, 2011.

[129] Mirzaeifar, R., Desroches, R., and Yavari, A. A combined analytical, numerical, and experimental study of shape-memory-alloy helical springs. *International Journal of Solids and Structures*, 48(3-4):611 – 624, 2011.

[130] Mirzaeifar, R., Desroches, R., Yavari, A., and Gall, K. Coupled thermo-mechanical analysis of shape memory alloy circular bars in pure torsion. *International Journal of Non-Linear Mechanics*, 47(3):118–128, 2012.

[131] Mirzaeifar, R., Shakeri, M., DesRoches, R., and Yavari, A. A semi-analytic analysis of shape memory alloy thick-walled cylinders under internal pressure. *Archive of Applied Mechanics*, 81(8):1093–1116, 2011.

[132] Miyazaki, S., Otsuka, K., and Wayman, C. The shape memory mechanism associated with the martensitic transformation in Ti-Ni alloysI. self-accommodation. *Acta Metallurgica*, 37(7):1873–1884, 1989.

[133] Müller, I. and Seelecke, S. Thermodynamic aspects of shape memory alloys. *Mathematical and Computer Modelling*, 34(12-13):1307–1355, 2001.

[134] Müller, I. and Xu, H. On the pseudo-elastic hysteresis. *Acta Metallurgica Materialia*, 39(3):263–271, 1991.

[135] Mutter, D. and Nielaba, P. Simulation of structural phase transitions in niti. *Physical Review B*, 82(22):224201, 2010.

[136] Mutter, D. and Nielaba, P. Simulation of the shape memory effect in a niti nano model system. *Journal of Alloys and Compounds*, page In Press, 2012.

[137] Nishida, M., Itai, I., Kitamura, K., Chiba, A., and Yamauchi, K. Effect of grain size of parent phase on twinning modes of b19' martensite in an equiatomic ti-ni shape memory alloy. *Journal De Physique. IV : JP*, 5(8 pt 2):C8 – 635, 1995.

[138] Ono, N., Satoh, A., and Ohta, H. Discussion on the mechanical properties of shape memory alloys based on a polycrystal model. *Materials Transactions, JIM*, 30 (10):756 – 764, 1989.

[139] Otsuka, K. and Ren, X. Physical metallurgy of TiNi-based shape memory alloys. *Progress in Materials Science*, 50(5):511 – 678, 2005.

[140] Otsuka, K. and Wayman, C. M. *Shape memory materials*. Cambridge University Press, 1999.

[141] Özışık, M. N. *Finite difference methods in heat transfer*. CRC-Press: Boca Raton, Florida, 1994.

[142] Padgett, J. E., DesRoches, R., and Ehlinger, R. Experimental response modification of a four-span bridge retrofit with shape memory alloys. *Structural Control and Health Monitoring*, 17(6):694–708, 2010.

[143] Paine, J. S. N. and Rogers, C. A. Using the adaptive SMA composite cylinder concept to reduce radial dilation in composite pressure vessels. In *Proc. SPIE Vol. 2443. Smart Structures and Materials Smart Structures and Integrated Systems*, pages 195–205, 1995.

[144] Paine, J. S. N., Rogers, C. A., and Smith, R. A. Adaptive composite-materials with shape-memory alloy actuators for cylinders and pressure-vessels. *Journal of Intelligent Material Systems and Structures*, 6(2):210–219, 1995.

[145] Paiva, A., Savi, M. A., Braga, A. M. B., and Pacheco, P. M. C. L. A constitutive model for shape memory alloys considering tensile-compressive asymmetry and plasticity. *International Journal of Solids and Structures*, 42(11-12):3439 – 3457, 2005.

[146] Panico, M. and Brinson, L. A three-dimensional phenomenological model for martensite reorientation in shape memory alloys. *Journal of the Mechanics and Physics of Solids*, 55(11):2491 – 2511, 2007.

[147] Papadimitriou, C. H. and Steiglitz, K. *Combinatorial Optimization: Algorithms and Complexity*. Prentice-Hall, Englewood Cliffs, NJ, 1982.

[148] Paradis, A., Terriault, P., and Brailovski, V. Modeling of residual strain accumulation of NiTi shape memory alloys under uniaxial cyclic loading. *Computational Materials Science*, 47:373–383, 2009.

[149] Park, H. S. Stress-induced martensitic phase transformation in intermetallic nickel aluminum nanowires. *Nano Letters*, 6(5):958 – 962, 2006.

[150] Park, H. S., Gall, K., and Zimmerman, J. A. Shape memory and pseudoelasticity in metal nanowires. *Physical Review Letters*, 95:255504, 2005.

[151] Patoor, E., Eberhardt, A., and Berveiller, M. Micromechanical modelling of superelasticity in shape memory alloys. *Journal De Physique IV*, 6(1):C1–277 – C1–292, 1996.

[152] Patoor, E., Lagoudas, D. C., Entchev, P. B., Brinson, L. C., and Gao, X. Shape memory alloys, part i: General properties and modeling of single crystals. *Mechanics of Materials*, 38(5-6):391 – 429, 2006.

[153] Patoor, E., Elamrani, M., Eberhardt, A., and Berveiller, M. Determination of the origin for the dissymmetry observed between tensile and compression tests on shape-memory alloys. *Journal De Physique IV*, 5(C2):495–500, 1995.

[154] Petrini, L., Migliavacca, F., Massarotti, P., Schievano, S., Dubini, G., and Auricchio, F. Computational studies of shape memory alloy behavior in biomedical applications. *Journal of Biomechanical Engineering*, 127:716–725, 2005.

[155] Peultier, B., Zineb, T. B., and Patoor, E. Macroscopic constitutive law for SMA: Application to structure analysis by FEM. *Materials Science and Engineering: A*, 438-440:454 – 458, 2006.

[156] Plietsch, R. and Ehrlich, K. Strength differential effect in pseudoelastic NiTi shape memory alloys. *Acta Materialia*, 45(6):2417 – 2424, 1997.

[157] Plietsch, R., Bourauel, C., Drescher, D., and Nellen, B. Analytical description of the bending behaviour of niti shape-memory alloys. *Journal of Materials Science*, 29(22):5892 – 5902, 1994.

[158] Plimpton, S. Fast parallel algorithms for short-range molecular dynamics. *Journal of Computational Physics*, 117(1):1 – 19, 1995.

[159] Popiel, C. O. Free convection heat transfer from vertical slender cylinders: a review. *Heat Transfer Engineering*, 29(6):521 – 536, 2008.

[160] Purohit, P. K. and Bhattacharya, K. On beams made of a phase-transforming material. *International Journal of Solids and Structures*, 39(13-14):3907 – 3929, 2002.

[161] Qidwai, M. A. and Lagoudas, D. C. Numerical implementation of a shape memory alloy thermomechanical constitutive model using return mapping algorithms. *International Journal for Numerical Methods in Engineering*, 47(6):1123 – 1168, 2000.

[162] Qidwai, M. A. and Lagoudas, D. C. On thermomechanics and transformation surfaces of polycrystalline NiTi shape memory alloy material. *International journal of plasticity*, 16(10):1309 – 1343, 2000.

[163] Rajagopal, K. and Srinivasa, A. Mechanics of the inelastic behavior of materials. part I: Theoretical underpinnings. *International Journal of Plasticity*, 14(10-11):945–967, 1998.

[164] Saint-Sulpice, L., Chirani, S. A., and Calloch, S. A 3D super-elastic model for shape memory alloys taking into account progressive strain under cyclic loadings. *Mechanics of Materials*, 41:12–26, 2009.

[165] San Juan, J. M., No, M. L., and Schuh, C. A. Superelasticity and shape memory in micro- and nanometer-scale pillars. *Advanced Materials*, 20(2):272 – 278, 2008.

[166] Sato, T., Saitoh, K.-I., and Shinke, N. Molecular dynamics study on microscopic mechanism for phase transformation of Ni-Ti alloy. *Modelling and Simulation in Materials Science and Engineering*, 14(5):S39 – S46, 2006.

[167] Sehitoglu, H., Karaman, I., Anderson, R., Zhang, X., Gall, K., Maier, H., and Chumlyakov, Y. Compressive response of niti single crystals. *Acta Materialia*, 48(13):3311 – 3326, 2000.

[168] Shin, D. D., Mohanchandra, K. P., and Carman, G. P. Development of hydraulic linear actuator using thin film sma. *Sensors and Actuators, A: Physical*, 119 (1):151 – 156, 2005.

[169] Simo, J. C. and Hughes, T. J. R. *Computational inelasticity, Vol. 7 of interdisciplinary applied mathematics*. Springer–Verlag, New York, 1998.

[170] Simonovski, I. and Cizelj, L. The influence of grains crystallographic orientations on advancing short crack. *International Journal of Fatigue*, 29(9 - 11):2005 – 2014, 2007.

[171] Simonovski, I. and Cizelj, L. Automatic parallel generation of finite element meshes for complex spatial structures. *Computational Materials Science*, 50(5):1606 – 1618, 2011.

[172] Sokolnikoff, I. S. *Mathematical theory of elasticity*. McGraw-Hill. New York, 1956.

[173] Speicher, M., Hodgson, D. E., DesRoches, R., and Leon, R. T. Shape memory alloy tension/compression device for seismic retrofit of buildings. *Journal of Materials Engineering and Performance*, (18):746 – 753, 2009.

[174] Stebner, A., Gao, X., Brown, D. W., and Brinson, L. C. Neutron diffraction studies and multivariant simulations of shape memory alloys: Empirical texture developmentmechanical response relations of martensitic nickeltitanium. *Acta Materialia*, 59(7):2841 – 2849, 2011.

[175] Sun, Q. P. and Hwang, K. C. Micromechanics modelling for the constitutive behavior of polycrystalline shape memory alloysII. study of the individual phenomena. *Journal of the Mechanics and Physics of Solids*, 41(1):19 – 33, 1993.

[176] Sutrakar, V. K. and Mahapatra, D. R. Asymmetry in structural and thermomechanical behavior of intermetallic NiAl nanowire under tensile/compressive loading: A molecular dynamics study. *Intermetallics*, 18(8):1565 – 1571, 2010.

[177] Tanaka, K. A thermomechanical sketch of shape memory effect: One-dimensional tensile behavior. *Res mechanica*, 18(3):251–263, 1986.

[178] Tanaka, K. A phenomenological description on thermomechanical behavior of shape memory alloys. *ASME Journal of Pressure Vessel Technology*, 112:158–163, 1990.

[179] Tanaka, K., Kobayashi, S., and Sato, Y. Thermomechanics of transformation pseudoelasticity and shape memory effect in alloys. *International Journal of Plasticity*, 2:59–72, 1986.

[180] Tanaka, K., Nishimura, F., Hayashi, T., Tobushi, H., and Lexcellent, C. Phenomenological analysis on subloops and cyclic behavior in shape memory alloys under mechanical and/or thermal loads. *Mechanics of Materials*, 19:281 – 292, 1995.

[181] Tanaka, Y., Himuro, Y., Kainuma, R., Sutou, Y., Omori, T., and Ishida, K. Ferrous polycrystalline shape-memory alloy showing huge superelasticity. *Science*, 327:1488–1490, 2010.

[182] Thamburaja, P. and Anand, L. Polycrystalline shape-memory materials: effect of crystallographic texture. *Journal of the Mechanics and Physics of Solids*, 49(4):709 – 737, 2001.

[183] Thamburaja, P. and Anand, L. Superelastic behavior in tensiontorsion of an initially-textured Ti - Ni shape-memory alloy. *International Journal of Plasticity*, 18 (11):1607 – 1617, 2002.

[184] Tobushi, H. and Tanaka, K. Deformation of a shape memory alloy helical spring: Analysis based on stress-strain-temperature relation. *JSME International Journal, Series I*, 34:83–89, 1991.

[185] Toi, Y., Lee, J. B., and Taya, M. Finite element analysis of superelastic, large deformation behavior of shape memory alloy helical springs. *Computers and Structures*, 82:1685–1693, 2004.

[186] Tyber, J., McCormick, J., Gall, K., DesRoches, R., Maier, H., and Maksoud, A. E. A. Structural engineering with NiTi-I: Basic materials characterization. *Journal of Engineering Mechanics*, 133(9):1009–1018, 2007.

[187] Vitiello, A., Giorleo, G., and Morace, R. E. Analysis of thermomechanical behaviour of nitinol wires with high strain rates. *Smart Materials and Structures*, 14: 215–221, 2005.

[188] Voit, W., Ware, T., Dasari, R. R., Smith, P., Danz, L., Simon, D., Barlow, S., Marder, S. R., and Gall, K. High-strain shape-memory polymers. *Advanced Functional Materials*, 20:162–171, 2010.

[189] Volkert, C. A. and Minor, A. M. Focused ion beam microscopy and micromachining. *MRS Bulletin*, 32(5):389–395, 2007.

[190] Wahl, A. M. *Mechanical springs*. Penton publishing company. Cleveland. USA, 1944.

[191] Xua, M. B. and Song, G. Adaptive control of vibration wave propagation in cylindrical shells using SMA wall joint. *Journal of Sound and Vibration*, 278:307–326, 2004.

[192] Zhang, P., Balint, D., and Lin, J. An integrated scheme for crystal plasticity analysis: Virtual grain structure generation. *Computational Materials Science*, 50 (10):2854 – 2864, 2011.

[193] Zhang, X. and Sehitoglu, H. Crystallography of the B2 $\rightarrow$ R $\rightarrow$ B19' phase transformations in NiTi. *Materials Science and Engineering: A*, 374(1-2):292 – 302, 2004.

[194] Zhong, Y. and Zhu, T. Patterning of martensitic nanotwins. *Scripta Materialia*, 67:883–886, 2012.

[195] Zhong, Y., Gall, K., and Zhu, T. Atomistic study of nanotwins in niti shape memory alloys. *Journal of Applied Physics*, 110(3):6301–6311, 2011.

[196] Zhong, Y., Gall, K., and Zhu, T. Atomistic characterization of pseudoelasticity and shape memory in niti nanopillars. *Acta Materialia*, 60:6301–6311, 2013.